Fall 2013

Solar Cell Temperature Dependent Efficiency and Very High Temperature Efficiency Limits

John Robert Wilcox
Purdue University

Graduate School ETD Form 9
(Revised 12/07)

PURDUE UNIVERSITY
GRADUATE SCHOOL
Thesis/Dissertation Acceptance

This is to certify that the thesis/dissertation prepared

By John Wilcox

Entitled
Solar Cell Temperature Dependent Efficiency and Very High Temperature Efficiency Limits

For the degree of Doctor of Philosophy

Is approved by the final examining committee:

JEFFERY L. GRAY
Chair

MARK S. LUNDSTROM

MUHAMMAD A. ALAM

RAKESH AGRAWAL

To the best of my knowledge and as understood by the student in the *Research Integrity and Copyright Disclaimer (Graduate School Form 20)*, this thesis/dissertation adheres to the provisions of Purdue University's "Policy on Integrity in Research" and the use of copyrighted material.

Approved by Major Professor(s): JEFFERY L. GRAY

Approved by: V. Balakrishnan 12-02-2013
Head of the Graduate Program Date

SOLAR CELL TEMPERATURE DEPENDENT EFFICIENCY AND VERY HIGH TEMPERATURE EFFICIENCY LIMITS

A Dissertation

Submitted to the Faculty

of

Purdue University

by

John R. Wilcox

In Partial Fulfillment of the

Requirements for the Degree

of

Doctor of Philosophy

December 2013

Purdue University

West Lafayette, Indiana

To my loving wife Amy T. Wilcox and wonderful family.

Many wonderful educators and friends that have inspired me.

This great country.

ACKNOWLEDGMENTS

I would like to thank Professors Jeffery Gray and Richard Schwartz for their excellent guidance and instruction. They have been wonderful mentors. I would also like to thank Professors Mark Lundstrom, Ashraf Alam and Rakesh Agrawal for serving on my thesis committee, and Dr. Alex Haas, for his collaboration and research. Many thanks to Dr. Allen Gray, Dr. Myles Steiner, Dr. Mark Osowski, Dr. James McCambridge and JP Whitlock, their feedback and measurements have been invaluable. I appreciate the superb learning opportunities available at Purdue University. This work was supported the by the Very High Efficiency Solar Cell project, Advanced Research Projects Agency-Energy and Semiconductor Research Corporation through the Network for Photovoltaic Technology. Facilities and computer resources have been provided by Purdue's Birck Nanotechnology Center, Network for Computational Nanotechnology, Engineering Computer Network and the School of Electrical and Computer Engineering

.

TABLE OF CONTENTS

Page

Page

Page

Page

Page

Page

LIST OF TABLES

Table Page

LIST OF FIGURES

Figure Page

Figure Page

Figure Page

Figure Page

Figure Page

Figure Page

Figure Page

Figure Page

Figure Page

Figure Page

Appendix Figure

LIST OF SYMBOLS

A_B	Area of the busbars [cm^2]
A_M	Metal conductor cross-sectional area [cm^2]
A_T	Total area of the solar cell surface [cm^2]
B	Radiative recombination coefficient [cm^3/s]
c	Speed of light [cm/s]
C	Total Auger recombination coefficient [cm^6/s]
C_n	Auger recombination coefficients for electrons [cm^6/s]
C_p	Auger recombination coefficients for holes [cm^6/s]
D	Diffusion coefficient [cm^2/s]
E_0	Vacuum energy level [eV]
E_C	Conduction band energy [eV]
E_D	Energy level of the donor states [eV]
E_G	Bandgap energy [eV]
$E_G(0)$	Bandgap at zero degrees K [eV]
E_i	Intrinsic Fermi energy [eV]
E_V	Valance band energy [eV]
E_{tot}	Total energy incident on the solar cell [$W/cm^2/s$]
E_λ	Photons energy [eV]
F_n	Quasi Fermi energy for electrons [eV]
F_p	Quasi Fermi energy for holes [eV]
FF	Fill factor

G	Generation rate [$cm^{-3}s^{-1}$]
g_A	Acceptor impurity level degeneracy factor
g_D	Donor impurity level degeneracy factor
h	Planck's constant [eV s]
J	Terminal current density [mA/cm^2]
$\vec{J}_{disp}$	Displacement current density [mA/cm^2]
J_{MP}	Maximum power circuit density [mA/cm^2]
J_n	Electron current density [mA/cm^2]
J_O	Reverse saturation current density [mA/cm^2]
J_p	Hole current density [mA/cm^2]
J_R	Recombination current density [mA/cm^2]
$J_{R,Auger}$	Auger recombination current density [mA/cm^2]
$J_{R,Rad}$	Radiative recombination current density [mA/cm^2]
$J_{R,SHR}$	Shockley-Read-Hall recombination current density [mA/cm^2]
J_{SC}	Short circuit density [mA/cm^2]
k	Boltzmann constant [eV/K]
$k_e(\lambda)$	Imaginary portion of the refractive index
l_G	Grid line length [cm]
l_B	Busbar length [cm]
l_M	Metal conductor length [cm]
L_D	Diffusion length [cm]
m^*	Effective mass [kg]
m_c^*	Conductivity effective mass [kg]
$m_{c,n}^*$	Conductivity effective mass for electrons [kg]
$m_{c,p}^*$	Conductivity effective mass for holes [kg]

m_d^*	Density of states effective mass [kg]
$m_{d,c}^*$	Density of states effective mass for electrons in the conduction band [kg]
$m_{d,v}^*$	Density of states effective mass for holes in the valence band [kg]
m_{hh}^*	Effective mass of holes in the heavy hole band [kg]
m_l^*	Longitudinal effective mass [kg]
m_{lh}^*	Effective mass of holes in the light hole band [kg]
m_{so}^*	Effective mass of holes in the split off band [kg]
m_t^*	Transverse effective mass [kg]
m_{th}^*	Thermal velocity effective mass [kg]
$m_{th,n}^*$	Thermal velocity effective mass for electrons [kg]
$m_{th,p}^*$	Thermal velocity effective mass for holes [kg]
m_o	Mass of a free electron [kg]
n	Electron concentration [1/cm^3]
$\bar{n}(\lambda)$	Complex refractive index
n_{Auger}	Auger recombination ideality factor
n_i	Intrinsic carrier concentration [cm^{-3}]
n_m	Ideality factor
n_o	Equilibrium electron concentration [cm^{-3}]
$n_r(\lambda)$	Real portion of the refractive index
n_{Rad}	Radiative recombination ideality factor
n_{SHR}	Shockley-Read-Hall recombination ideality factor
n_T	Filled SHR trap states
N	Net bound charge [cm^{-3}]
N_A	Acceptors doping concentration [cm^{-3}]
N_A^-	Ionized acceptor doping concentration [cm^{-3}]

N_B	Ionized doping concentration [cm^{-3}]
N_C	Effective density of conduction band states [cm^{-3}]
N_D	Donor doping concentration [cm^{-3}]
N_D^+	Ionized donor doping concentration [cm^{-3}]
N_G	Number of grid lines
N_{it}	Fixed interface charges [cm^{-3}]
$NOCT$	Nominal operating cell temperature [K]
N_{other}	Other charges [cm^{-3}]
N_S	Fixed surface charges [cm^{-3}]
$N_{ST,n}$	Surface density of trap states for electrons [cm^{-2}]
$N_{ST,p}$	Surface density of trap states for holes [cm^{-2}]
N_{SLT}	Concentration of charge in SLT recombination sites [cm^{-3}]
N_T	Density of traps [cm^{-3}]
N_V	Effective density of valence band states [cm^{-3}]
p	Hole concentration [cm^{-3}]
p_o	Equilibrium hole concentration [cm^{-3}]
p_T	Empty SHR trap states [cm^{-3}]
$\vec{P}$	Polarization [C/cm^2]
P_{In}	Input power [mW/cm^2]
P_{Max}	Maximum output power [mW/cm^2]
q	Electric charge [C]
$R(\lambda)$	Wavelength dependent reflectance
R_{Auger}	Auger recombination rate [$cm^{-3}s^{-1}$]
R_B	Busbar resistance [Ω/cm^2]
R_C	Grid electrode-emitter contact resistance [Ω/cm^2]
R_{eq}	Equivalent resistance [Ω-cm]

R_L	Resistance of the top lateral conducting layers [Ω/cm^2]
R_G	Grid electrode resistance [Ω/cm^2]
R_I	Interface traps recombination rate [cm^{-3}s^{-1}]
R_M	Metal conductor resistance [Ω]
R_n	Electron recombination rate [cm^{-3}s^{-1}]
R_{other}	Recombination rate of other types of recombination [cm^{-3}s^{-1}]
R_p	Hole recombination rate [cm^{-3}s^{-1}]
R_R	Resistance of the back lateral conducting layers [Ω/cm^2]
R_S	Surface recombination rate [cm^{-3}s^{-1}]
R_{Series}	Series resistance [Ω/cm^2]
R_{Sheet}	Sheet resistance [Ω/□]
R_{SHR}	Shockley-Read-Hall recombination rate [cm^{-3}s^{-1}]
R_{Shunt}	Shunt resistance [Ω/cm^2]
R_{SLT}	Single layer traps recombination rate [cm^{-3}s^{-1}]
R_T	Total recombination rate [cm^{-3}s^{-1}]
R_λ	Radiative recombination rate [cm^{-3}s^{-1}]
S	Optical obscuration
S_B	Busbar obscuration
S_G	Grid line obscuration
S_n	Surface recombination coefficients for electrons [cm/s]
S_{other}	Any other structure causing obscuration
S_p	Surface recombination coefficients for holes [cm/s]
t	Time [sec]
t_E	Emitter layer thickness [cm]
t_G	Gird electrode thickness [cm]

t_B	Busbar electrode thickness [cm]
t_A	Absorber layer thickness [cm]
T	Operating temperature [K]
T_a	Ambient air temperature [K]
T_f	Final temperature [K]
T_i	Initial temperature [K]
T_M	Characterization temperature [K]
T_N	Normalized operating temperature [K]
T_O	Operating temperature [K]
T_λ	Transmission of light through a material
v_{th}	Thermal velocity [cm/s]
v_{wind}	Wind speed [cm/s]
V	Terminal voltage [V]
V'	Node voltage [V]
V_{MP}	Maximum power voltage [V]
V_{OC}	Open circuit voltage [V]
w	Solar cell thickness [cm]
w_B	Width of the busbar [cm]
w_G	Width of the grid lines [cm]
w_T	Width of a tile [cm]
x	Position inside the solar cell [cm]
X	Solar concentration [suns]
$\alpha(\lambda)$	Wavelength dependent absorption coefficient [cm^{-1}]
α_L	Linear thermal expansion coefficient [K^{-1}]
ΔE	Optical or electrical bandgap change [eV]
ΔE_G	Temperature dependent bandgap change [eV]

$\Delta E_{G,C}$	Minority free carrier concentration dependent bandgap narrowing [eV]
$\Delta E_{G,D}$	Doping dependent bandgap narrowing [eV]
$\Delta E_{G,F-K}$	Franz-Keldysh stark effect bandgap narrrowing [eV]
$\Delta E_{G,S}$	Stark effect bandgap narrowing [eV]
ΔE_S	Split off band energy difference [eV]
Δn	Excess electron concentration [1/cm^3]
Δp	Excess hole concentration [1/cm^3]
ΔT	Temperature difference between T_a and T [K]
Δw	Change in metal width [cm]
$\vec{\mathcal{E}}$	Electric field [V/cm]
$\vec{\mathcal{E}}_{br}$	Breakdown electric field [V/cm]
ε_0	Permittivity in a vacuum [F/cm]
ε_r	Relative permittivity
ε_s	Dielectric constant [F/cm]
$\varepsilon_S(0)$	Dielectric constant at zero K [F/cm]
η	Solar cell conversion efficiency [%]
$\eta_{PV}^{'}$	Effective conversion efficiency [%]
λ	Wavelength [nm]
λ_G	Semiconductor bandgap wavelength [nm]
λ_0	Wavelength of photon λ in a vacuum [nm]
μ_{ii}	Ionized impurity scattering [cm^2/Vs]
μ_L	Acoustic phonon scattering mobility [cm^2/Vs]
μ_o	Magnetic permeability in a vacuum [H/cm]
μ_n	Electron mobility [cm^2/Vs]
μ_p	Hole mobility [cm^2/Vs]

μ_{POP}	Polar-optical-phonon scattering mobility [cm^2/Vs]
μ_r	Relative magnetic permeability
υ	Wave propagation velocity [cm/s]
ρ_M	Metal resistivity [Ω cm]
ρ_S	Emitter layer resistvity [Ω cm]
$\sigma_{S,n}$	Capture cross sections for electrons [cm^2]
$\sigma_{S,p}$	Capture cross section for holes [cm^2]
τ_n	Electron SHR recombination lifetime [s]
τ_p	Hole SHR recombination lifetime [s]
τ_{Auger}	Auger recombination effective lifetime [s]
τ_{Eff}	Effective lifetime [s]
τ_{Rad}	Radiative recombination effective lifetime [s]
τ_{SHR}	SHR recombination lifetime [s]
ϕ	Electrostatic potential [V]
ϕ_n	Valance band parameter [V]
ϕ_p	Conduction band parameter [V]
$\phi_i(\lambda)$	Wavelength dependent photon flux density [W/cm^2]
$\Phi(\lambda)$	Photon flux density incident on the front surface of the solar cells
χ	Electron affinity [V]

NOMENCLATURE

1-D	One-dimensional
1-Sun	Unconcentrated solar irradiance
2-D	Two-dimensional
3-D	Three-dimensional
a-Si	Amorphous Silicon
ADEPT	A device emulation program and toolbox
AM 0	Solar spectrum above the atmosphere
AM 1.5 D	Standard DNI solar spectrum
AM 1.5 G	Standard global solar spectrum
ARC	Anti-reflectance coatings
ASTM	American Society for Testing and Materials
AZO	Aluminum zinc oxide
BSF	Back surface field
c-Si	Crystalline silicon
C-V	Capacitance-voltage measurement
CCD	Charge-coupled device
CIGS	Copper indium gallium selenide
CMOS	Complementary-symmetry metal–oxide–semiconductor
CO_2	Carbon dioxide
CPV	Concentrator photovoltaic
CPV-T	Hybrid CPV and thermal CSP system
CSP	Concentrated solar power
DNI	Direct normal incidence
Dark I-V	Current-voltage sweep in the dark

EQE	External quantum efficiency
FELES	Finite element light emitter simulator
GaAs	Gallium Arsenide
GaInAs	Gallium Indium Arsenide
GaInP	Gallium Indium Phosphide
GaN	Gallium Nitride
GaP	Gallium Phosphide
Ge	Germanium
HIT	Heterojunction with intrinsic thin layer
IMM	Inverted metamorphic
III-V	Semiconductors with a group 13 element(s) and a group 15 element(s)
ITO	Indium tin oxide
IQE	Internal quantum efficiency
Laser	Light amplification by stimulated emission of radiation
LCL	Lateral conducting layers
LED	Light-emitting diode
Light I-V	Illuminated current-voltage sweep
MODTRAN	Moderate resolution atmospheric transmission
MOSFET	Metal oxide semiconductor field effect transistor
MPF	Material parameter framework
NREL	National Renewable Lab
PL	Photoluminescence spectroscopy
Quasi-2D	1-D simulation of 1-D elements
Quasi-3D	2-D simulation of 1-D elements
S-Q	Shockley-Quisser detailed balance limit
SMARTS	Simple model of the atmospheric radiative transfer of sunshine
Si	Silicon
SiC	Silicon Carbide
SiO_2	Silicon dioxide
SHR	Shockley -Hall-Read

SLT	Single layer traps
SRRL	Solar Radiation Research Laboratory at NREL
TCL	Transparent conducting layers

ABSTRACT

Wilcox, John R., Purdue University, Ph.D., Purdue University, December 2013. Solar Cell Temperature Dependent Efficiency and Very High Temperature Efficiency Limits. Major Professor: Jeffery Gray.

Clean renewable solar energy is and will continue to be a critically important source of electrical energy. Solar energy has the potential of meeting all of the world's energy needs, and has seen substantial growth in recent years. Solar cells can convert sun light directly into electrical energy, and much progress has been made in making them less expensive and more efficient. Solar cells are often characterized and modeled at 25 °C, which is significantly lower than their peak operating temperature. In some thermal concentrating systems, solar cells operate above 300 °C. Since increasing the temperature drastically affects the terminal characteristics, it is important to quantify the losses caused by raising the temperature. Methodologies for including the temperature dependent material parameters in analytical and detailed numerical models have been examined. The analytical model has been developed to analyze Shockley-Queisser detailed balance limit, as well as the Auger, Radiative and SHR recombination limiting cases from 25 °C to 800 °C, at 1x, 500x and 2000x suns concentrations. The results of this analysis show that the efficiency of a direct bandgap material with an optimal bandgap could reach 19 % at 400 °C and 2000x suns, if the SHR recombination is reduced to an acceptable level. An analytical solar cell model was also used in a quasi-3D numerical model to simulate the temperature dependent resistivity losses. It was found that the resistive losses can double when the temperature of a solar cell increases from 25 °C to 100 °C. This will cause the conversion efficiency temperature coefficient to deteriorate by 10%. By using the temperature dependent material parameters for Si in

a detailed numerical model, it was found that some of the adjustable parameters, such as the base thickness, increase the conversion efficiency temperature coefficient and the V_{OC}, while other parameters would only increase the V_{OC}. This conclusion can be used by solar cell manufactures to improve the solar cell parameters with the biggest possible gain in device performance.

1. INTRODUCTION

1.1 The Value of Solar Energy

Interest in renewable energy has surged in recent years, as the world strives to reduce its dependence on fossil fuels, while at the same time reducing the greenhouse gas emissions and pollutions. The usages of all forms of renewable energy have increased over the past few years. Some types of renewable energies, such as hydropower and corn based ethanol, have reached limits in what is currently technically feasible. Other forms, such as wind and solar energy, have experienced enormous growth over the past 5 years [1]. Wind increased 27.6% and solar has increased 69% from 2000 to 2009 [2]. Solar cell installation has experienced a 130% year-on-year growth from 2009 to 2010 [2, 3]. Solar energy is one form of renewable energy that has the potential to provide all of the world's current energy usage. More energy reaches the earth's atmosphere in one hour, 174,000 [TWh] [4], than all forms of primary energy used worldwide in the last reported year (2008) which was a total of 144,453 [TWh] [5], (similar to analysis by [6]).

Many +200 MW utility sized power plants are being installed around the world [7, 8]. In 2010, 17 GW of solar cells were installed globally [2]. Solar cells are a reliable energy conversion device, which can have warranties of up to 25 years [9]. Most solar cells are a safe and clean way to produce electricity; they can also be recycled to reduce waste. While generating electrical power, solar cells do not require a fuel source, other than the sun, and do not produce emissions of any kind. Typically, solar cells only use a limited amount of water, which is used primarily to wash the solar cell modules [10]. In comparison, a coal power plant produces 36 times more CO_2 and uses 41 times more water. Electricity generated from a solar thermal system uses over 100 times more water than solar cells; and hydroelectric losses are 200 times more than solar due to the evaporation from the reservoir.

Clearly there are many advantages to generating more electrical energy using solar cells. Two of the primary limitations of the future growth of solar energy are the installation cost and the cost of the available storage options, to store the energy for later use. Methods for reducing the cost of solar cells will be discussed in Section 1.2. Approaches to increase the value of solar energy will be discussed in Section 1.3.

1.2 Reducing the Cost of Solar Energy

The solar cell industry has experienced double digit year over year growth for the past 10 years [11]. The growth in the solar industry has been fueled by decreasing production costs, which are currently below $0.75/watt [12], as well as government incentives and feed in tariffs. At the same time, significant improvements have been made in cell and module efficiencies of each type of solar cell material [13].

The cost of electric energy is often reported as a Levelized Cost of Electricity (LCOE). LCOE is a common metric used to compare the cost of generating electricity. It includes the cost to build the power plant, financing, maintenance and fuel. Until very recently, the LCOE of solar cells has been much higher than many other types of electrical energy generation on the grid.

A significant amount of money and resources are being devoted to reduce the cost of installing a solar cell system. In 2011, the U.S. Department of Energy launched the SunShot Initiative, which aims to reduce the installed cost of solar energy 75%, to $0.05 per kilowatt-hour and $1 per watt by 2020 [14]. This ambitious goal is ontrack to occur if the cost of solar cell systems continues to decrease at the same rate it has for the past 10 years. This will make solar energy cost competitive with other forms of electricity on the grid.

1.2.1 Solar Cell Research

There are a variety of ways in which the LCOE of solar energy can and is being reduced even further. Research is currently under way on a wide variety of solar cell materials and systems in an ongoing effort to reduce the LCOE in the following ways:

1. Reduce the manufacturing and production costs.
2. Increase the efficiency of existing solar cell systems and technologies.
3. Use low cost substrates and materials, such as thin films and organic materials.
4. Use concentrators to reduce the amount of solar cell material needed.
5. Reduce the cost of the balance of system components, such as mounting hardware and inverters.
6. Decrease the efficiency temperature coefficients of existing technology

In addition to reducing the LCOE of an installed solar electricity generation, research is also being conducted to improve the way in which solar energy is connected and used on the electricity gird. One method to more easily incorporate renewable energy on the grid, is through the use of load balancing. Another method would be to create a smarter electrical grid that can react quickly to changes in the electrical generation.

The work presented in this report uses measured data and solar cell modeling to identifying ways in which the value of solar energy can be increased. Possible methods to increase the value of solar energy, such as focusing on increasing the conversion efficiency or reducing the conversion efficiency temperature coefficient will be examined.

1.2.2 Solar Cell Modeling

In order to improve the efficiency of solar cells, it is important to identify the loss mechanisms reducing the efficiency. A variety of solar cell models have been developed to better understand the internal physical operation. These range from simple analytical expressions, to analytical models, to advanced detailed numerical models. Well-developed models allow the solar cell loss mechanisms to be quantified, enabling researchers to identify ways to reduce these losses. The models also allow parameter sensitivities to be located, which then can be used to direct tolerances during manufacturing processes. Reliable models can also be used to estimate the available improvements to be gained from redesigning the solar cell. In addition, detailed numerical models allow the internal operation to be analyzed, which can be difficult or

near impossible to accurately measure. Thus solar cell models can speed up development time and reduce the number of experimental devices needed by testing a variety of possibilities quickly.

1.3 Increasing the Value of Solar Energy

Presently there is a significant amount of interest in increasing the value of solar energy through lowering the installaed cost, as well as improving both the quality and flexibility of the power generated. Recently a 2 day workshop was conducted by ARPA-E which was focsed on identifying possible new ways of increasing the the overall value and usefulness of solar [15]. This is a particularly important topic because as the price of solar energy produced by solar cells has decreased and approached the cost of other forms of electricity generation it has become a far more competitive and viable energy option. The cost of electricity produced by solar cells has continued to decrease for many years. This is being aided by research efforts such as the DOE SunShot Initiative. While it is likely that the price of installed solar will increase in the near term, as demand catches up with the over supply, the price will likely continue to decrease as solar cells become more of a commodity. The rising amount of installed solar power is causing problems in the electrical grid. This is also causing problems when costumers are paid full retail rate for the power they produce, leading to fewer users paying for the power grid mantainance. This could further destabilize the electrical grid. It is therefore important to identify ways in which solar energy can limit these affects.

There are four ways in which this can be done: improve consistency, dispatchability, portability and long term storability of solar energy. Improving consistency of solar energy makes it more valuable to electric grid operators, because they will need less backup generation capacity. Increasing the dispatchability means being able to store the solar energy until the grid needs it. Converting the solar energy into a dense fuel source would increase the portability allowing it to be used as a transportation fuel or used as an energy source at remote locations. Using a transportation fuel derived from solar energy would reduce the amount of other transportation fuels used, such as petroleum. Long-term storage is the ability to store the energy derived from solar for days, weeks, or

months, before it is used. This is particularly useful since the energy can be stored when solar energy is most abundant and used whenever the storage energy is most valuable.

Solar cells are a useful way of harnessing solar energy. They can very efficiently convert photons directly into electrical energy. Since energy is lost in each energy conversion, this simple direct conversion of photons to electricity leads to the high conversion efficiency. This also leads to an important limitation of solar cells. Once electricity is generated it must be used or stored immediately. Conventional methods of storaging electricity such as batteries, pumped storage and fly wheels in large scale are currently prohibitively expensive. Because solar cell technologies available today convert photons directly into electrical energy, there are no intermediate steps where storage could be conveniently added. This limits the consistency and dispatchability of solar energy from solar cells.

Concentrated solar power (CSP) is another solar energy technology which converts photons into thermal energy and then converts the thermal energy into electricity. Since the thermal energy can be easily stored, it can be more consistent and dispatchable than solar cells. A variety of CSP systems are currently being built and tested. These systems include heliostats towers, parabolic troughs and parabolic dishes. Large scale utility CSP systems are currently in use throughout the world. Due to the decreasing price of solar cells, CSP systems recently have become more expensive than flat plate solar cell systems. They are also limited by the water usage, which is often scarce in high solar insolation areas. Using the inherent advantages of each, it could be possible to build a hybrid system that overcomes the limitations of each technology.

It may be possible to increase the value of solar energy by creating a system that collects both electrical energy using solar cells and thermal energy using a thermal absorber [15]. Such a system could potentially convert more energy per square meter into usable energy. This type of combined photovoltaic and thermal system has been analyzed by Luque [16]. The availability of electrical and thermal energy also makes it possible to use a variety of storage methods, which could harness both forms of energy, increasing the value. This includes battery systems that are heated thermally to reduce the amount of energy needed to charge them electrically. Another approach would be to

use the common molten salt method of the thermal storage and use a pumped heat electrical storage system to store the electricity as thermal energy until it is needed [17, 18]. It may also be possible to directly combine the thermal storage and pumped heat system to create an even better hybrid system.

1.4 Operating Temperature

While an extensive amount of research has been conducted measuring and modeling solar cells near the standard test conditions, 25° C, a much smaller amount of research has been conducted measuring and modeling solar cells at other temperatures, T, and over the expected operating temperature, T_O, range. Solar cells installed in most locations will operate above and below the standard test conditions. The T_O is set by the ambient air temperature, T_a, plus the difference between the T_a and the solar cell junction temperature, ΔT.

$$T_O = T_a + \Delta T \tag{1.1}$$

At moderate latitudes terrestrial flat panel Si solar cells can operate between -10 °C and 60 °C , and solar cells inside of concentrator photovoltaics (CPV) systems can reach temperatures as high as 100 °C [19]. Solar cells used on space satellites typically operate between 50 °C to 80 °C, and in one system are being designed to operate up to 350 °C [20], for missions into the outer corona of the Sun [21]. The solar cells used on probes to the outer planets of the solar system operate at much lower temperatures. Cryogenic systems have been used to measure solar cells down to -173 °C (100 K) [22]. Hybrid CPV and thermal CSP (CPV-T) systems are being considered that could operate up to 400 °C or higher [23, 24]. Published solar cell performance has been measured over 350 °C [23]. This is important because the conversion efficiency of most crystalline solar cells decreases as the T_O increases.

The temperature of a solar cell while it is operating depends on many parameters, such as the total energy incident on the solar cell, E_{tot}, the air temperature (ambient), T_a, the nominal operating cell temperature, *NOCT*, and the wind speed, v_{wind}. The

parameters E_{tot}, T_a, and v_{wind} have been measured [25] and modeled for a typical metrological year [26], throughout each day and year, for a wide variety of locations in the United States. Because of thermal resistance between the solar cell and air, there will be a temperature difference between T_a and *T*, equation (1.1).

When wind speed is not accounted for, the operating temperature equation used by Emery is [27]

$$\Delta T = \left((NOCT - 20\ ^\circ C) E_{tot} / 800\,[W/m^2] \right) \tag{1.2}$$

Methods for calculating ΔT including wind speed have also been derived [28]. This will allow the ΔT of the solar cell to be calculated throughout each day for every day of the year. The T_O can then be used to model the performance of the solar cell over the each day of the year.

1.5 Dissertation Synopsis

The focus of this work is analyzing the temperature dependencies of solar cells, as well as identifying possible ways in which solar cells can be redesigned to reduce the temperature dependent losses. This is particularly important for solar cell systems where the T_O will vary over a wide range of temperatures and when operating solar cells at very high temperatures. This work is dividing into three main topics: very high temperatures (Chapter 3 and Chapter 4), 3-D resistive losses (Chapter 5) and detailed numerical modeling of Si solar cells (Chapter 6). Chapter 2 reviews the related published literature. Chapter 7 summarizes the completed work and discusses possible future work. The appendices provide additional information about models used in this work. These chapters will support a number of interesting and unexpected conclusions:

Conclusion #1: Improving the V_{OC} will not always yield a better $\frac{1}{\eta}\frac{d\eta}{dT}$

Many groups have noticed that as the V_{OC} increases the $\frac{1}{V_{OC}}\frac{dV_{OC}}{dT}$ improves. While it might be easy to think that this is always true, it may not be true in every case.

Improving the V_{OC} leads to an improved η and a better $\frac{1}{V_{OC}}\frac{dV_{OC}}{dT}$ will lead to an improved $\frac{1}{\eta}\frac{d\eta}{dT}$. However, it is easy to over look how changing the V_{OC} will affect the J_{SC} and FF, which will also affect the $\frac{1}{\eta}\frac{d\eta}{dT}$.

Conclusion #2: A solar cell with the highest η may not have the best $\frac{1}{\eta}\frac{d\eta}{dT}$

This related to conclusion 1. There are conditions where improving the η at one T_O will cause the $\frac{1}{\eta}\frac{d\eta}{dT}$ to become worse. This will lead to lower η at higher T_O.

Conclusion #3: A solar cell with the highest η or with the best $\frac{1}{\eta}\frac{d\eta}{dT}$ may not yield the best performance over a range of temperature

Because of conclusion #3 optimizing for a solar cell with the highest possible η or the best possible $\frac{1}{\eta}\frac{d\eta}{dT}$ at one temperature can lead to a device with a lower performance over a range of T_O.

Conclusion #4: Need to optimize for the best yearly performance

While research groups continue to work to achieve the highest possible conversion efficiency at 25 °C. Because of conclusions #1, #2 and #3, the best solar cell design can be achieved by optimizing for the optimal yearly performance. There are a number of yearly performance metrics by which the solar cell designs could be judged.

Possible optimization metrics:

- Highest kWh out per year
- Lowest LCOE
- Higher energy during a particular season
  - Need more energy during the Summer
  - More efficient during the Winter
- Most beneficial for the power grid
  - Reduce the peak load

        - Broad over the entire day
    - Longest system lifetime

Conclusion #5: A detailed numerical model can be used to understand the operating condition dependencies

While the MPF model developed and presented in this work has some limitations, it shows that it is possible to simulate the dependencies over a wide range of T_O. It also shows that the material parameter dependencies can be measured and modeled. The results of this model can be used to identify the missing material parameter dependencies.

Each of these conclusions will be discussed further in Chapter 3 through Chapter 6. While each of these effects might not be large in every situation, it is important to understand how they will affect the overall performance.

1.5.1 Detailed Balance Limited Very High Temperature Terminal Characteristics

Chapter 3 explorers the Shockley-Queisser (S-Q) detailed balance limited terminal characteristics and the temperature dependent terminal characteristics over a wide range of T_O, from 100 °C to 800 °C. These calculations are similar to calculations by other groups. The temperature dependent affects of each of the terminal characteristics and the temperature dependent terminal characteristics will be evaluated and compared. The results in this chapter will be helpful in understanding the temperature dependent affects in later chapters.

1.5.2 Recombination Limited Very High Temperature Terminal Characteristics

Chapter 4 estimates the recombination limited terminal characteristics of solar cells at very high temperatures. These calculations give a sense of the conversion efficiency that could be achieved with high quality solar cells over this temperature range. They also allow for the bandgap energy with the highest estimated peak conversion efficiency to be found (Section 4.3.1). This is useful in determining how close to the absolute peak a particular material can reach.

In order to simulate the very high temperatures terminal characteristics, the intrinsic carrier concentration, radiative recombination, and Auger recombination are needed over temperature and bandgap energy. Curve-fits based on measured values were created to estimate each of these parameters (Section 4.2). These curve-fits were used to estimate the terminal characteristics for each of the recombination limited cases. Sufficiently high quality material was assumed leading the SHR recombination to be negligible.

The peak conversion efficiency and associated bandgap energy have been calculated from 100 °C to 800 °C and from 1 sun to 2000 suns concentration (Section 4.3.2). This is useful in determining the system level trade-offs between the solar concentration and the temperature. In addition to the one junction performance, the optimal two junction conversion efficiency and associated top and bottom bandgap energies have been calculated (Section 4.3.6). The peak conversion efficiency for the S-Q detailed balance limit from 1 to 10 junctions for a range of temperatures from 100 °C to 800 °C.

1.5.3 Temperature Dependent Resistive Losses

The recombination limited very high temperatures model and the detailed numerical model in this work are 1-dimensional (1-D) models. These models are useful in identifying the temperature dependencies of the solar cell's internal layers and doesn't take into account the 3-dimensional (3-D) effects. Some of the 3-D affects of particular importance are the resistivity losses, which are enhanced by the lateral flow of current through the lateral conducting layers (LCL) and the grid/busbar electrodes (Section 5.3).

As the current flows laterally through the solar cell, the resistivity of the LCL and the grid/busbar electrodes cause a voltage differential across the surface. In addition to voltage drop caused resistivity, a bias point loss also occurs due to the fact that only a small part of the solar cell can operate at the intrinsic max power point.

Since the recombination limited very high temperatures model and the detailed numerical model work will be a 1-D model, a quasi-3D resistance model was used to calculate the temperature dependents of the series resistance and bias point loss. Over the temperature range of interest, the resistivity of the metal and semiconductor will increase

by over 30%. This will cause the overall performance of the solar cell to degrade (Section 5.6).

1.5.4 Temperature Dependent Numerical Model

The first steps in developing a detailed numerical model was to identify the temperature, doping density, minority free carrier concentration, and electric field dependencies that are needed to numerically model the solar cells over a range of T_O (Chapter 6). The parameter dependencies have been combined into the material parameter framework (MPF).

The flow diagram in Figure 1.1 illustrates the process used to calculate the solar cell's performance at each T_O. The arrows indicate the the movement of parameters through the model. At the top, the T_O is passed into the MPF.

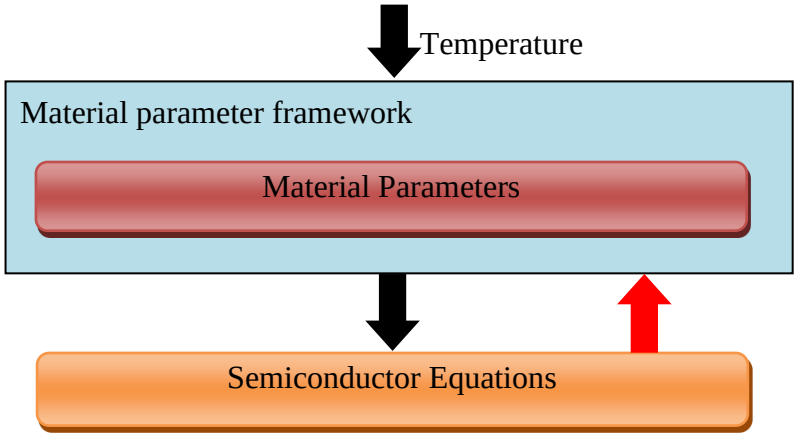

Figure 1.1. Flow diagram showing the inclusion of material parameter dependencies, with a numerical model. The black arrows show the flow of parameters from the material parameter framework (MPF) to the semiconductor equations. The red arrow shows the parameters being passed back to MPF during the numerical solution process.

The MPF has been used to simulate a Si PERC soalr cell. The simulatinos show good agreement with the measured device performance near 25 ℃. The temperature dependent performance is also evaluated and ways of improving the model are discussed.

2. LITERATURE REVIEW

Section 2.1 will focus on the history and Section 2.2 will cover the fundamentals of solar cells. The benefits of modeling solar cells will be discussed in Section 2.3. Section 2.4 will review the essentials of simple analytical modeling and Section 2.5 explains how solar cells can be modeled numerically. Additional related research will be discussed in Section 2.6.

2.1 Solar Cell History

The photoelectric effect, where bound electrons are freed by the energy contained in photons, was discovered by Alexandre Edmond Becquerel in 1839 [29]. He immersed two metal electrodes in an electrolyte and observed that the current generated by the electrolytic cell increased under a light source. Photoconductivity was first reported by Willoughby Smith in 1873 [30]. The number of free carriers was increased in Selenium when exposed to light, which caused a measured change in conductivity.

In 1876, William Adams and Richard Day were able to detect a small current generated by a rod of Selenium when it was exposed to light in the visible spectrum [31]. They were able to prove that the current was generated by exposure to light. When they exposed the rod to candle light it immediately generated a detectable current and when the candle was covered the current stopped. This photoelectric conversion of light to energy does not require moving parts. They also detected a difference of resistance depending on the polarity of the voltage applied. Even though the current generated was too small to power any devices, it was a clear demonstration that photons were affecting the solid.

Charles Fritts created a photoelectric device by coating Selenium with a thin layer of gold in 1883 [32]. In the previous examples, both of the electrodes used in the experiment were similar, but in the devices created by Fritts they were different. This was a novel design both in structure and electrodes. He wanted the electric field created by the photon absorption to assist, instead of being transverse to the current flow. He melted the Selenium on a metal conductor and then applied a second transparent conductor to the surface, a thin film of gold leaf. This solar cell was less than 1% efficient. He was able to create a reduction in resistance that was 20 times larger than Werner Siemens.

Four years later, in 1887, Heinrich Hertz was able to detected and measure the photoelectric effect using a spark gap [33]. In this experiment the voltage needed to cause a spark across a gap was reduced when ultra-violet light was shined on the metal. That same year James Moser reported the first dye sensitized solar cell. The following year Aleksandr Stoletov measured the relationship between light intensity and J_{SC} using a solar cell [34], which lead to Stoletov's law and constant.

In 1902, Philipp Lenard discovered that the color and energy of light was directly correlated by measuring the voltage required to stop a photon of a given energy. This seemed to contradict Maxwell's wave theory of light. Then in 1905, Albert Einstein resolved the contradiction, by predicting the absorption of light quanta, which are now referred to as photons [35]. This theory stated the clear connection between the photon frequency and energy, not the intensity as had been previously thought. For this and other discoveries Albert Einstein was award the Noble Prize in 1921.

Good quality, single-crystal silicon, c-Si, was produced in 1918 by Jan Czochralski [36]. This coupled with the float zone method provided low defects and high lifetimes that were very important to the developing integrated computer chip industry and would be needed to produce high efficiency solar cells [37]. In 1946, Russell Ohl patented a solar cell design [38].

In 1953, Dan Trivich made the first theory based efficiency calculations for various materials, taking into consideration the bandgap and solar spectrum [39]. The first solar cell capable of powering electronic devices was created at Bell Labs by Daryl Chapin,

Calvin Fuller and Gerald Pearson in 1954 [40]. The efficiency was 4% and was later improved to 11%. Solar cells quickly became common in many low power devices such as handheld calculators. Vanguard 1, the first space satellite with solar cells was launched in 1958 [40]. This satellite has been in orbit for more than 50 years. Solar cells have become an important power source for satellites orbiting the earth.

By this time there were a variety of materials being tested as solar cells. In 1979, Jerry Woodall and Harold Hovel working at IBM's Watson research center developed a 21.9% efficient GaAs solar cell [41], a world record. The efficiency of this solar cell was 8 absolute percentage points above the best c-Si solar cell developed by Mobil Solar near the same time. In 1980, one 1 MW of solar cells was manufactured in one year by ARCO Solar [42].

In 1994, NREL developed the first solar cell with a conversion efficiency over 30% [43], which was 30.2%. This two-junction solar cell consisted of a GaInP junction on top of a GaAs junction in a CPV system. By placing a higher bandgap material on top of a lower bandgap material, the solar cell was able to achieve a higher conversion efficiency. Then in 2006, a triple-junction solar cell created by Boeing-Spectral Lab was the first solar cell with a conversion efficiency over 40% [44]. The most recent world record efficiency was set by Solar Junction in 2011, with a conversion efficiency of 43.5% [45].

The efficiency of solar cells continues to improve. Some of the highest efficiency solar cells have been made using some of the highest purity substrates, such as Si and GaAs. Si has been purified to nine nines, 99.9999999% pure, though this level of purity is not required for solar cells [46]. In 2011, the highest Si solar cell efficiency was 25% and the highest GaAs non-CPV solar cell efficiency was 29.1%. A more complete overview of current and future solar technology is covered in a paper by Larry Kazmerski [13]. The world record best research cell efficiencies from 1979 to present, are plotted on page 17 of that paper.

2.2 Solar Cell Fundamentals

Photovoltaic solar cells convert photons directly into electricity. Solar cells have two fundamental functions. First, it converts photons into electron and hole charge carriers,

called photogeneration. Second, it separates the two types of charge carriers quickly so that they are not lost when the electron and hole recombine. How well a solar performs depends primarily on how well it can do these two primary functions. A solar cell with high values of photogeneration and low values of charge separation will not perform well, just like a solar cell with low values of photogenreation and high values of charge separation will also not perform well.

In order to make solar cells with the highest possible performance, a wide variety of semiconductor materials and device designs have been evaluated. The world record performance values have been published by Green [47]. A chart of the record efficiencies over time has been report by Kazmerski [13]. This chart shows how research and development has significantly improved the performance of solar cells.

2.3 Modeling Solar Cells

The efficiency of each type of technology has been improved experimentally and through modeling work. Both methods start by measuring a control solar cell. In the experimental case, changes are made to the processing in an attempt to improve the efficiency of the experimental solar cell. The experimental cell is then tested and compared to the control cell. This process is repeated to find the best way to process the cell. The other method for improving the efficiency involves fitting models to the measured data. These models are then evaluated to identify ways in which the efficiency of the solar cell can be improved. Those ideas are then transferred back to the manufacturing process, solar cells are produced and then measured to compare with the control cell.

There are a wide variety of models that have been used to simulate solar cells. The simple models are useful for their ease of use; the detailed numerical models are valuable for their more complete physics and their ability to analyze the solar cells' internal operation.

A primary focus of these models will be to identify temperature dependent losses mechanisms that can be reduced by redesigning the solar cell. The temperature

dependent material parameters could be used in any modeling program for many types of semiconductor devices.

2.4 Simple Solar Cell Models

There are three partial differential equations that are used to model the physics inside of semiconductor devices, such as solar cells. These equations are discussed in section 6.3 through section 6.8. Because there are three coupled differential equations, no solution is available to solve these equations analytically. Assumptions and simplifications must be made before the performance of the solar cell devices can be solved analytically.

The following sections will describe a variety of simple models that have been used to estimate the performance of solar cells.

2.4.1 Linear Temperature Dependent Curve-fits

The measured temperature coefficients of most solar cells can be fit with a linear curve-fit. Temperature coefficients have been measured by Emery *et al*., Green *et al*., Yoon *et al*. and others [48-50]. Linear curve-fits can be applied to measured J_{SC}, V_{OC}, *FF* and efficiency data for a Si solar cell [48].

In the paper by Green *et al*., a linear temperature dependent bandgap fit from 0 K to 400 K was used to predict the bandgap from 300 K to 400 K [48]. In addition, a coefficient was added to the *FF* equation, to account for the series resistance. Even with this coefficient the equation was still off by 5%. Despite these shortcomings, good fits were still achieved.

The temperature dependence of a high concentration Si solar cell was examined by Yoon *et al*. [49]. In this paper the reverse saturation current was again described with a single expression. The paper points out that the exponent in the reverse saturation is important to the temperature dependence, however it fails to include a fitting parameter or ideality factor in the denominator. This will affect the overall performance because the devices appear to be limited by Auger recombination

A linear curve-fit is a useful way to predict the performance between measured data points. These linear curve-fits provide very little information about the temperature dependent losses that are contributing to these temperature coefficients.

2.4.2 Ideal Diode With Resistance

Since many solar cells are p-n junctions, the ideal-diode equation with series resistance, shunt resistance and photo-generation current added, has been used quite extensively to model solar cells.

In 1960, Wysocki calculated the temperature dependencies of Si and GaAs solar cells, as well as others [51]. Many temperature dependent relationships were included in this model, such as intrinsic carrier concentration, lifetime, recombination current, and resistance.

In the paper by Fan, the temperature dependence of the reverse saturation current is given with two empirical fitting parameters, which are related to the ideality factor of the material [52]. However, no method for analytically determining these parameters was given. One of the reasons for this has to do with the fact that this simple equation is being used to describe the effect of many different types of recombination happening spatially throughout the device. This equation provides very little insight into the effect each recombination mechanisms has on the overall performance of the device.

Photon current generation can be added to these simple models by calculating the total generation for the device. Both measured and modeled wavelength dependent absorption can be used [53]. This approach does not account for the spatial dependence of the generation.

Another big limitation of using the ideal diode equation with resistance is the fact that there are many types of recombination occurring inside of a solar cell. These mechanisms do not all have the same ideality factor. So as the amount of various types of recombination changes, the ideality factor of the device will also change. This is particularly true when modeling solar cells over a range of concentrations. These effects cannot be incorporated into a single constant ideality factor.

2.4.3 Two or More Diode Model

To avoid the problem caused by using a single constant ideality factor, a two diode model has been used by Hovinen [54]. While this approach does allow for two ideality factors and reverse saturation currents to be used, it is not always possible to fit the measured data. This is particularly important for Si solar cells, which can have voltage dependent recombination [37].

Attempts have been made to use a two diode model to predict the performance of a multi-junction tandem solar cell [55]. Due to the current matching of two junctions and the spatial dependence of the generation and recombination, it can be difficult to model multi-junction solar cells over a range of solar concentrations.

To avoid the difficulties associated with fitting a two diode model, a concentration dependent curve-fit model has also been developed by Haas *et al.* [56]. This model can fit the data well over a range of concentrations, while at the same time reducing the measurement noise.

An attempt was made by the author to extend this simple curve-fit model to include temperature dependence. This model was significantly limited by the intricate relationship been the ideality factor and series resistance near max power.

2.4.4 Other Temperature Dependent Solar Cell Models

Temperature dependent solar cell models have been used by Friedman [57] and Kurtz *et al.* [58]. Their models have proven to be useful for predicting the performance and optimizing solar cells with one or more junctions. These analytical models make simplifying assumption, and do not account for the spatial dependence of the generation and recombination.

Friedman modeled a GaInP/GaAs tandem solar cell. A modified fundamental absorption was used to calculate the photo current and the bottom junction was assumed to be infinitely thick [57]. The bottom junction was filtered by the absorption of photons in the junction above it. The absorption was shifted by the temperature dependent bandgap, ignoring other bandgap effects. The bandgap temperature coefficient was

assumed to be linear near 300 K. The series resistance was assumed to be zero and the ideality factor was assumed to be 1. Additional material temperature dependent parameters, such as effective masses, mobilities and minority carrier lifetimes were not included. Friedman derived a V_{OC} temperature coefficient equation that matches Fan's with the addition of an additional term that is calculated numerically.

Kurtz *et al.* attempted to predict the performance of three and four junction tandem solar cells that are optimized for AM 0 and AM 1.5 D 500 suns [58]. The fundamental absorption was used to calculate the photo current for each junction. The surface recombination was assumed to be zero. The intrinsic carrier concentration and other material temperature dependent parameters, such as effective masses, mobilities and minority carrier lifetimes were assumed constant. Losses due to grid obscuration, series resistance and shunt resistance were also not included. The bandgap of the third junction was optimized for maximum efficiency for clear sky conditions at 500 suns, AM1.5 D at 500 suns, AM 0 at 10 suns and AM0 at 1 sun. The optimized bandgap shifted 50 meV depending on the solar spectrum.

These temperature models rely on simplifying assumptions, and ignore spatial effects such as the surface recombination and generation. Only a few of the temperature dependent material parameter dependencies were included in the models, and only a limited amount of information is available about the internal operation of the solar cell.

2.4.5 Summary of Analytical Solar Cell Models

A variety of analytical models have been developed to model solar cells. These models are useful to analyze solar cell performance. Each of these models includes simplifying assumption that could significantly affect the temperature dependent performance. Other effects such as the surface recombination are difficult to examine due to the lack of spatial calculations. Only a limited amount of information can be inferred about the operation of the solar cell. A detailed numerical model will be used in Chapter 6. This will allow fewer simplifying assumptions to be made, and a deeper understanding on the internal operation of the solar cells.

2.5 Detailed Numerical Models of Semiconductor Devices

Numerical models have been used to probe the internal operation of semiconductors. They require fewer simplifying assumptions than analytical equations. The proposed temperature dependent losses mechanisms and parameter sensitivities will be identified using a numerical model.

In 1950, Van Roosbroeck laid out the equations needed to model the physical operation of semiconductor devices [59]. Books by Markowich [60] and Snowden [61] discuss the mechanics of how detailed numerical models work. The MPF equations found in Chapter 3 can be found in a book chapter by Gray [27], in a thesis by Pinto [62] and a semiconductor book by Sze [63].

There are a wide variety of numerical models available. They have been used to model semiconductor devices from heterojunction bipolar transistors [64], to lasers [65], to solar cells. In addition to the semiconductor equations, the numerical model used in this work must also include the photon-induced generation of carriers.

2.5.1 Detailed Modeling Programs

There are a wide variety of numerical modeling programs that have been used to model solar cells. These modeling programs range from general semiconductor device models to optical-electrical models to solar cell models. Many general detailed numerical modeling programs can model semiconductors, such as Sentaurus [66] (Medici), ATLAS [67], Crosslight [68] and COMSOL [69].

There are quite a few numerical models that have been used to model optical-electrical semiconductor devices such as photodiodes, CMOS photodiodes, CCD and solar cells. HIFIELDS [70] was developed at Bologna University by Maria Cristina Vecchi. This program can model photodiodes, CMOS photodiodes, CCD, solar cells and other non-emitting optical devices. Finite Element Light Emitter Simulator (FELES) [65] has been used primarily to model Lasers. A number of detailed numerical models have also been used to model solar cells (Table 2.1)

2.5.2 Temperature Dependent Solar Cell Modeling

Every numerical model includes a set of built-in equations. Some of these equations are used by the solver, to solve the semiconductor equations. Other built-in equations are added to incorporate the temperature dependent relationship of a particular parameter. For example, the input parameter of the numerical model for SHR recombination might be a capture cross section, instead of a carrier lifetime. This would allow the numerical model to calculate the lifetime using a temperature dependent thermal velocity. Simply changing the numerical model's input parameter for temperature will not automatically calculate any potential temperature dependencies of the effective mass, capture cross section or doping. The temperature dependence of these parameters would need to be varied independently.

The detailed numerical modeling program ADEPT, SCAPS and PC1D have built-in equations to calculate the temperature dependence of the density of state, thermal velocity, diffusion coefficient and lifetime. They do not have built-in equations for other important temperature dependent parameters, such as effective mass or mobility.

Some modeling programs, such as Sentraurus, use dynamic diktat (input) files that can calculate temperature dependent input parameters.

Table 2.1
Detailed numerical model programs commonly used to model solar cells [71].

Program	Head developer	University	Radiative recombination	SLT recombination	Auger recombination	Heterojunction	Tunneling	Thermionic emission	Website or reference
ADEPT	J. Gray	Purdue University	√	√	√	√			[72]
SCAPS	M. Burgelman	University of Gent	√	√		√	√	√	[73]
PC1D	P. Basore	The University of New South Wales	√	√	√	√	√	√	[74]
AFORS-HET	R. Stangl	Hahn-Meitner Institude of Berlin	√	√	√	√		√	[75]
AMPS-1D	S. Fonash	Pennsylvania State University	√	√		√		√	[76]
ASA	B. Pieters	Delft University of Technology	√	√	√	√	√	√	[77]
ASPIN*	M. Vukadinovic	University of Ljubljana	√	√		√	√		[78]
SimWindows[•]	D. Winston	University of Colorado at Boulder	√	√		√	√	√	[79]

* Not publicly available

[•] No longer supported, last updated 1996 (update log [80], manual [81]), program website no longer accessible [79].

2.5.3 Compare Modeled and Measured Temperature Coefficients

This step is important to validate the solar cell simulations and has already been done by many other groups. Theoretical equations have been developed by Green *et al*., Yoon *et al*., and others [48, 49] to calculate the temperature coefficients. Details about these theoretical equation and using linear curve-fits to predict the temperature dependent coefficients was discussed in section 2.4.1.

2.6 Related Work

This work focuses on using analytical and numerical models to simulate how the operating temperature affects the terminal characteristics of solar cells. A more detailed description was covered in Section 1.5. A review of the pertinent literature for each of the three main topics is covered in the following three sections.

2.6.1 Simulating the Recombination Limited Terminal Characteristics at Very High Temperatures

As the temperature increases the saturation current will increase significantly. This chapter will show that this causes the optimal E_G for a single junction solar cell to increase. Other solar cell design parameters such as the grid pattern and spacing will also be affected. This will be discussed in Chapter 5. For non-ideal solar cells, additional parameters such as mobility and carrier lifetime will also influence the design over temperature.

Analytical and simple numerical models based on semiconductor theory or empirical measurements have proven to be very useful. One of the first theoretical papers to use an analytical model was published by Fan [52]. This paper includes a temperature dependent reverse saturation current. It also provides some useful expressions and results for the terminal characteristics temperature dependencies. In 1996, Friedman included

the temperature dependent material parameters, bandgap, absorption and intrinsic carrier concentration [57].

A theoretical model for calculating efficiencies over temperature and bandgap was developed by Landis [82, 83]. However, this model was based on an assumed saturation current over bandgap expression and a fixed value for the FF [23]. This paper also describes developing a SiC solar cell that might be able to operate as high as 600 ℃. A model developed by Braun estimated the conversion efficient over a range of bandgaps and solar concentration [84], however it estimates the open circuit voltage with a fix voltage difference from the bandgap energy. It also does not account for Auger recombination. Singh developed a related model that was used to estimate the conversion efficiency over bandgap energy from 0 ℃ to 250 ℃ [85].

Others have also developed saturation current over bandgap expressions or functions, which are useful to estimate the efficiency over bandgap and optimizing the bandgap energy. Levy developed a method for calculating the detailed-balance saturation current using Riemann zeta functions [86]. An analytical expression was developed by Gray, which has a high degree of accuracy for solar cell bandgaps above $E_G > 3kT$ [87].

Presently missing from the published literature is a model that can be used to simulate the recombination limited conversion efficiency of solar cells over a broad range of solar cell operating temperatures, solar concentrations and simulated bandgap energies.

2.6.2 Calculating the Series Resistance and Bias Point Losses

The efficiency loss due to series resistance and bias point loss have been calculated. This work can be used as a reference guide that will aid in designing the sheet resistance in the semiconductor and resistivity in the metal and will include temperature effects.

The effect of series resistance and non-uniform illumination was analyzed by Mitchell in 1977 [88]. In this work a two dimensional distributed resistance model was used to analyze the effect of the resistance on the solar cell performance.

In 2007, Sabry analyzed the effect of temperature on the series resistance and measuring series resistance of Si solar cell [89]. In this paper he identified and compared

seven methods of determining the series resistance. Some of the methods yield series resistance values that were vastly different.

A paper by Haas *et al.* [90] was the first to quantify the effect of the bias point loss. This paper showed that a relatively small voltage drop across the emitter lead to a significant loss in output power. In some cell geometries, this loss can be as significant as the loss caused by series resistance [91]. The work presented in Chapter 5 will extend the published work by Haas to simulate the temperature dependencies caused by the series resistance and bias point losses.

2.6.3 Detailed Numerical Modeling Temperature Dependencies

The MPF is an important component of this work, however it is not in and of itself novel. Temperature models have been developed for a variety of devices, these range from CMOS transistors to Lasers[65]. Only photo-electric devices that absorb photons, such as photo diodes, CCD and CMOS imagers have similar models. Numerical models of other semiconductor devices contain only part of the temperature, carrier density and electric field dependent material parameter relationship needed to model a solar cell.

Green carefully analyzed measured material parameters for Si from a variety of sources [92]. The parameters studied were the intrinsic concentration, valance band effective density of states, conduction band effective density of states and average thermal velocity. Useful theoretical fits were also applied to mobility and the conductivity/resistivity.

Temperature dependent material parameters were used by Radziemska to calculate the performance of Si and GaAs solar cells [93]. The temperature dependent parameters included were the bandgap and intrinsic carrier concentration. These parameters were then used in temperature coefficient equations to calculate the performance of the solar cells.

The goal of this step is to identify which material parameter relationships the solar cells are sensitive to and to identify ways in which the solar cell could be redesigned to reduce these sensitivities. This has been done by other groups, but not with the detail that it will be done in this work.

It has been determined that the BSF of high quality Si solar cells significantly affect the performance of the solar cell [37]. Since the number of carriers that make it over the BSF is influenced by the operating temperature, the BSF is a temperature dependent loss mechanism.

2.7 Uncertainty in Temperature Dependent Measurements

There are two important sources of uncertainty that can be reduced while taking temperature dependent measurements. The first is the junction temperature of the solar cell. The second is the spectrum used to measure the solar cells. Both of these uncertainties will be discussed in this section.

The measured temperature coefficients of most solar cells are nearly linear over the operating temperature range of interest. These coefficients have been measured for a wide variety of solar cells. Results have been published by Emery *et al.* and Osterwald *et al.* [50, 94]. Solar cells with a larger V_{OC} generally have a better conversion efficiency temperature coefficient than solar cells with a smaller V_{OC}, however this is not always the case.

There is a significant amount of uncertainty in determining the solar cell junction temperature. Methods for reducing this uncertainty was discussed by Emery *et al.* [50].

- Use a temperature controlled vacuum chuck.
- Preheat the solar cell and then measure it in an insulated box. The front of the cell will cool faster than the back of the cell.
- Measure the solar cell inside of a temperature controlled chamber.
- Measure the solar cell while changing the room temperature. Additional uncertainty is caused by the temperature coefficient of the equipment.

Another source of uncertainty is caused by the spectrum used to test the solar cell [50, 95]. This uncertainty is due to the unequal absorption of photons of different energies. Photons of higher energy are more likely to be absorbed closer to the front of the solar cell. Photons with less energy are more likely to be absorbed deeper in the device. Because the recombination is not uniform throughout the device, the spectral

distribution of the incident spectrum will affect the performance of the solar cell. This uncertainty can be reduced by improving the spectrum or analytically using the information about the solar cell's performance.

3. DETAILED BALANCE LIMITED VERY HIGH TEMPERATURE TERMINAL CHARACTERISTICS

It is well known that the η of most solar cells will decrease as the temperature increases. While some characteristics can improve η as the temperature increases, such as the J_{SC}, other important terminal characteristics, such as the V_{OC} can reduce the η more quickly. These temperature dependent terminal characteristics will be explored in more detail in the following sections, and examples will be given for the S-Q detailed balance limit.

Since solar cells in most applications will operate over a wide range of temperatures, understanding the temperature dependent trade-offs between the terminal characteristics can help researchers develop solar cells that will perform better over the desired range of temperatures. Picking a solar cell design or a solar cell material with the highest η at a particular temperature may not yield a solar cell with the best performance over the desired operating range.

Examples will be shown were a solar cell that has been optimized for one T_O will operate less efficiently at another T_O with-in its desired operating range. Often solar cell systems are designed, optimized and tested at the standard test conditions of 25 °C or 300 K (26.85 °C). It is therefore important to take into consideration the range of solar cell T_O and the amount of time that the solar cell will operate over that range of temperatures.

This chapter has been divided into 2 parts. Section 3.1 will explore the terminal characteristics and temperature dependent terminal characteristics for S-Q detailed balance limited solar cells over a wide range of T_O and simulated E_G. Section 3.2 will explore the temperature dependent bandgap narrowing of real materials

3.1 Terminal Characteristics

The terminal characteristics, J_{SC}, V_{OC}, *FF*, and η, are the most common method for characterizing the solar cell's performance. Due to the temperature dependent device physics governing the operation of a solar cell, each of terminal characteristics are inherently dependent on the T_O of the solar cell.

$$\eta = \frac{P_{Max}}{P_{In}} = \frac{J_{MP}V_{MP}}{P_{In}} = \frac{J_{SC}V_{OC}FF}{P_{In}} \tag{3.1}$$

Where, P_{in} is the power density incident on the solar cell, with a total input area, A_T, P_{Max} is the maximum power out and J_{MP} is the max power current density terminal characteristic and V_{MP} is the max power voltage terminal characteristic. The *FF* can be defined as

$$FF = \frac{J_{MP}V_{MP}}{J_{SC}V_{OC}}. \tag{3.2}$$

Where, each of the terminal characteristics are dependent on the T_O.

The S-Q detailed balance limited η is plotted for a wide range of T_O in Figure 3.15. For low E_G the η increases as the E_G increases, this due to the V_{OC} increasing. For high E_G the η decreases as the E_G increases, this due to the J_{SC} decreasing

The J-V curves of an example solar cell at two values of T_O are shown in Figure 3.1.

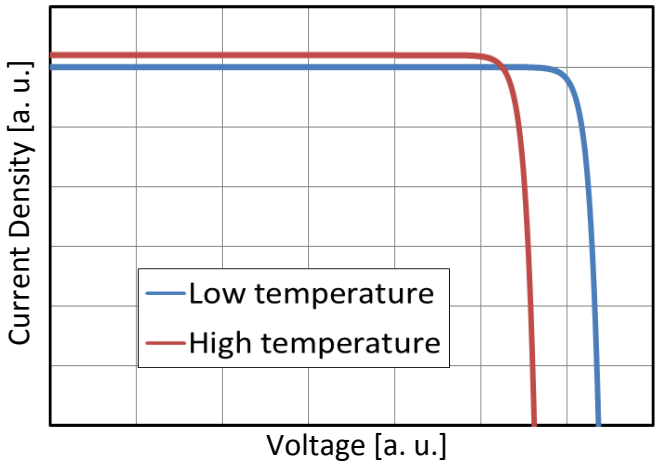

Figure 3.1. Example J-V curves of a solar cell at two values of T_O. In most solar cells the J_{SC} increases as the temperature increases, while the V_{OC} and FF typically decrease as the temperature decreases.

In most solar cells, the J_{SC} goes up as the temperature increases, while the V_{OC} and FF decrease as the temperature decreases. The J_{SC} of a solar cell generally increases due to the temperature dependent bandgap narrowing, which can increase the photon absorption. The J_{SC} can also decrease as the temperature increases, when there is bandgap narrowing in a filter layer or there is an optical element which is impeding the absorption of additional photons. This will be explained in Section 3.1.4. The temperature dependent decrease of the V_{OC} and FF are primarily due to the increasing J_O and the T_O. The FF can also be reduced by additional temperature dependent factors such as the series resistance, shunt resistance and the biasing point loss, see Chapter 5.

The P_{in} in Equation (3.1) is weakly dependent on the ambient atmospheric temperature and is not be affected significantly by the T_O of the solar cell.

3.1.1 Temperature Dependent Terminal Characteristics

In addition to the standard terminal characteristics discussed in the previous section, the temperature dependence of the terminal characteristics, or temperature coefficients as

they often called, are often measured [96]. Not only can these measurements be used in conjunction with non-temperature dependent parameters to predict the performance of the solar cell over a range of T_O, they can also be used to further constrain the possible values for the material parameters and to verify the device physics used in models. These characteristics can be used when developing analytical models and detailed numerical models.

There are two types of commonly used temperature coefficients, the absolute temperature coefficients and the relative temperature coefficients, shown in Table 3.1. As will be shown in the following subsections the absolute temperature coefficient, which is the derivative of each terminal characteristic over T_O, will not change significantly over a ranges of T_O. Therefore, when the terminal characteristics are plotted over T_O, they appear to change linearly over a ranges of T_O.

Table 3.1
Commonly measured terminal characteristics, along with the associated absolute temperature coefficient and relative temperature coefficients for each terminal characteristic.

Terminal characteristic	J_{SC}	V_{OC}	FF	η
Absolute temperature coefficient	$\frac{dJ_{SC}}{dT}$	$\frac{dV_{OC}}{dT}$	$\frac{dFF}{dT}$	$\frac{d\eta}{dT}$
Relative temperature coefficient	$\frac{1}{J_{SC}}\frac{dJ_{SC}}{dT}$	$\frac{1}{V_{OC}}\frac{dV_{OC}}{dT}$	$\frac{1}{FF}\frac{dFF}{dT}$	$\frac{1}{\eta}\frac{d\eta}{dT}$

Similar to the terminal characteristics, the temperature at which the absolute temperature coefficients and the relative temperature coefficients were measured must be specified for these measurements to be useful.

The terminal characteristics and temperature coefficients have been explored by

A useful equation was published by Fan [52] and further utilized by many others [57, 97].

The η absolute temperature coefficient is,

$$\frac{d\eta}{dT} = \frac{V_{OC}FF}{P_{In}}\frac{dJ_{SC}}{dT} + \frac{J_{SC}FF}{P_{In}}\frac{dV_{OC}}{dT} + \frac{J_{SC}V_{OC}}{P_{In}}\frac{dFF}{dT} \quad . \tag{3.3}$$

Each parameter in this equation will be examined in the following sections. The results of this equation for a wide range of T_O are shown in Figure 3.17.

The η relative temperature coefficient is,

$$\frac{1}{\eta}\frac{d\eta}{dT} = \frac{1}{J_{SC}}\frac{dJ_{SC}}{dT} + \frac{1}{V_{OC}}\frac{dV_{OC}}{dT} + \frac{1}{FF}\frac{dFF}{dT} \tag{3.4}$$

This equation shows that the $\frac{1}{\eta}\frac{d\eta}{dT}$ is simply the sum of the other relative temperature coefficients, and therefore each one equally affects the result. This will be discussed further in Section 3.1.8. A similar equation can be developed if the J_{MP} relative temperature coefficient, $\frac{1}{J_{MP}}\frac{dJ_{MP}}{dT}$, and V_{MP} relative temperature coefficient, $\frac{1}{V_{MP}}\frac{dV_{MP}}{dT}$, are known.

$$\frac{1}{\eta}\frac{d\eta}{dT} = \frac{1}{J_{MP}}\frac{dJ_{MP}}{dT} + \frac{1}{V_{MP}}\frac{dV_{MP}}{dT} \tag{3.5}$$

3.1.2 Temperature Dependent Terminal *J*-*V* Relationship

Each of the common terminal characteristics can be found on the *J*-*V* curve of the solar cell. An example of a *J*-*V* curve was shown in Figure 3.1. Figure 3.2 shows the circuit diagram of an intrinsic solar cell, which has zero R_{Series} and infinite R_{Shunt}.

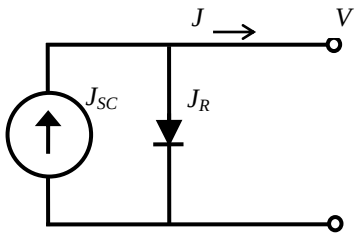

Figure 3.2. Circuit diagram of an intrinsic solar cell

The terminal current density, *J*, of a solar cell can be obtained by using Kirchoff's circuit law.

$$J = J_{SC} - J_R \tag{3.6}$$

The recombination current density, J_R, of a single recombination mechanism inside of a solar cell can be analytically modeled using an intrinsic non-ideal diode equation.

$$J_R = J_O\left[\exp\left(\frac{qV}{n_m kT}\right) - 1\right] \tag{3.7}$$

Where V is the intrinsic terminal voltage, n_m is the diode ideality factor, k is boltzmann constant and T_O is the temperature. The J_O is strongly temperature dependent. The n_m can also change over T_O, if the dominate recombination mechanism changes as the T_O increases. Section 3.1.4 will discuss the J_{SC} and Section 3.1.5 will discuss the J_O. The E_G is needed in order to calculate the J_{SC} and J_O.

3.1.3 Bandgap Energy

The bandgap energy is a material dependent parameter that has been measured for common semiconductor materials over T_O. A variety of fits have been developed to estimate the bandgap energy of a given material over a wide range of temperatures. The bandgap energy has been measured to over 500 °C for Si [98, 99], 800 °C for GaAs [100, 101], 900 °C for GaP [100] and 400 °C for SiC [102]. The material specific fit for Si is

compared to measurements in Figure 3.3. The fits for additional materials have been compared to measurements by Passler [103].

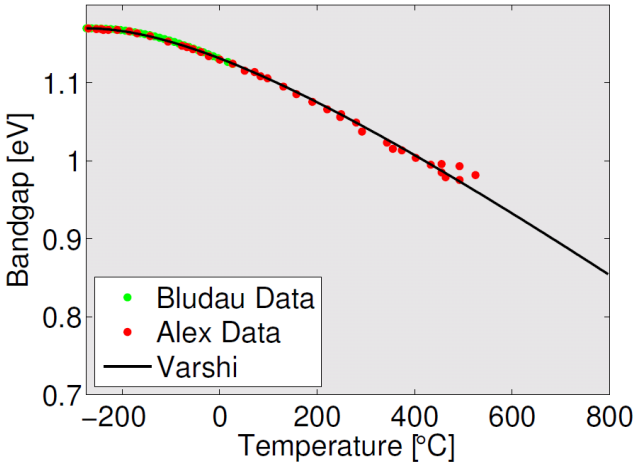

Figure 3.3. The material specific temperature dependent bandgap narrowing fit for Si compared to measurements.

Since the bandgap energy varies significantly over the T_O range of interest, it would be convenient to plot the simulated E_G at a single temperature, such as 25 °C. This would require a single fit that estimates the temperature dependent bandgap narrowing over the range of simulated bandgaps and T_O. A model was previously developed by the author for use over short T_O ranges [104]. This fit is useful for small temperature ranges, and the V_{OC} estimated using this model was accurate to within 1/2kT from 250 K to 350 K. More about this model can be found in Section B.2.1.

A related model was later developed to estimate the bandgap energy over a similar range of temperatures [105]. This fit also works well over a smaller range of operating temperatures. In order for the bandgap energy at each temperature to be adjusted back to a single temperature, such as 25 °C, a fit is needed that will work over a wider range of temperatures.

The material specific temperature dependent fits for a wide range of semiconductor materials are shown in Figure 3.4(a) [106]. The temperature dependent bandgap narrowing relative to 25 °C is shown in Figure 3.4(b). Many of the material specific fits plotted in the figure have been extrapolated beyond the measured data used to create the material specific fit.

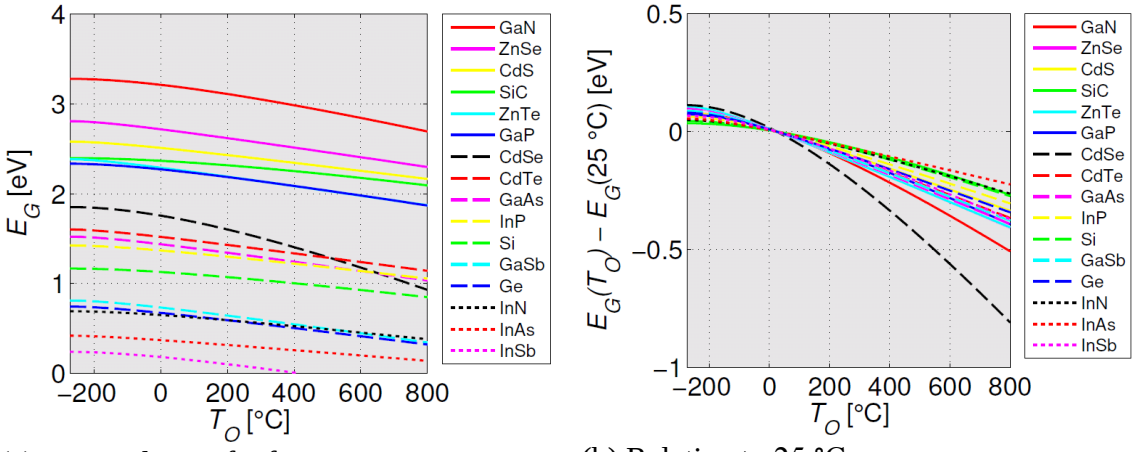

(a) Material specific fits (b) Relative to 25 °C

Figure 3.4. The material specific temperature dependent E_G narrowing fits for a wide range of direct and indirect bandgap semiconductor materials [106]. Many of the material specific fit plotted in the figure have been extrapolated beyond the measured data used to create the fit.

For a small range of temperatures near 25 °C, the amount of variation between materials is small relative to the total bandgap. This coupled with the exponential bandgap dependence of n_i made it possible to develop a J_O model over a small range of temperatures, however, for this work a very wide range of simulated bandgap energies are needed. The spread of the temperature dependent bandgap narrowing at 800 °C is larger than the total temperature dependent bandgap narrowing between 25 °C and 800 °C of many of the materials.

Other methods were used to evaluate the temperature dependent E_G narrowing, such as dividing the temperature E_G narrowing by the E_G at 25 °C to see if the narrowing could be normalized. Unfortunately, due to the fact that both narrow and wide bandgap materials have small and large temperature dependent E_G narrowing, each operating temperature E_G can have more than one 25 °C E_G, so the best that a fit can do is offer a range of possible room temperature E_G for each operating temperature E_G.

These semiconductor materials represent a wide range of semiconductor types, which include direct and indirect bandgap materials, single element and compound semiconductors, a wide variety of lattice spacing and atom sizes, binding energies, as well as crystal structures. Due to all of these factors, it is not possible to develop a simple analytical fit that does not incorporate these factors. If a fit was developed, which did incorporate all of these factors, it could not be used to predict the bandgap narrowing between measured semiconductors. In addition, such a model would predict more than one possible bandgap at each bandgap for a single operating temperature; which defeats the purpose of the model. It was therefore determined that the best way to proceed with this model is by reporting the result at the operating temperature bandgap and not adjusting them back to a single temperature.

It is possible to develop a temperature dependent bandgap narrowing fit for a limited set of semiconductor materials, such as ternary and quaternary compounds made with GaAs and InP, which will likely have similar narrowing factors. This type of fit could be used to optimize the bandgap once a material system has been chosen.

A generic fit for all materials could not be found. The examples used in this Chapter will be examined for three different cases, no temperature dependent E_G narrowing, moderate temperature dependent E_G narrowing, Figure 3.5(a), and high temperature dependent E_G narrowing, Figure 3.5(b). The moderate case roughly corresponds to the average temperature dependent E_G narrowing in Figure 3.4(b), and the high case approximates the CdSe, which was found to have the largest temperature dependent E_G narrowing of the measured materials.

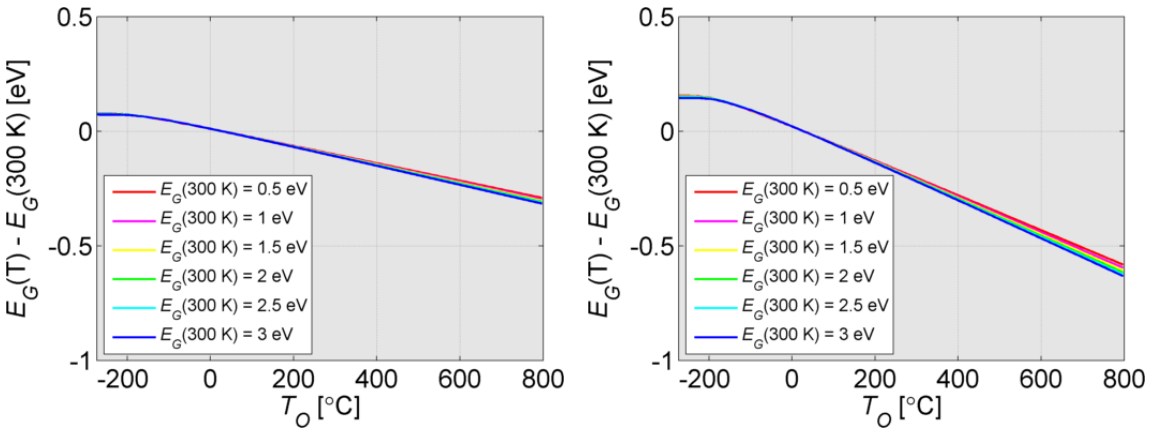

(a) Moderate narrowing (a) High narrowing

Figure 3.5. Generic fit for moderate temperature dependent E_G narrowing (a), and high temperature dependent E_G narrowing (b).

3.1.4 Short Circuit Current

The J_{SC} is a terminal characteristic that may be used to determine how well a solar cell is converting available photons into current. While it is common that the J_{SC} of a solar cell will increase as the temperature increases, this is not always the case. As the T_O of the solar cell increases, there are factors that will cause the J_{SC} to increase and there are factors that will cause the J_{SC} to decrease. Whether the J_{SC} will increase or decrease depends on which one is changing faster.

There are many factors that can cause the J_{SC} to increase as the temperature increases. One of the many factors that will cause the J_{SC} to increase is the bandgap narrowing in the absorbing layers of the solar cell. Since a solar cell can usually absorb more photons with a narrower bandgap this will cause the J_{SC} to increase. This increase will not occur if there is an absorption band between the lower temperature bandgap and the higher temperature bandgap. Optical elements such as the anti-reflectance coatings (ARC), as well as other filtering or reflecting optics can reduce the photons available

below the bandgap at the lower temperature, which will reduce the photons that will be absorbed by the solar cell, and thereby reduce the rate at which the J_{SC} will increase. Another way in which the J_{SC} of a solar cell can increase as the temperature increases occurs when the J_{SC} of one junction is limited by the other junctions in the tandem stack. If the J_{SC} of a limiting junction increases, it will increase the J_{SC} of the other junctions in the stack. The opposite can also occur when the J_{SC} of one junction is reduced when the J_{SC} of another junction decreases as the temperature increases.

In addition to the factors that will increase the J_{SC} of a solar cell as the temperature increases, there are additional internal and external factors that will decrease the J_{SC} as the temperature increases. One of the main ways in which this will occur is when the bandgap of a layer above the absorbing layers of the solar cell also narrows as the temperature increases. This can occur in many different types of layers, such as the dead layer at the front of the emitter, a passivation layer, a conducting layer, a window layer, an ARC layer, another solar cell junction, or another optical component which has temperature dependent absorption of energies in the solar spectrum. At higher temperatures the free carrier absorption in these layers may also become important. Internal factors that can reduce the J_{SC} as the temperature increases include parameters such as the diffusion length which can decrease as the temperature increases.

As will be discussed in Section 3.1.3, the temperature dependent E_G narrowing is material dependent. Therefore, the results in this Chapter will be examined for three different cases, no temperature dependent E_G narrowing, moderate temperature dependent E_G narrowing, and high temperature dependent E_G narrowing.

While more elaborate methods have been devised to calculate J_{SC} more accurately [107]. These methods include incorporating the incomplete absorption and angle dependencies. The very high temperatures model will assume that all of the photons with energy larger than the bandgap can be converted into current and that there is no other factor increasing or decreasing the J_{SC} as the temperature increases, and each photon can

only generate one electron-hole pair. This method is often used to calculate the J_{SC}. In addition, many methods are being developed to increase the absorption near and even below the bandgap, such as multiple-exciton generation, intermediate band cells and quantum wells [27]. While each of these approaches have limitations, they may eventually lead to the J_{SC} values that are equal to or greater than the J_{SC} value calculated using this method.

The J_{SC} is defined as,

$$J_{SC} = q\int_{\lambda_G}^{0} \frac{\Phi(\lambda)}{hc/\lambda} d\lambda . \tag{3.8}$$

Where, q is the electric charge, $\Phi(\lambda)$ is the photon flux density incident on the front surface of the solar cell, h is Plank's constant, c is the speed of light, λ is the photon wavelength, λ_G is the semiconductor bandgap wavelength, E_λ is the photon energy.

The λ can be found by using the Plank relation

$$\lambda = hc / E_\lambda \tag{3.9}$$

Since the results in this work include concentrated cases, the ASTM Standard G173-03 direct solar spectrum (AM 1.5 (d) will be used [108], Figure 3.6(a). This solar spectrum is commonly used to evaluate solar cell concentrator systems. The P_{In} for this 1-Sun spectrum is 90 mW/cm^2. The J_{SC} and P_{In} will be multiplied by the solar concentrations, X.

The J_{SC} and P_{in} available above a given bandgap are plotted over bandgap in Figure 3.6(b),(d), for the AM 1.5 D standard spectrum. Figure 3.6(c) shows the P_{In} above the simulated E_G divided by the total P_{In}. The steps in the plotted lines, Figure 3.6(b),(c),(d), are caused by the absorption gaps in the solar spectrum, Figure 3.6(a).

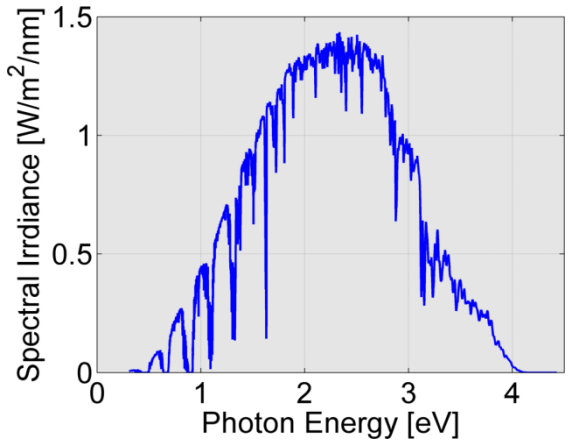

(a) ASTM Standard G173-03 [108]

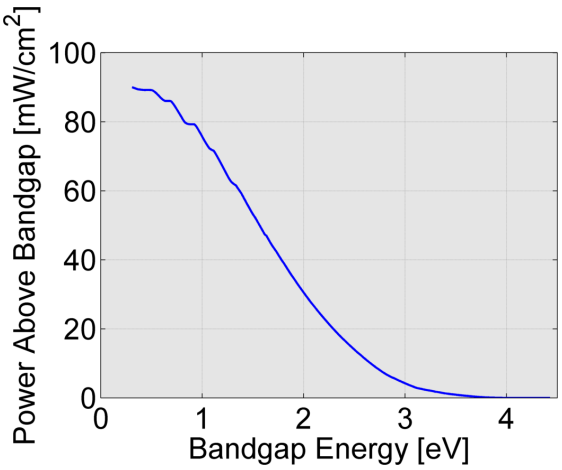

(b) Power density above the simulated E_G

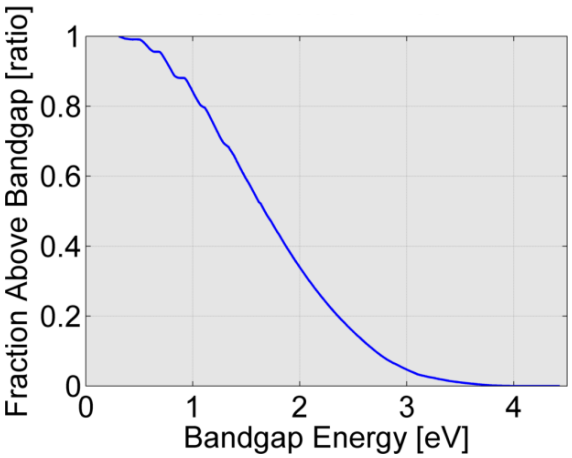

(c) Fraction of power above the simulated E_G

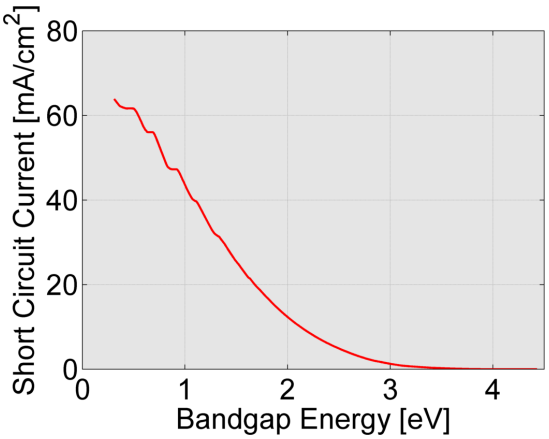

(d) The J_{SC} above the simulated E_G

Figure 3.6. Spectral irradiance (a), power available above the simulated E_G (b), fraction of power above the simulated E_G (c), and 1-Sun J_{SC} available above the simulated E_G in the ASTM Standard G173-03 direct spectrum (AM 1.5 D) (d) [108]

A moderate concentration of 500 Suns was chosen for the results in this chapter. The J_{SC} available above the simulated E_G is shown in Figure 3.7. Because the J_{SC} is plotted for the E_G at the simulated T_O, the plotted J_{SC} does not change with temperature.

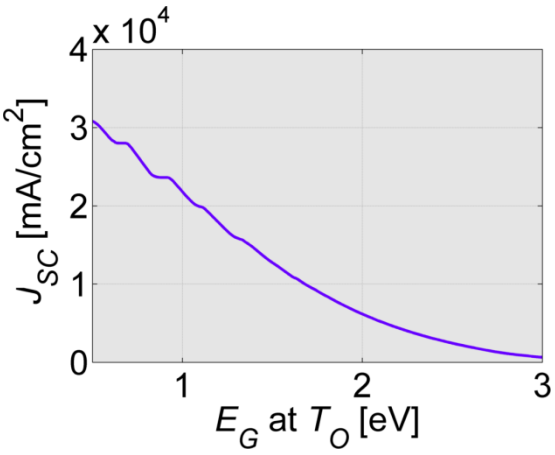

Figure 3.7. The integrated J_{SC} available above the simulated E_G at 500 Suns.

Due to the irregularities of the solar spectrum shown in Figure 3.6(c), the the J_{SC} absolute temperature coefficient, $\frac{dJ_{SC}}{dT}$, and the J_{SC} relative temperature coefficient, $\frac{1}{J_{SC}}\frac{dJ_{SC}}{dT}$, will be found numerically. Figure 3.8 shows the $\frac{dJ_{SC}}{dT}$ and $\frac{1}{J_{SC}}\frac{dJ_{SC}}{dT}$ values when there is no T dependent E_G narrowing (a) & (b), moderate T dependent E_G narrowing (c) & (d) and high T dependent E_G narrowing (e) & (f). The T dependent variation of the J_{SC} is relatively small compared to the variation caused by the absorption gaps in the solar spectrum.

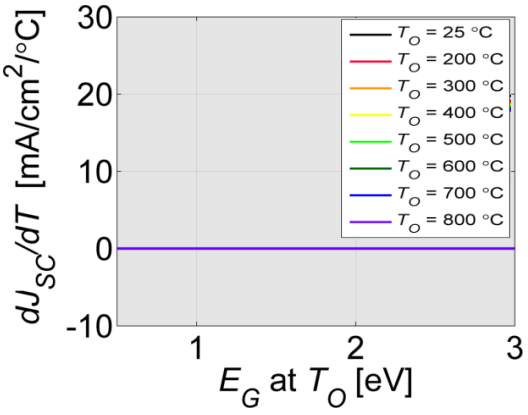

(a) No T dependent E_G narrowing

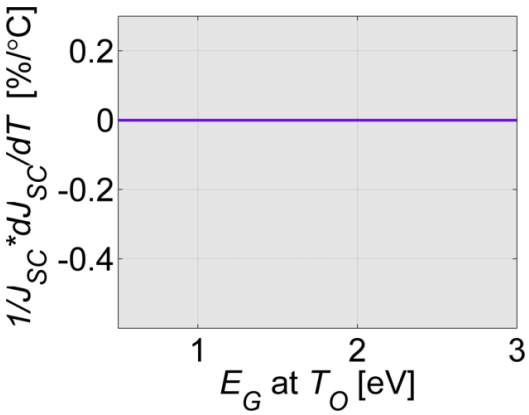

(b) No T dependent E_G narrowing

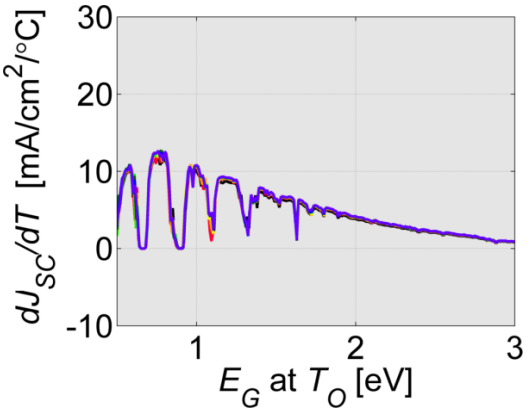

(c) Moderate T dependent E_G narrowing

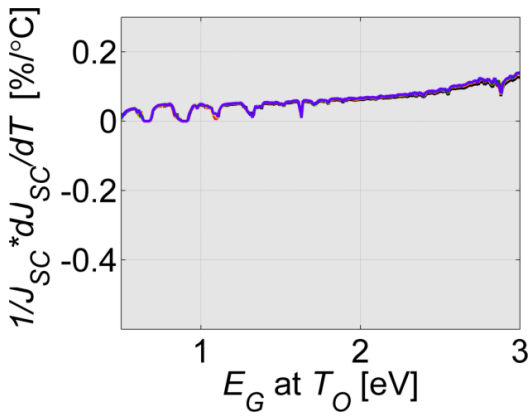

(d) Moderate T dependent E_G narrowing

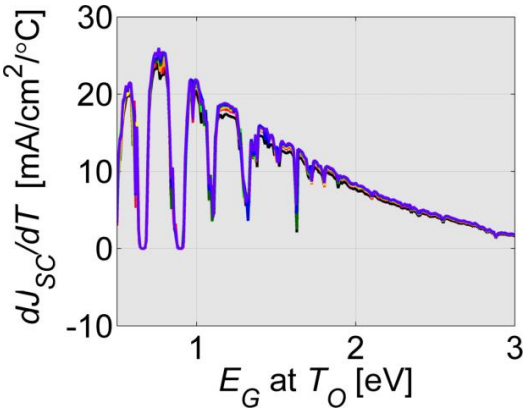

(e) High T dependent E_G narrowing

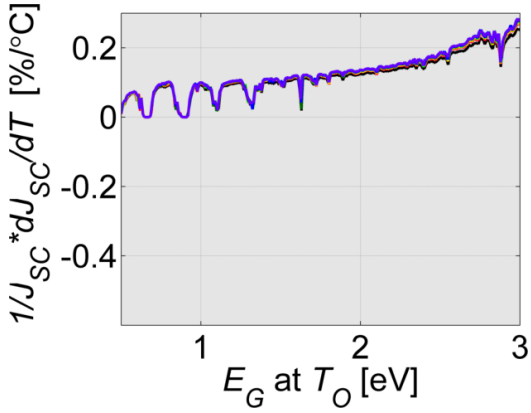

(f) High T dependent E_G narrowing

Figure 3.8. The the $\frac{dJ_{SC}}{dT}$ and $\frac{1}{J_{SC}}\frac{dJ_{SC}}{dT}$ values for cases with no T dependent E_G narrowing (a) & (b), moderate T dependent E_G narrowing (c) & (d) and high T dependent E_G narrowing (e) & (f). The T dependent variation of the J_{SC} is relatively small compared to the variation caused by the absorption gaps in the solar spectrum.

3.1.5 Recombination Current Density

The J_O is one of the primary parameters controlling the *FF* and V_{OC} of most high quality solar cells. Approaches have been developed to reduce the J_O of these recombination mechanisms. The easiest way to reduce the J_O of all of these recombination mechanisms is to reduce the thickness of the solar cell. The radiative recombination can be reduced by incorporating light management techniques. The simplest way to do this is to create a reflective surface on the back surface of the solar cell. This reflects the radiatively generated photons that could have escaped through the back surface of the solar cell. The radiative recombination can be reduced by more than a factor of 10 using light trapping and photon recycling [109, 110]. The upper limit on reducing the radiative recombination is the Shockley-Queisser detailed-balance limit. A number of methods have been developed to calculate the Shockley-Queisser detailed-balance limit. Levy developed a method for calculating the detailed-balance saturation current using Riemann zeta functions [86]. An simple to use analytical expression was developed by Gray [87].

$$J_O \approx q\left[\frac{2\pi(kT)^3}{h^3c^2}\right]e^{-E_G/kT}\left[\left(\frac{E_G}{kT}\right)^2+2\left(\frac{E_G}{kT}\right)+2\right] \tag{3.10}$$

This expression has a high degree of accuracy for solar cell devices with E_G above $>3kT$, which is ~77 meV at 25 °C and ~277 meV at 800 °C. The highest order polynomial term will dominate the other two at higher E_G values. The results of this equation plotted over a range of E_G from 0.5 eV to 3 eV and T_O from 25 °C to 800 °C are shown in Figure 3.9. The J_O increases exponentially as the T_O increases, it also increases roughly T_O to the 3/2 power.

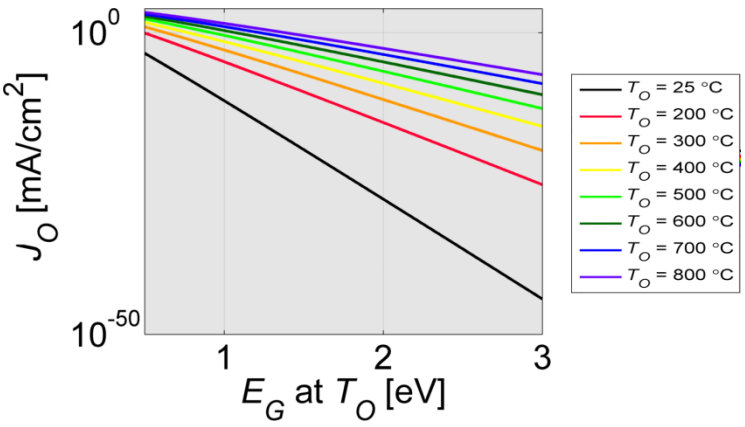

Figure 3.9. The J_O at the simulated E_G for 500 Suns. The J_O increases as the T_O increases and the J_O increases exponentially as the E_G decreases.

Due to the multiple temperature dependencies in Equation (3.10), it is difficult to identify the dominate components of the J_O absolute temperature coefficient,

$$\begin{aligned}\frac{dJ_O}{dT} \approx H\left\{3T^2\right\}e^{-E_G/kT}\left[\left(\frac{E_G}{kT}\right)^2+2\left(\frac{E_G}{kT}\right)+2\right]- \\ HT^3\left\{\left(\frac{1}{kT}\frac{dE_G}{dT}-\frac{E_G}{kT^2}\right)e^{-E_G/kT}\right\}\left[\left(\frac{E_G}{kT}\right)^2+2\left(\frac{E_G}{kT}\right)+2\right]+ \\ HT^3e^{-E_G/kT}\left\{\left[\frac{2E_G}{k^2T^2}\left(\frac{dE_G}{dT}\right)-\frac{2E_G{}^2}{k^2T^3}+\frac{2}{kT}\left(\frac{dE_G}{dT}\right)-\frac{2E_G}{kT^2}\right]\right\},\end{aligned} \tag{3.11}$$

where, *H* contains the constant parameters in Equation (3.10).

Dividing Equation (3.11) by Equation (3.10) to find the relative temperature coefficient, $\frac{1}{J_O}\frac{dJ_O}{dT}$, simplifies the first two terms in Equation (3.11). However, the 3rd term is more complicated. This makes it difficult to interpret the temperature dependencies of this equation.

$$\frac{1}{J_O}\frac{dJ_O}{dT} \approx \frac{3}{T}-\left(\frac{1}{kT}\frac{dE_G}{dT}-\frac{E_G}{kT^2}\right)+\frac{\left[\frac{2E_G}{k^2T^2}\left(\frac{dE_G}{dT}\right)-\frac{2E_G{}^2}{k^2T^3}+\frac{2}{kT}\left(\frac{dE_G}{dT}\right)-\frac{2E_G}{kT^2}\right]}{\left[\left(\frac{E_G}{kT}\right)^2+2\left(\frac{E_G}{kT}\right)+2\right]} \tag{3.12}$$

Understanding the temperature dependencies of Equations (3.11) and (3.12) will require the $\frac{dE_G}{dT}$ and $\frac{1}{E_G}\frac{dE_G}{dT}$ to be found in Section 3.1.3, for moderate temperature dependent E_G narrowing and high temperature dependent E_G narrowing. For semiconductor materials with little or no temperature dependent E_G narrowing. Equation (3.11) simplifies to

$$\frac{dJ_O}{dT} \approx HT^3 e^{-E_G/kT}\left(\left\{\frac{3}{T}+\frac{E_G}{kT^2}\right\}\left[\left(\frac{E_G}{kT}\right)^2+2\left(\frac{E_G}{kT}\right)+2\right]-\frac{2}{T}\left[\left(\frac{E_G}{kT}\right)^2+\frac{E_G}{kT}\right]\right), \tag{3.13}$$

and Equation (3.12) simplifies to

$$\frac{1}{J_O}\frac{dJ_O}{dT} \approx \frac{3}{T}+\frac{E_G}{kT^2}-\frac{\frac{2}{T}\left[\left(\frac{E_G}{kT}\right)^2+\frac{E_G}{kT}\right]}{\left[\left(\frac{E_G}{kT}\right)^2+2\left(\frac{E_G}{kT}\right)+2\right]}. \tag{3.14}$$

Figure 3.10 shows the $\frac{dJ_O}{dT}$ and $\frac{1}{J_O}\frac{dJ_O}{dT}$ when there is no temperature dependent E_G narrowing (a) & (b), moderate temperature dependent E_G narrowing (c) & (d) and high temperature dependent E_G narrowing (e) & (f). The $\frac{dJ_O}{dT}$ increases and the $\frac{1}{J_O}\frac{dJ_O}{dT}$ decreases quickly as the E_G decreases and the T_O increases.

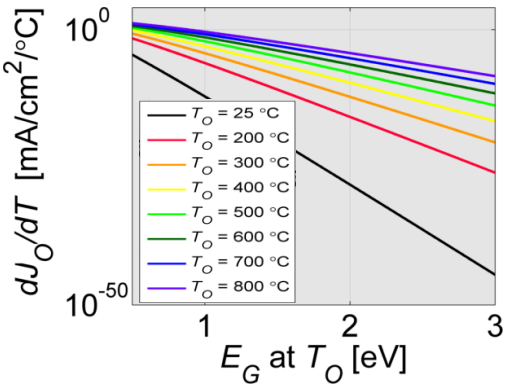

(a) No T dependent E_G narrowing

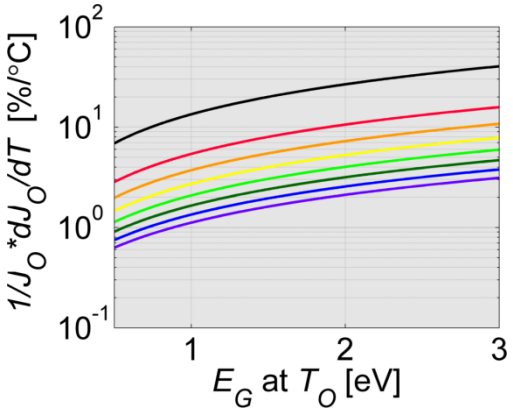

(b) No T dependent E_G narrowing

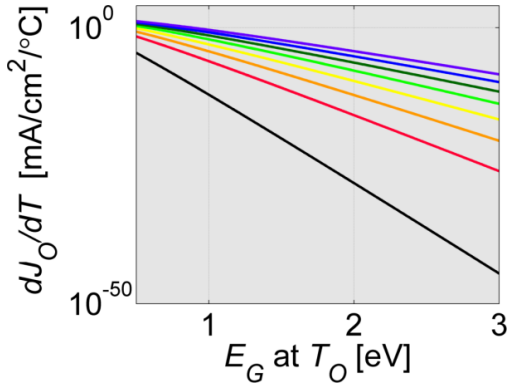

(c) Moderate T dependent E_G narrowing

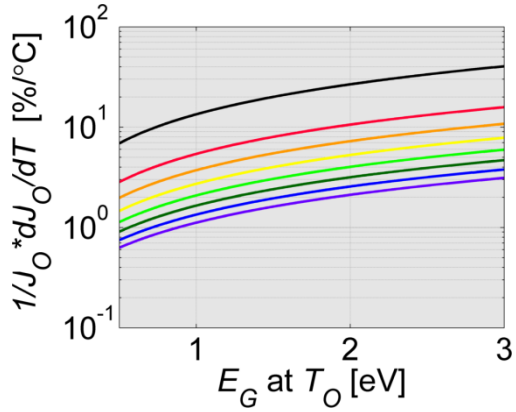

(d) Moderate T dependent E_G narrowing

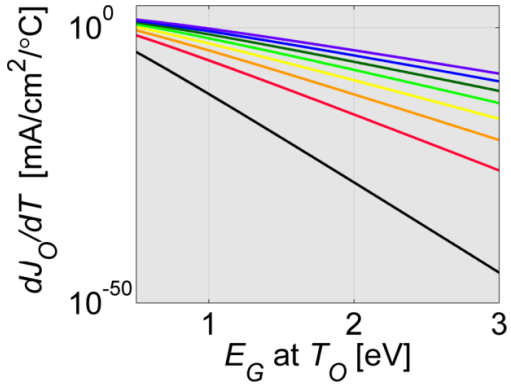

(e) High T dependent E_G narrowing

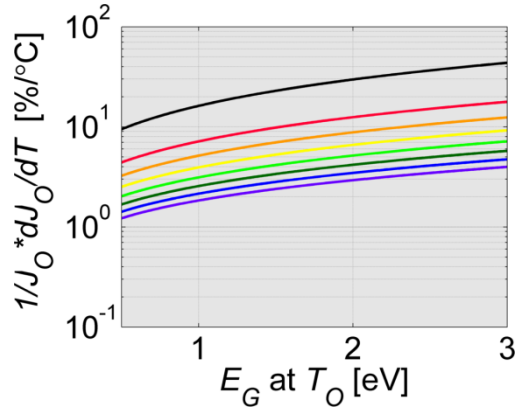

(f) High T dependent E_G narrowing

Figure 3.10. The $\frac{dJ_O}{dT}$ and $\frac{1}{J_O}\frac{dJ_O}{dT}$ values for cases with no T dependent E_G narrowing (a) & (b), moderate T dependent E_G narrowing (c) & (d) and high T dependent E_G narrowing (e) & (f). The $\frac{dJ_O}{dT}$ increases and $\frac{1}{J_O}\frac{dJ_O}{dT}$ decreases quickly as the E_G decreases and the T_O increases.

Simpler equations for $\frac{dJ_O}{dT}$ and $\frac{1}{J_O}\frac{dJ_O}{dT}$ can be found by further simplifying Equation (3.10). This simplification is helpful to get a sense of the overall temperature dependencies of the J_O.

$$J_O \approx HT^3 e^{-E_G/kT}\left(\frac{E_G}{kT}\right)^2 \tag{3.15}$$

This expression is 10% lower than Equation (3.10) above $20kT$, which is ~0.5 eV at 25 °C and ~1.8 eV at 800 °C.

The $\frac{dJ_O}{dT}$ of Equation (3.15) is then,

$$\frac{dJ_O}{dT} \approx \frac{HT}{k^2} e^{-E_G/kT} E_G{}^2 \left[\frac{E_G}{T^2 k} + 1 + \frac{2}{E_G}\frac{dE_G}{dT} - \frac{1}{Tk}\frac{dE_G}{dT}\right], \tag{3.16}$$

and the $\frac{1}{J_O}\frac{dJ_O}{dT}$ is then,

$$\frac{1}{J_O}\frac{dJ_O}{dT} \approx \frac{E_G}{T^2 k} + 1 + \frac{2}{E_G}\frac{dE_G}{dT} - \frac{1}{Tk}\frac{dE_G}{dT}. \tag{3.17}$$

For semiconductor materials with little or no temperature dependent E_G narrowing Equation (3.16) simplifies to

$$\frac{dJ_O}{dT} \approx \frac{HT}{k^2} e^{-E_G/kT} E_G{}^2 \left[\frac{E_G}{T^2 k} + 1\right], \tag{3.18}$$

and Equation (3.17) simplifies to

$$\frac{1}{J_O}\frac{dJ_O}{dT} \approx \frac{E_G}{T^2 k} + 1. \tag{3.19}$$

The $\frac{1}{J_O}\frac{dJ_O}{dT}$ is therefore approximately equal to $\frac{E_G}{T^2 k}$, since the $\frac{E_G}{T^2 k}$ term will be larger than the unity term in this equation, for all of the E_G values where Equation (3.15) is a good approximation of J_O, see Figure 3.10(b). The E_G decreases slowly as the T_O increases and the T_O increases to the 2 power as the T_O increases. The same

simplification can also be applied to Equation (3.18) to examine the temperature dependent of the $\frac{dJ_O}{dT}$, see Figure 3.10(a).

3.1.6 Open Circuit Voltage

This chapter focuses on finding the terminal characteristics and terminal coefficients of the S-Q detailed balance limit, which has only one recombination mechanism, Equation (3.10). Methods for calculating the V_{OC} with more than one recombination mechanism will be discussed in section 4.1.1. The V_{OC} for a single dominate recombination mechanism can be found by solving for V in the intrinsic non-ideal diode equation, Equation (3.6), when J is zero.

$$V_{OC} = \frac{nkT}{q} \ln\left(\frac{J_{SC}}{J_O} + 1\right) \tag{3.20}$$

In this equation the J_O reduces the V_{OC} faster than the T_O term or J_{SC} can increase it. This causes the V_{OC} to decrease for a given E_G as the T_O increases. Due to the exponentially increase of J_O as the E_G decreases, the V_{OC} decreases nearly linearly as the E_G decreases.

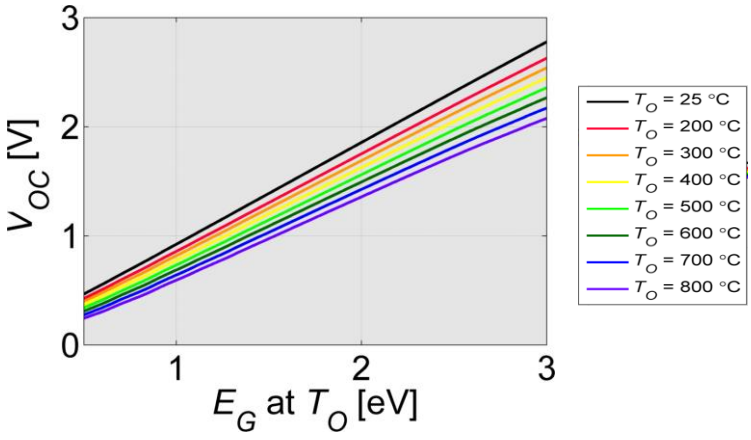

Figure 3.11. The V_{OC} at the simulated E_G for 500 Suns. As the T_O increases the V_{OC} decreases for a given E_G at T_O, this is caused by J_O. The V_{OC} increase nearly linearly as the E_G increases.

The V_{OC} absolute temperature coefficient, $\frac{dV_{OC}}{dT}$, can be found from Equation (3.20).

$$\frac{dV_{OC}}{dT} = \frac{nk}{q}\left[\ln\left(J_{SC}+J_O\right)+T\frac{1}{J_{SC}+J_O}\frac{dJ_{SC}}{dT}\right]-\frac{nk}{q}\left[\ln\left(J_O\right)+T\frac{J_{SC}}{J_O\left(J_{SC}+J_O\right)}\frac{dJ_O}{dT}\right] \quad (3.21)$$

Since the $\frac{dV_{OC}}{dT}$ is negative in all three T dependent E_G narrowing cases, Figure 3.12(a),(c),(e), the second term which is negative must be significantly larger than the first term. It is unlikely that the first term will be negative, due to the fact that the $\frac{dJ_{SC}}{dT}$ is usually positive, Figure 3.8.

The V_{OC} relative temperature coefficient is,

$$\frac{1}{V_{OC}}\frac{dV_{OC}}{dT} = \frac{1}{T}+\frac{\left[\frac{dJ_{SC}}{dT}-\frac{J_{SC}}{J_O}\frac{dJ_O}{dT}\right]}{\left(J_{SC}+J_O\right)\left[\ln\left(J_{SC}+J_O\right)-\ln\left(J_O\right)\right]}. \quad (3.22)$$

Figure 3.12(b),(d),(f) shows that the $\frac{1}{V_{OC}}\frac{dV_{OC}}{dT}$ is negative in all three cases, which means that the $\frac{J_{SC}}{J_O}\frac{dJ_O}{dT}$ term must be larger than the $\frac{J_{SC}}{dT}$ term. The denominator of the second term is expected to always be positive, since the natural log of $J_{SC} + J_O$ will be larger than the natural log of J_O.

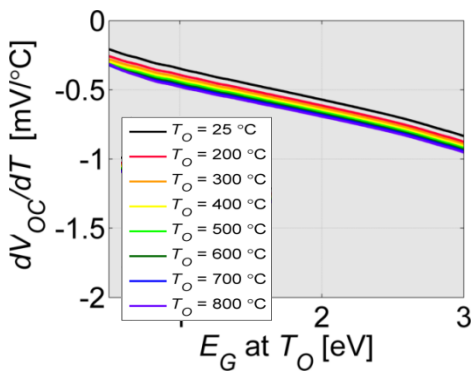

(a) No T dependent E_G narrowing

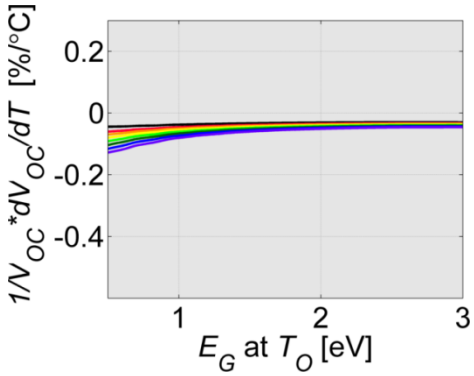

(b) No T dependent E_G narrowing

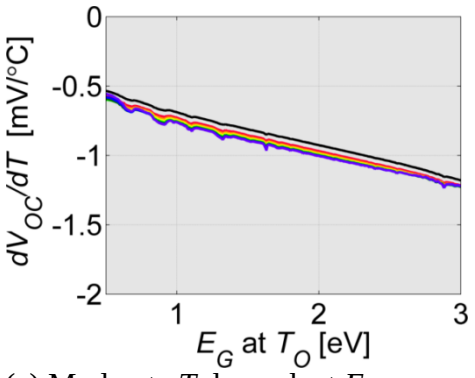

(c) Moderate T dependent E_G narrowing

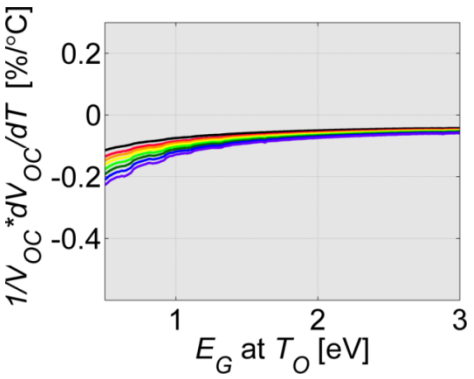

(d) Moderate T dependent E_G narrowing

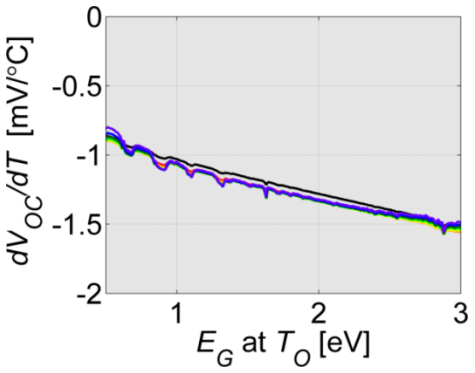

(e) High T dependent E_G narrowing

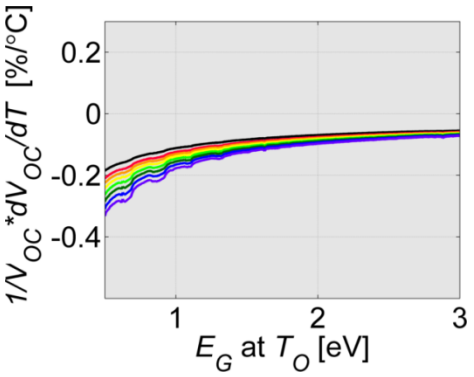

(f) High T dependent E_G narrowing

Figure 3.12. The $\frac{dV_{OC}}{dT}$ and $\frac{1}{V_{OC}}\frac{dV_{OC}}{dT}$ values for cases with no T dependent E_G narrowing (a) & (b), moderate T dependent E_G narrowing (c) & (d) and high T dependent E_G narrowing (e) & (f). The $\frac{dV_{OC}}{dT}$ becomes more negative as the E_G increases and as the T_O increases. As T_O dependent E_G narrowing increases, the $\frac{dFF}{dT}$

becomes less sensitive to the T_O. The $\frac{1}{FF}\frac{dFF}{dT}$ becomes more negative as the E_G decreases, as the T_O increases and as the E_G narrowing increases.

The $\frac{dV_{OC}}{dT}$, Equation (3.21), can be simplified by assuming that the J_{SC} is significantly larger than J_O. This is true for E_G values above 0.5 eV at 200 °C and E_G values above 1.5 eV at 800 °C, Figure 3.9.

$$\frac{dV_{OC}}{dT} \approx \frac{nk}{q}\left[\ln\left(J_{SC}\right)+T\frac{1}{J_{SC}}\frac{dJ_{SC}}{dT}\right]-\frac{nk}{q}\left[\ln\left(J_O\right)+T\frac{1}{J_O}\frac{dJ_O}{dT}\right] \tag{3.23}$$

And the simplified $\frac{1}{V_{OC}}\frac{dV_{OC}}{dT}$ is,

$$\frac{1}{V_{OC}}\frac{dV_{OC}}{dT} \approx \frac{1}{T}+\frac{\left[\frac{1}{J_{SC}}\frac{dJ_{SC}}{dT}-\frac{1}{J_O}\frac{dJ_O}{dT}\right]}{\left[\ln\left(J_{SC}\right)-\ln\left(J_O\right)\right]}. \tag{3.24}$$

3.1.7 Fill Factor

The *FF*, defined in Equation (3.2), is an important catch all terminal characteristic that is affected by device parameters such as *n*, R_{Series} and R_{Shunt}.

The J_{MP} and V_{MP} of the intrinsic single diode case can be found by using Equation (3.6) and Equation (3.7).

$$J_{MP} = J_{SC} - J_O\left[\exp\left(\frac{qV_{MP}}{nkT}\right)-1\right] \tag{3.25}$$

An analytically intrinsic *FF* is solution as well as other analytical solutions were developed by Green [111].

$$FF \approx \frac{\frac{qV_{OC}}{nkT}-\ln\left(\frac{qV_{OC}}{nkT}+0.72\right)}{\frac{qV_{OC}}{nkT}+1} \tag{3.26}$$

Analytical and numerical methods for calculating the *FF* for various combinations of resistances, multiple diodes in parallel and number of solar cell junctions in series is discussed in Appendix C. The S-Q detailed balance limit *FF* is shown in Figure 3.13. The denominator in Equation (3.26) will always be positive, because the V_{OC} is always

positive, Figure 3.11. Since the *FF* is always positive the first term is always larger than the second term.

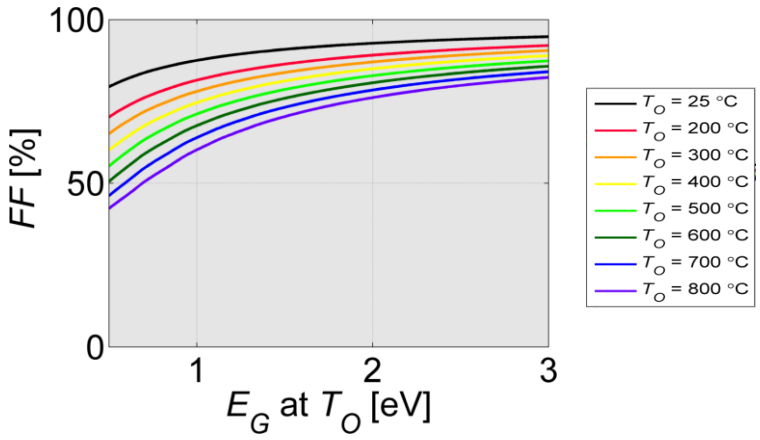

Figure 3.13. The *FF* at the simulated E_G for 500 Suns. As the T_O increases the *FF* decreases for a given E_G at T_O, this is caused by J_O.

The *FF* absolute temperature coefficient, using Equation (3.2) is,

$$\frac{dFF}{dT} = \frac{J_{MP}}{J_{SC}V_{OC}}\frac{dV_{MP}}{dT} + \frac{V_{MP}}{J_{SC}V_{OC}}\frac{dJ_{MP}}{dT} - \frac{J_{MP}V_{MP}}{J_{SC}^2V_{OC}}\frac{dJ_{SC}}{dT} - \frac{J_{MP}V_{MP}}{J_{SC}V_{OC}^2}\frac{dV_{OC}}{dT} \tag{3.27}$$

Solving this equation requires the values J_{MP}, V_{MP}, $\frac{dJ_{MP}}{dT}$ and $\frac{dV_{MP}}{dT}$. All three cases of E_G narrowing in Figure 3.14 show that this equation is negative. As expected the value of $\frac{dFF}{dT}$ becomes more negative as the E_G decreases. It also becomes more negative as the T_O increases and the E_G narrowing increases.

The *FF* absolute temperature coefficient, using the analytical equation is,

$$\frac{dFF}{dT} \approx \frac{FF\left(\frac{qV_{OC}}{nkT^2} - \frac{q}{nkT}\frac{dV_{OC}}{dT}\right)}{\left(\frac{qV_{OC}}{nkT}+1\right)} - \frac{\frac{\frac{q}{nkT}\frac{dV_{OC}}{dT} - \frac{qV_{OC}}{nkT^2}}{\frac{qV_{OC}}{nkT}+0.72} - \frac{q}{nkT}\frac{dV_{OC}}{dT} + \frac{qV_{OC}}{nkT^2}}{\frac{qV_{OC}}{nkT}+1} \tag{3.28}$$

The *FF* relative temperature coefficient, using Equation (3.2) is,

$$\frac{1}{FF}\frac{dFF}{dT} = \frac{1}{V_{MP}}\frac{dV_{MP}}{dT} + \frac{1}{J_{MP}}\frac{dJ_{MP}}{dT} - \frac{1}{J_{SC}}\frac{dJ_{SC}}{dT} - \frac{1}{V_{OC}}\frac{dV_{OC}}{dT} \tag{3.29}$$

Just like $\frac{dFF}{dT}$ the $\frac{1}{FF}\frac{dFF}{dT}$ is negative in all three cases in Figure 3.14. In Equation (3.29) the first and the third terms are negative while the second and the fourth terms are positive.

The *FF* relative temperature coefficient, using analytical equation is,

$$\frac{1}{FF}\frac{dFF}{dT} \approx \left[\frac{\left(\frac{qV_{OC}}{nkT^2} - \frac{q}{nkT}\frac{dV_{OC}}{dT}\right)}{\left(\frac{qV_{OC}}{nkT}+1\right)} - \frac{\left(\frac{qV_{OC}}{nkT}-0.3\right)\left(\frac{qV_{OC}}{nkT^2} - \frac{q}{nkT}\frac{dV_{OC}}{dT}\right)}{\left(\frac{qV_{OC}}{nkT}+0.7\right)\left(\frac{qV_{OC}}{nkT} - \ln\left(\frac{qV_{OC}}{nkT}+0.72\right)\right)}\right] \tag{3.30}$$

,

The denominator of both terms will always be positive, the first term is obvious and the second term won't become negative, because the numerator of Equation (3.26) cannot be negative.

The result if the *FF* term is not substituted.

$$\frac{1}{FF}\frac{dFF}{dT} \approx \left[\frac{\left(\frac{qV_{OC}}{nkT^2} - \frac{q}{nkT}\frac{dV_{OC}}{dT}\right)\left(FF\frac{qV_{OC}}{nkT} - \frac{qV_{OC}}{nkT} + FF\,0.7 + 0.3\right)}{FF\left(\frac{qV_{OC}}{nkT}+0.7\right)\left(\frac{qV_{OC}}{nkT}+1\right)}\right] \tag{3.31}$$

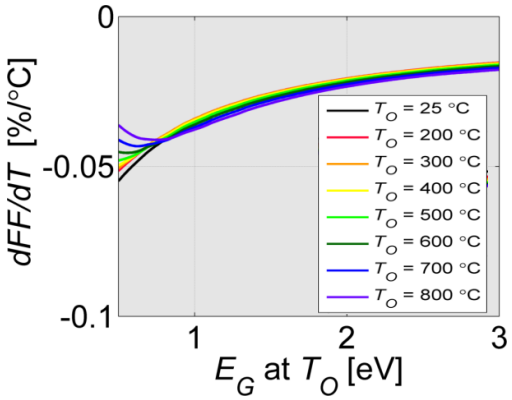

(a) No T dependent E_G narrowing

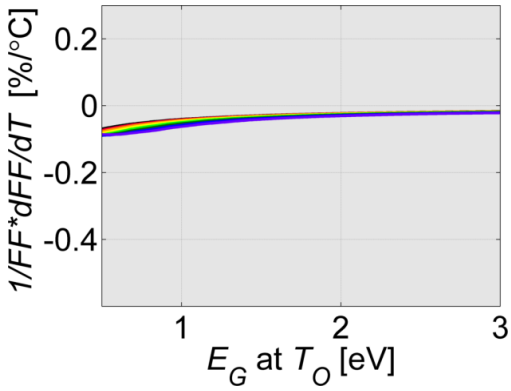

(a) No T dependent E_G narrowing

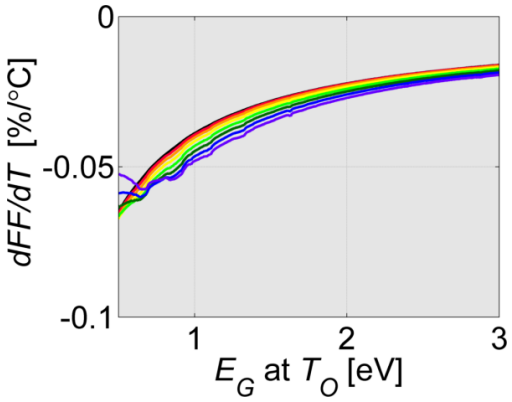

(c) Moderate T dependent E_G narrowing

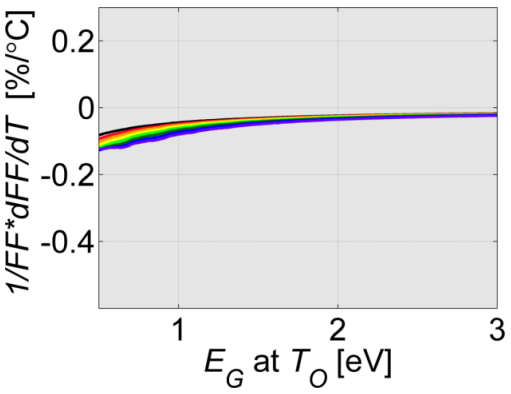

(d) Moderate T dependent E_G narrowing

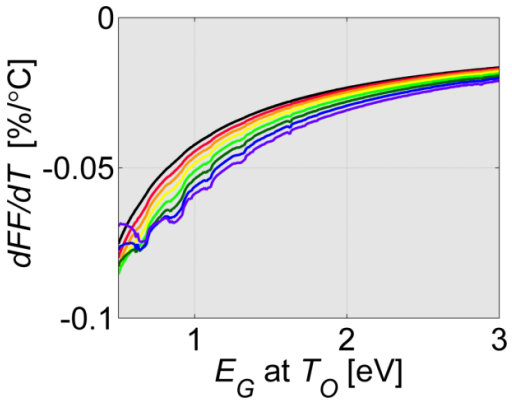

(d) High T dependent E_G narrowing

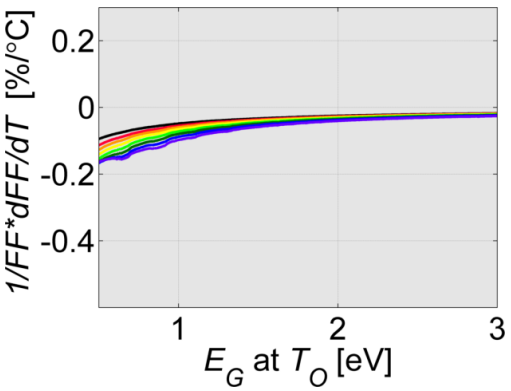

(e) High T dependent E_G narrowing

Figure 3.14. The $\frac{dFF}{dT}$ and the $\frac{1}{FF}\frac{dFF}{dT}$ values for cases with no T dependent E_G narrowing (a) & (b), moderate T dependent E_G narrowing (c) & (d) and high T dependent E_G narrowing (e) & (f). Similar to the V_{OC} temperature coefficients, Figure 3.12, the $\frac{dFF}{dT}$ and the $\frac{1}{FF}\frac{dFF}{dT}$ both becomes more negative as the E_G decreases, as the T_O increases and as the E_G narrowing increases.

3.1.8 Conversion Efficiency

The most important terminal characteristic is the P_{Max}, which is often measured relative to the P_{In}, to give the η, Equation (3.1). The temperature dependencies of J_{SC}, V_{OC}, and *FF* all affect the η. In most cases as the T_O increases the η decreases, however this is not always the case. For lower values of E_G, the η increases as the E_G increases, this is caused by the increase in the V_{OC}, Figure 3.15. For higher values of E_G, the η decreases as the E_G increases, this is caused by the decrease in the J_{SC}. This balance between the J_{SC} and the V_{OC}, causes the E_G of the optimal peak η to increase as the T_O increases. In addition the 25 °C E_G will be at a higher E_G, due to the *T* dependent E_G narrowing.

Each η curve in Figure 3.15 has an optimal peak as well as multiple local maxima. The optimal peak η over T_O is shown in Figure 3.16. The multiple peaks are caused by the absorption gap in the solar spectrum, which are shown in Figure 3.6(a). Because the η decrease more quickly for lower E_G devices, these peaks will lead to steps in the simulated E_G over T_O of the optimal peak η. The effect of these steps will be explored in Section 4.3.3.

The η plot also shows that solar cells which approach the S-Q detailed balance limit could have high η at high T_O. These results show that it is possible to reach 29 % at 400 °C and 20 % at 800 °C. At high T_O, real devices will likely be limited by other factors before reaching these high η values.

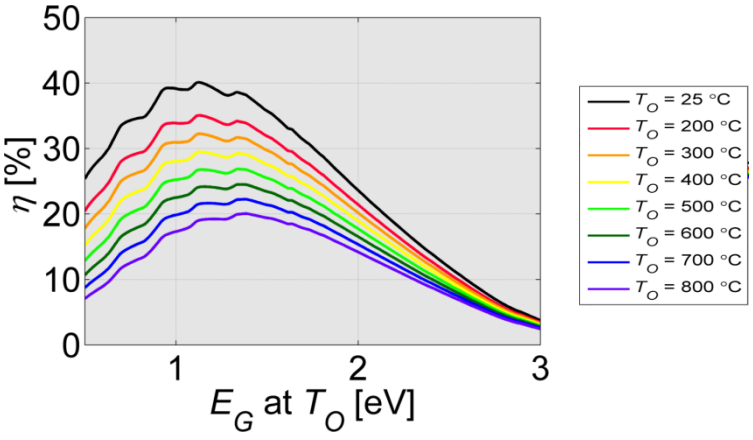

Figure 3.15. The η at the simulated E_G for 500 Suns. As the T_O increases the η decreases for a given E_G at T_O. In most values of E_G as the T_O increases the η decreases. For lower values of E_G, the η increases as the E_G increases, this is caused by the increase in the V_{OC}. For higher values of E_G, the η decreases as the E_G increases, this is caused by the decrease in the J_{SC}.

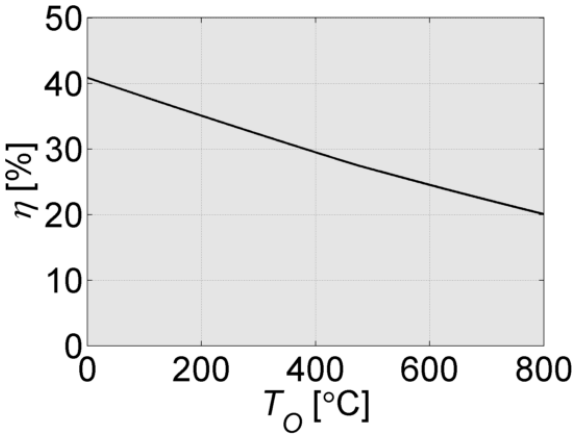

Figure 3.16. The optimal peak η over T_O for a concentration of 500 Suns. As the T_O increases the η decreases.

The $\frac{d\eta}{dT}$, as defined in Equation (3.3), and $\frac{1}{\eta}\frac{d\eta}{dT}$, as defined in Equation (3.4), are typically negative for most E_G values, Figure 3.17. However, for high E_G values it is possible that the temperature dependence of the J_{SC} will cause the $\frac{d\eta}{dT}$ and $\frac{1}{\eta}\frac{d\eta}{dT}$ to be positive. This can be seen by comparing the relative temperature coefficient terms in Equation (3.4). At high E_G values both $\frac{1}{V_{OC}}\frac{dV_{OC}}{dT}$ and $\frac{1}{FF}\frac{dFF}{dT}$ become small, while at the same time the $\frac{1}{J_{SC}}\frac{dJ_{SC}}{dT}$ is becoming larger, leading to a positive $\frac{1}{\eta}\frac{d\eta}{dT}$.

In S-Q detailed balance limited solar cells this occurs above 2 eV in solar cells with moderate T dependent E_G narrowing and above 1.75 eV in solar cells with high T dependent E_G narrowing.

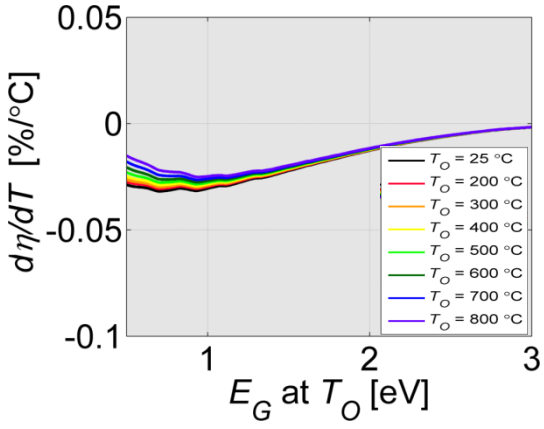

(a) No T dependent E_G narrowing

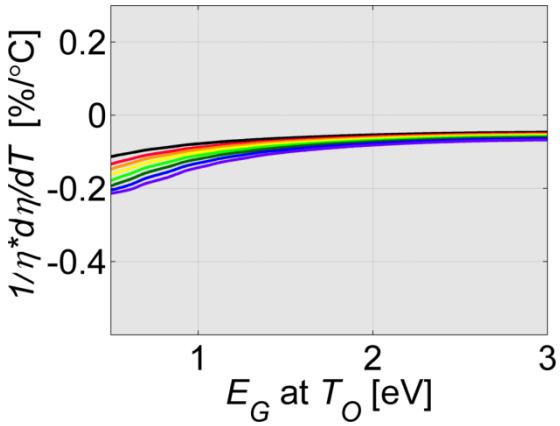

(b) No T dependent E_G narrowing

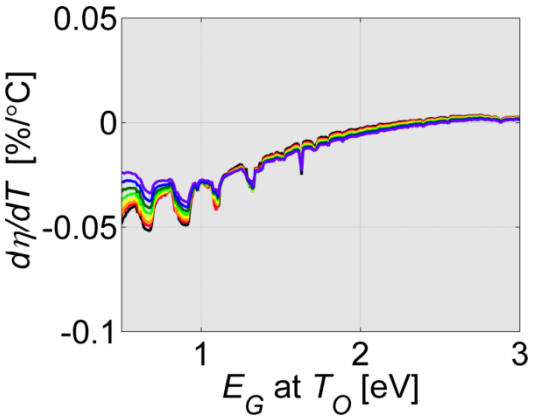

(c) Moderate T dependent E_G narrowing

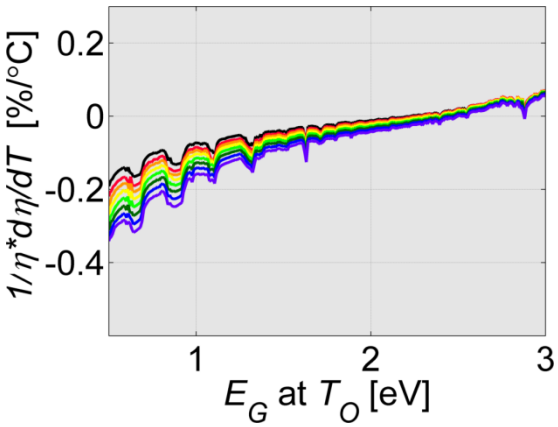

(d) Moderate T dependent E_G

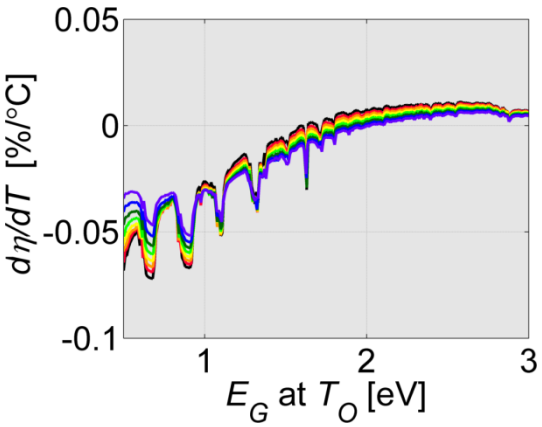

(e) High T dependent E_G narrowing

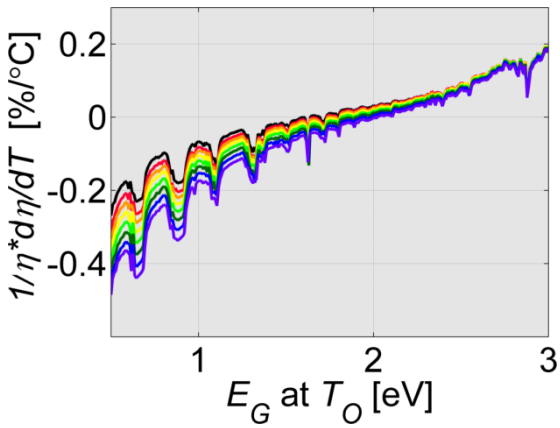

(f) High T dependent E_G narrowing

Figure 3.17. The $\frac{d\eta}{dT}$ and $\frac{1}{\eta}\frac{d\eta}{dT}$ values for cases with no T dependent E_G narrowing (a) & (b), moderate T dependent E_G narrowing (c) & (d) and high T dependent E_G

narrowing (e) & (f). The $\frac{1}{\eta}\frac{d\eta}{dT}$ is the sum of the $\frac{1}{J_{SC}}\frac{dJ_{SC}}{dT}$, $\frac{1}{V_{OC}}\frac{dV_{OC}}{dT}$ and $\frac{1}{FF}\frac{dFF}{dT}$, this causes the S-Q detailed balance limited $\frac{d\eta}{dT}$ and $\frac{1}{\eta}\frac{d\eta}{dT}$ to be positive above 2 eV in solar cells with moderate *T* dependent E_G narrowing and above 1.75 eV in solar cells with high *T* dependent E_G narrowing.

The S-Q detailed balance limit over simulated E_G and T_O has been evaluated in Section 3.1. These results are particularly useful in understanding how the terminal characteristics and temperature coefficients vary over E_G and T_O. The peak η for a given T_O was also determined. In addition, these results provide insight into what level of performance is available for solar cells that approach this limit. The next section will look at the S-Q detailed balance limited terminal characteristics using measured T dependent E_G narrowing of real semiconductor materials.

3.2 Real Semiconductor Materials

It is important to know how solar cells will perform at high T_O, when planning, designing and optimizing solar cell systems that operate at high T_O. While the temperature dependence of the terminal characteristics are nearly linear near room temperature, care must be taken when extending these results to higher T_O, where the performance is no longer linear. This section will explore how the physical material property, T dependent E_G narrowing, of real materials will affect the η over a wide range of T_O. These results are particularly useful in understanding how the T dependent E_G narrowing will affect the semiconductor material chosen and the optimization of the high temperature systems.

3.2.1 Extrapolating the Temperature Coefficients

The T dependence of the terminal characteristics are often thought to vary linearly over T_O. While this is true of solar cells over a narrow range of T_O, it frequently does not hold over a wide range of T_O. For solar cells operating near the S-Q detailed balance limit, this is due primarily to the T dependent E_G narrowing. Therefore, generally solar cells with larger T dependent E_G narrowing will deviate more quickly away from the linear trend, than solar cells with smaller narrowing.

There are four cases in which the η of real materials deviate from the linear trend, Figure 3.19 and Figure 3.19. The black lines are the S-Q detailed balance limit η for each material, using the published T dependent E_G narrowing for each of the materials. The red line is the linear extrapolated η at 25 °C. The dips in the black line are caused by the absorption gaps in the solar spectrum.

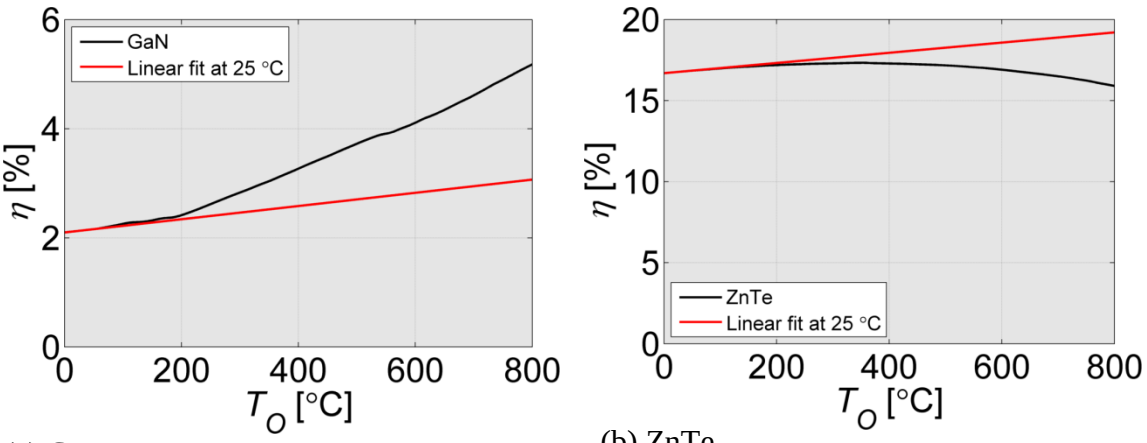

(a) GaN (b) ZnTe

Figure 3.18. The black lines are the S-Q detailed balance limit η for each material, using the T dependent E_G narrowing for each of the materials. The red lines are the linear extrapolated η at 25 °C. The dips in the black line are caused by the absorption gaps in the solar spectrum. For wide E_G materials such as GaN (a), the S-Q detailed balance limit η can increase faster than the linear extrapolated η at 25 °C as the T_O increases. For some moderate E_G materials such as ZnTe (b), the η can increase as the T_O increases at lower temperatures, due to the T dependence of the J_{SC} and then decrease as the T_O increases at higher temperatures, due to the T dependence of the V_{OC}. The lower E_G materials, SiC, GaAs, Si and Ge are plotted in Figure 3.19

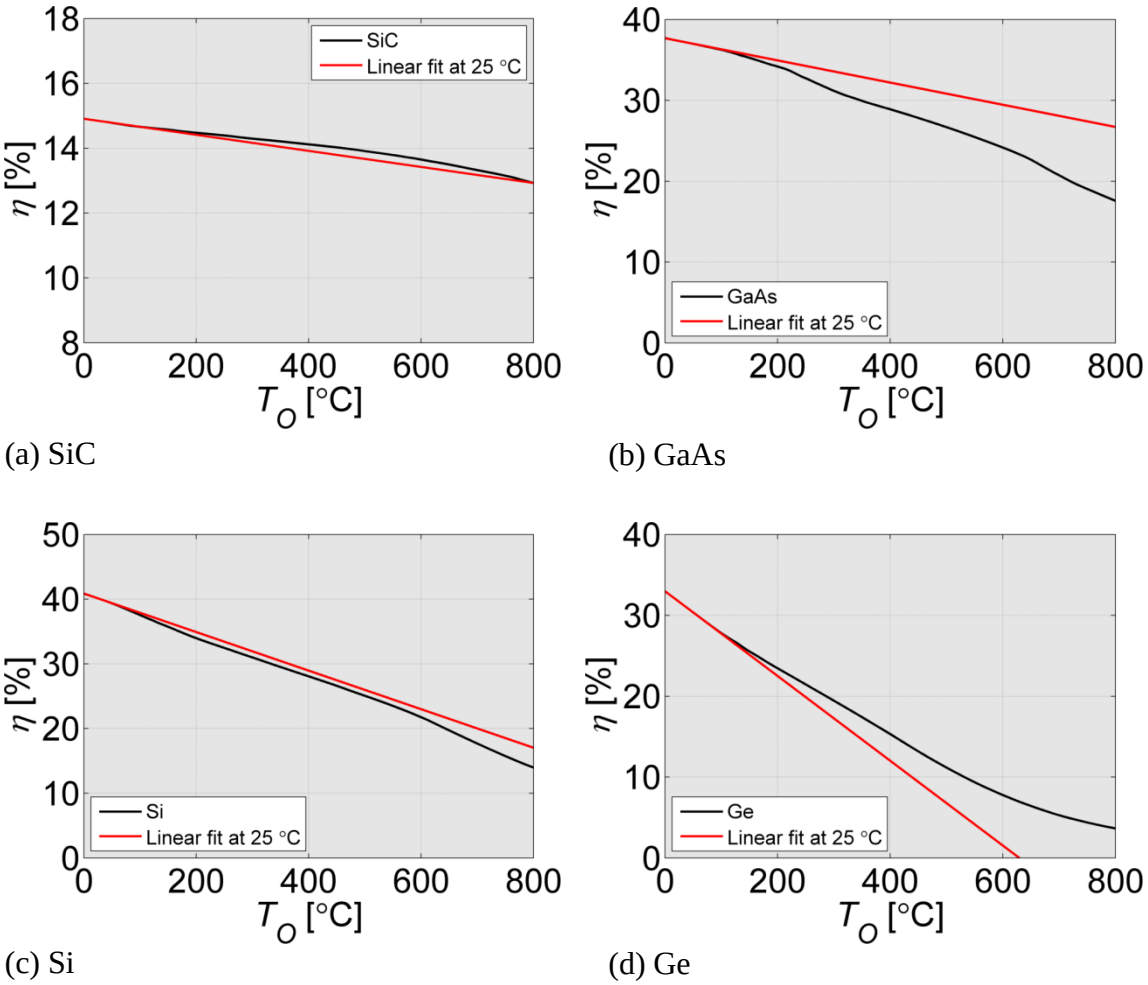

Figure 3.19. The black lines are the S-Q detailed balance limit η for each material, using the T dependent E_G narrowing for each of the materials. The red lines are the linear extrapolated η at 25 °C. The dips in the black line are caused by the absorption gaps in the solar spectrum. For the moderate E_G material SiC (a), the η simulated using the S-Q detailed balance limit and the linear extrapolated η at 25 °C are almost exactly the same. For GaAs (b), the S-Q detailed balance limit η decreases faster than the linear extrapolated η at 25 °C as the T_O increases. As was the case with SiC (a), the Si (c) η simulated using the S-Q detailed balance limit and the linear extrapolated η at 25 °C are almost exactly the same. For low E_G materials such as Ge (d), the S-Q detailed balance limit η decreases slower than the linear extrapolated η at 25 °C as the T_O increases. The Higher E_G materials, GaN and ZnTe are plotted in Figure 3.19

For each of the materials plotted in Figure 3.19 and Figure 3.19, the η simulated using the S-Q detailed balance limit and the η linear extrapolated from 25 °C are nearly

identical from 0 °C to 100 °C. Above this temperature the linear extrapolated η of many of the materials begans to deviate from the η simulated using the S-Q detailed balance limit and the T dependent E_G narrowing for each material. The materials can be seperated into 4 different cases.

The first case occurs in wide E_G materials such as GaN, Figure 3.18(a). Here the η increase faster than the T dependent η linearly extrapolated from 25 °C, which agrees with the results in Figure 3.17 for semiconductors with moderate and high T dependent E_G narrowing. This is due to the $\frac{1}{J_{SC}}\frac{dJ_{SC}}{dT}$ term, Figure 3.8(d) and (e), being larger than the $\frac{1}{V_{OC}}\frac{dV_{OC}}{dT}$ and $\frac{1}{FF}\frac{dFF}{dT}$ terms, Figure 3.12 and Figure 3.14.

In the second case, the η of moderate E_G materials, such as ZnTe (b), will first increase and then decrease as the T_O increases. The η begins to decrease when the $\frac{1}{V_{OC}}\frac{dV_{OC}}{dT}$ and $\frac{1}{FF}\frac{dFF}{dT}$ terms become larger than the $\frac{1}{J_{SC}}\frac{dJ_{SC}}{dT}$ term.

For both SiC Figure 3.19(a) and Si (c) the η simulated using the S-Q detailed balance limit and the linear extrapolated η at 25 °C are almost exactly the same over the simulated T_O range. This may be primarily due to the smaller η over T_O bumps in both of these material, which are caused by the $\frac{1}{J_{SC}}\frac{dJ_{SC}}{dT}$.

The third case occurs in materials such as, GaAs Figure 3.19(b). In these materials the η decreases more quickly than the linear fit. The $\frac{1}{J_{SC}}\frac{dJ_{SC}}{dT}$ which is improving the $\frac{1}{\eta}\frac{d\eta}{dT}$ at lower T_O, is causing the linear extrapolated η at 25 °C to predict η values that are higher than the η simulated using the S-Q detailed balance limit at higher T_O.

In the forth case, which occurs in narrow E_G materials such as Ge (d), the S-Q η decreases more slowly than the linear fit. The $\frac{1}{J_{SC}}\frac{dJ_{SC}}{dT}$ is improving the $\frac{1}{\eta}\frac{d\eta}{dT}$ at

higher T_O, which is causing the linear extrapolated η at 25 °C to predict η that are lower than the the η simulated using the S-Q detailed balance limit at these higher T_O.

Figure 3.19 and Figure 3.19 showed that the linearly extrapolated η at 25 °C was very accurate for most semiconductor materials with T_O up to 100 °C. It was also shown that the linearly extrapolated η, was not as accurate for T_O above 100 °C.

3.2.2 Finding the Optimal Material

Even when modeling the relatively simple S-Q detailed balance limit, finding the optimal material is complicated by the *T* dependent E_G narrowing and the absorption gaps in the solar spectrum. In addition, while the *T* dependent E_G narrowing causes the E_G of real semiconductor materials to decrease as the T_O increases, the E_G of the optimal peak found in Section 3.1.8, Figure 3.15, increases as the T_O increases. Therefore, without developing a material in which the E_G widened as the T_O increased, no material will be at the optimal peak η over a broad T_O range. This will be discussed more in Section 3.2.3. There are a number of ways around this problem.

One way of mitigating this problem would be to switch the solar cell at the focal point of the concentrator system. In such a system, a lower E_G solar cell would be placed at the focal point of the concentrator when the system is operating at a lower T_O. As the T_O increases one or more additional solar cells with wider E_G, that are closer to the optimal peak η, would be places at the focal point of the concentrator. This would allow the system to operate closer to the optimal peak η over a wider T_O range. Because, this is expected to significantly increase the cost of the system, it is improbable that this would be a viable solution.

Another way of mitigating this problem would be to identify a solar cell with a E_G that allowed it to performed best over the desired T_O range. Figure 3.20(a) compares the S-Q detailed balance limited η of five wide E_G materials with optimal peak η (Figure

3.16). The η of these wide E_G materials are nearly flat, because the T dependent increase of the J_{SC} is compensating for the decrease of the V_{OC} and FF. None of these materials reach the peak η line below 800 °C.

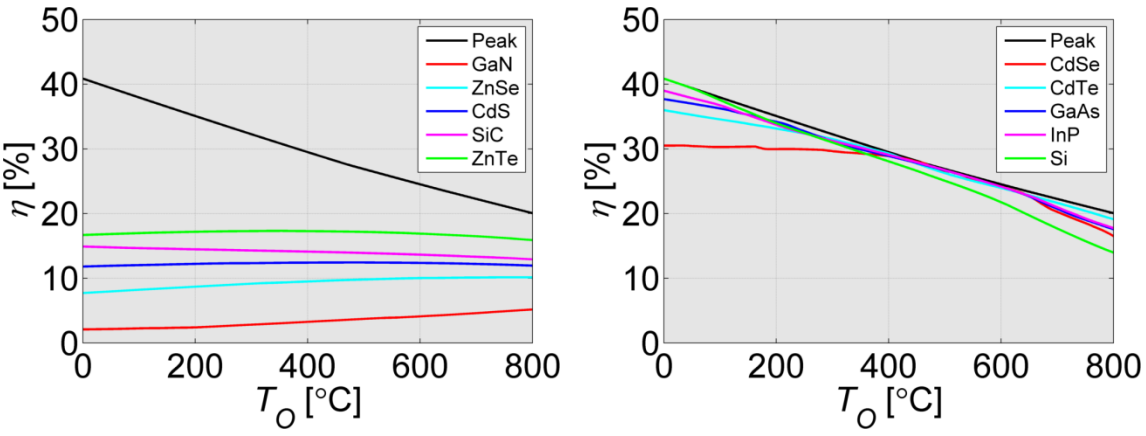

(a) Wide E_G materials (b) Moderate E_G materials

Figure 3.20. The η calculated using the T dependent E_G narrowing of real materials, compared to the optimal peak η calculated in Section 3.1.8. The high E_G material (a) does not reach the optimal peak η, while the moderate E_G materials will reach the optimal peak η.

Figure 3.20(b) examines the η of the five moderate E_G materials. Each of these materials approaches the optimal peak η line at different T_O points. The materials with wider E_G, such as CdSe, materials do so at higher T_O and the materials with narrower E_G materials such as Si, are at lower T_O. CdSe, CdTe, GaAs and InP are all relatively close to the optimal peak η line from 400 °C to 800 °C. Above 400 °C CdSe is nearly constant while the other materials continue to increase. If the solar cell was needed to operate at 425 °C, CdSe would give the highest η. However, it would not perform as well if the system operated between 300 °C and 450 °C. It is therefore important to consider the full range of T_O where the solar cells will be operating.

Due to the steps in the optimal peak E_G, which will be explained in Section 4.3.3, some of the materials do not reach the optimal peak η. There is a wide range of T_O, from 150 °C to 300 °C, over which these materials are more than 0.8 absolute % points below the optimal peak η, Figure 3.21. There are also points at 180 °C and 270 °C that are more than 1 absolute % point below the optimal peak η. This is primarily due to the steps in the optimal peak E_G, as well as the dearth of elemental and binary compound semiconductor materials with E_G between InP and Si. Using ternary compound semiconductors such as GaInAs or quaternary compound semiconductors such as GaInAsP can fill this void.

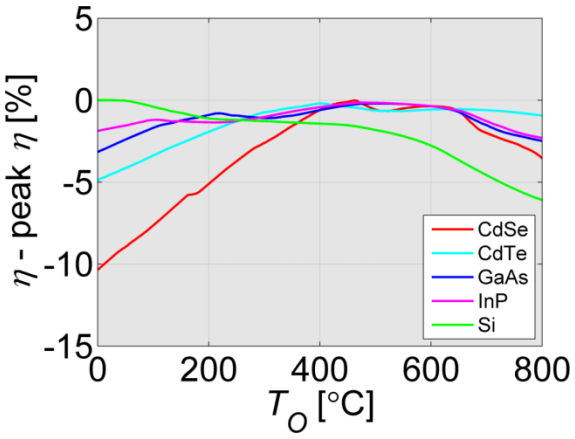

Figure 3.21. The absolute % difference between the η calculated using the T dependent E_G narrowing of real materials and the optimal peak η calculated in Section 3.1.8. Due to the steps in the E_G at the optimal peak η, not all of the materials reach the optimal peak η.

The η of real materials cannot go above the optimal peak η, unless the absorption of the solar cell and the electrical E_G are decoupled. A number of research groups are designing solar cell to absorb photons below electrical E_G using with quantum wells and quantum dots. It may be possible to find a material or a device design where this is possible [27].

3.2.3 Improving the Temperature Coefficients

The η of solar cells over T_O and the reliability have a profound effect on the economics and the LCOE of solar cells. If two solar cells have the same η at one T_O, the one with a better $\frac{d\eta}{dT}$ will produce more electrical energy at a higher T_O. In addition, areas with higher solar irradiance have the potential to produce more electrical energy. However, these locations are often hotter, than areas with lower soalr irradiance. It is possible that the $\frac{d\eta}{dT}$ of a solar cells could remove the benefit of the higher solar irradiance, if the higher T_O in this location causes the solar cell to operate at a lower η and generate less electrical energy. Therefore any changes that can be made to the solar cell that will improve the $\frac{d\eta}{dT}$, while at the same time improving or not significantly reducing the η, will be beneficial.

There are only two parameters that can be modified in a S-Q detailed balance limited model. One of those is the device thickness, which will affect the absorption and the emission of the devices. This model does not include this parameter. The other parameter that can be changed is the E_G. There are two ways in which the E_G can be changed. This includes picking the E_G at some point such as 25 °C, the other is the T dependent E_G narrowing of the material. While the T dependent E_G narrowing is a physical parameter of the semiconductor material, it might be possible to vary it by changing other material parameters.

The E_G is affected by a number of other material parameters, such as the T_O, electric field strength, strain, pressure and carrier densities. If desirable, it may be possible to adjust the rate at which the E_G varies by adjusting one of these other parameters, such as exerting pressure on the solar cell [112] or by straining the junction layers, as the T_O increases. In this section, two cases are compared to evaluate if controlling the E_G could be beneficial. In the first case the cell is unmodified, the T dependent E_G narrowing

reduces the E_G. In the second case the E_G is held constant over T_O. This could be achieved by varying another parameter over T_O, in such a way that it compensates for the T dependent E_G narrowing, such as exerting pressure on the solar cell [112] or by straining the junction layers.

Figure 3.22 shows how (a) GaN, (b) GaAs, (c) Si and (d) Ge will perform in these two cases. Holding the E_G constant of wide E_G material will eliminate the T dependent J_{SC} improvement, which will significantly reduce the overall performance as the T_O increases. Holding the E_G of GaAs constant reduces the η from 25 °C to 300 °C, has no affect from 300 °C to 600 °C and then improves the performance above 600 °C. Holding the E_G of Si constant will improve the η one full absolute % above 200 °C. Holding the E_G of Ge constant will significantly improve the η as the T_O increases.

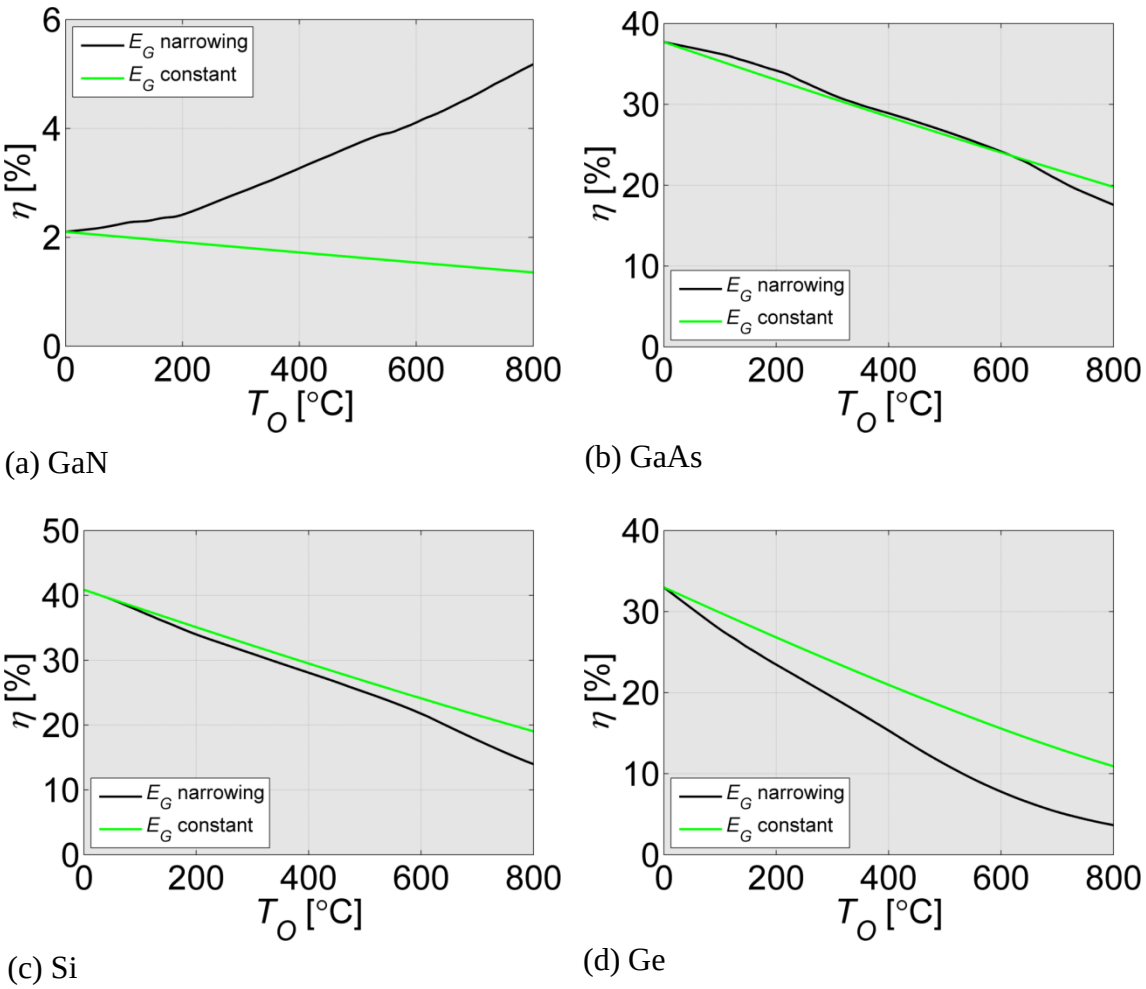

(a) GaN (b) GaAs

(c) Si (d) Ge

Figure 3.22. Compares the case with E_G narrowing and the case where the E_G is held constant over T_O, for (a) GaN, (b) GaAs, (c) Si and (d) Ge. For wide E_G materials such as GaN, holding the E_G constant will decreae the performance over T_O. For moderate E_G materials, such as GaAs and Si there may be a small improvement or a small loss. For narrow E_G materials, such as Ge, holding the E_G constant increases the performance over T_O.

The results presented above compare the cases where the E_G narrows as the T_O increases and where the E_G is stays constant over T_O. The E_G at the optimal peak η increases as the T_O increases, therefore in some cases it may be beneficial to design a

solar cell where the E_G becomes wider as the T_O increases, allowing the solar cell to operate closer to the optimal peak η over a wider range of T_O.

3.2.4 3-D effects

The S-Q detailed balance limit and other diode models, such as the recombination limited model in Chapter 4, model the solar cell in 1-D. This is possible since the semiconductor junction is uniform in 2-D in most solar cells. Therefore, a 1-D model can be used successfully to represent the device physics. These models are particularly useful in the initial design and planning stages, when it is common to evaluate a large number of possible solar cell designs. However, these models cannot accurately account for the 3-D effects occurring in the solar cell.

Two types of 3-D structures commonly used are grid and busbar electrodes. These 3-D structures affect the terminal characteristics and *T* dependencies of the solar cell, which will be explored further in Chapter 5. In an effort to boost the η, more elaborate 3-D designs have been developed for solar cells. These include line and point contacts, which will also affect the terminal characteristics and the *T* dependent performance.

The J_{SC} can be reduced by un-illuminated regions of the solar cell, which act as a sink for current. Some of the current generated in the illuminated regions will flow laterally through the solar cell and recombine in the un-illuminated regions.

The V_{OC} can be reduced by circulating currents, which are also caused by current flowing from the illuminated regions to the un-illuminated regions of the solar cell [113]. This can cause the V_{OC} to be reduced below the value predicted by the 1-D model.

Another important 3-D effect is the joule and bias-point resistive losses, which is also caused by lateral currents flowing through the LCL. This current causes a voltage drop which leads to parts of the solar cells being biased away from the ideal P_{Max}.

Each of the terminal characteristics and *T* dependencies of the solar cell are affected by the 3-D structures used on solar cells. It is therefore not possible to completely model the terminal characteristics and *T* dependencies using a 1-D model.

3.3 Summary and Conclusions

Through extensive research efforts, the η of each type of solar cell has improved over time [13, 47]. This has been achieved by improving the material quality and device designs. As the η of solar cells improve, they come closer to the S-Q detailed balance limit. This chapter has identified the terminal characteristics and the T dependent coefficients that could be achieved by solar cells that approach this limit, over a broad range of T_O and E_G. These calculations are particularly helpful in identifying the potential of solar cells that approach this limit. In addition, this chapter has also shown that T dependent E_G narrowing does not affect all solar cells in the same manner, which is particularly important when trying to optimize a solar cell operating at high temperature.

Solar cells that operate at high T would be useful in a wide range of applications, from high concentration photovoltaic systems, to hybrid thermal photovoltaic systems, to near sun photovoltaic space probes, to space concentrator photovoltaic systems. This chapter showed that the T dependent E_G narrowing improves the potential η of wide E_G material. While at the same time, it has little effect on moderate E_G materials and it will reduce the η of narrow E_G materials. As expected the simulations show that as the T_O goes up the η decreases and the optimal E_G at the optimal peak η increases.

In addition, it was found that the optimal E_G is strongly affected by the absorption gap in the terrestrial solar spectrum. This causes steps in the optimal E_G over temperature. It was also shown that there is range of bandgaps near the optimal E_G with η relatively close to the optimal peak η. It was also shown that the temperature dependence of the optimal E_G and the E_G of real semiconductor materials have the opposite slope. However, due to the flat portions of the optimal E_G steps, it might be possible to find a material with an E_G, which is close to the optimal E_G over a wider range of T_O.

After the regions with the peak η and optimal E_G have been identified, the material parameters of real materials can be used to identify candidate materials that are closest to the optimal peak over the temperature range of interest. The candidate materials can be further verified using additional detailed numerical models and 3-D models to more accurately determine the potential of the individual material and develop optimal device designs. Solar cell fabricators can then use these designs to develop and characterize the actual solar cells. The measurement data can then be used to improve the models and identify ways to improve the performance of the solar cells.

Based on these simulations it appears that the η of an appropriately designed solar cell operating above 300 °C could be quite high. These solar cells could be very useful in high T applications. The next Chapter will explorer the other bulk recombination mechanisms which are limiting the η.

3.3.1 Future Work

The calculations in this chapter assume that 100% of the photons above the simulated E_G are absorbed and converted to current. This is useful for determining the upper limit of the J_{SC}, for devices that do not absorb photons below the bandgap energy. This model could be further improved by including realistic partial absorption for direct and indirect bandgap materials [114]. Doing this could change the optimal peak bandgap by a few tens of millivolts. It would also allow the thickness of the solar cell to be studied. Thinning the solar cell will reduce the photogenerated current, and it will also reduce the volume over which recombination can occur. The optimal thickness could be found, by varying the thickness at each temperature.

The optical absorption coefficient, $\alpha(\lambda)$, of semiconductors are strongly influenced by the operating temperature. This has been measured for the direct bandgap material GaAs over a wide range of photon energies [101] and near the band edge [115]. Therefore it will likely be necessary to include the temperature dependent optical bandgap narrowing in the absorption model, when optimizing the device thickness. In addition to being temperature dependent, the optical $\alpha(\lambda)$ of semiconductor materials is

also doping dependent. However, this dependence is not the same for all materials or dopants. For p-type GaAs the measured $\alpha(\lambda)$ changes very little as the doping concentration increases from $2x10^{17}$ [cm^{-3}] to $1.2x10^{18}$ [cm^{-3}], and for n-type GaAs the measured $\alpha(\lambda)$ varies from that of a direct bandgap material, to an $\alpha(\lambda)$ that is more similar to an indirect bandgap material [116].

4. RECOMBINATION LIMITED VERY HIGH TEMPERATURE TERMINAL CHARACTERISTICS

While the η of solar cells have improved over time, thus moving closer to the S-Q detailed balance limit discussed in Chapter 3, they are still primarily limited by other recombination mechanisms. Developing a model that includes these additional loss mechanisms and can be used over the same very wide range of T_O, E_G and X would be particularly useful to program managers and system designers. The model developed in this chapter can estimate the η that could potentially be achieved based on the measured bulk recombination parameters of existing materials. This would allow them to determine if it is technically feasible to reach a certain design goal. The simulated η in this chapter will be closer to the measured high efficiency world record solar cells than the S-Q detailed balance limit η simulated in Chapter 3.

This chapter has been divided into four parts. The first part (Section 4.1) will examine the analytical model used to simulate multiple recombination mechanisms and the theoretical temperature dependencies of solar cells over T_O and E_G. The second part (Section 4.2) will present the semi-empirical material parameter fits needed to simulated the η over T_O and E_G. The third part (Section 4.3) will discuss the results of the analytical simulations. The last part (Section 4.4) will explore additional affects, such as the 3-D resistivity, that is not incorporated into this model.

4.1 Terminal Characteristics

Similar to Chapter 3, in this chapter an analytical model will be used to simulate the possible solar cell performance over a very wide range of T_O and simulated E_G. This analytical model can incorporate all three of the common bulk recombination

mechanisms in solar cells; radiative recombination, Shockley-Hall-Reed (SHR) recombination, and Auger recombination. Each of these recombination mechanisms can limit the performance of a solar cell under different conditions. Solar cells with low material quality are limited by SHR. Direct bandgap materials are often limited by radiative recombination. And solar cells with high V_{OC} are often limited by Auger recombination. Methods are being used and investigated to reduce each of these recombination mechanisms. The first to be reduced is the SHR recombination.

Through extensive research, growth methods have been developed for many semiconductor materials, such as Si and GaAs, to significantly reduce the SHR recombination. This has led the SHR recombination to be a small part of the total recombination in some devices. Because the SHR recombination has continued to decrease over time, in the results presented in this chapter, it will be assumed negligible. The radiative recombination and Auger recombination used in this model are based on semi-empirical fits to the measured values for these material parameters.

4.1.1 Multiple Diode Equation

There are many types of recombination mechanisms inside of solar cells. Some of these recombination mechanisms such as interface and surface recombination can be significant in some types of solar cell, and be insignificant in other types of solar cells. The interface recombination has been reduced to insignificant levels in some solar cells, through careful growth techniques, which reduce the number of defects present in the interface. The surface recombination can be reduced through the use of passivation layers or by adding a heterojunction layer, such as the amorphous Si layer in HIT solar cells or the GaInP layers in GaAs solar cells.

Three types of recombination are common in most types of solar cells, radiative recombination, $J_{R,\lambda}$, SHR recombination, $J_{R,SHR}$, and Auger recombination, $J_{R,Auger}$. The extrinsic terminal characteristics of this model, with series resistance, R_{Series}, and shunt resistance, R_{Shunt}, is defined as (Figure 4.1)

$$J = J_{SC} - J_{R,\lambda} - J_{R,SHR} - J_{R,Auger} - \frac{V + JR_{Series}}{R_{Shunt}} . \tag{4.1}$$

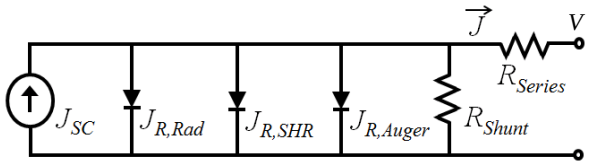

Figure 4.1. Multiple diode circuit diagram, with radiative recombination, $J_{R,\lambda}$, SHR recombination, $J_{R,SHR}$, and Auger recombination, $J_{R,Auger}$, as well as series resistance, R_{Series}, and shunt resistance, R_{Shunt}.

The sum of the recombination currents is

$$J_R = \sum_{m=\lambda,SHR,Auger} J_{O,m}\left(\exp\left[\frac{V + JR_{Series}}{n_m kT}\right] - 1\right). \tag{4.2}$$

In most cases, when more than one type of recombination is simulated, the J_{MP}, V_{MP} and *FF* cannot be solved analytical. Many researchers have used Newton's method to solve for these parameters. A computationally quicker and simpler bisection approach was developed by Gray to solve for the *FF* in cases with one or more series connected junctions each with a single diode, as well as R_{Series}, is described in Section C.2.1. This type of approach was extended by the author to other cases including multiple diodes in parallel, Section C.2.2, which is needed to solve Equation (4.1) when R_{Series}=0. Methods to solve for the *FF* in a variety of other cases, which were also developed by the author, such as many parallel diodes when R_{Series}≠0, are described in the Subsection of C.2.

4.1.2 Recombination Current Density

The SHR recombination depends on the material quality and the number of defects in the material. It has been reduced through the use of careful fabrication methods that reduce defects in the semiconductor crystal. Reducing the Auger recombination directly would require developing nanostructures or finding a material that quantum mechanically

restricted the Auger recombination mechanisms. This might be achieved by creating a structure that has a narrow conduction band with a gap above it that was larger than the primary bandgap of the device.

A variety of reverse saturation current models could have been used. However, the high-level injection limit and low-level injection limit models were chosen because they are independent of device design. These models represent good quality solar cells, where the SHR recombination is small compared to the radiative and Auger recombination. This will cause the excess minority carriers to be uniform in the base region of the device. The high-level injection limit and low-level injection limit are valid when the diffusion length, L_D, is more than three times the thickness of the device.

The emitter of a solar cell is typically much smaller than the base region. This model assumes that the emitter thickness is negligible compared to the base thickness. This will cause the recombination in the emitter to also be negligible.

The recombination current density for each recombination mechanism is shown in Equation (3.7). In the high-level injection limit and the low-level injection limit, the excess carrier densities will be uniform throughout the base region. This will cause the recombination to also be uniform throughout the base region. The saturation current for each recombination mechanisms is,

$$J_{O,m} = qwR_m . \tag{4.3}$$

Where w is the width of the device and R_m is the recombination rate for each recombination mechanism.

The non-degenerate radiative recombination rate is

$$R_\lambda = B(pn - n_i^2) . \tag{4.4}$$

Where B is the radiative recombination coefficient, n is the electron concentration, p is the hole concentration and n_i is the intrinsic carrier concentration (Equation (4.16)). The n and p will be defined in Section 6.4.1.1.

The non-degenerate SHR recombination rate is

$$R_{SHR} = \frac{pn - n_i^2}{\tau_n(p + p_T) + \tau_p(n + n_T)} . \tag{4.5}$$

Where τ_n is the electron SHR lifetime, p_T is the number of empty SHR trap states, τ_p is the hole SHR lifetime and n_T is the number of filled SHR trap states,

The non-degenerate Auger recombination rate is

$$R_{Auger} = (C_n n + C_p p)(pn - n_i^2) \quad (4.6)$$

Where C_n and C_p are the Auger recombination coefficients for electrons and holes.

In the very high temperatures model the radiative recombination and Auger recombination will be calculated based on measured material parameters, and the SHR lifetime needed to achieve a L_D is more than three times larger than the device thickness. When the L_D that is less than three times the device thickness, a more complete model, which includes the SHR lifetime is needed. This is discussed in more detail in section 4.2.3.

In Section 4.3.2, it will be shown that for direct bandgap materials with a L_D larger than three times the base thickness, the Auger recombination will be small compared to the radiative recombination. It will also be shown in section 4.3.1 that since the n_m for radiative recombination is the same for high-level injection and low-level injection the recombination current density will be equivalent in both cases and the terminal characteristics will be essentially the same.

4.1.3 Low-level Injection Limit

The low-level injection limit occurs when Δn and Δp are much smaller than the acceptors doping concentration, N_A, for p-type materials or the donor doping concentration, N_D, for n-type materials.

The radiative recombination current density simplifies to

$$J_{R,Rad} = qwBn_i^2\left[\exp\left(\frac{qV}{kT}\right) - 1\right]. \quad (4.7)$$

The SHR recombination current density for p-type materials simplifies to

$$J_{R,SHR} = qw\frac{n_i^2}{\tau_n N_A}\left[\exp\left(\frac{qV}{kT}\right)-1\right]. \tag{4.8}$$

The SHR recombination current density for n-type materials simplifies to

$$J_{R,SHR} = qw\frac{n_i^2}{\tau_p N_D}\left[\exp\left(\frac{qV}{kT}\right)-1\right]. \tag{4.9}$$

The Auger recombination current density for p-type materials simplifies to

$$J_{R,Auger,p} = qwC_p N_A n_i^2\left[\exp\left(\frac{qV}{kT}\right)-1\right] \tag{4.10}$$

The Auger recombination current density for n-type materials simplifies to

$$J_{R,Auger,n} = qwC_n N_D n_i^2\left[\exp\left(\frac{qV}{kT}\right)-1\right] \tag{4.11}$$

Because each of the low-level injection recombination current densities have the same unity ideality factor, it is possible to sum the individual components and solve for the *FF* using a single diode circuit.

The very high temperatures model will need each of the $J_{R,m}$ over the simulated E_G and T_O. In order to calculate the $J_{R,m}$ it will be necessary to know the material parameters, n_i, B, τ_n, τ_p, C_n and C_p over the same range of simulated E_G and T_O. Fits for these material parameters will be developed in section 4.2.

4.1.4 High-level Injection Limit

The high-level injection limit occurs when Δn and Δp are much larger than the acceptors doping concentration, N_A, for p-type materials or the donor doping concentration, N_D, for n-type materials.

The radiative recombination current density simplifies to the same expression as the low-level injection limit,

$$J_{R,Rad} = qwBn_i^2\left[\exp\left(\frac{qV}{kT}\right)-1\right]. \tag{4.12}$$

The SHR recombination current density simplifies to

$$J_{R,SHR} = qw\frac{n_i}{\tau_n + \tau_p}\left[\exp\left(\frac{qV}{2kT}\right) - 1\right]. \tag{4.13}$$

The Auger recombination current density simplifies to

$$J_{R,Auger} = qw\left(C_n + C_p\right)n_i^3\left[\exp\left(\frac{qV}{2/3\,kT}\right) - 1\right]. \tag{4.14}$$

Unlike the low-level injection limit, the *n* will be different for each recombination mechanism. For radiative recombination, $n_\lambda = 1$, for SHR recombination, $n_{SHR} = 2$ and for Auger recombination, $n_\lambda = 2/3$. In order to solve for the V_{OC} and *FF* in the high-level limit, it is necessary to solve a multiple diode model.

4.1.5 Theoretical Recombination Current Density

The theoretical temperature dependence of the recombination current density can be developed for the low-level injection limit and the high-level injection limit, by incorporating the temperature dependencies of the n_i, the effective conduction band density-of-states, N_C, and the effective valence band density-of-states, N_V.

The temperature dependence of J_O was investigated by Fan [52]. The temperature dependence of J_O was further developed by the author [117], for recombination mechanisms of the form.

$$R_m = K_{R,m}n_i^{2/n_m} \tag{4.15}$$

Where $K_{R,m}$ is the temperature independent term. This term will be examined further in section 4.2.1.

The n_i is defined as

$$n_i = \sqrt{N_C N_V}\exp\left(\frac{-E_G}{2kT}\right). \tag{4.16}$$

The N_C is defined as

$$N_C = 2\left[\frac{m_n^* kT}{2\pi\hbar^2}\right]^{3/2}. \tag{4.17}$$

The effective density-of-states effective mass for electrons, m_n^*, varies slowly for most semiconductors [92]. A coefficient term can be defined as

$$K_C = 2\left[\frac{m_n^* k}{2\pi\hbar^2}\right]^{3/2}, \tag{4.18}$$

and $N_C = K_C T^{3/2}$.

Likewise, the N_V is defined as

$$N_V = 2\left[\frac{m_p^* kT}{2\pi\hbar^2}\right]^{3/2}. \tag{4.19}$$

The effective density-of-states effective mass for hole, m_p^*, also varies slowly for most semiconductors [92]. A coefficient term can be defined as

$$K_V = 2\left[\frac{m_p^* k}{2\pi\hbar^2}\right]^{3/2}, \tag{4.20}$$

and $N_V = K_V T^{3/2}$.

The n_i with the K_C and K_V coefficient terms is

$$n_i = \sqrt{K_C K_V}\, T^{3/2} \exp\left(\frac{-E_G}{2kT}\right). \tag{4.21}$$

A coefficient term for n_i can be defined, which combines the K_C and K_V coefficient terms, $K_{n_i} \equiv \sqrt{K_C K_V}$, and the parameters contained in this term are

$$K_{n_i} \equiv \sqrt{\frac{1}{2} m_C^{*3/2} m_V^{*3/2} \left[\frac{k}{\pi\hbar^2}\right]^3}. \tag{4.22}$$

Finally the n_i with the K_{n_i} coefficient term is

$$n_i = K_{n_i} T^{3/2} \exp\left(\frac{-E_G}{2kT}\right). \tag{4.23}$$

Combining Equations (4.3), (4.15) and (4.23) gives the general form of the temperature dependent $J_{O,m}$.

$$J_{O,m} = qwK_{R,m}K_{n_i}^{2/n_m}T^{3/n_m}\exp\left[\frac{-E_G}{n_m kT}\right] \tag{4.24}$$

Where $K_{R,m}$ is the J_O coefficient term for each recombination mechanism of the form Equation (4.15).

4.1.5.1 Low-Level and High-Level Injection

In low-level injection the n_m will be 1 for all three of the bulk recombination mechanisms. The form of Equation (4.24) can be checked and the $K_{R,m}$ can be found for each recombination mechanism in the high-level injection limit.

The high-level injection saturation current density for radiative recombination can be found by combining Equation (4.23) with the J_O from Equation (4.12).

$$J_{O,Rad} = qwBK_{n_i}^{2}T^{3}\exp\left[\frac{-E_G}{kT}\right], \tag{4.25}$$

The high-level injection saturation current density for radiative recombination which matches Equation (4.24), with n_{Rad} equal to 1, is then

$$J_{O,Rad} = qwK_{R,Rad}K_{n_i}^{2}T^{3}\exp\left[\frac{-E_G}{kT}\right]. \tag{4.26}$$

And the $K_{R,m}$ is the radiative recombination J_O coefficient term is $K_{R,m} \equiv B$.

The high-level injection saturation current density for SHR recombination can be found by combining Equation (4.23) with the J_O from Equation (4.13).

$$J_{O,SHR} = \frac{qwK_{n_i}}{\tau_n + \tau_p}T^{3/2}\exp\left[\frac{-E_G}{2kT}\right] \tag{4.27}$$

The high-level injection saturation current density for SHR recombination which matches Equation (4.24), with n_{SHR} equal to 2, is then

$$J_{O,SHR} = qwK_{R,SHR}K_{n_i}T^{3/2}\exp\left[\frac{-E_G}{2kT}\right]. \tag{4.28}$$

And the $K_{R,m}$ is the SHR recombination J_O coefficient term is $K_{R,m} \equiv \frac{1}{\tau_n + \tau_p}$

The high-level injection saturation current density for Auger recombination can be found by combining Equation (4.23) with the J_O from Equation (4.14).

$$J_{O,Auger} = qw(C_n + C_p)K_{n_i}{}^3T^{9/2}\exp\left[\frac{-E_G}{2/3\,kT}\right] \tag{4.29}$$

The high-level injection saturation current density for Auger recombination which matches Equation (4.24), with n_{Auger} equal to 2/3, is then

$$J_{O,Auger} = qwK_{R,Auger}K_{n_i}{}^3T^{9/2}\exp\left[\frac{-E_G}{2/3\,kT}\right]. \tag{4.30}$$

And the $K_{R,Auger}$ is the Auger recombination J_O coefficient term is $K_{R,Auger} \equiv C_n + C_p$.

Therefore in high-level injection Equation (4.24) can be used for each of the bulk recombination mechanisms, with the appropriate $K_{R,m}$ and n_m for each recombination mechanism.

Identifying a method to estimate the E_G over the simulated E_G and T_O will be discussed in section 3.1.3.

4.2 Semiconductor Material Parameters

In order to solve for the terminal characteristics in the very high temperatures model over a simulated E_G and T_O it is necessary to estimate the semiconductor material parameters over these ranges. The material parameter fits described this section are used in conjunction with these equations to estimate the $J_{R,m}$ values and the terminal characteristics.

4.2.1 Intrinsic Carrier Concentration over Bandgap Fit

The most important material parameter needed in the very high temperatures model is n_i. Not only is it in each of the $J_{R,m}$ equations, Equations (4.7) through Equation (4.14), it varies by many orders of magnitude over both simulated E_G and T_O. Therefore the temperature dependence and the multiplicative power of n_i in the $J_{R,m}$ equations are very important to the overall temperature dependence of the model.

After carefully analyzing the n_i at 300 K for a wide range of semiconductor materials over a large range of bandgap energies, it was determined that the direct and indirect materials needed to have separate n_i fits, Figure 4.4.

In order to fit n_i over the simulated E_G and T_O, two different curve-fits were evaluated. The first consisted of fitting the K_C and K_V coefficient terms over the simulated E_G. This method did not work well because of the large variability of m_n^* and m_p^* for the direct bandgap and indirect bandgap materials over simulated bandgap, Figure 4.2 [106].

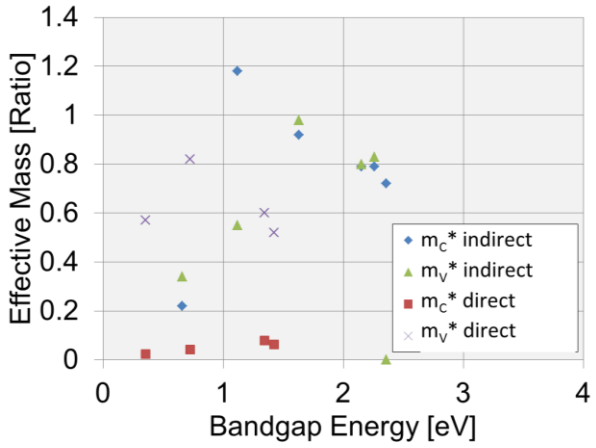

Figure 4.2. Measured m_n^*/m and m_p^*/m for a wide range of direct and indirect bandgap semiconductor materials [106].

The second fit consisted of fitting K_{n_i} over simulated E_G. This lead to a better fit over simulated E_G. The measured $K_{n_i}300^{3/2}$ for a wide range of direct and indirect bandgap semiconductor materials are shown in Figure 4.3. Linear curve-fits for direct bandgap and indirect bandgap materials are shown in Figure 4.3(a) with a log y axis and Figure 4.3(b) with a linear y axis. The indirect bandgap fit becomes non-physical below 0.5 eV.

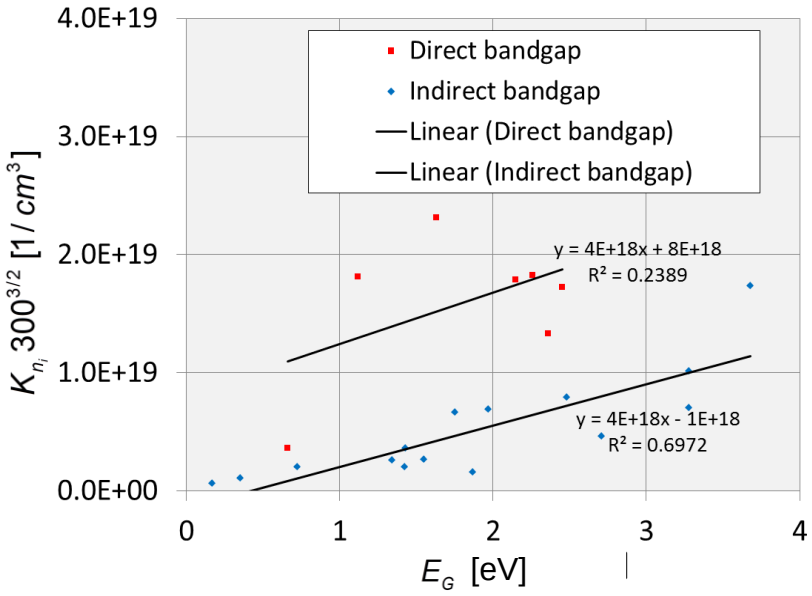

Figure 4.3. Measured $K_{n_i}300^{3/2}$ for a wide range of direct and indirect bandgap semiconductor materials. Linear curve-fits for direct bandgap and indirect bandgap materials [106]. The indirect bandgap fit becomes non-physical below 0.5 eV.

As shown in Figure 4.4, the n_i curve-fit for direct bandgap materials was a factor of 10 smaller than the n_i curve-fit for indirect bandgap materials, near the GaAs E_G of 1.42 eV at 300 K [106].

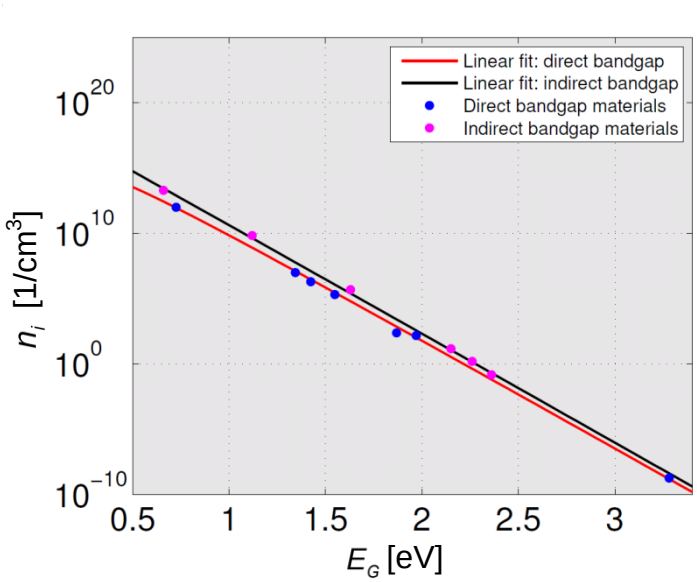

Figure 4.4. Measured n_i for a wide range of direct and indirect bandgap semiconductor materials [106]. Linear curve-fits of $K_{n_i} 300^{3/2}$ were used to predict the n_i for direct bandgap and indirect bandgap materials. There is a factor of 10 difference between the n_i curve-fit for direct bandgap materials and n_i curve-fit for indirect bandgap materials

Using the n_i curve-fit for indirect bandgap materials to calculate the $J_{R,Auger}$ for the direct bandgap semiconductor GaAs in high-injection would lead to a recombination current densities values that are 1000 times higher than the $J_{R,Auger}$, calculated using the measured n_i values for GaAs. The difference between the direct bandgap and indirect bandgap n_i curve-fits is primary caused by the generally narrower conduction band valley in direct bandgap materials, which generally lead to significantly smaller values of m_n^*, for direct bandgap materials. This causes the N_C and n_i to be lower in direct bandgap materials.

In order to assess the accuracy of the n_i curve-fits, the percentage difference between the measured and curve-fit predicted values were plotted.

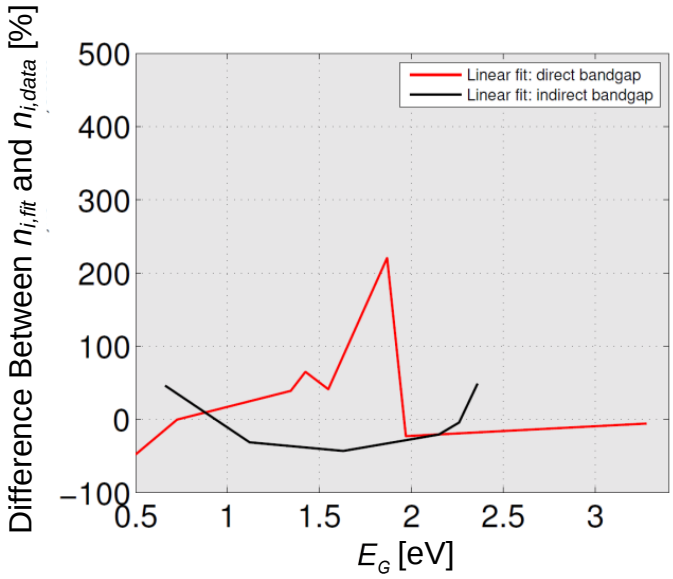

Figure 4.5. The percentage difference between the measured and the linear curve-fit predicted values.

The measured value of only one material, GaInP, was off by more than a factor of two, which is acceptable for the purposes of the very high temperatures model.

To further validate the n_i curve-fits, they will be compared to material specific n_i curve-fits, over a range of temperatures. The lines are the n_i curve-fits for direct bandgap and indirect bandgap materials. The dots represent a variety of material specific curve-fits for n_i over T_O.

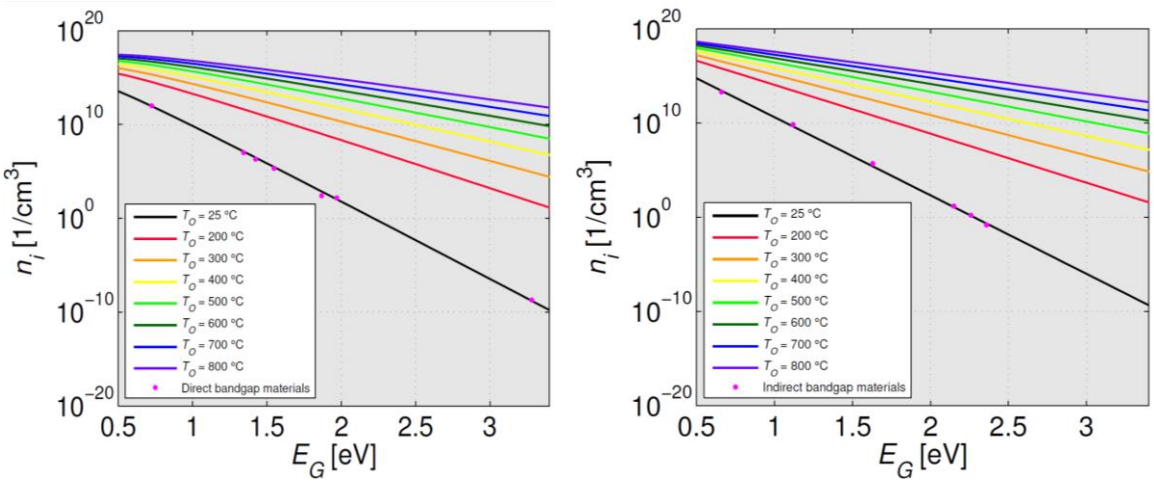

(a) Direct bandgap material (b) Indirect bandgap material

Figure 4.6. Comparison of the n_i curve-fits with material specific n_i values at 300 K. The lines show the n_i curve-fits for direct bandgap and indirect bandgap materials over a range of T_O.

The dots and the lines appear to match-up reasonably well for the wide range of E_G and T_O. There also appears to be some variability in the measured data. For each individual material the dots appear to be roughly the same distance above or below the simulated line for each of the selected T_O. The direct bandgap and indirect bandgap n_i curve-fits could be further evaluated and improved by fitting the dots at each selected T_O separately and then relating the curve-fits over the range of T_O.

The direct bandgap and indirect bandgap n_i curve-fits over a wide range of simulated E_G and T_O have been describe in this section. These curve-fits are used in the very high temperatures model. The recombination coefficients over simulated E_G and T_O are still needed to calculate $J_{R,m}$ for each of the recombination mechanisms over simulated E_G and T_O.

4.2.2 Recombination Coefficients

The recombination coefficients for radiative and Auger recombination over simulated E_G and T_O are needed to calculate the terminal characteristics in the very high temperatures model. These coefficients are material specific. The SHR lifetimes will be calculated, which are needed to achieve the low-level injection limit and the high-level injection limits valid.

4.2.2.1 Radiative recombination coefficients over bandgap fit

As will be shown later in section 4.3, the radiative recombination is limiting the device performance in most of the very high temperatures model cases. The radiative recombination coefficient is material specific and varies by material. It can also be temperature dependent. The measured B values plotted in Figure 4.7, for both direct bandgap materials and indirect bandgap materials. As expected, there is a large difference between direct bandgap materials, shown as red squares, and indirect bandgap materials, shown as blue diamonds. There is also a large amount of scatter in the B for direct bandgap. Using III-V compound semiconductors it is possible to create materials with the same E_G and vary different element compositions.

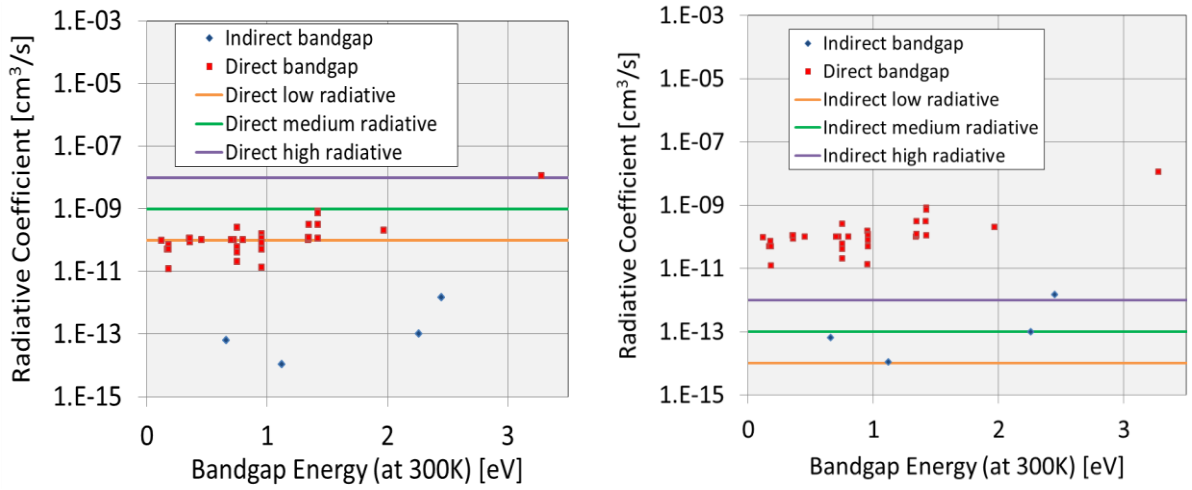

(a) Direct bandgap material (b) Indirect bandgap material

Figure 4.7. The red squares are measured *B* values for direct bandgap materials. The blue diamonds are measured *B* values for direct bandgap materials. Low, medium and high lines have been developed to bracket the *B* for direct bandgap and indirect bandgap materials.

Three fits have been developed for the radiative coefficients for direct bandgap and indirect bandgap materials. These fits bracket the range of measured radiative coefficients, with low, medium and high levels of radiative recombination. The direct bandgap material fits are 4 orders of magnitude larger than the indirect bandgap material fits. The direct bandgap material fits do not cover the full range of the *B* for direct bandgap materials with a bandgap below 1 eV. In section 4.3 it will be shown that materials below 1 eV do not perform well at higher temperatures.

Based on the data collected, it appears that the *B* may generally increase with increased bandgap energy. Empirical fits could be developed to incorporate this increase. The approach used with three ranges was deemed to be the most useful in the very high temperatures model. The measured value of a real material can be matched to one of the three ranges to predict the performance of that material.

The fits described in this section predicted the range of possible *B* over E_G. In order to calculate the very high temperatures model over a wide range of temperatures, it is also important to know how the *B* varies with temperature.

4.2.2.2 Radiative recombination coefficients temperature dependence

A theoretical model for B was developed by Varshi [118, 119]. This model predicted that the B of direct bandgap materials, GaAs, GaSb, InP, InAs and InSb would decrease as the temperature increases. This model also predicted that the B of indirect bandgap material Si would increase as the temperature increases. Early published measurements indicated that it would increase, later measurements indicated that the B of Si decreases as the temperature increases [120, 121]. The difference of the measured B increasing and decreasing in Si is thought to be due to a difference in the n_i value and the absorption data, which is affected by the emission of photons. Measurements of GaAs indicate that the B increases as the temperature decreases [122], this has also been found in GaAs quantum wells [123].

Based on the measured data it is possible that B could increase for some materials and decrease for others as the temperature increases. Furthermore, very little is known about the B for all of these materials above 200 °C, so any temperature dependence would be extrapolated far from the measurements. It was determined that the best option was to not vary the B over T_O. If there is a general trend that B decreases as the temperature increases then the very high temperatures model will somewhat under predict the performance of these devices at higher temperatures.

The B value measured in literature is typically for the bulk material, factors such as photon recycling will reduce the effective B [124]. If the B is reduced due to the changing temperature or photon recycling by a factor of 10, the low B fit results could be used for a material which has a bulk medium B at room temperature.

4.2.2.3 Comparing radiative recombination saturation current density

Many attempts have been made to create a saturation current fit to predict the quality of solar cells. These fits have been referred to as state-of-the-art or empirical fits. Without being able to quantify the B over E_G these models are often based on empirical data [87] or voltage shifted [84] from the junction bandgap. As the solar cell device

performance improves, solar cells have [125] and will continue to past these empirical fits.

By using the *B* fits developed over E_G in Section 4.2.2.1, it is possible to predict the lowest possible $J_{O,\lambda}$ that can be achieved for a semiconductor material with the low, medium or high values for *B*. Since the Shockley - Queisser detailed balance limit has the same *n*, as Equation (4.7) and Equation (4.12), it can also be plotted for reference. This is particularly useful for predicting the performance of direct bandgap materials, which have high SHR lifetimes, since the Auger recombination will be small in a direct bandgap material, and these devices will be limited by the radiative recombination.

Figure 4.8(a) shows the $J_{O,\lambda}$ for the radiative recombination in direct and indirect materials. Figure 4.8(b) shows the ratio of the reverse saturation divided by the Shockley - Queisser detail balance limited current for each of the radiative recombination cases. The red dot below the solid blue line, was fabricated by Alta Devices [47]. This solar cell has a very good back reflector and photon recycling. It is only a factor of ten larger then Shockley – Queisser detail balance limit, solid black line. This red dot falls below the solid blue line, which is the calculated saturation current based on the bulk low radiative recombination coefficient fit for measured direct bandgap materials. This shows that the actual $J_{O,\lambda}$, due to radiative recombination, can be significantly lower than the value predicted by measurements of the bulk materials [126].

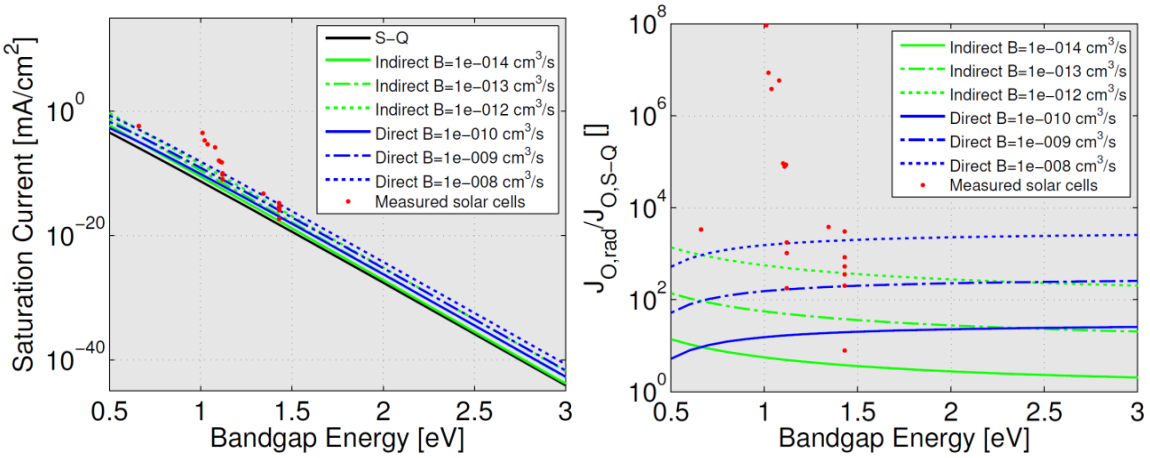

(a) Saturation current density (a) Normalized saturation current density

Figure 4.8. The solid black line is the Shockley – Queisser detailed balance limit. The red dots are the estimated $J_{O,\lambda}$ for measured solar cells. The blue lines are the $J_{O,\lambda}$ predicted by the model for direct bandgap materials. The green lines are the $J_{O,\lambda}$ values predicted by the model for indirect bandgap materials.

The $J_{O,\lambda}$ is estimated for the measured devices. This assumes that the radiative recombination is limiting these solar cells. If other recombination mechanisms are significantly affecting the performance of these devices, the radiative recombination will be a smaller percentage of the total and the actual reverse saturation for the radiative recombination would be smaller. This would move the red dots closer to the black line. This would indicate that these solar cells have $J_{O,\lambda}$ values that are even better than the plots indicate.

4.2.2.4 Auger recombination coefficients over bandgap fit

Just like the B, a fit for C_n and C_p is needed over E_G and T_O to calculate the very high temperatures model. The Auger recombination is an important parameter for solar cells constructed out of indirect bandgap materials, which are often 100 times thicker than the direct bandgap solar cells. This causes the indirect bandgap solar cells to have a significantly larger amount of Auger recombination.

Due to the fact that the measured C_n and C_p values were not available for all types of materials, C_n and C_p values were combined to create the ambipolar Auger coefficient,

$$C = C_n + C_p . \tag{4.31}$$

This parameter has been plotted for direct bandgap and indirect bandgap materials, over a wide range of semiconductor types and E_G, in Figure 4.9 [106, 127, 128].

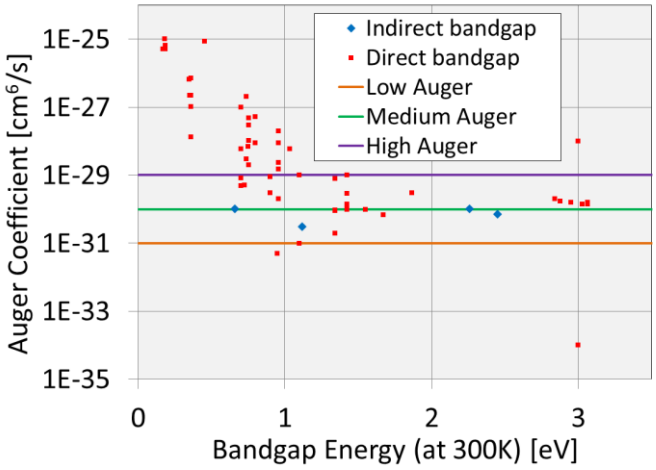

Figure 4.9. The red squares are the measured C values for direct bandgap materials and the blue diamonds are the measured C values for indirect bandgap materials.

The red squares are the measured C values for direct bandgap materials, and the blue diamonds are the measured C values for indirect bandgap materials. There is a significant amount of scatter in the measured values, which represent a wide range of semiconductor materials, particularly in the compound III-V semiconductors where material of different compositions can have same E_G.

The measured values of C for low bandgap materials appear to reduce as E_G increases. This E_G dependent decrease of the C has been fit by many [106, 129]. This is likely caused by a decrease of the intraband Auger recombination [130]. The data point with a bandgap energy of 3 eV and $1\text{x}10^{-34}$ cm^6/s was extrapolated from the C values of lower bandgap materials and is far below the measured values [106]. The reduction of

the *C* appears to stop for semiconductors with bandgap energies above 1 eV, and since the bandgap above 1 eV are of interest in the very high temperatures model, the low, medium and high Auger coefficient ranges have been chosen to bracket the measured semiconductors materials above 1 eV. With the only exception being a InGaN, 3.0 eV, measurement [128], which is much too high for a single junction solar cell.

4.2.2.5 Auger recombination coefficient over temperature

The measured *C* values of different semiconductor material have been shown in literature to increase or decrease over temperature. The total Si Auger recombination rates is often assumed to be [131]

$$C = 1.4x10^{-30}\left(\frac{T}{300}\right)^{0.5}. \tag{4.32}$$

The measured *C* value for Si increases as the temperature increases [132], while the measured *C* value for SiC decreases as the temperature increases [133]. These measured values appear to have significantly different slopes. In addition, three different theoretical and empirical fits have been developed for Si over T_O. These three fits lead to very different results for *C* at high T_O. The total GaAs *C* rate increases by an order of magnitude, from ~10^{-30} [cm^6/s] at 300 K to ~10^{-29} [cm^6/s] at 500 K [134].

Because of the variability in the temperature dependence of *C* for different materials, the Auger coefficient will not be varied over temperature in this model. In addition, it will be shown in Section 4.3.2 that the temperature dependence of *C* will have little effect on the results of the very high temperatures model for many of the cases considered.

4.2.3 Shockley Hall Read Recombination

The defects in the crystal lattice create energy states, which are in-between the valance and conduction band. Recombination caused by these trap states is commonly referred to as Shockley Hall Read recombination. This type of recombination depends

primarily on the quality of the material, which is related to the density of the defects. The SHR lifetime is

$$\tau_{SHR} = \frac{1}{\sigma v_{th} N_T}. \tag{4.33}$$

Where σ is the trap capture cross section, v_{th} is the thermal velocity and N_T is the density of traps.

Due to the fact that τ_{SHR} is dependent on the quality of the material and the number of defects in the material, it will be improved as the growth method is improved. Therefore, it does not have a fixed value like the radiative and Auger recombination coefficients. It was decided that the best way to incorporate the τ_{SHR} into these calculations would be to compare it to the effective lifetime of the other two recombination mechanisms. This value will be used to determine how small the SHR lifetime can be before it increases the recombination.

An effective lifetime will be calculated for the radiative recombination and Auger recombination mechanisms,

$$\frac{1}{\tau_{Eff}} = \frac{1}{\tau_{Auger}} + \frac{1}{\tau_{Rad}}. \tag{4.34}$$

Where τ_{Auger} is the Auger recombination effective lifetime and τ_{Rad} is the radiative recombination effective lifetime.

In order to calculate the effective lifetime, the radiative effective lifetime and Auger effective lifetime are needed.

4.2.3.1 Radiative recombination effective lifetime

There are different radiative recombination effective lifetimes for low-level injection and for high-level injection. From Equation (4.12), the high-injection radiative recombination effective lifetime is

$$\tau_{Rad} = \frac{1}{B n_i \exp(qV / 2kT)} \tag{4.35}$$

When the material is in high-level injection, the calculated radiative recombination effective lifetime is dependent on the bias voltage.

From Equation (4.7), in n-type materials the low-injection the radiative recombination effective lifetimes is

$$\tau_{Rad} = \frac{1}{BN_D}. \tag{4.36}$$

From Equation (4.7), in p-type materials the low-injection the radiative recombination effective lifetimes is

$$\tau_{Rad} = \frac{1}{BN_A}. \tag{4.37}$$

4.2.3.2 Auger effective lifetime

There are different Auger recombination effective lifetimes for low-level injection and for high-level injection. From Equation (4.14), the high-injection the Auger recombination effective lifetimes is

$$\tau_{Auger} = \frac{1}{(C_n + C_p)n_i^2 \exp(qV / kT)}. \tag{4.38}$$

As with the radiative effective lifetime, Equation (4.35), when the solar cell is in high-level injection, the calculated Auger recombination effective lifetime is dependent on the bias voltage.

From Equation (4.11), in n-type materials the low-injection the Auger recombination effective lifetimes is

$$\tau_{Auger} = \frac{1}{C_p N_A^2}. \tag{4.39}$$

From Equation (4.10), in p-type materials the low-injection the Auger recombination effective lifetime is

$$\tau_{Auger} = \frac{1}{C_p N_D^2}. \tag{4.40}$$

The Auger effective lifetimes and radiative effective lifetimes have been used in the very high temperatures model to calculate an effective recombination lifetime. This value can be used to determine if the SHR recombination will be comparable to the Auger and radiative recombination in existing materials.

4.2.3.3 Carrier diffusion coefficient

In addition to calculating the τ_{Eff}, the diffusion coefficient, *D*, has also been calculated. The *D* can be calculated using the L_D, and τ_{Eff}.

$$L_D = \sqrt{D\tau_{Eff}}\,. \tag{4.41}$$

L_D can be used to determine if the low-level injection and high-level injection assumptions are valid. For these assumptions to hold the L_D must be roughly 3 times larger than the thickness of the solar cell.

$$L_D = 3w \tag{4.42}$$

The *D* can be found by equating Equation (4.41) and Equation (4.42) and solving for *D*.

$$D = \frac{9w^2}{\tau_{eff}} \tag{4.43}$$

The carrier mobility can also be predicted using the Einstein relation

$$D = \mu kT \tag{4.44}$$

In order for the low-level injection and high-level injection assumptions to remain valid, the measured *D* of the chosen material must be less than or equal to the *D* predicted by the very high temperatures model. For materials where the *D* is larger than the value predicted by the model, the actual solar cell performance for that device can be found using the measured *D*.

4.3 Analytical Simulations

This section contains the results of the very high temperatures analytical model. The analytical expression and material parameter fits over E_G and T_O, described in this chapter, were used to calculate the terminal characteristics of a solar cell over a wide range of T_O, over solar concentrations and for a variety of different materials. These results can be used to identify the bandgap energy that produces the maximum conversion efficiency for a range of selected temperatures.

4.3.1 Bandgap Optimization Over a Range of Temperatures

Due to the large number of possible material parameters combinations, a representative case was chosen to illustrate terminal characteristic trends. A case with a direct bandgap material in high-level injection, with medium radiative and medium Auger recombination was chosen. A direct bandgap material was chosen because the bandgap can be varied over a range of bandgaps and there are a variety of existing solar cells. The medium radiative recombination material parameter fit was chosen because all of the measurements were better than the medium fit and medium Auger recombination material parameter fit was chosen because the direct bandgap material measurements were close to this fit. The high-level injection assumption was chosen because solar cells are often close to high-level injection in solar concentrators. In addition, the direct bandgap devices were found to be strongly limited by radiative recombination, so there is essentially no difference between the results calculated using high-level injection or low-level injection, which have the same diode ideality factor.

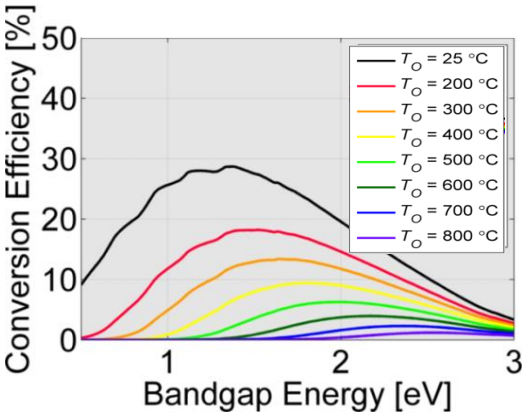

(a) 1 sun concentration

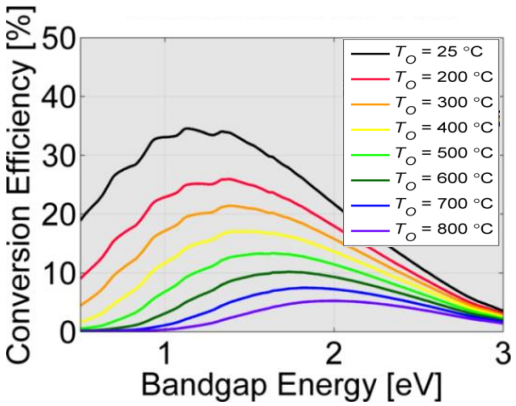

(b) 500 suns concentration

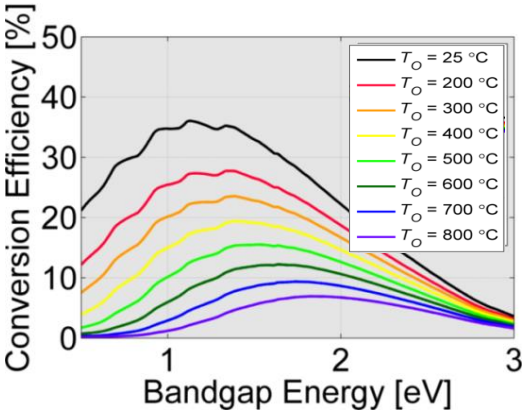

(c) 2000 suns concentration

Figure 4.10. The conversion efficiency predicted by the utlra high temperature model over simulated bandgap energy for a wide range of selected temperatures. As the temperature increases the saturation current density increases. This causes the conversion efficiency to decrease. Also as the temperature increases the bandgap energy with the highest conversion efficiency for a given temperature increases.

Solar cell system designers can chose a specific material system and then identify the 25 °C bandgap energy that would lead to the optimal bandgap energy at the chosen energy.

As the temperature increases the saturation current density increases. This causes the conversion efficiency to decrease. Also as the temperature increases the bandgap energy with the highest conversion efficiency for a given temperature increases. Increasing the temperature reduces both of these affects, thereby increasing the conversion efficiencies

at higher temperatures and reducing the peak bandgap energy. At 1 sun solar concentration and 800 °C the J_R is larger than the J_{SC} for the simulated bandgap energies below 1.75 eV. This results in a conversion efficiency that is essentially zero. The peak conversion efficiency and corresponding simulated E_G is plotted in Figure 4.13.

The main reason the conversion efficiency goes down so quickly as the temperature increases is that the V_{MP} and V_{OC} are dropping. This decrease is caused by the rapid increase of the J_R as the temperature increases. Figure 4.11 shows the V_{OC} for the same cases in Figure 3.13. As the temperature increases the V_{OC} for the simulated E_G decreases. As the solar concentration increases the V_{OC} increases and the rate of V_{OC} reduction decreases. The conversion efficiency is zero below 1.75 eV for 1 sun solar concentration and 800 °C, because the J_R is larger than the J_{SC} for the simulated bandgap energies which results in a V_{MP} and a V_{OC} that are essentially zero.

V_{MP}

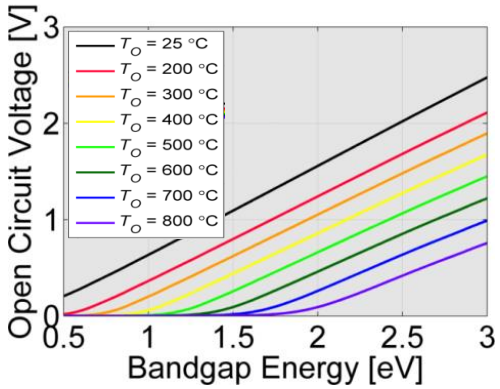

(a) 1 sun concentration

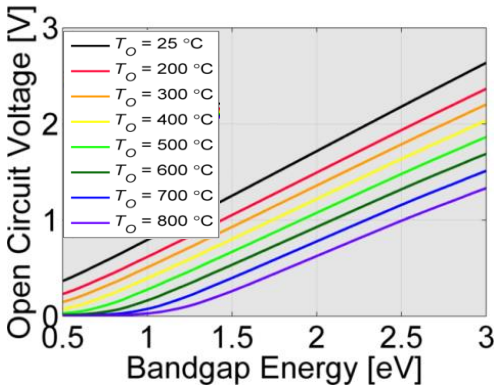

(b) 500 suns concentration

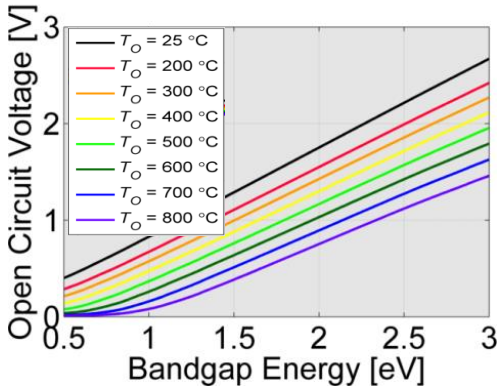

(c) 2000 suns concentration

Figure 4.11. Open circuit voltage predicted by the very high temperatures model over simulated E_G for a wide range of selected temperatures. As the temperature increases the V_{OC} for the simulated E_G decreases. Also, as the solar concentration increases the V_{OC} increases and the rate of V_{OC} reduction decreases.

In addition to the conversion efficiency, an additional efficiency parameter, $\eta_{PV}^{'}$, was calculated. This terminal characteristic is defined as the maximum power out divided by the power above the simulated bandgap. It is useful when calculating the efficiency of a system that includes additional elements, such as dichroic mirrors. This parameter has temperature dependencies that are similar to the conversion efficiency. The main difference is that this value does not approach zero as the bandgap energy increases.

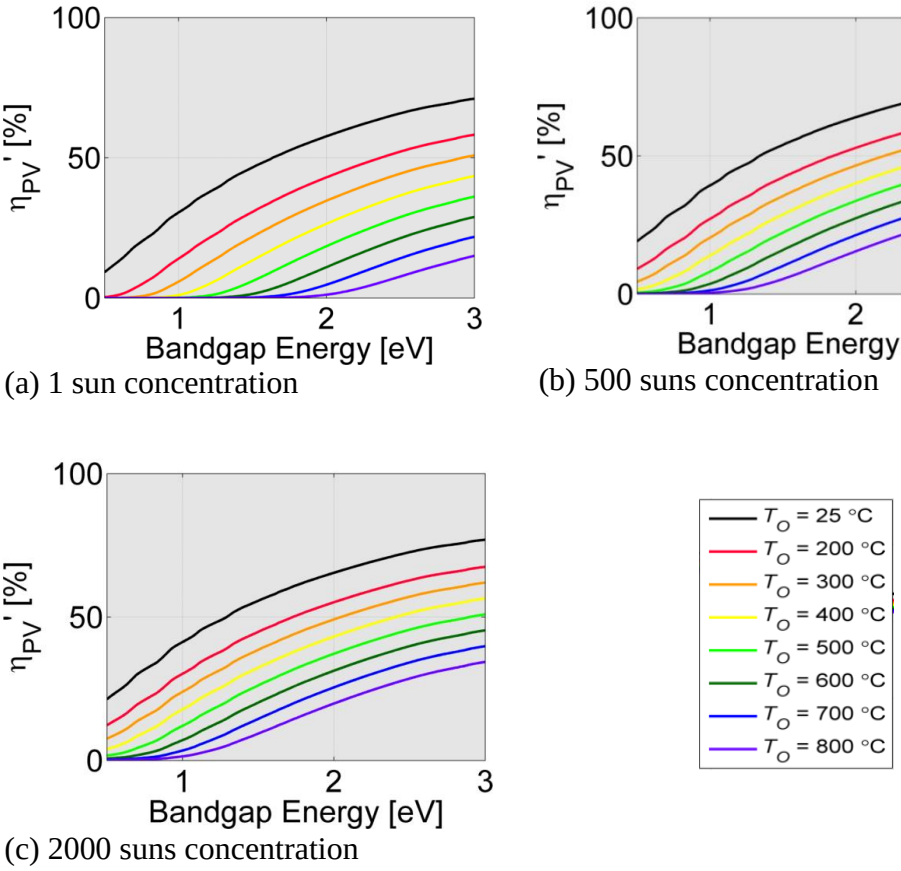

(a) 1 sun concentration

(b) 500 suns concentration

(c) 2000 suns concentration

Figure 4.12. The effective conversion efficiency, $\eta_{PV}^{'}$, predicted by the utlra high temperature model over simulated E_G for a wide range of selected temperatures. This parameter has temperature dependencies that are similar to the conversion efficiency, however it does not approach zero as the bandgap energy increases.

To further understand the connection between the peak conversion efficiency and the operating temperature. The peak conversion efficiency was found for each of the selected temperature and was then plotted with the associated values of E_G, η_{PV}' and f' for the peak efficiency. This provides a way to more carefully track these parameters as they change over temperature. Figure 4.13 shows that the conversion efficiency decreases smoothly as the temperature increases. It also shows that the E_G increases as the temperature increases. One part of the plot that is particularly interesting is temperature regions over which the optimal E_G does not changes very quickly. This can be seen in the optimal E_G between 200 °C and 400 °C at 2000 suns concentration. Here the E_G is

essentially constant, whereas over the same range of temperatures, at 1 sun concentration, the optimal E_G changed by 0.3 eV. This temperature insensitivity is coming from the gaps in the solar spectrum. This effect could be helpful when designing the complete solar cell system, due to the fact that the solar cells can operate over a rather larger range of temperatures and still be close to the optimum E_G and peak power out over this range of temperatures.

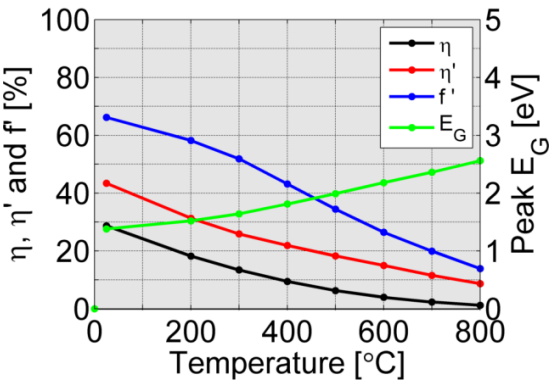

(a) 1 sun concentration

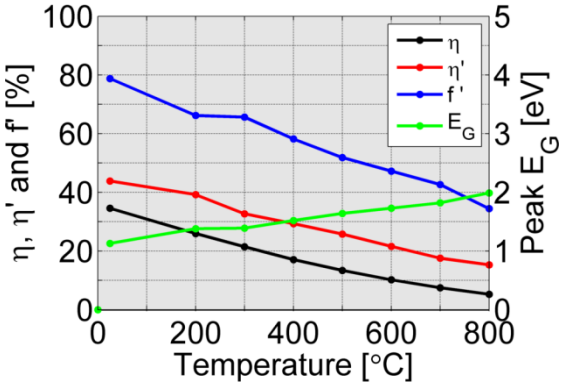

(b) 500 suns

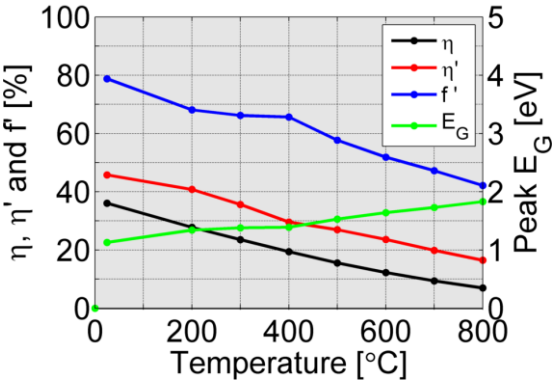

(c) 2000 suns concentration

Figure 4.13. The optimal peak η, η_{PV}', f' and E_G plotted for a wide range of selected temperatures. As the temperature increases the optimal peak η decreases. In the 2000 suns cases the optimal E_G changes very little between 200 °C and 400 °C.

4.3.2 Conversion Efficiency over Operating Temperature

The plots in the other Sections of this Chapter are the simulation results for the case with medium radiative recombination coefficient and medium Auger recombination coefficient. This Section will evaluate what affect each recombination mechanism has on the overall conversion efficiency.

The η for five different recombination limited cases is shown in Figure 4.14. In these simulation the bandgap energy is 1.5 eV and it is held constant over temperature. In each case the radiative recombination is not allowed to go below S-Q detailed-balance limit. The first case shown in black is the S-Q detailed-balance limit. The second case shown in red is for the case with low Auger recombination coefficient and the radiative recombiantion equal to the S-Q detailed-balance limit. The third case shown in light blue is the low Auger recombination coefficient and the low radiative recombination coefficient limit. The fourth case shown in bark blue is for the case with high Auger recombination coefficient and the radiative recombiantion equal to the S-Q detailed-balance limit. The fifth case shown in light green is the low Auger recombination coefficient and the low radiative recombination coefficient limit.

As in Figure 4.10, as the temperature increases the saturation current density increases. This causes the conversion efficiency in each case to decrease. Also, as the solar concentration increases the conversion efficiency increases. At 1 sun concentration, the cases two and four are nearly identical to case one, which indicates that the Auger recombination is insignificant at this concentration. At 2000 suns concentration, the case two and case one are still nearly identical, and in case four the conversion efficiency is now being limited by the high Auger recombination coefficient. This is still small compared to case three and five, with low and high radiative recombination coefficients repectively, which are clearly reducing the conversion efficiency more than the Auger recombination.

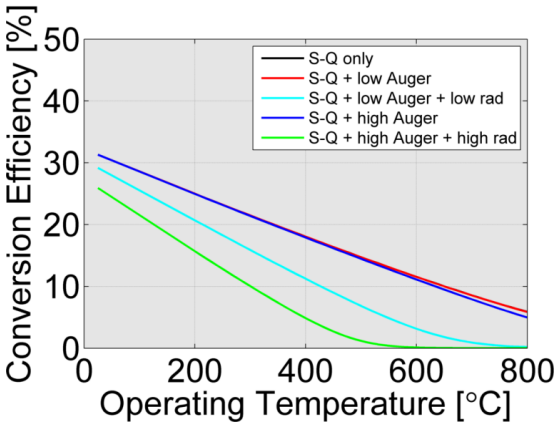

(a) 1 sun concentration

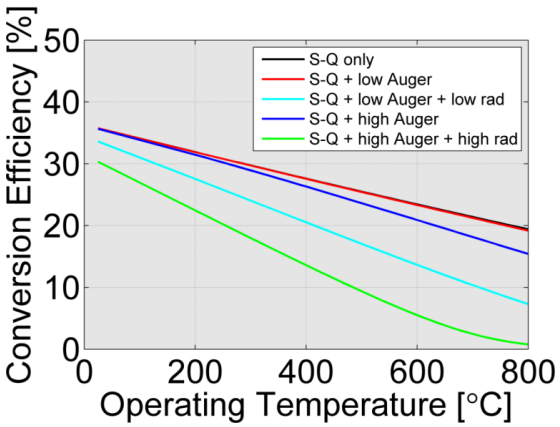

(b) 500 suns concentration

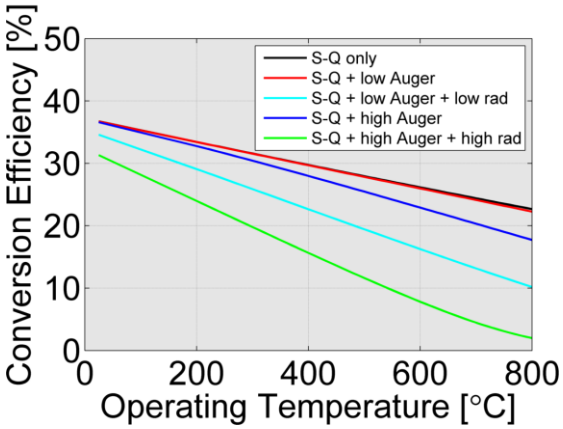

(c) 2000 suns concentration

Figure 4.14. The η simulated for five different recombination cases. At 1 sun the cases with low and high Auger recombination coefficients and the radiative recombination equal to the S-Q limit are nearly identical to the S-Q only limit, which indicates that the Auger recombination is insignificant at this concentration. At 2000 suns the case with only S-Q and low Auger recombination are still nearly identical, and the case with a high Auger recombination coefficient and radiative recombination equal to the S-Q limit is now reducing the conversion efficiency. This is still small compared to the cases with low and high radiative recombination, which are clearly reducing the conversion efficiency more than the Auger recombination.

This shows that the temperature dependence of the Auger recombination coefficient is not important so long as it does not significantly increase the Auger recombination coefficient above the high recombination coefficient limit.

4.3.3 The Peak Conversion Efficiency and Optimal Bandgap Energy Over Temperatures and Solar Concentration

The temperature insensitivity of the optimal E_G can be seen in more detail by plotting the peak efficiency with more temperatures and solar concentration. The optimal efficiency is plotted over temperature and concentration in Figure 4.15. It is plotted assuming medium Auger recombination, medium radiative recombination, direct bandgap materials and high-level injection. The optimal E_G over the same range is plotted in Figure 4.15 and Figure 4.16.

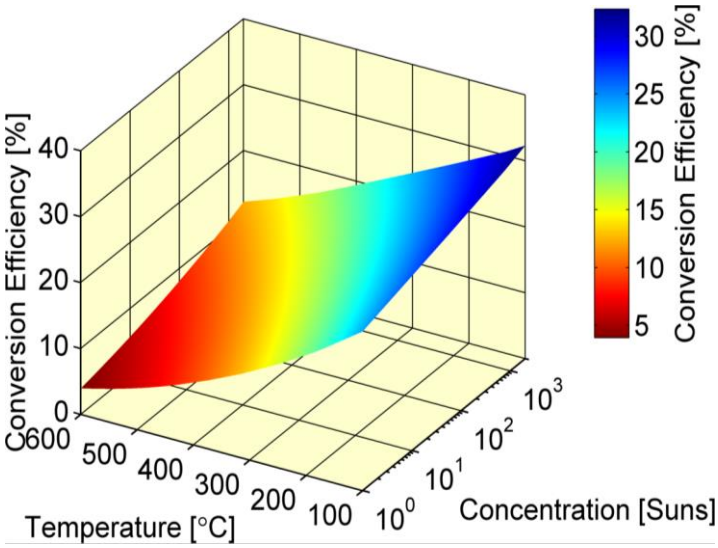

Figure 4.15. The optimal efficiency plotted over temperature and solar concentration. It deceases as the temperature increases and the solar concentration decreases.

As expected from Figure 4.13, the conversion efficiency decreases smoothly as the temperature increases and the solar concentration decreases.

A simple curve-fit of the conversion efficiency over temperatures and solar concentration will be discussed in Section 4.3.5.

The optimal simulated E_G plotted over temperature and concentration has more structure then the optimal conversion efficiency. It increases as the operating temperature increases and the solar concentration decreases.

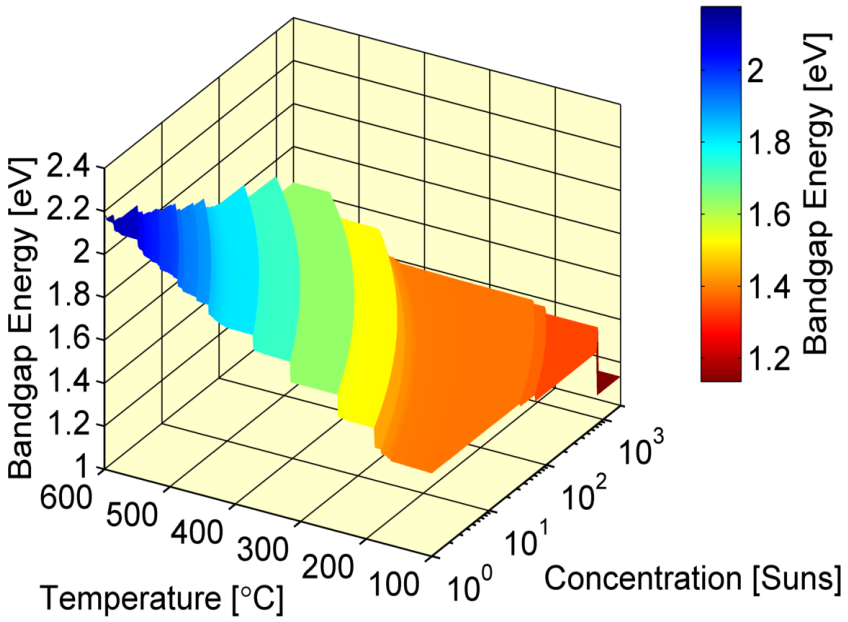

Figure 4.16. The optimal E_G plotted over temperature and solar concentation. The steps are caused by the local maxima in Figure 4.10

The gaps in the solar spectra, Figure 3.6(a), cause local maxima in the conversion efficiency over bandgap energy. This can be seen in the conversion efficiency over bandgap energy plots, Figure 4.10. It is easy to see the local maxima in the conversion efficiency at 25 °C. These local maxima in the conversion efficiency are caused by the gaps in the solar spectrum and the conversion efficiency temperature coefficient, which increases as the solar cell E_G decreases.

As the temperature increases the conversion efficiency at lower simulated bandgap energies decreases more quickly than the conversion efficiency at higher simulated bandgap energies. This will cause the optimal bandgap to jump from one local maximum to another local maximum at a higher bandgap as the temperature increases. This causes the steps seen in the optimal bandgap energy over temperature and solar concentration.

These optimal E_G transitions can be seen in Figure 4.17. The solid lines are the conversion efficiency over the simulated E_G for each of the plotted temperatures. The black dots are the peak conversion efficiency for each of the temperatures. The arrows shows the otpimal E_G transitions between each temperature. As the T_O increases from 394 °C to 395 °C there is a small change in the optimal E_G, from 395 °C to 396 °C there is no change in the optimal E_G, and from 396 °C to 397 °C there is a large change in the optimal E_G. These large optimal E_G transitions are causing the steps in Figure 4.16.

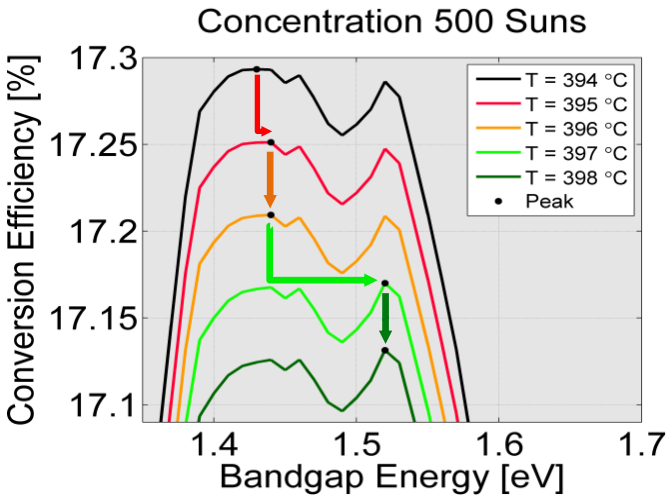

Figure 4.17. The lines are the conversion efficiency over E_G at each of the temperatures. The local maxima are caused by the gaps in the solar spectra. The black dots are the peak conversion effiicency and optimal E_G at each of the temperatures. The arrows shows the otpimal E_G transitions between each temperature. As the T_O increases from 394 °C to 395 °C there is a small change in the optimal E_G, from 395 °C to 396 °C there is no change in the optimal E_G, and from 396 °C to 397 °C there is a large change in the optimal E_G. These large optimal E_G transitions are causing the steps in Figure 4.16.

The steps in displayed in Figure 4.16 can be seen in Figure 4.18(a) for selected concentrations. There are large ranges of temperature over which the optimal E_G is constant. The fraction of energy in the spectrum above the optimal E_G is shown in Figure 4.18(b).

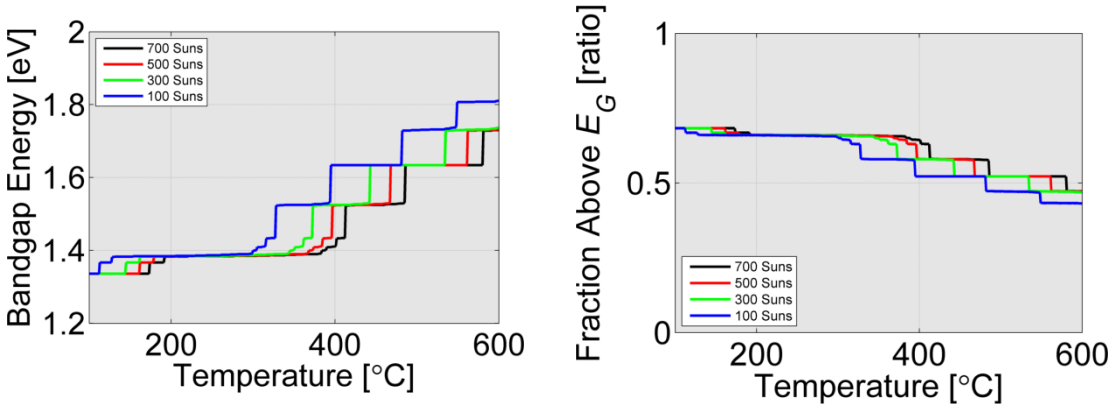

(a) Optimal bandgap energy (b) Fraction of incident light

Figure 4.18. (a) The optimal E_G for selected concentrations over a range of temperatures. The steps caused by the solar spectrum can clearly be seen. (b) The fraction of energy in the spectrum above the optimal E_G.

The steps in the optimal E_G maybe be helpful from a system and solar cell design standpoint since a chosen E_G could be close to the optimal E_G over a wide range of temperature and solar concentrations. The E_G of most real materials decreases as the T_O increases, so the optimal E_G steps increase the range over which the E_G of a real material will be close to the optimal E_G. If the optimal E_G strictly monotonically increased, the range over which the E_G of a real material is close to the optimal E_G would be smaller.

It will be shown in Section 4.3.4 that there is a range of bandgaps near the peak conversion efficiency, which are less than few relative percent below the peak conversion efficiency.

It would be beneficial to the system if the E_G of the real solar cell remained constant as the T_O increased, and even better if it were designed to increase as the temperature increased. It may be possible to counteract the temperature dependent E_G narrowing, by adjusting other physical properties which affect the E_G, such as exerting pressure on the solar cell [112] or by straining the junction layers. Clearly the reliability of these approaches would need to be thoroughly investigated.

4.3.4 Conversion Efficiency Over Temperature and Solar Concentration

The conversion efficiency plotted over temperature and solar concentration is helpful in understanding how quickly the conversion efficiency decreases as the simulated E_G moves away from the optimal E_G of the peak conversion efficiency at each temperature. The conversion efficiency at 100 suns is plotted in Figure 4.19. Figure 4.19(a) is a corner view and (b) is a top-down-view.

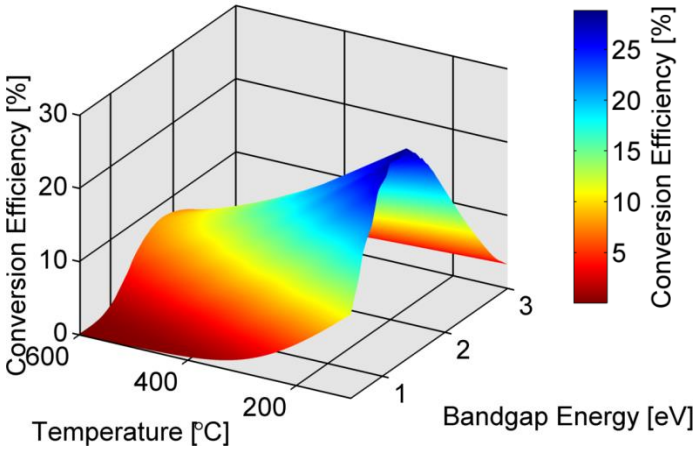

(a)

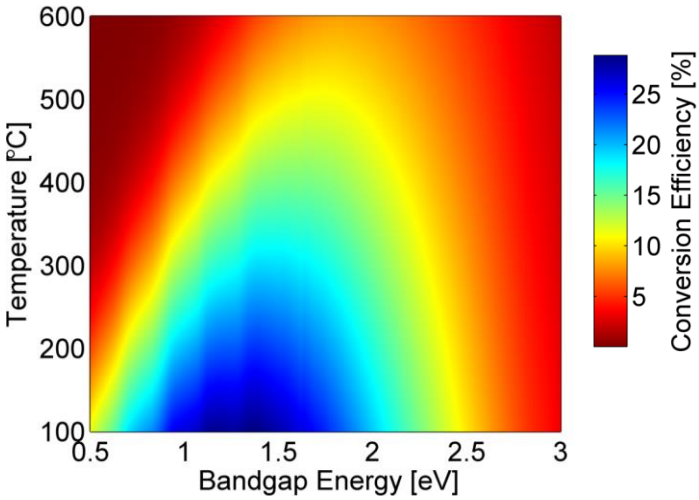

(b)

Figure 4.19. (a) is a corner view and (b) is a top-down view of the conversion efficiency over temperature and bandgap energy at 100 suns concentration. These plots show how quickly the conversion efficiency decreases for a given temperature from the optimal E_G. The conversion efficiency decreases as the bandgap increases and as the bandgap decreases. These plots also show the peak conversion efficiency shifted to a higher optimal E_G as the temperature increases.

As shown in Figure 4.10, there is a optimal E_G at the peak efficiency for each temperature. For a paticular temperature the conversion efficiency of a simulted E_G above or below the optimal E_G will be below the peak. Near the optimal E_G this difference will be small. Figure 4.20 shows the change of the conversion efficiency over E_G relative to the peak conversion efficiency at each temperature. The optimal E_G is the

dark blue regions inside the navy blue regions. The flat portions of the optimal E_G steps can be seen when the dark blue peak conversion efficiency region remains constant over a range of temperatures.

Despite the optimal E_G steps, in this plot it is easier than Figure 4.19 to see that the optimal E_G is increasing as the temperature increases. For most materials the opposite is true, the E_G is decreases as the temperature increases. The optimal E_G steps provide regions where a material could match the optimal E_G over a wider range of temperature, more than would be possible if the optimal E_G strictly monotonically increasing over the entire range of temperatures.

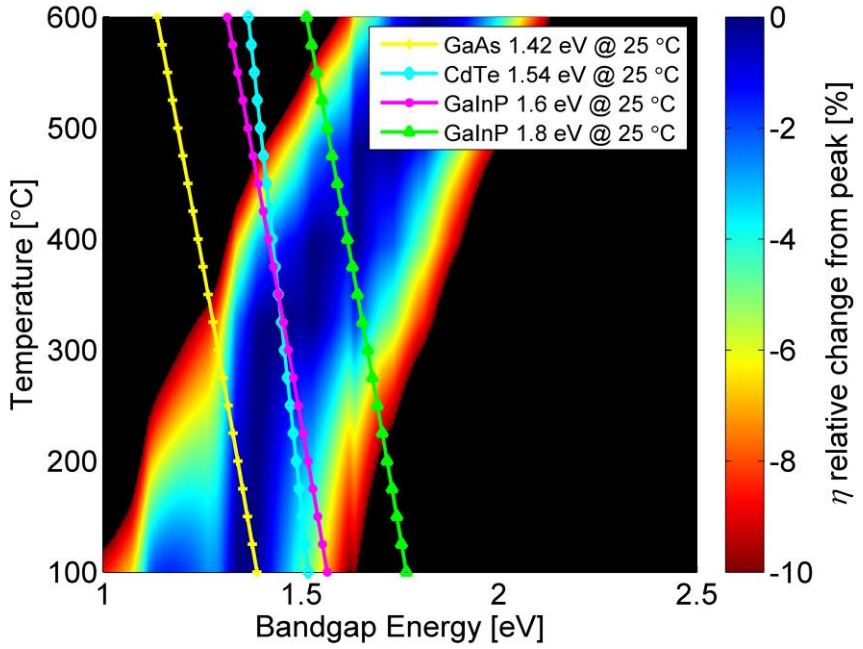

Figure 4.20. The conversion efficiency over E_G relative to the peak conversion efficiency at each temperature. The four lines through the plot show the temperature dependent bandgap narrowing of GaAs, CdTe, GaInP with a 25 °C bandgap of 1.6 eV and GaInP with a 25 °C bandgap of 1.8 eV. At some temperatures, the range of E_G with a conversion efficiency less than 5% from the peak is fairly narrow, for other temperatures this range is considerably wider. The optimal E_G clearly increases as the temperature increases.

The four lines show the temperature dependent bandgap narrowing of GaAs, CdTe, GaInP with a 25 ℃ bandgap of 1.6 eV and GaInP with a 25 ℃ bandgap of 1.8 eV.

This plot shows that for some operating temperatures there a narrow range of simulated E_G that are less than 5% below the peak, such as 200 ℃ which has a E_G range that is only 100 meV range. While at other temperatures, the range of simulate E_G within 5% is much wider, such as at 400 ℃ which has an E_G range that is nearly 500 meV wide. This range and the corresponding effect on the range of temperatures for which a given E_G is within 5% of the peak conversion efficiency at each temperature, is important for optimizing the systems to generate the most energy over the expected range of operating temperatures.

It would be preferable to find a high quality material with an E_G range that will be highly efficiency over the expected range of operating temperatures. GaAs covers the range from 100 ℃ to 200 ℃. The GaInP material with a 25 ℃ bandgap of 1.6 eV and the CdTe bandgaps E_G pass through the step face and therefore never quite reach the peak conversion efficiency. If the system was being designed to operate at 275 ℃ to 325 ℃, a material with an E_G of 1.38 eV at 300 ℃, would likely be close to the ideal for that system, which is between GaAs and GaInP with a 25 ℃ bandgap of 1.6 eV.

4.3.5 The Peak Conversion Efficiency Curve-fit Over Temperatures and Solar Concentration

An easy to use curve-fit was developed to estimate the peak conversion efficiency over the temperature and solar concentration range of interest. This curve-fit was used by APRA-E to evaluate the potential of hybrid CPV and thermal concentrated solar power CSP systems, sometimes referred to as hybrid CPV-T systems [24]. There are a wide variety of possible CPV-T applications, ranging from small systems [135] to large utility systems [136].

$$\eta(T_C, X) = 27.8732 + 1.8734\times10^{-5}T_C^2 - 0.054662T_C + 1.3\ln(X) \qquad (4.45)$$

Figure 4.21(a) shows the peak conversion efficiency at 100, 300, 500 and 700 suns from 100 ℃ to 600 ℃. The solid lines are the results of the analytical model. The dots

are the results of the simple curve-fit, Equation (4.45). Figure 4.21(b) shows that the absolute error between the analytical model and the simple curve-fit is less than 0.3 percentage points. Therefore the simple curve-fit can be used to give a first order approximation of the peak conversion efficiency.

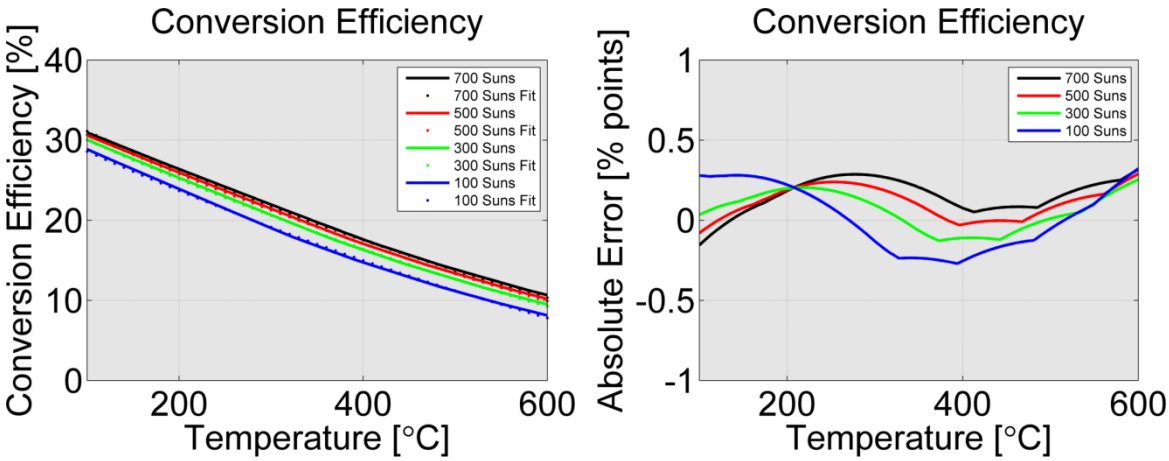

Figure 4.21. (a) The lines are the modeled conversion efficiencies over temperature at each of the concentrations. The dots are estimated using the simple curve-fit. (b) The absolute error between the results of the model and the curve-fit.

4.3.6 Multiple Junctions

Multiple junction solar cells can increase the overall conversion efficiency by collecting photons more efficiently with more than one bandgap. Due to the higher saturation current density at high temperature it may seem like there is little to be gained from using a multiple junction device at high temperatures, however, due to the exponential E_G dependence of the saturation current density, there is potential to significantly increase the conversion efficiency by using multiple junction devices.

To illustrate the possible conversion efficiency improvement a two junction three terminal device was simulated over a range of possible top junction and bottom junction bandgaps at 100 suns and 330 °C. The peak conversion efficiency for a tandem two

junction solar cell device can be found by using a three terminal device, which does not constrain the two tandem junctions to be current matched.

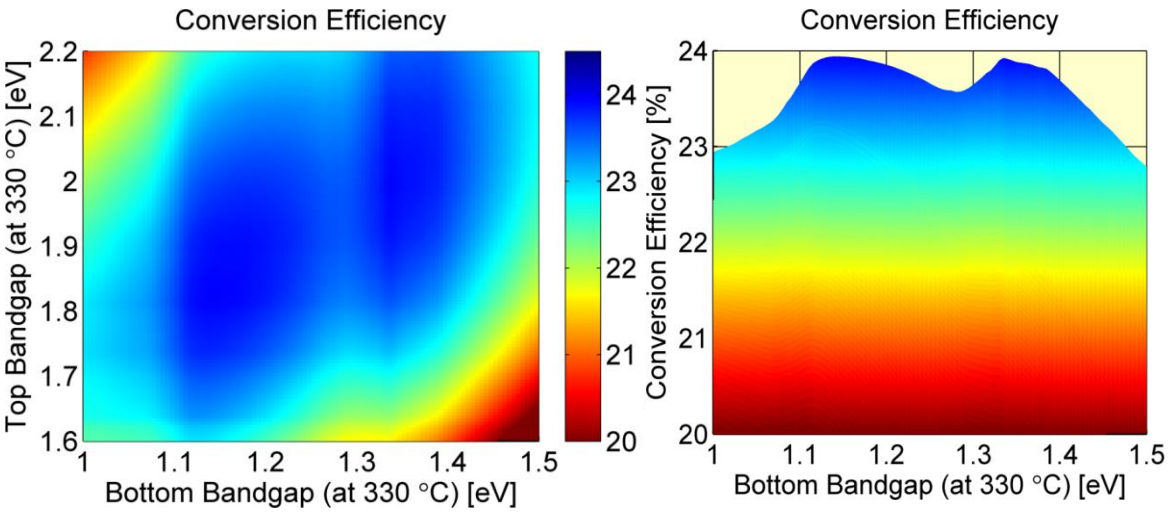

(a) (b)

Figure 4.22. Simulated conversion efficiency over (a) top junction and bottom junction E_G, as well as, (b) bottom junction E_G for a two junction three terminal tandem device operating at 100 suns and 330 °C. The conversion efficiency peaks are caused by the gaps in the solar spectrum.

The simulated conversion efficiency for a two junction three terminal tandem device operating at 100 suns and 330 °C is plotted in Figure 4.22(a) over ranges of possible top junction and bottom junction E_G., Figure 4.22(b) shows the same simulation for a range of possible bottom junction E_G. The single junction efficiency for a 1.6 eV device at 330 °C is 17.3 %. The peak conversion efficiency for the two junction case under the same conditions is 23.9%. As with the single junction case, the peaks in the conversion efficiency are caused by the gaps in the solar spectrum.

In addition to the two junction tandem simulations, the peak conversion for Shockley-Queisser detailed balance limit from 1 to 10 junctions was calculated over a range of selected temperatures, Figure 4.23. The novel method used to quickly find the

global peak η of an independently connected multiple junction solar cell system, is described in Appendix D.

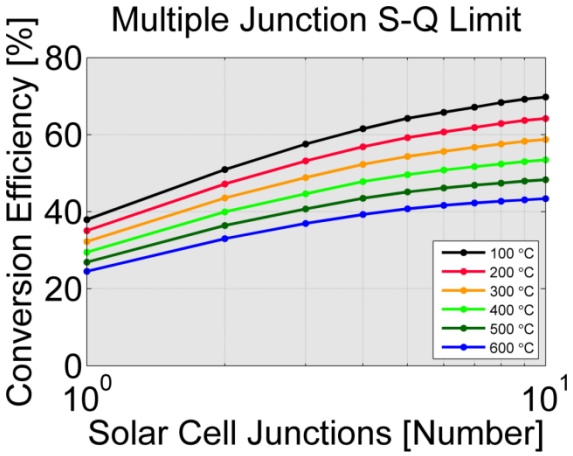

Figure 4.23. The peak conversion for Shockley-Queisser detailed balance limit from 1 to 10 junctions calculated over a range of temperatures.

4.4 Additional Effects

The analytical model described in this chapter has focused on simulating solar cells in ideal cases, the Shockley-Queisser detailed balance limit and various possible recombination levels. While it may be possible to develop solar cells that reach or even surpass these cases, there are also physical effects that can reduce the solar cells performance below these cases. This section will only briefly examine some of the important effects that could limit the solar cell when operating at high temperatures. It is therefore important to consider these when choosing a material which can mitigate these effects in this extreme operating temperature range. These effects should be studied in more detail when developing and test solar cells. One material that may be a good choice in this operating range is SiC. Functioning MOSFET SiC devices have been fabricated to operate at 600 °C [137] and a SiC solar cell has been fabricated [83].

Some of these are internal effects, while others are 3-D effects that will not be captured by 1-D analytical or numerical models. The effects can also be classified

according to whether they will appear immediately or whether they have a reliability effect that will appear after the solar cell has operated for an extended period of time.

4.4.1 Internal Effects

The immediate internal affects include the temperature dependent decrease of the mobility and the temperature dependent increase of the thermal velocity, which will increase the SHR recombination. These types of losses can be identified by reviewing the temperatures dependent material properties of a particular material. A numerical model has used to study these internal material parameters in Chapter 6.

The internal reliability affects include: atom diffusion, defect migration and melting. High temperature diffusion is a common method used to dope semiconductor materials. These effects can slowly degrade the performance of the solar cell over time.

Sources of atom diffusion include: dopant atoms, intrinsic atoms from other heterojunction layers, metal layers, passivation layers, anti-reflectant coating layers, and the atmosphere/environment. The effect of atom diffusion would be difficult to generalize in an analytical model because it is material dependent [138], device structure dependent, varies for each atom inside of each semiconductor material and is spatially dependent. At 600 °C an unprotected Si solar cell could fully oxidize. One way to limit the oxide growth would be to encapsulate the solar cell. Another method would be to seal the solar cell inside of a container, which had an oxygen free environment. This container could be filled with Nitrogen.

The melting point for various indirect bandgap and direct bandgap materials are shown in Figure 4.24. The melting points for materials above 1 eV are well above 600 °C.

For many reliability reasons it is important to operate the solar cell well below the melting point of the semiconductor layers. The melting point is above 1000 °C for semiconductors above 1 eV. The upper end of the temperature range chosen, 800 °C, is close to the melting point of semiconductors in the E_G range of interest.

Not only is it important to identify the operating temperature, or average temperature, it is even more important to identify the region which could experience

localized heating. This heating could be caused by current crowding and joule loss, it could be caused by defects in the semiconductor material, or it could be caused by non-uniform illumination of the solar cell.

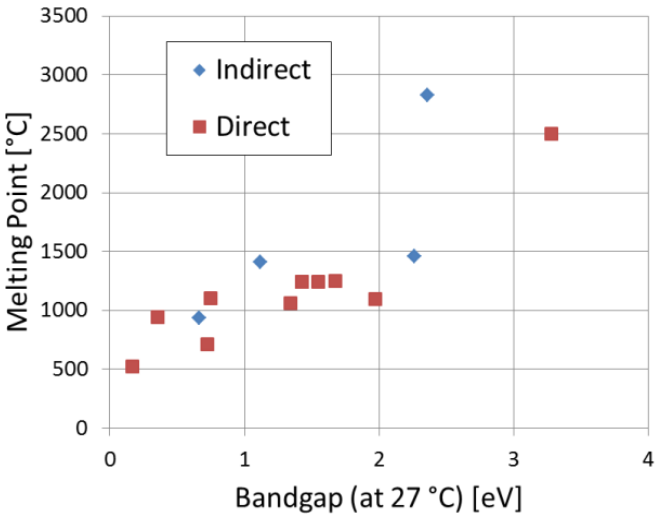

Figure 4.24. Melting points for indirect bandgap and direct bandgap materials over the bandgap range of interest.

4.4.2 External and 3-D Effects

There are many other temperature dependent mechanisms that could hinder the temperature dependent performance; one of these is the temperature dependent increase of the resistivity in the emitter and metal layers. This will be discussed in more detail in Chapter 5.

Some of the 3-D reliability effects include delamination of adhesives, thermal expansion, UV degradation of optical elements, expansion of trapped gases, and thermal acceleration of room temperature reliability effects.

4.5 Summary and Conclusions

While a high performance high temperature solar cell may not exist today, that does not limit the possibility of such a device being developed in the future. The recombination limited cases analyzed in this chapter indicate that it is possible to develop a high performance solar cell at much higher T_O than are currently being developed. In addition, this chapter identified parameters such as the optimal E_G that will be strongly affected by the T_O.

In order to simulate the recombination limited cases over a broad range of operating temperatures and bandgap energies, novel curve-fits were developed to calculate the material parameters n_i, B and C over these ranges. Because the temperature dependence of B and C was found to be material dependent, these parameters were held constant over temperature. The recombination limited cases are necessary in the initial design phase to quickly simulate the potential of solar cell operating over a broad range of T_O and E_G. The temperature dependent of B and C can be used after a candidate material has been chosen.

The results of this work showed that the simulated recombination limited η of direct bandgap solar cells operating at temperatures above 300 °C can be significantly higher than previously estimated [83]. In the case were B=1x10^{-9} cm^3/s, C=1x10-30 cm^6/s and τ_{SHR} is significantly smaller than the τ_{Eff} of the other two recombination mechanisms, the 300 °C peak η at 500 suns could be over 20% and at 2000 suns over 22%, with an optimal peak E_G of 1.8 eV in both cases.

The η of a tandem two junction devices were analyzed to evaluate the potential of using multiple junction solar cells at high temperatures. The three terminal simulations showed that the peak conversion efficiency of a tandem two junction device can be over 35% higher than the peak single junction device at the same temperature.

Based on these simulations it appears that the conversion efficiency of an appropriately designed solar cell operating above 300 °C could be quite high. These solar cells could be very useful in high temperature applications. Chapter 5 will show the

importance of considering the T_O when optimizing the grid electrodes of the 3-D solar cell. Chapter 6 will show that it is possible to match the temperature dependent terminal characteristics using detailed numerical models.

4.5.1 Future Work

The calculations in this chapter assume that 100% of the photons above the simulated E_G are absorbed and converted to current. This is useful for determining the upper limit of the J_{SC}, for devices that do not absorb photons below the bandgap energy. This model could be extended by including realistic partial absorption for direct and indirect bandgap materials [114, 139]. Doing this will likely change the optimal peak E_G by a few tens of millivolts. It would also allow the thickness of the solar cell to be studied. Thinning the solar cell will reduce the photogenerated current, and it will also reduce the volume over which th bulk recombination can occur. The optimal thickness could be found, by varying the thickness at each temperature.

The $\alpha(\lambda)$ of semiconductors are strongly influenced by the T_O. This has been measured for the direct bandgap material, such as GaAs, over a wide range of photon energies [101] and near the band edge [115]. Therefore it will likely be necessary to include the temperature dependent optical bandgap narrowing in the absorption model, when optimizing the device thickness. In addition to being temperature dependence, the $\alpha(\lambda)$ of semiconductor materials is also doping dependent. However, this dependence is not the same for all materials or dopants. For p-type GaAs the measured $\alpha(\lambda)$ changes very little as the doping concentration increases from $2\text{x}10^{17}$ [cm^{-3}] to $1.2\text{x}10^{18}$ [cm^{-3}], and for n-type GaAs the measured $\alpha(\lambda)$ varies from that of a direct bandgap material, to an absorption coefficient that is more similar to an indirect bandgap material [116].

5. TEMPERATURE DEPENDENT RESISTIVE LOSSES

The goal of Chapter 4 was to estimate the conversion efficiency for a variety of recombination limited cases. This allowed the model to simulate the maximum possible conversion efficiency that could be reached in each case. This model assumed that the solar cell can be designed so that all other loss mechanisms are negligible. However, in practice it is not possible to completely eliminate all of the other loss mechanisms, many of which arise from the 3-D structure of the solar cell. One important 3-D loss mechanism that can significantly affect the performance of a solar cell is the resistive loss.

This Chapter will examine how the total external R_{series} can significantly affect the temperature dependent solar cell performance. This is found to be even more important when operating solar cells at higher temperatures. As the solar cell temperature increases, the resistivity of most materials also increase. Therefore it is important to consider the resistive losses at the expected operating temperature when optimizing a solar cell design.

The results of the quasi 3-D distributed emitter model described in this chapter can be used in conjunction with analytically solar cell models, Chapter 4, as well as detailed numerical solar cell models, Chapter 6. The focus will be the T_O range of terrestrial CPV solar cells. It is expected that the resistive losses will be even more significant, over the temperature range explored in Chapter 4.

It is not possible to completely eliminate the resistivity in materials that are not super conducting. Common sources of series resistance are the Lateral Conducting Layers (LCL), the metal semiconductor contacts, the grid electrodes, the busbar electrodes and the semiconductor bulk. The grid electrodes and LCL are typically optimized to produce the largest possible conversion efficiency, by limiting the overall resistivity of the solar

cells, while balancing other losses, such as the shadowing caused by the electrodes and the optical loss caused by the LCL. This is particularly important in solar cells which have very thin LCL, which can lead to high values of sheet resistance, R_{sheet}. For materials with low enough R_{sheet} in the emitter layer will act as the LCL. In some cases the R_{sheet} can be reduced by adding a semiconductor window layer on top of the emitter layer. For solar cell materials with a high R_{sheet} in the emitter, a transparent conducting layer (TCL) is often added. Common TCL used on solar cells include Indium Tin Oxide (ITO) and Aluminum Zinc Oxide (AZO).

A wide variety of grid geometries and patterns have been examined !Flat, 1979 #623;Moore, 1979 #624?. Many different approaches have been implemented by others to quantify and reduce the resistive losses. One common approach is to fabricate a large number of test devices. Another common approach is to use a simple analytical model, often in 1-D. More recently, a variety of quasi-2D and quasi-3D models have been used. Each of these approaches has some benefits and limitations, and will be discussed in more detail. They are often used in combinations to take advantage of the benefits of each approach and diminish the associated limitations.

One of the most common approaches to reduce the resistive losses is empirical; it involves fabricating a large number of devices with different design parameters, such as changing the number of grid electrodes, N_G, their spacing, their width and their thickness. Other design parameters that can be varied include the busbar thickness, the thicknesses of the LCL and doping of the semiconductor LCL. The performance of these devices is then measured and the optimal design is identified. This approach to quantify and optimize the grid electrode and busbar electrode design is limited by a number of factors. First, the fabrication variations can significantly affect the uncertain and variability of the measurements. Second, the gird electrode patterns that will be tested are limited by the predefined mask. Third, the number of device parameters that can be varied are limited by the number of test solar cells that can be fabricated. Fourth, the device parameters to be tested are limited by the fabrication technology, therefore it is not possible to test what will happen if a device parameter is changed or improved beyond the capabilities of the current fabrication processes. Lastly, the fabrication and

characterization of a large number of devices can be a slow and time consuming process. Despite the many draw backs to the empirical approach, it is often used to optimize the grid electrode and busbar electrode pattern. The results from these measurements are often used to develop analytical and quasi-3D models.

Another common approach to analyze the resistivity losses is to use a simple analytical model. These analytical models can be 1-D and 2-D. Wolf was among the first to study series resistance in a solar cell in 1963 [140]. The model he developed included an equivalent resistance, which was calculated using the measured R_{sheet}. Later Wyeth developed an analytical model using the power loss [141]. Since then a number of quasi-2D models have been developed [142], these models are limited to 1-D current flow in the LCL.

A more advanced quasi-3D numerical model has been developed by Haas [143]. This model could quantify the bias-point loss and did not limit the current flow through the LCL to 1-D. The bias-point loss is caused by the voltage drop across the LCL which causes parts of the solar cell to operate away from the intrinsic maximum power point of the solar cell.

The work described in this chapter extends the quasi-3D model developed by Haas, by adding temperature dependent material parameters into this model. This allows the effect of temperature on the terminal characteristics to be quantified.[1]

The temperature coefficient of the 3-D solar cell will be affected by the front-surface grid electrode pattern and the LCL. There are many important trade-offs in optimizing the grid electrodes. These include the minority carrier lifetime in the emitter and the grid electrode shadowing. If the emitter is too thick, more than 1/3 the diffusion length, the carriers will not be efficiently collected, which will decrease the J_{SC} and the η of the device. Increasing the N_G will decrease the resistivity, which will reduce resistive

[1] Sections 5.1 through 5.6 are based on the paper "A distributed emitter model for solar cells: Extracting a temperature dependent lumped series resistance" by J. R. Wilcox and J. L. Gray, which was published in the Photovoltaic Specialists Conference (PVSC) proceedings, 2012 38th IEEE ({Wilcox, 2012 #544}).

losses, however, it will also increase shadowing, which will decrease the J_{SC}, which will also decrease the η.

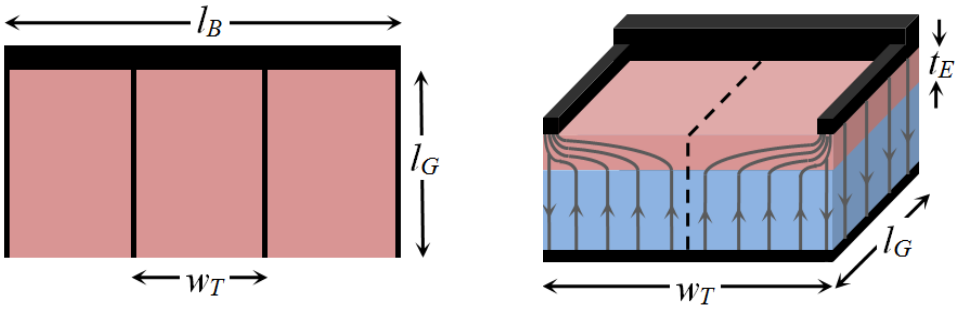

(a) Top view (b) Corner view

Figure 5.1. (a) Top and (b) corner view of the typical comb shaped grid and busbar electrodes on the emitter of a generic solar cell. The thick black line is the busbar and the thin black lines are the grid electodes. The area between two grid electrodes is a tile and the area between a grid electrode and the dashed line in (b) is a half-tile. The pink region is the emitter layer and the light blue region is the absorber layer. The gray arrows and lines indicate the current flow within the device (after [144] © 2012 IEEE).

There are a number of resistive losses in solar cells. Figure 5.1(a) shows the grid and busbar electrode pattern of a generic solar cell. This figure is not to scale. Here, l_B is the length of the busbar, l_G is the length of the grid lines, w_T is width of a tile, and t_E is the emitter layer thickness. The area between grid electrodes will be defined as a tile. In Figure 5.1(b), the area between a grid electrode and the dashed lined is defined as a half-tile. The gray arrows and lines indicate the flow of current out of the absorber layer into the pink emitter layer, the current then flows laterally into the grid electrodes and on to the busbar electrode.

There are a variety of resistive losses in a typical solar cell, these include back conductor joule loss, the back contact joule loss, the internal joule loss, the bias-point loss, the emitter joule loss, the front contact joule loss, the front grid electrode loss and the front busbar joule loss.

In most solar cells, the back conductor can be designed so that the resistive losses are negligible. The back contact resistance is often small, and must be balanced with the surface recombination caused by the back contacts. Because the carrier lifetime necessitates the solar cells to be very thin, on the order of a few microns for direct bandgap materials and tens to hundreds of microns for indirect bandgap materials, the internal joule loss from the back to the front is typically negligible.

The LCL, front contact resistance, front grid electrodes, and front busbar, must be optimized together to achieve the highest possible solar cell η. Increasing the thickness of the emitter will reduce the resistivity, while at the same time it will increase the recombination of carriers in the emitter. Increasing the number and width of grid electrodes will reduce the resistance between the emitter and the busbar. It will also increase the shadowing, which will reduce the photons that enter the solar cell and thereby reduce the photo generated current. If the busbar is over the active regions of the solar cell, as the width is increased, the shadowing will also increase.

It is relatively straight forward to calculate the components of the effective R_{Series} caused by joule losses. In order to determine additional effective R_{Series} components such as bias point loss, it is necessary to model the 3-D structure of the solar cell. The bias-point loss was carefully quantified by Haas [143]. This loss is caused by the resistance in the front surface and to a lesser extent in the back surface. Because the resistance causes a voltage drop across the surfaces of the solar cell, not all of the solar cell can operate at the intrinsic optimal max power point for the solar cell junction. Large regions of the solar cells will be forced to operate away from the intrinsic max power voltage. Areas close to the contact pads will operate at voltages below the optimal max power point and the regions in-between the grid electrodes will operate at higher voltages. The regions of the solar cell that operate away from the intrinsic max power point, contribute to the bias-point loss. The extrinsic max power point of the 3-D solar cell is found by adjusting the terminal voltage near the intrinsic max power voltage until the peak extrinsic output power is located.

5.1 Series Resistance Losses

As the operating temperature increases, nearly all of the series resistance losses in the solar cell will increase. In this model the effect of each of these losses will be summed to find the total equivalent series resistance, R_T.

$$R_T = R_B + R_G + R_C + R_L + R_A + R_R \tag{5.1}$$

Here the busbar resistance, R_B, is defined to include any resistive loss from the terminal contact pad to the grid electrodes. The grid electrode resistance, R_G, includes the resistive losses caused by the grid electrodes. The contact resistance, R_C, includes the resistive losses between the gird electrodes and the front LCL. The resistance of the front LCL, R_L, accounts for the resistive losses inside of the TCL and emitter layers. Any resistive losses between the emitter and the back contact are included in the semiconductor resistance, R_A. And the resistive losses between the semiconductor and the back contact pad are included in, back LCL resistance, R_R.

Some types of solar cells may have additional components, specific to that type of solar cell. These might include additional solar cell junctions or unique structures specific to that type of solar cell.

The resistive losses caused by each component of R_T can be found by using the quasi-3D model. In the quasi-3D model, each tile is broken up into very small vertical elements which connect to the front LCL and the back LCL of the solar cell. The LCL connects to the grid electrodes, which connect to the busbar electrode, and then to the terminal contact pads. Each vertical element in the quasi-3D model is simulated as an intrinsic solar cell. Measured values of the resistance are used to simulate the 2-D LCL and the electrodes.

5.2 Temperature Dependent Non-Ideal Diode Parameters

Many different types of solar cell models can be used to simulate the 1-D characteristics of the intrinsic solar cell elements. These models can range from

measured *J-V* data to a simple diode equation all the way up to the simulation results of a complete detailed numerical model.

A simple diode model such a non-ideal diode equation (Equation (3.6)) can be used during the development stage to provide useful insight into the effect that temperature has on the R_T. The extrinsic non-ideal diode equation is,

$$J = J_{SC} - J_O\left[\exp\left(\frac{q\left[V + JR_{Series}\right]}{nkT_O}\right) - 1\right] - \frac{V + JR_{Series}}{R_{Shunt}}. \tag{5.2}$$

This entire equation can be used to simulate the characteristics of a solar cell element, if the R_{Shunt} of a particular material is low or the R_{Series} of the solar cell element is high. However, for high quality solar cells, R_{Shunt} is high and R_{Series} is low. In this Chapter the R_{Shunt} of the solar cell element is assumed to ∞. Since most of the R_{Series} comes from the front LCL and back LCL, it will be assumed that the series resistance of the solar cell element is 0. This gives the intrinsic non-ideal diode equation,

$$J = J_{SC} - J_O\left[\exp\left(\frac{qV}{nkT_O}\right) - 1\right]. \tag{5.3}$$

The results of the quasi-3D simulations can be used during the initial development stage. A detailed numerical model of the solar cell could later be used to more carefully simulate the characteristics of the solar cell elements, which would allow the resistive losses to be refined, which could be used to further optimize the solar cell design.

In this chapter, the intrinsic non-ideal diode equation will be used inside of the quasi-3D numerical model to simulate the solar cell junction at each point across the solar cell. The quasi-3D model will then be used to numerically solve for the extrinsic max power point of the entire 3-D solar cell. The numerical solution contains the voltage bias point for each of the solar cell elements simulated. These voltage bias points can be used to estimate the bias-point loss and each form of joule loss. The resistance terms in Equation (5.1) can be extracted from these power losses.

The simple extrinsic non-ideal diode Equation (5.2) can be used to fit the *J-V* characteristics of the quasi-3D distributed emitter simulations. However, due to the 3-D

resistive effects simulated, the *J-V* curve modeled by the extrinsic non-ideal diode equation will only match the quasi-3D *J-V* curve at the J_{SC}, P_M and V_{OC} points.

In order to simulate the intrinsic non-ideal diode elements over a range of T_O, the values of J_{SC}, J_O and *n* over this range are needed. For the purposes of this broad study, it will be assumed that *n*=1 over the range of T_O. The *n* of real devices can change over T_O if the dominate recombination mechanism changes.

5.2.1 Temperature Dependent J_{SC}

As described in Section 3.1.3, generally as the T_O increases, the E_G deceases, this will cause the J_{SC} of a typical solar cell to increase. However, there are many other affects that will influence the J_{SC}. The bandgap of the absorbing material will decease as the temperature increases, this will typical cause the J_{SC} of the solar cell to increase. However, if this occurs in a region of the solar spectrum where the solar irradiance is zero due to absorption in the atmosphere, the J_{SC} will not increase. This can also happen if optical elements such as a dichroic or filter are limiting the photons in the solar spectrum just below the bandgap energy. Another way in which the J_{SC} of one solar cell can be restrained from changing as the temperature increases is when more than one solar cell junction is in series, and another solar cell junction is limiting the J_{SC} of the series connected tandem. In addition, the J_{SC} can be affected by the internal parameters of the devices, such as the material lifetime which can decrease the J_{SC} as the temperature increases. The J_{SC} can also be reduced by the passivation, window or emitter layers on the front of the solar cell. The bandgaps of these layers will decrease as the temperature increases; this can reduce the high energy photons collected by the solar cell, which will cause the J_{SC} to decrease.

Because the J_{SC} can increase or decrease as the temperature increases, it will be held constant when calculating the distributed emitter resistance in this Chapter. Since the

J_{SC} of an unrestricted GaAs solar cell will increase less than 5% over this range of T_O, resistive losses estimated by the quasi-3D will not change significantly over this range of temperatures. For this study a J_{SC} value of 1500 mA/cm^2 was chosen. This is approximately the J_{SC} of a GaInP/GaAs tandem solar cell at 100 suns [145] or a single GaAs solar cell at 50 suns [125].

5.2.2 Temperature Dependent J_O

The J_O will increase when the temperature increases or the bandgap energy decreases. A temperature dependent J_O which includes the temperature dependence of E_G is needed to calculate the temperature dependent terminal characteristic for the solar cell elements in the quasi-3D model.

A generalized form of the temperature dependence of J_O, developed by the author was described in Section 4.1.5. For the common recombination mechanisms radiative, SHR and Auger the generalized form is shown in Equation (4.24), which can be used for low-level and high-level injection. This model is useful to estimate the recombination limits, however, it was not possible to include the E_G dependence, due to the wide variation of E_G over temperature for various materials. Therefore, a curve-fit method for estimating the J_O over a range of E_G and a short range of T_O was developed by the author [144]. This method which will be described below and in more detail in Appendix B.2, will be used to estimate the J_O. This curve-fit method is particularly useful because the temperature dependent J_O with bandgap narrowing can be found using the E_G at 300 K, $E_{G,300K}$ [2].

[2] Based on the paper "Estimating saturation current based on junction temperature and bandgap" by J. R. Wilcox A. W. Haas, J. L. Gray and R. J. Schwartz, which was published in the *7th International Conference on Concentrating Photovoltaic Systems, 2011* ({Wilcox, 2011 #99}). ©2011 PSE AG

Because the J_O depends on E_G, and the temperature dependent bandgap narrowing is material dependent, a generic temperature dependent fit was created to approximate the J_O over simulated material bandgap energy and temperature.

$$J_O\left(T, E_{G,300K}\right) = K_O J_O\left(300\ K, E_{G,300K}\right), \tag{5.4}$$

$$\text{where } K_O = exp\left(S' * E_{G,300K} + I'\right). \tag{5.5}$$

The S' and I' are temperature dependent polynomials which account for the temperature dependence of E_G and the J_O.

Table 5.1
Temperature dependent J_O curve-fit model S' coefficients (after [104] © 2011 PSE AG).

Coefficient	Value
A_0	-145
A_1	1.17
A_3	$3.72\text{x}10^{-3}$
A_4	$5.91\text{x}10^{-6}$
A_5	$-3.76\text{x}10^{-9}$

Table 5.2
Temperature dependent J_O curve-fit model I' coefficients (after [104] © 2011 PSE AG).

Coefficient	Value
B_0	-24.587
B_1	$1.79\text{x}10^{-1}$
B_3	$5.19\text{x}10^{-4}$
B_4	$7.97\text{x}10^{-10}$
B_5	$-4.97\text{x}10^{-10}$

This equation can be used with any $J_O(300K, E_{G,300K})$ that has been evaluated at 300 K. In this chapter, the state-of-the-art J_O model developed by Gray was used [87].

The development of this curve-fit method is described in Appendix B.2. The validity of this method was checked by comparing the J_O estimated using this method, with the J_O calculated using the temperature dependent E_G narrowing of the measured materials plotted in Figure B.2(a) and Figure 5.2(a). Figure 5.2(b) shows that the V_{OC} calculated using this method and material specific J_O are off by less than ½kT at 350 K.

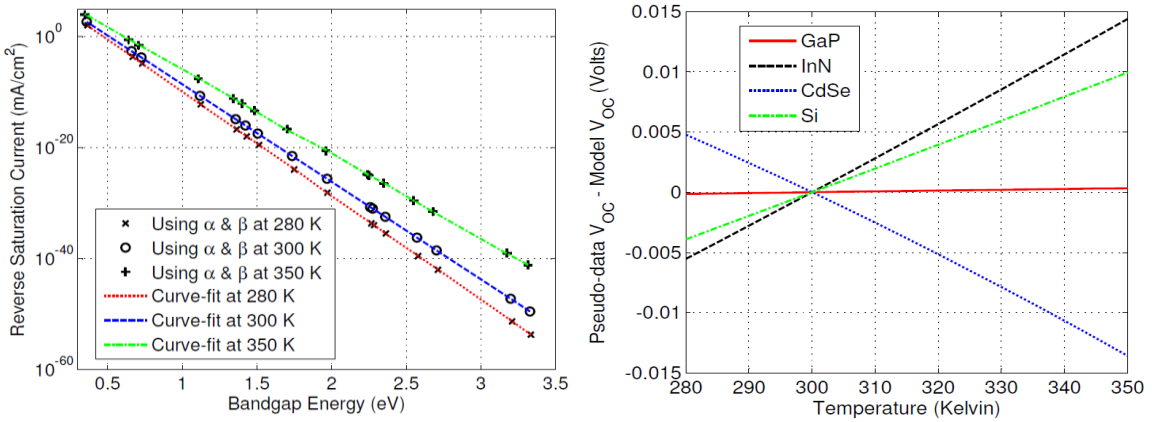

(a) (b)

Figure 5.2. (a) Reverse saturation current density over bandgap for three of the eight temperatures modeled. (b) Comparison of the pseudo-data V_{OC} over temperature and the values calculated using the polynomial slope and intercept $J_O(T, E_G(300\ \text{K}))$ curve-fit (after [104] © 2011 PSE AG).

5.3 Temperature Dependent Resistance

The resistance of most metals, TCL and semiconductors increase as the temperature increases. This can lead to significant resistive losses. It is therefore important to consider the range of possible operating temperatures when designing the resistive layers.

A big source of resistance in most solar cells is the TCL and emitter layer R_{Sheet}. Typically these layers must be thin to limit others losses, such as carrier recombination absorption.

Due to the thinness of these layers, the temperature dependent change of the t_E will not change significantly. This will be discussed more in Section 6.3.1. In this chapter t_E will be held constant. Near room temperature the dopants will be nearly fully ionized, so $N_A^- \approx N_A$ or $N_D^+ \approx N_D$. On the other hand, the mobility of most semiconductors will decrease to the power, γ. This will be discussed in more detail in the following section. The R_{Sheet} of a TCL will be similar.

5.3.1 Temperature Dependent Lateral Sheet Resistance

The mobility of most semiconductors are sensitive to the temperature, free carrier concentration, doping density and the electrical field inside the semiconductor. These dependencies for Si will be explored in more detail in Section 6.6.

The R_{Sheet} can cause a significant voltage drop to occur as current transverses laterally through these layers. The R_{Sheet} due to both carrier types is

$$R_{sheet} = \frac{1}{q\mu_n nt + q\mu_p pt}, \tag{5.6}$$

where μ_n is the electron mobility, μ_p is the hole mobility and t_E is the emitter thickness. The current flow in a semiconductor will often be dominated by the majority carrier. At the max-power point of a solar cell the minor carrier concentration can be significant. High quality solar cells and concentrator solar cells can have high minor carrier concentrations.

When $\mu_n n$ is significantly larger than $\mu_p p$ the R_{Sheet} simplifies to,

$$R_{sheet} = \frac{1}{q\mu_n nt} \tag{5.7}$$

When $\mu_p p$ is significantly larger than $\mu_n n$ the R_{Sheet} simplifies to,

$$R_{sheet} = \frac{1}{q\mu_p pt} \tag{5.8}$$

In this chapter, the other dependent parameters held constant, the mobility can be fit over temperature.

$$\mu = \mu\left(\frac{T_O}{T_M}\right)^{\gamma} \tag{5.9}$$

The temperature dependent slope of the mobility, γ, can be found by fitting measured data. When a semiconductor is heavily doped, which is typical of solar cell emitter layers, γ will decrease (Section 6.6). It will also be reduced when the free carrier concentration is high and when the electric field is high.

The intrinsic γ values for common semiconductor materials at 25 °C are displayed in Table 5.3, the typical values range from -3 to 0.

Table 5.3
The intrinsic γ values for common semiconductors at 300K (after [144] ©2012 IEEE).

	n-type	p-type
Si γ	-2.42 [146]	-2.20 [146]
GaAs γ	-1.0 [147]	-2.1 [147]
Ge γ	-1.66 [148]	-2.33 [149]
GaP γ	-1.7 [150]	-2.3 [150]

The temperature dependent conducting layer sheet resistance can be found by substituting Equation (5.7) into Equation (5.9).

$$R_{Sheet} = R_{Sheet,T_M}\left(\frac{T_M}{T_O}\right)^{\gamma} \tag{5.10}$$

Due to the wide range of possible γ values, the front LCL R_{Sheet} will be calculated over T_O for a selected range of γ values from -3 to 0. Figure 5.3 shows LCL R_{Sheet} as a

percent change relative to the LCL R_{Sheet} at 25 °C. When the γ value of a semiconductor is 0, the R_{Sheet} will not change as the temperature increases. When the γ value is -3, the R_{Sheet} will increase nearly 100% between 25 °C and 100 °C.

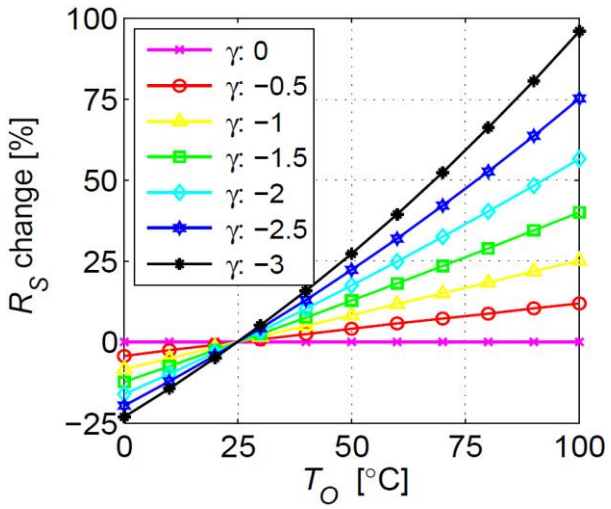

Figure 5.3. The temperature dependent LCL R_{Sheet} change compared to the LCL R_{Sheet} at 25 °C, for a selected range of the temperature dependent mobility factor, γ. As γ decreases the R_{Sheet} above 25 °C increases. For a γ value of -3, the R_{Sheet} can increase nearly 100% at 100 °C (after [144] ©2012 IEEE).

The R_{Sheet} not only causes the joule loss in the LCL to increase, it will also cause the bias-point loss of the LCL to increase. This effect will be explored further in Section 5.4.

5.3.2 Temperature Dependent Metal Resistivity

The resistivity of most metals increase as the temperature increases. To the first order the temperature dependences of the metal resistivity is given by

$$\rho_M = \rho_{M,25°C}[1+\alpha_\rho(T-25°C)] \tag{5.11}$$

As the temperature increases, ρ_M, varies according to the temperature dependent metal resistivity coefficient, α_ρ. Most of the metals commonly used in solar cell electrodes have α_ρ values that are around 0.004 K^{-1}. Therefore the resistivity of the solar cell electrodes increase as the temperature increases 26 % as the temperature is raised from 25 °C to 100 °C. The percent change of ρ_M is plotted in Figure 5.4, for α_ρ values ranging from 0 K^{-1} to 0.008 K^{-1}.

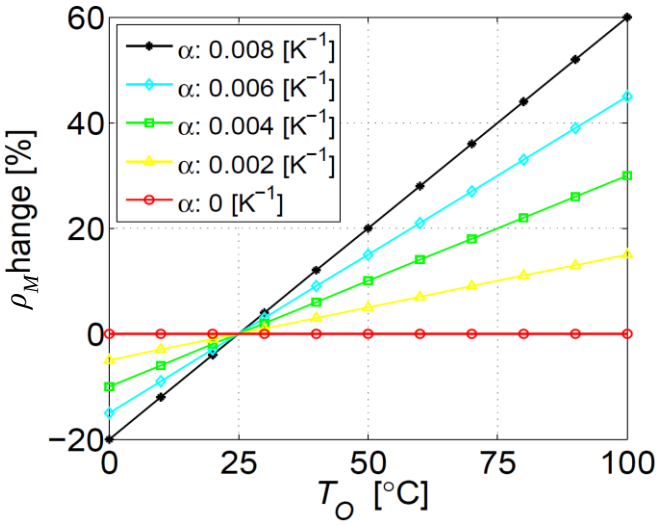

Figure 5.4. The temperature dependent change of the metal resistivity, ρ_M, compared to ρ_M at 25 °C, for a selected range of the temperature dependent metal resistivity coefficient, α_ρ. As α_ρ increases, the ρ_M above 25 °C increases. For an α_ρ value of 0.008 K^{-1}, the ρ_M can increase nearly 60% at 100 °C (after [144] ©2012 IEEE).

5.4 Temperature Dependence of the Equivalent Series Resistance

The next step is to calculate the equivalent series resistance, R_{eq}, of the conductor layer. The R_{eq} can account for all of the resistive losses in the LCL, such as the LCL joule losses and the biasing-point loss. The LCL joule losses can be estimated analytically for a half tile [143].

$$R_{eq} = \frac{R_{Sheet}}{3l_G}\left(\frac{w_T}{2}\right) \tag{5.12}$$

The analytical solution does not account for bias-point loss, and will therefore be a better approximation at lower temperatures, when R_{Sheet} is small or the absolute value of γ is small. It will be calculated over a range of temperatures and compared to the quasi-3D numerical model for R_{Sheet} = 100 Ω/□ and R_{Sheet} = 500 Ω/□, for γ = -0.5, -1.5 and -2.5, Figure 5.5.

The R_{eq} will be extracted from the quasi-3D numerical model, using a method developed by Haas [143]. This method uses the power loss due to the bias-point loss, $P_{L,BP}$, and the front LCL joule loss, $P_{L,CJ}$, along with the max-power current modeled to find R_{eq}.

$$R_{eq} = \frac{\left(P_{L,BP} + P_{L,CJ}\right)l_G}{J_{MP}{}^2 A_T{}^2} \tag{5.13}$$

In order for this expression to be valid, the extrinsic J_{MP} must be close to the intrinsic lossless J_{MP}. Simulations with more than a 1 % difference will not be included in the plotted data. The R_{eq} is simulated using the quasi-3D model for 25 °C, 50 °C, 75 °C and 100 °C. In addition the 25 °C analytical solution is also displayed.

The R_{eq} simulation shown in Figure 5.5, are for n = 1. The effect of higher values of n will be discussed in Section 5.5. A J_{SC} value of 1,500 mA/cm^2 was used in these simulations. This is equal to a GaInP/GaAs solar cell at 100 suns concentration, which has a 1 sun J_{SC} of 15 mA/cm^2 [145]. It is also equal to a GaAs solar cell with a concentration of 50 suns concentration, which has a 1 sun J_{SC} of 30 mA/cm^2 [125]. Figure 5.5(a), (c) and (e) were simulated for R_{Sheet} = 100 Ω/□ at 25 °C and (b), (d) and (f) were simulated for R_{Sheet} = 500 Ω/□ at 25 °C. Equation (5.10) was used to calculate the R_{Sheet} at the higher operating temperature. The quasi-3D model parameters are summarized in Table 5.4.

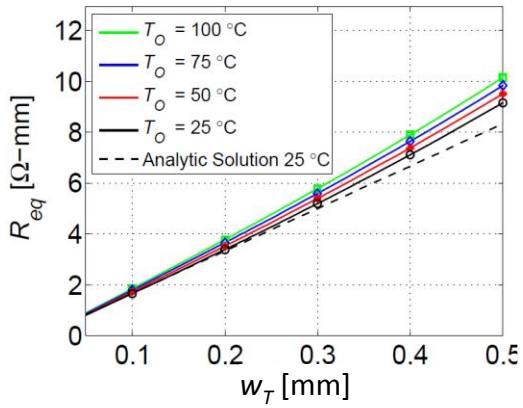

(a) γ = -0.5 and R_{Sheet} = 100 Ω/□

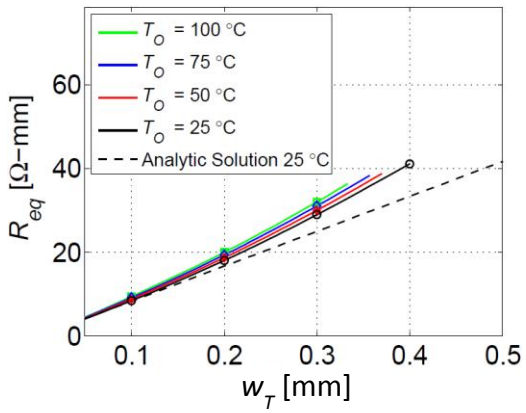

(b) γ = -0.5 and R_{Sheet} = 500 Ω/□

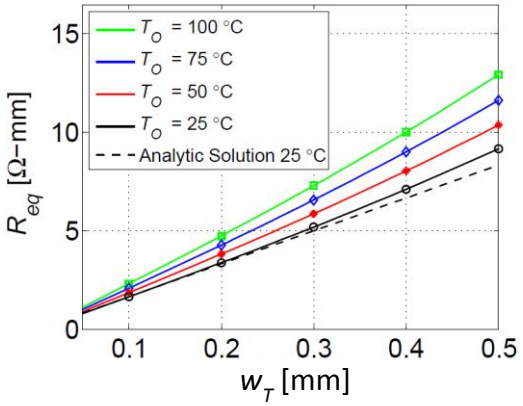

(c) γ = -1.5 and R_{Sheet} = 100 Ω/□

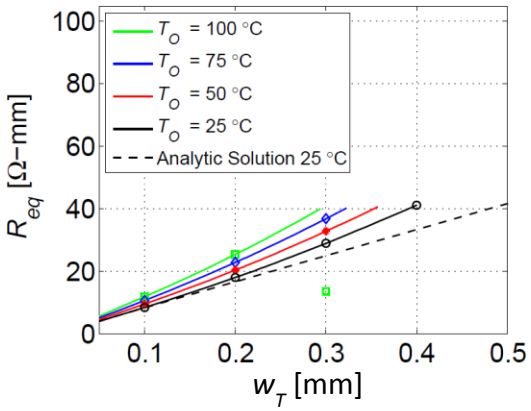

(d) γ = -1.5 and R_{Sheet} = 500 Ω/□

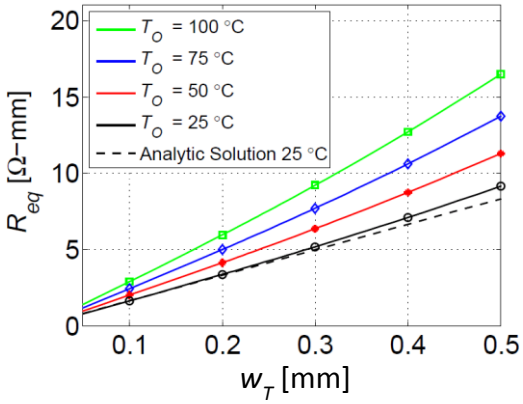

(e) γ = -2.5 and R_{Sheet} = 100 Ω/□

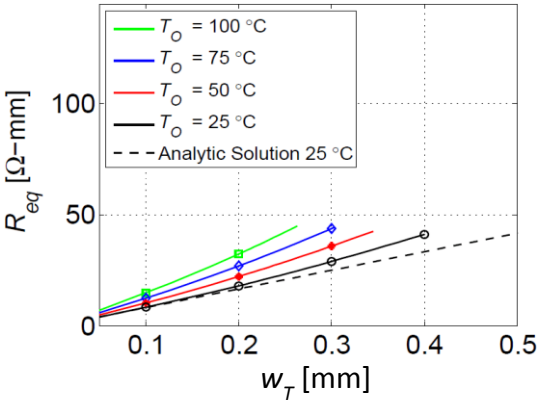

(f) γ = -2.5 and R_{Sheet} = 500 Ω/□

Figure 5.5. The simulated R_{eq} for R_{Sheet} = 100 Ω/□ (a), (c) and (e), also for R_{Sheet} = 500 Ω/□ (b), (d) and (f). The dashed line is the analytical solution at 25 °C. The solid lines were simulated using the quasi-3D distributred emitter model. These lines are closer together in (a) and (b), where γ = -0.5 and further apart in (e) and (f), where γ = -2.5. The difference between the dashed black line and the solid black line is caused by the bias-point loss, which is higher when the R_{Sheet} is higher (after [144] ©2012 IEEE).

It is easy to distinguish the front LCL joule loss and the biasing-point loss. At 25 °C the front LCL joule loss is shown by the dashed black line and calculated using Equation (5.12). The solid black line, was calculated using the quasi-3D model, which includes the biasing-point loss. Therefore the bias-point loss causes the solid black line to be higher than the dashed black line, which does not contain bias-point loss. The temperature dependent change of the R_{Sheet} in Figure 5.3 causing the four solid lines in (e) to spread out more than those same lines in (a).

As the R_{Sheet} increases the bias-point loss increases, this causes the four lines in (b), (d) and (f) to bend further up away from the analytical solution than the lower R_{Sheet} cases (a), (c) and (e). For conductive layers with a R_{Sheet} value of 500 Ω /□ the bias-point becomes significant for w_T above 0.2 mm, and for conductive layers with a R_{Sheet} of 500 Ω /□ the bias-point becomes significant for w_T above 0.3 mm. When the magnitude of γ is small (Figure 5.5(a) and (b)), R_{Sheet} increases slowly with temperature. When the magnitude of γ is larger (Figure 5.5(e) and (f)), the R_{Sheet} nearly doubles when the temperatures changes from 25 °C to 100 °C.

In Section 5.6 it will be shown that for a uniformly illuminated solar cell at 25 °C with J_{SC} = 1,500 mA/cm^2, the optimized grid electrode pattern will have a w_T that is larger than 0.2 mm. Haas showed that solar cells which are non-uniformly illuminated have local concentrations that are significantly higher than the average concentration of the solar cell [143]. This causes these solar cells to be even more sensitive to the bias-point loss.

When the grid electrode and busbar resistivity is negligibly low, the R_C can be approximated analytically [143].

$$R_C = \frac{R_{eq}}{2\left(N_G - 1\right) l_G} \tag{5.14}$$

This equation is a good approximation, when the resistivity of the grid electrodes and the busbar electrodes are negligible. Under these conditions each of the half-tiles will operate exactly the same way. When resistivity of the grid electrodes or the busbar

electrodes is larger, a voltage drop will occur along the length of the electrodes. This will cause each half-tile to be biased differently, which will increase the bias-point loss of the entire solar cell.

5.5 Non-unity Ideality Factor and Tandems

When the front LCL R_{Sheet} is sufficiently high enough to cause a significant voltage drop across the conductor layer, regions of the solar cell are forced to operate away from the intrinsic max power point. The width of this range of operating max points, are affected by the resistance of the LCL as well as the shape of the *J-V* near the max power point. When the R_{Shunt} is very large, the shape of the intrinsic *J-V* will be determined by the *n* of the solar cell. This ideality factor is strongly affected by the dominate recombination mechanism. Another situation in which the ideality will change is when solar cells are connected in series, which will be discussed in more detail below.

Because the bias-point loss is predominately dependent on the shape of the J-V curve near the max power point, the result will not be affected significantly by the magnitude of the max power for a given value of J_{SC}. The similarity of the *J-V* shape can be shown by shifting the *V* points of one *J-V* curve by the difference of the open circuit voltage of a second curve, with equal ideality factors (Append E.1). This shows that the shape of the first *J-V* curve near the max power point is identical to the shape of the second *J-V* curve near the max power point of the second *J-V* curve. This will not be the case when J_O is on the order of the J_{SC} which can happen at low E_G and high T_O.

The other case in which the *n* will change is when two or more solar cells are connected in series. If their short circuit currents are nearly equal, the *n* of the tandem stack will be the sum of the *n* of the individual junctions. Because the combined shape of the tandem stack can be compared to a single junction diode, the results calculated for higher *n* can be used for both single junction with the higher *n* and series connected multi junction solar cells.

Calculations performed over a range of n values show the bias-point loss and therefore the R_{eq} decreases as the ideality factor increases. This causes the simulated R_{eq} to be closer to the analytical solution to a higher value of w_T. This is caused by the curvature of the *J-V* curve near the max-point, which decreases as the n increases. Because there is more bias-point loss to reduce, the reduction of the R_{eq} is more significant in the cases were R_{Sheet} is higher, shown in Figure 5.6(b), compared to the cases were R_{Sheet} is lower, Figure 5.6 (a).

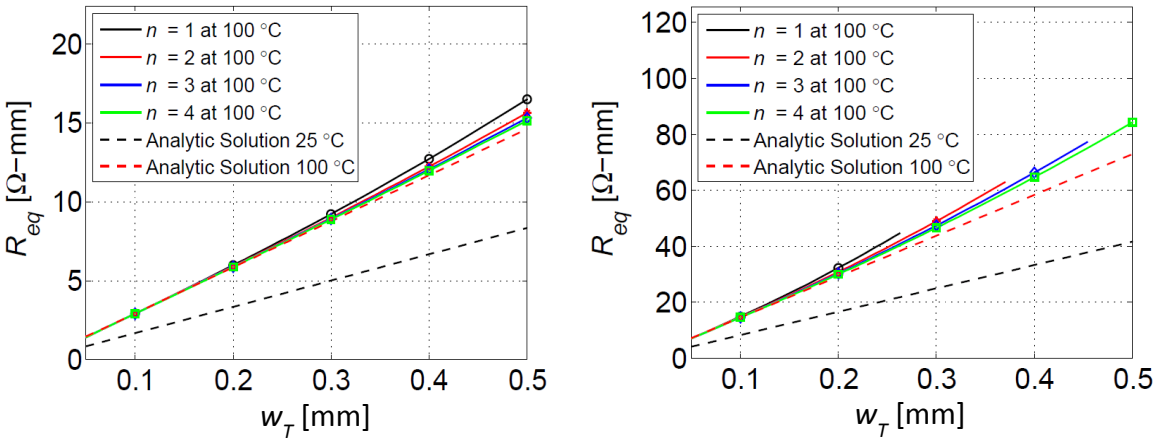

(a) γ = -2.5 and R_S = 100 Ω/□ (b) γ = -2.5 and R_S = 500 Ω/□

Figure 5.6. Plots of the R_{eq} simulated over w_T for a range of n, for J_{SC} = 1,500 mA/cm2, T_O = 100 °C and γ = -2.5. (a) is for a R_{Sheet} value of 100 Ω/□ and (b) is for a R_{Sheet} value of 500 Ω/□. The quasi-3D simulated R_{eq} approaches the analytical approximation of R_{eq} at 100°C as the *n* of the solar cell increase (after [144] ©2012 IEEE).

5.6 Conversion Efficiency Temperature Dependence

Analytical equations have been developed to estimate the R_G and R_B [143]. These equations do account for the joule loss in these electrodes. However, they do not account for the additional bias-point loss, caused by the voltage drop developed along these

electrodes. In high concentration and non-uniform illuminated solar cells, this effect can be significant.

The grid and busbar electrode resistivity will increase the joule and bias-point losses. In an optimized solar cell, these resistive losses have been balanced with the other losses associated with the grid and busbar electrodes, such as shadowing and surface recombination velocity. A grid and busbar electrodes can be optimized by varying the electrode design and the N_G.

In order to demonstrate the importance of the temperature dependent LCL R_{Sheet} on the joule and bias-point loss in the LCL, the resistivity of the grid and busbar electrodes will be assumed to be negligible. Including the temperature dependent grid and busbar electrodes will increase the overall temperature dependence and bias-point loss. A summary of the parameters used in the quasi-3D model are shown in Table 5.4.

Table 5.4
Summary of quasi-3D model parameters.

Parameter	Values
J_{SC}	1,500 mA/cm^2
n	1
T	25 °C and 100 °C
R_{Sheet}	100 Ω/□ and 500 Ω/□
R_B, R_G, R_C, R_A, R_R	0 Ωcm^2

The optimal N_G can be determined for a given design by varying the N_G used. Figure 5.7 shows the possible conversion efficiency from 10 to 100 grid lines, at 25 °C black circles and at 100 °C blue triangles. At 25 °C the N_G needed to achieve the peak conversion efficiency was found, as well as the corresponding efficiency at 100 °C for that N_G. Likewise the 100 °C peak conversion efficiency was also found along with the corresponding efficiency at 25 °C.

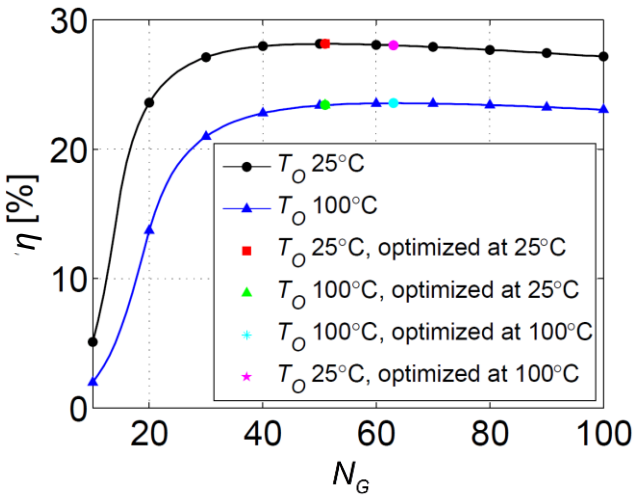

Figure 5.7. The simulated η over a range of grid electrodes at 25 °C and 100 °C. The difference between the 25 °C and 100 °C η is caused by the temperature dependence of the R_L. The red square shows the optimal N_G for the peak efficiency at 25 °C. The green triangle shows the corresponding η at 100 °C for the optimal N_G at 25 °C. The light blue asterisk shows the optimal N_G for the peak efficiency at 100 °C. The pink star shows the corresponding η at 25 °C for the optimal N_G at 100 °C (after [144] ©2012 IEEE).

Optimizing the electrode design and N_G at 25 °C will lead to a lower η when operated at 100 °C then is possible if the N_G was optimized for 100 °C. As the temperature increases the front LCL R_{Sheet} increases, this causes the bias-point loss to increase. When the N_G was optimized for 100 °C, more grid electrodes were added which lead to a lower bias-point loss in the front LCL. Therefore it is important to consider the expected range of T_O when optimizing the grid and busbar electrode design. These effects will be significantly larger for cases with higher solar concentrations (higher J_{SC} values) and for cases with non-uniform illumination. It will also be larger when the temperature dependent grid and busbar electrodes resistivity is included in the model.

The temperature coefficient of η over the range of possible γ values is shown in Figure 5.8. The solid black line shows the case in which R_L is equal to zero, which causes the R_T to be zero for all values of γ. This is the best possible case, in which the resistivity losses will be zero. The thin blue line with circles shows the temperature coefficient of η when R_L = 500 Ω/□. This shows that the η temperature coefficient becomes worse as the γ value becomes more negative. The η at 100 °C for γ = -2.5 is -0.4 absolute percentage points higher than the case in which R_L is the same and γ = 0.

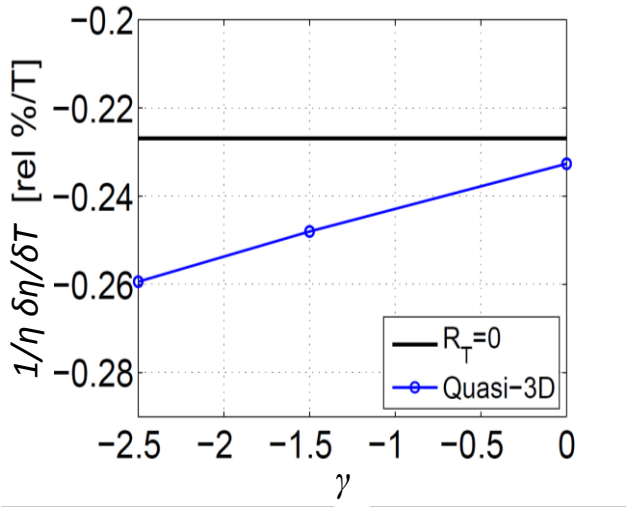

Figure 5.8. The η temperature coefficient over γ for R_L = 0 Ω/□, shown in solid black, and R_L = 500 Ω/□, shown by blue line with circles. The value of γ has no affect in the R_L = 0 Ω/□ case. The temperature coefficient becomes worse as the as the γ value becomes more negative (after [144] ©2012 IEEE).

5.7 Summary and Conclusions

In Chapter 3 and Chapter 4 it was shown that the terminal characteristics of a solar cell are strongly influenced by the T_O. The temperature dependent parameters in the intrinsic non-ideal diode equation are T_O, J_{SC}, and J_O. In these simulations the J_{SC} was held constant, since depending on the system design, it can increase or decrease as the T_O

increases. The J_O was estimated over the range of T_O. It was also shown that the R_T was strongly temperature dependent. This is caused by the strongly temperature dependent resistivity parameters R_{Sheet} and ρ_M, which also lead to a large increase in the bias-point loss.

Due to the temperature dependencies, the T_O range should be considered when optimizing the grid and electrode design, particularly at high temperature. Optimizing the design at lower temperatures can lead to non-optimized performance at higher temperatures. These effects will be significantly larger for cases with higher solar concentrations (higher J_{SC} values) and for cases with non-uniform illumination. It will also be larger when the temperature dependent grid and busbar electrodes resistivity is included in the model. In addition, it will also be much higher when operating at the ultra temperatures examined in Chapter 3 and Chapter 4.

6. TEMPERATURE DEPENDENT NUMERICAL MODEL

In the three previous chapters, analytical models have been used to represent a solar cell's terminal characteristics. In each case, numerical methods were implemented to solve for the terminal characteristics of these analytical models. Where appropriate, the temperature dependent material properties have been used. These models have been used to match a solar cell at a single operating point. They are often not particularly useful over a range of operating conditions, such as T_O or X. In this chapter, a physics based detailed numerical model will be employed to represent a Si solar cell over a range of T_O. The results of this model will be used to calculate the terminal characteristics and T dependent terminal characteristics.

Detailed numerical models are particularly useful because they can model the non-homogenous spatial nature of a solar cell better than an analytical model, which requires assumptions to be made about the device performance. Some of the spatial device parameters include the local carrier densities and the potential inside of the device. It also allows additional effects such as surface recombination to be included in the model. It is expected that a well-developed numerical model will be able to more closely match terminal characteristics and T dependent terminal characteristics of a solar cell over a wider range of operating conditions. One of the main reasons this is possible is due to the fact that each of the recombination mechanisms can be simulated separately, using the local carrier densities throughout the device. This reduces the number of simplifying assumptions that need to be made. It also allows for the internal effects, such as the depletion width, to be accounted for. One of the limitations of this approach is that each of the semiconductor material properties needs to be well defined over the operating

range modeled. This includes any material parameter dependencies caused by the operating conditions.

In addition to being able to represent a solar cell over a range of operating conditions, numerical models are also particularly useful in identifying material parameter sensitivity of the terminal characteristics. Model parameters can be varied to identify how much the material parameters affect the terminal characteristics. This can help identify ways in which the solar cell performance might be improved.

Most of the semiconductor material parameters are dependent on other material parameters. Four of the most common dependencies are *T*, doping density, minority free carrier densities and $\vec{\mathcal{E}}$. Each of these four parameters can vary throughout the device. Many of these dependencies, in particular the T_O and doping density will affect the terminal characteristics, and significantly affect the *T* dependent terminal characteristics. The minority free carrier concentration will be small enough when operating in low-level injection that it will not significantly affect the terminal characteristics. Which material parameter dependencies are important will depend on the type of solar cells, the T_O, the other operating conditions and solar spectrum.

6.1 Numerical Modeling

A large number of research groups have used a wide range of simulation programs to successfully numerically model wide variety of solar cells. A list of the simulation programs are shown in Table 2.1. These models are often developed to model the solar cell at 25 °C, with a few being developed at other T_O. In these models the material parameters are input into the model at the desired T_O. The dependencies of many of the parameters are often neglected, since they are small relative to the material parameter itself, and therefore will not significantly change the absolute value of the terminal characteristics.

As will be shown in this chapter, the material parameter dependencies which have little effect on the terminal characteristics can still significantly affect the *T* dependent terminal characteristics. This is primarily due to the fact that the *T* dependence of the

terminal characteristics per degree Celsius are typically 3 orders of magnitude smaller than the associated terminal characteristics. Therefore, while it may be possible to ignore a material parameter with a small *T* dependence when modeling the device numerically at one temperature, that same small *T* dependence will become important when attempting to determine the *T* dependent terminal characteristics. An example of this which will be discussed in Section 6.10, is the *T* dependence of the Urbach tails in the $\alpha(\lambda)$. When numerically modeling a solar cell at one *T*, using an $\alpha(\lambda)$ measured at a *T* close to the model T_O, will likely give a J_{SC} value that is relatively close to the expected value. However neglecting to include the *T* dependence of the $\alpha(\lambda)$, or even over simiplifying this dependency when modeling the $\frac{1}{J_{SC}}\frac{J_{SC}}{dT}$, will often make it difficult to get the correct value.

Solar cells and many other semiconductor devices are commonly modeled numerically using a set of 5 equations (Equation (6.1) to Equation (6.5), in Section 6.2), referred to as the semiconductors equations, which were proposed by Van Roosbroeck [59]. The physical material parameters needed to solve the semiconductor equations are shown in Figure 6.1. The dependencies of each of these material parameters will be discussed in Section 6.3 through Section 6.8. The results of the numerical model will be compared to the measured device in Section 6.10.

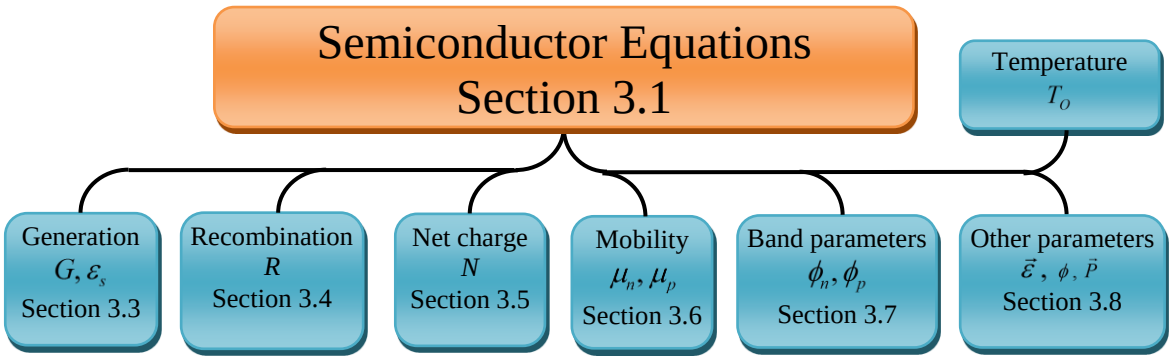

Figure 6.1. Physical material parameters used in the semiconductor equations, Section 6.2. Each of these material parameters will be discussed in Section 6.3 through Section 6.8.

Each of the material parameters in Figure 6.1 will be broken down into constituent material parameters. Physics based analytical expressions, semi-empirical relations and interpolated data, will be used to identify the operating condition dependencies of each substituent material parameters. It is likely that most if not all of the material parameters will be dependent on each of the operating conditions.

The operating condition dependent material parameter framework discussed in this chapter is based upon similar frameworks developed by [52, 92]. This framework can be used to simulate any type of semiconductor device. The materials that have been identified as being T dependent are shown in Figure 6.2. Each of these dependencies will be evaluated in Section 6.3 through Section 6.8

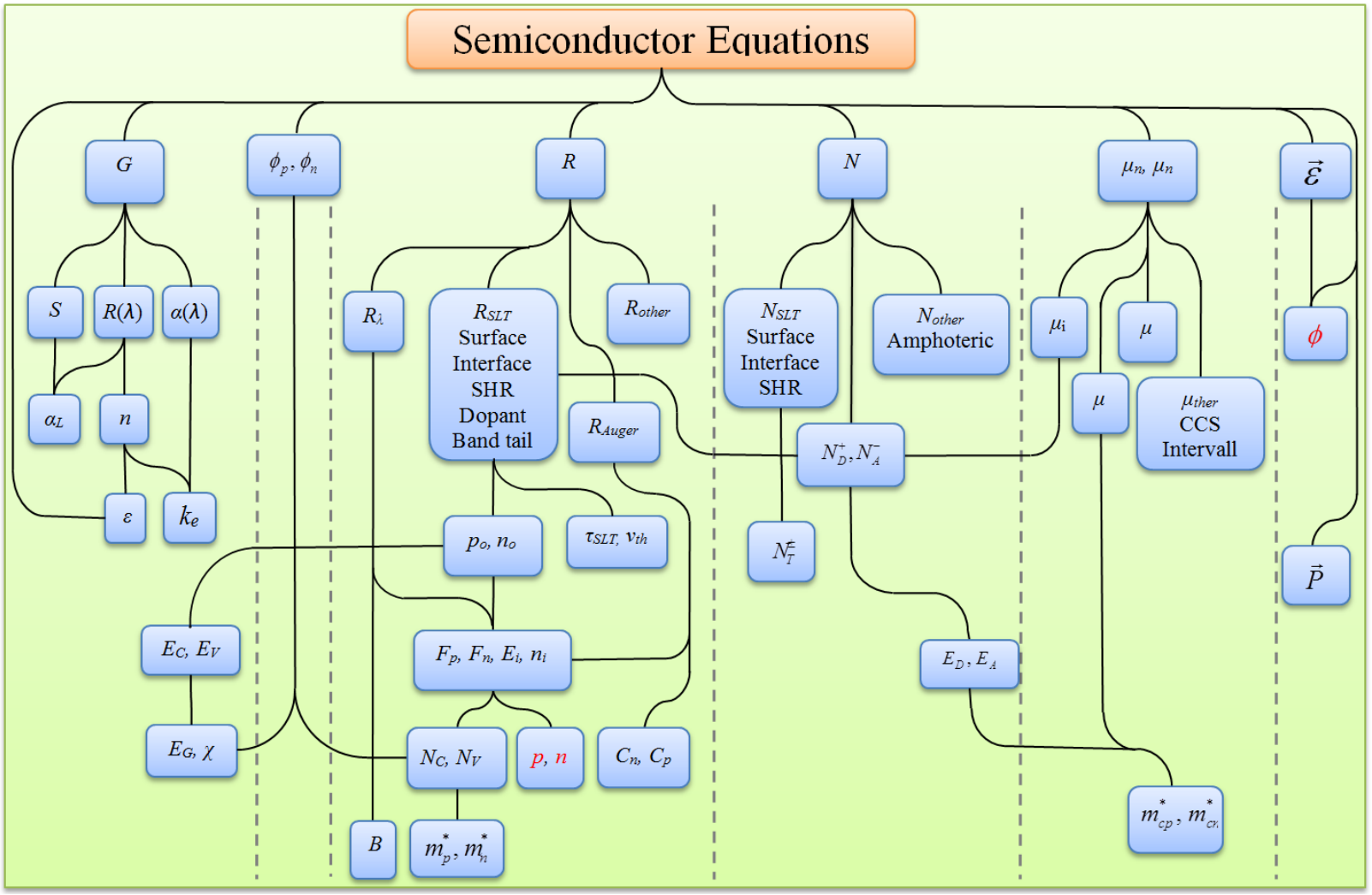

Figure 6.2. The substituent T dependent material parameter dependencies, are needed to solve the semiconductor equations. These parameters will be discussed in the following subsections.

In addition to the *T* dependencies, many of the material parameters have also been shown to be doping concentration (Figure 6.3), minority free carrier concentration (Figure 6.4) and electric field (Figure 6.5) dependent.

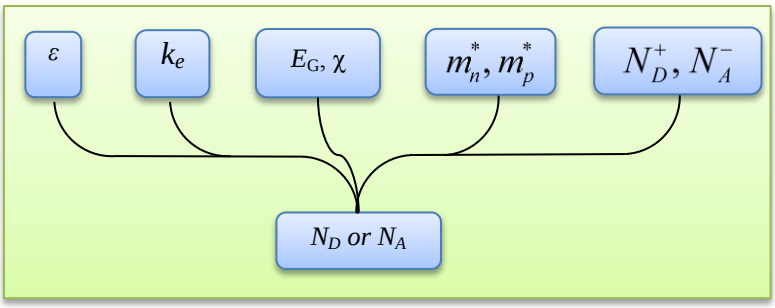

Figure 6.3. Doping dependent material parameters. The real and imaginary components of the dielectric constant are doping dependent. The bandgap, electron affinity, effective masses and ionized dopants will also vary with material doping.

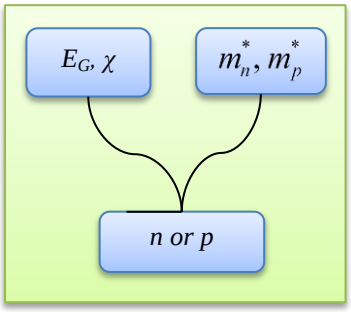

Figure 6.4. Minority free carrier concentration dependent material parameters, beyond the common dependencies. The bandgap, and effective masses will vary with material doping.

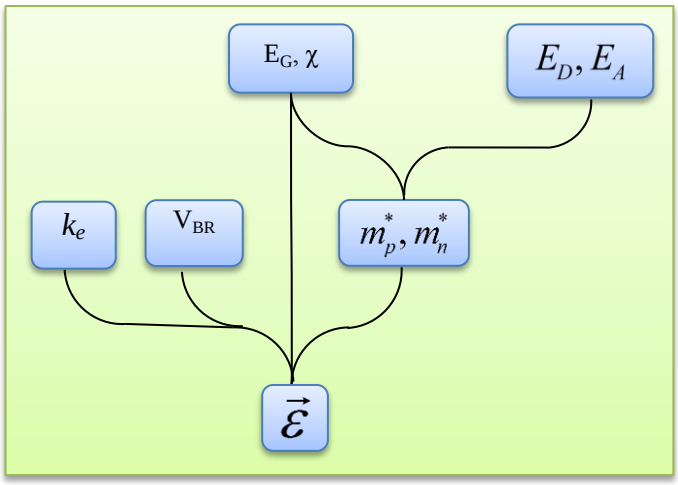

Figure 6.5. Electric field dependent material parameters. The electric field affects the imaginary component of the dielectric constant, the break down voltage, bandgap, electron affinity, effective masses and dopant ionization energies.

Each of these material parameters dependencies will be evaluated in Section 6.3 through Section 6.8. Where possible, the material parameter with more than one dependency will be combined. Care must be taken to avoid double counting a dependency.

6.2 The Semiconductor Equations

Solar cells and many other semiconductor devices are often modeled numerically using a set of equations referred to as the semiconductors equations. These equations model most semiconductor phenomena, such as carrier generation, carrier transport and carrier recombination. They also assume that the device is isothermal. The material parameters that are known to have temperature dependencies are shown in a blue font. The temperature dependencies of each parameter will be explored in the following sections. Most of the material parameters in the semiconductor equations are spatial varying. The equations found in this chapter can be found in a book chapter by Gray [27], in a thesis by Pinto [62] and a semiconductor book by SZE [63].

The first semiconductor equation is known as Poisson's equation, which relates electric field to the charge in the semiconductor.

$$\nabla \cdot (\varepsilon_s \vec{\mathcal{E}} + \vec{P}) = q(p - n + N) \tag{6.1}$$

Here ε_s is the dielectric constant, $\vec{\mathcal{E}}$ is the electric filed, $\vec{P}$ is the polarization and N_G is the net charge due to ionized dopants and other trapped charges.

The next two semiconductor equations are the hole and electron continuity equations. These equations relate the hole current, J_p, and the electron current, J_n, to the generation rate, *G*, hole recombination, R_p, and the electron recombination rate, R_n. They ensure that the electrons in the semiconductor are conserved.

$$\nabla \cdot \vec{J}_p = q\left(G - R_p - \frac{\partial p}{\partial t}\right) \tag{6.2}$$

$$\nabla \cdot \vec{J}_n = q\left(R_n - G - \frac{\partial n}{\partial t}\right) \tag{6.3}$$

Here *t* is time. In the proposed work the solar cells will be assumed to be operating in steady state, and therefore will not vary with time.

The last two semiconductor equations are the drift-diffusion equations; these equations related the drift and diffusion components of the current.

$$\vec{J}_p = -q\mu_p p \nabla \phi - kT\mu_p \nabla p \tag{6.4}$$

$$\vec{J}_n = -q\mu_n n \nabla \phi + kT\mu_n \nabla n \tag{6.5}$$

Here μ_p is the hole mobility, μ_n is the electron mobility and ϕ is the electrostatic potential. The band parameters ϕ_p and ϕ_n will be added to the drift terms, to model heavy doping effects and heterostructure solar cells [151, 152].

$$\vec{J}_p = -q\mu_p p \nabla\left(\phi - \phi_p\right) - kT\mu_p \nabla p \tag{6.6}$$

$$\vec{J}_n = -q\mu_n n \nabla\left(\phi + \phi_n\right) + kT\mu_n \nabla n \tag{6.7}$$

The total current at each point inside the solar cell with the displacement current density, $\vec{J}_{disp}$.

$$\vec{J} = \vec{J}_p + \vec{J}_n + \vec{J}_{disp} \tag{6.8}$$

$$\vec{J}_{disp} = \frac{\partial \varepsilon_s \vec{\mathcal{E}}}{\partial t} \tag{6.9}$$

The T dependency of each parameter in Equation (6.1) through Equation (6.9), highlighted in blue, will be examined in the following sections.

The semiconductor equations are coupled with differential equations. A number of numerical methods can be used to solve these equations; these include finite difference and finite element. Two value books that cover these methods are [61] and [60].

The simulator used in this work ADEPT [153] employed in this work simultaneously solves for the 3 independent variables n, p and the ϕ. In each iteration of the solution, the independent variables will be used with the material parameters to evaluate the semiconductor equations, until the desired convergence has been reached.

6.3 Generation Rate

The G term, is the generation of free electron and hole carriers caused by the absorption of photons in the solar cell. The thermal generations of carriers are included in the recombination terms in Section 6.4.

Equations (6.2) and Equation (6.3) need the photon induced generation rate of holes and electrons, which incorporates the Beer-Lambert law, at each point in the device, is

$$G(x) = (1-S)\int_{\lambda} \left(1-R(\lambda)\right)\Phi(\lambda)\alpha(\lambda)e^{-\alpha(\lambda)x}d\lambda \tag{6.10}$$

Here x is the position, S is the obscuration, which is also called shadowing, λ is the wavelength, $R(\lambda)$ is the reflectance and $\Phi(\lambda)$ is the photon flux density incident on the front surface of the solar cells.

One common method of modeling the absorption of photons in a material is the Beer-Lambert law, Equation (6.11), other methods of modeling the absorption include the wave or matrix methods.

$$T_{\lambda}(\lambda) = \frac{\Phi_2(\lambda)}{\Phi_1(\lambda)} = e^{-\alpha(\lambda)x} \tag{6.11}$$

Here T_λ is the transmission of light through a material, x is the distance between positions 1 & 2, $\Phi_1(\lambda)$ is the photon flux at position 1 in the material and $\Phi_2(\lambda)$ is the photon flux at position 2 in the material.

The sunlight that reaches the solar cells can either be thought of as particles or waves. The particles are called photons, which have an energy, E_p, that can be related to the wavelength of the photon.

$$E_p = \frac{hc}{\lambda} \tag{6.12}$$

The temperature dependencies of the S, $R(\lambda)$, $\alpha(\lambda)$, α_L and ε_S will be analyzed in the following subsections.

6.3.1 Obscuration

Any structure on the top surface of the solar cell can cause obscuration. Common types of obscuration are caused by the metal conducting layers, which include busbars and grid lines. These structures are made of optically thick metals, which block photons from entering the solar cell.

A diagram of the layers in a solar cell is shown in Figure 6.6.

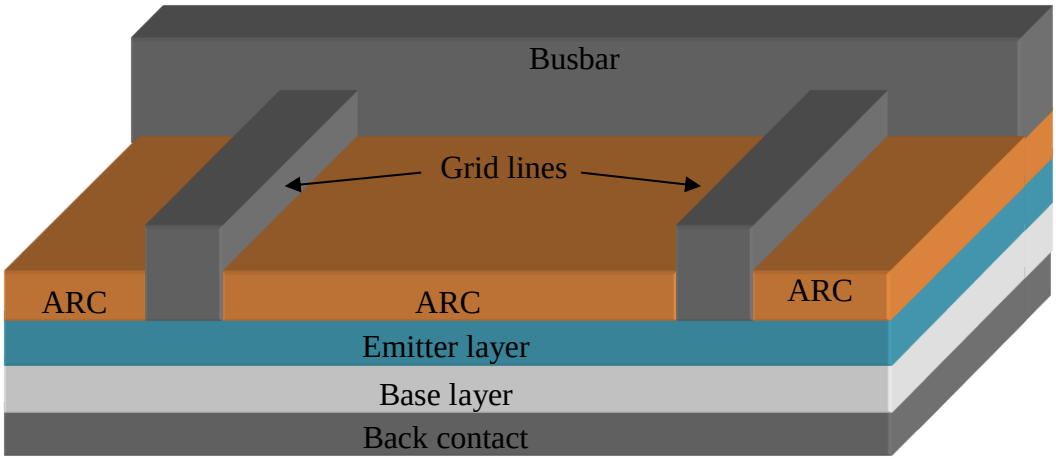

Figure 6.6. Diagram of a basic solar cell. Busbars and grid lines are added to solar cell to reduce the resistivity. Texturing [37] (not shown in figure) and ARCs are added to the top of the solar cells to reduce the reflectivity.

Any structures on the front surface that are covering the semiconductor material of the solar cell will affect the generation. Most solar cells are constructed with one or more large metal busbars for conducting current to the contacts. Grid lines and/TCL are used to conduct current out of the emitter layer. Anti-reflectance coatings (ARC) are used to reduce the reflectivity. The top surface is often textured, such as the world record Si solar cell [154], (not shown in figure) to further reduce the reflectance.

The total solar cell obscuration is therefore

$$S = S_B + S_G + S_{other}, \tag{6.13}$$

where S_B is the busbar obscuration, S_G is the grid line obscuration, and S_{other} is any other structure that is causing obscuration.

A significant amount of work has been done to reduce the obscuration. Some solar cells use a TCL with or in place of grid lines, to reduce the obscuration, such as the world record Copper Indium Gallium Selenide (CIGS) [155]. However TCLs can cause a small amount of absorption loss, particularly of high energy photons [156]. The grid line obscuration can be reduced by making the grid lines taller and narrower, which makes them more fragile. On some cells the grid lines are buried inside the semiconductor material [157], or eliminated entirely by placing the *p* and *n* contacts on the back of the

cell [158]. Reflective structure can be added on top of the grid lines, to reduce obscuration. In addition, CPV can be designed to avoid focusing light on the busbars [159].

The grid line obscuration is

$$S_G = \frac{N_G l_G w_G}{A_T}, \tag{6.14}$$

where l_G is the grid line length, w_G is the width of the grid lines and A_T is the total area of the solar cell. When the metal is optically thick, one of the only dependencies is the thermal expansion of the metal. The linear thermal expansion coefficient, α_L, of metal is defined as

$$\frac{\Delta w}{w_M} = \alpha_L (T_f - T_i), \tag{6.15}$$

where w_M is the initial metal width, Δw is the change in width, T_f is the final temperature and T_i is the initial temperature. If the change in thickness is large for the temperature range of interest, it could potentially increase the obscuration, and there by decrease the number of photons generated.

Aluminum is commonly used to make solar cell grid lines. It has a thermal expansion coefficient at 23 °C of 24×10^{-6} [°C $^{-1}$] [160], which means that the change in thickness will be 0.0024% of the initial width for a 100 °C temperature increase. This is much smaller than the uncertainty of the grid line width, and therefore will not significantly affect the obscuration. Other types of metals, such as Ag and Au, have similar thermal expansion coefficients [160]. The thermal expansion coefficient for a metal would need to be more than 50 times larger, before it would significantly affect the obscuration.

Any change in the grid line height will not affect the obscuration for solar cells exposed to normal incident irradiance, and that will not significantly affect the obscuration at other angles. The change in the length of a grid line can be significant; however the width of the grid line is small so the increase in length will not significantly affect the total obscuration.

The busbar obscuration is

$$S_B = \frac{A_B}{A_T}, \tag{6.16}$$

where A_B is the area of the busbars. As was the case with the grid lines, the busbars obscuration is not expected to change significantly with T_O or any other operating condition parameter.

6.3.2 Reflectivity

The reflectivity of the front surface of a solar cell depends primarily on the dielectric constant and thicknesses of the solar cell layers, as well as texturing. The reflectivity of a single interface with no texturing is

$$R = \frac{\bar{n}_2(\lambda) - \bar{n}_1(\lambda)}{\bar{n}_2(\lambda) + \bar{n}_1(\lambda)}. \tag{6.17}$$

The reflectivity of multiple layers can be calculated using the matrix method [161]. The absorption of the ARC can be included in the reflectivity calculations using the complex refractive index, $\bar{n}(\lambda)$.

$$\bar{n}(\lambda) = n_r(\lambda) - ik_e(\lambda) \tag{6.18}$$

The complex refractive index is composed of a real, $n_r(\lambda)$, and an imaginary part, $k_e(\lambda)$. The real part is

$$n_r(\lambda) = \frac{c}{\upsilon(\lambda)} = \frac{\lambda_0}{\lambda} = \sqrt{\varepsilon_r(\lambda)\mu_r(\lambda)}. \tag{6.19}$$

Here λ_0 is the wavelength of photon λ in a vacuum. The real portion of the refractive index is related to the wave propagation velocity, $\upsilon(\lambda)$, as well is the relative permittivity, $\varepsilon_r(\lambda)$, and the relative magnetic permeability, μ_r. Here $\varepsilon_s(\lambda) = \varepsilon_r(\lambda)\varepsilon_0$, where ε_0 is the permittivity in a vacuum, and $\mu_s(\lambda) = \mu_r(\lambda)\mu_0$, where μ_o is the magnetic

permeability in a vacuum. The imaginary portion of the refractive index is the extinction coefficient, and is directly related to the absorption coefficient, $\alpha(\lambda)$.

$$\alpha(\lambda) = \frac{4\pi k_e(\lambda)}{\lambda} \tag{6.20}$$

Since the reflectivity depends on the thicknesses of all of the layers in a solar cell, a change in thickness of these layers will change the reflectivity. The thermal coefficient of Si near the operating temperature is $2.6\text{x}10^{-6}$ [K^{-1}] and a thick Si base layer is 500 um, the thickness of the base layer will change by 130 nm which might be enough to affect the reflectivity. The emitter and ARC layers tend to be much smaller [154]. A 50 nm layer of Si would change by 0.013 nm, which is small enough that it might not be significant.

The temperature dependence of the real portion of the dielectric constant will be covered in section 6.3.2.1, and the imaginary portion will be covered with the absorption, in section 6.3.3.

6.3.2.1 Dielectric constant temperature dependence

There are two primary uses for the ε_S. One is the reflectance and the other use is with the ε_S in Equation (6.1). In this work, the measured reflectance on a similar solar cell will be used for the reflectance in the numerical model. Not only is the ε_S both λ and T dependent, it has also been reported that it is doping, minority free carrier concentration and electric field dependent. The ε_S has been fit over T using the same equation used by Varshni for the E_G, which will be discussed in Section 6.3.4.1 [162].

$$\varepsilon_S = \varepsilon_S(0) + \frac{\alpha_S T^2}{\beta_S + T} \tag{6.21}$$

Here $\varepsilon_S(0)$ is the dielectric constant at zero K, α_S and β_S are coefficients. The measured dielectric constant temperature dependence for Si at 300 K is 11.97 with a linear temperature coefficient of $\frac{d\varepsilon_s}{dT} = 9.3\text{x}10^{-4}$ [K^{-1}] near 300 K [162].

6.3.3 Photon Absorption

As described in section 6.3, the absorption of photons in a material is affected by the thickness of the solar cell and the absorption coefficient. The change in the base material thickness caused by the change in temperature, calculated in section 6.3.2, is small enough that it should not significantly affect the absorption of photons in the solar cell. The absorption coefficient on the other hand, can change significantly over the temperature range of interest. In addition to the temperature, the absorption coefficient is also affected by the doping concentration (Section 6.3.4.2), minority free carrier concentration and electric field of the material (Section 6.3.4.3).

Each of the operating conditions that affected the $\alpha(\lambda)$ can either be measured, or they can be estimated by using semi-empirical and analytical expressions.

6.3.3.1 Absorption coefficient temperature dependence

Generally the $\alpha(\lambda)$ will increase as the temperature increases. This will typically increase the number of photons that are absorbed. The most significant change will occur to photons near the bandgap energy. Photons at energies that would pass through the device at lower T can now be absorbed. The T dependent increase in the $\alpha(\lambda)$ of the layers above the emitter and base (absorber layers) of the solar cell can reduce the number of photons that reach the solar cell.

The $\alpha(\lambda)$ and the electrical E_G are related by the energy it takes to move an electron from the valence band to the conduction band. The optical bandgap energy, E_λ, [163] can be estimated from the $\alpha(\lambda)$, it can also be estimated from the Internal Quantum Efficiency (IQE) or External Quantum Efficiency (EQE) [164]. In most materials these two energies will be very similar. In materials with large band tails, such as amorphous Si, the E_λ and E_G can be different. A small difference between the E_λ and E_G Si bandgap narrowing has been measured by van Overstraeten [165]. These materials can have a low density of states, in the band tails, below the conduction band energy and

above the valence band energy. Because of the low density of states, the electrons and holes will conduct at energy levels that are significantly larger, than the E_λ. This makes it possible for a material to have a $\alpha(\lambda)$ with a lower E_λ, than the E_G.

In addition to the three common methods that material parameter dependencies parameters can be included in the detailed numerical model, discussed in Section 6.1, the $\alpha(\lambda)$ can be adjusted using a shifting method described in Sections 6.3.3.1.1 and B.1.3. This is possible due to the way that the $\alpha(\lambda)$ increases as a function of T_O.

6.3.3.1.1 Shifting the photon absorption

The $\alpha(\lambda)$ shift caused by the change in the temperature dependent bandgap is

$$\alpha(E_2) = \alpha(E_1 + \Delta E_{\lambda,T}). \tag{6.22}$$

Here E_1 is the initial energy at one T_O, E_2 is the shifted energy at another T_O. and $\Delta E_{\lambda,T}$ is the T dependent E_λ narrowing.

For most materials the $\Delta E_{\lambda,T}$ is close enough to the T dependent EG narrowing, $\Delta E_{G,T}$, that it can be used to shift the $\alpha(\lambda)$. In more careful calculations, the $\Delta E_{\lambda,T}$ or the measured $\alpha(\lambda)$ could be used. A method for determining the E_λ based on the $\alpha(\lambda)$ was described by Smestad [166].

6.3.3.1.2 Temperature dependent photon absorption coefficient

The intrinsic Si $\alpha(\lambda)$ temperature dependence has been measured over a wide range of photon energies [167, 168] and near the band edge. Additional temperature dependence measurements of intrinsic Si are reported in a paper by Trupke and Green [121].

The measured $\alpha(\lambda)$ data near the band edge will be combined with the absorption data over a large photon energy range. This combined absorption will then be adjusted to account for the change in temperature.

6.3.3.1.3 Doping dependent photon absorption coefficient

In addition to the temperature dependence, the doping concentration and electric field will also affect the photon absorption near the band edge. The doping dependent effect on $\alpha(\lambda)$ has been published [169].

6.3.3.1.4 Semi-empirical method

A semi-empirical $\alpha(\lambda)$ model has been published that includes the E_G and phonon energies [170] [171]. The fundamental photon absorption in direct bandgap materials is

$$\alpha(h\nu) = A_\alpha \sqrt{(h\nu - E_G)}, \tag{6.23}$$

here A_α is a constant and the $h\nu$ is the energy of the photon.

The fundamental absorption in indirect bandgap materials is the sum of the phonon assisted photon absorption coefficient, α_a, and the phonon emission photon absorption, α_e [170].

$$\alpha(h\nu) = \alpha_a(h\nu) + \alpha_e(h\nu) \tag{6.24}$$

Photon absorption process that absorbs a phonon is

$$\alpha_a(h\nu) = \frac{A_\alpha \left(h\nu - E_G + E_{ph}\right)^2}{e^{E_{ph}/kT} - 1}, \tag{6.25}$$

here E_{ph} is the energy of the phonon. And the photon absorption process that emits a phonon is

$$\alpha_e(h\nu) = \frac{A_\alpha \left(h\nu - E_G - E_{ph}\right)^2}{1 - e^{-E_{ph}/kT}}. \tag{6.26}$$

While this $\alpha(\lambda)$ model could be used in the detailed numerical model, it over simplies the $\alpha(\lambda)$. It is helpful in understanding the T dependent $\alpha(\lambda)$ of direct bandgap materials and indirect bandgap materials.

6.3.4 Electrical Bandgap Energy and Electron Affinity

The electrical E_G electron affinity, χ, are important parameters in the detailed numerical model. The E_G is defined as the difference between the conduction band energy level, E_C, and the valance band energy level, E_V.

$$E_G = E_C - E_V \tag{6.27}$$

Between these two energy levels there is a gap of energy level that electrons cannot have due to quantum mechanics.

The dependencies of the E_G are

$$E_G = E_G(0) - \Delta E_G - \Delta E_{G,D} - \Delta E_{G,C} - \Delta E_{G,S} - \Delta E_{G,F-K} - \Delta E_{other}, \tag{6.28}$$

where $E_G(0)$ is the bandgap at 0 K, $\Delta E_{G,T}$ is the temperature dependent E_G change from 0 K, $\Delta E_{G,D}$ is the doping dependent E_G narrowing, $\Delta E_{G,C}$ is the minority free carrier concentration dependent E_G narrowing, and $\Delta E_{G,S} + \Delta E_{G,F-K}$ are the stark and Franz-Keldysh electric-field E_G narrowing effects. In this work, it will be assumed that the bandgap narrowing affects are independent of each other. The dependencies of each of these terms will be discussed in the following sections.

The χ is defined as the energy difference between the vacuum energy level, E_0 and the conduction band energy level at 0 K, $E_C(0)$.

$$\chi = E_0(0) - E_C + \Delta E_C \tag{6.29}$$

Each of the E_G dependency terms in Equation (6.28) may affect the change of the conduction band energy level dependencies, ΔE_C, and the valence band energy level dependencies, ΔE_V. This is particularly important in a hetro-junction device if most of the narrowing occurs in the conduction band in one material and most of the narrowing occurs in the valance band of the other material. This will cause the χ of each material to change differently, even if the E_G was the same in both materials before the narrowing. The χ could also be affected by the dependencies of $\Delta E_{G,D}$, $\Delta E_{G,C}$, $\Delta E_{G,S}$ and $\Delta E_{G,F-K}$ of both hetro-junction and homo-junction devices. In this work the narrowing will be evenly split between the ΔE_C and the ΔE_V.

The following four sub-sections will discuss the bandgap energy, doping dependent bandgap narrowing, stark effects and electron affinity in more detail.

6.3.4.1 Temperature dependent bandgap energy narrowing

For most semiconductors materials as the temperature goes up the conduction and valence band energy levels broaden, causing the bandgap to narrow. There are a wide variety of semi-empirical and physics based functions for the bandgap energy over temperature [172, 173]. Some of these models have been developed for specific types of materials. Often temperature ranges will be included for a set of coefficients. These fits are discussed in Appendix F. Figure 6.7 shows the variety of Si curve-fits available. The fits are plotted over their recommended T ranges. Experiments show that at low temperatures many materials are nearly temperature independent [98].

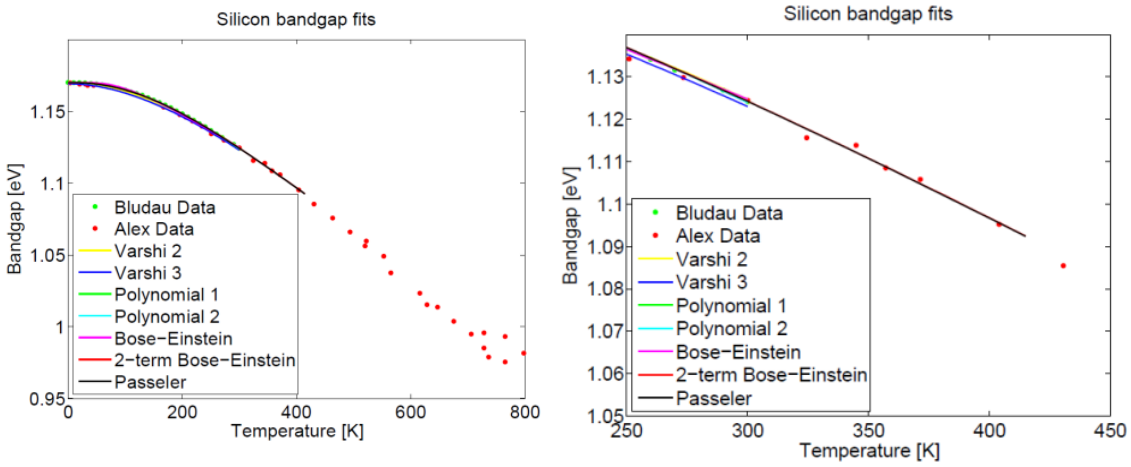

Figure 6.7. Si bandgap energy over a wide range of temperatures (left) and near the operating temperature range of interest [98, 99, 103, 168, 172, 173]. Fits are plotted over their recommended temperature ranges. The red and black lines are almost identical over the temperature range of interest.

The T dependence of the Si E_G has been measured by Macfarlane [174], Haynes [175] and Shaklee [176], and more recently by Alex [98] and Bludau[99]. The 2-term

Bose-Einstein and Pässler's equations fit the data well in the T range of interest. The other curve-fits could be adjusted to be valid over the T range of interest. All of the equations except for Varshni 3 are nearly the same near 300 K.

6.3.4.2 Doping and minority carrier dependent bandgap energy narrowing

The doping dependent bandgap narrowing, which is also referred to as shrinkage or bandgap shift, has been measured and modeled by a number of research groups, for n-type Si [177, 178], with a curve-fit by Slotboom [179].

The doping dependent bandgap narrowing curve-fits, $\Delta E_{G,D}$, will be included in the parameter framework with the T dependent parameters. For donor doped regions,

$$\Delta E_{G,D} = 0.321x10^{-3}\left(\frac{N_D}{1.45x10^{10}}\right)^{1/4}, \tag{6.30}$$

there is a similar fit for acceptor doped regions

Solar cells that operate at 1 sun solar concentration, such as the solar cell being modeled in this work, typically have minority free carrier concentrations that are less than $1x10^{17}$ cm^3. This is below the range where the minority free carries will significant reduce the E_G. Solar cells that operate at higher solar concentrations could go above this value. Also, if the majority carrier concentration approaches the doping concentration, it will likely affect the doping dependent bandgap narrowing

6.3.4.3 Electric field dependent bandgap effects

In addition to the T and doping, the bandgap is also affected by the $\vec{\varepsilon}$ dependent Stark and Franz-Keldysh effects [170]. This can affect the optical and transport properties, in regions of the semiconductor with very high $\vec{\varepsilon}$. In a solar cell operating near the maximum power point, there is typically a large $\vec{\varepsilon}$ in the depletion region and near other types of junctions such as the BSF. Because this only occurs in a narrow region of the solar cell, it has a very small affect on the device performance.

The first-order Stark Effect is eccentricity of the electron orbit, d.

$$\Delta E_{G,S} = qd\vec{\mathcal{E}} \tag{6.31}$$

The Franz-Keldysh Effect accounts for the average distance that electrons travel above the bandgap, when the band edges are tilted.

$$\Delta E_{G,F-K} = \frac{3}{2}\frac{\left(q\hbar\vec{\mathcal{E}}\right)^{2/3}}{\left(m_d^*\right)^{1/3}} \tag{6.32}$$

Here m_d^* is the density of state effective mass, which will be discussed in Section 6.4.1.3.

6.3.4.4 Electron affinity

Since the E_G decreases as the temperature increases, either E_C, E_V or both will change as the temperature increases. In homo-junction solar cells the χ will not be affected by $\Delta E_{G,T}$, since any relative change will be the same in each layer of the solar cell. However, the other E_G narrowing effects could affect the band gap on both sides of the junction differently and therefore could cause the χ to change. If the χ changes differently on each sides of the junction, it will create E_C and E_V offsets at the junction in the homo-junction devices, as well as change the offsets in the hetero-junction devices.

One way to measure the χ, is using the barrier height in a metal-semiconductor junction. The use of this measurement is complicated by the fact that the barrier can be lowered by other effects such as carrier imaging. Groups have measured the Si barrier height lowered to be -0.623 meV/K [180] and -0.24 meV [181] also [182], used as a fitting parameter. The T dependent E_G narrowing is often assumed to be evenly split between the E_C and E_V [66].

6.3.5 Additional Generation Effects

The solar cell generation can be further reduced by additional loss mechanisms. One of these mechanisms is absorption in dead layers. These layers can occur in the emitter

layer, between the emitter and the passivation or ARC layer. If the Si [183] or GaAs [184] Fermi energy is pinned at this interface, it can create a well, from which it is difficult for generated carriers to escape. The absorption in these layers will depend on the *T*, as well as other factors. This will cause a *T* dependent reduction of the high energy photons that are absorbed by the solar cell and contribute to the J_{SC}. This can be seen as a reduction in the EQE and IQE for higher energy photons.

6.4 Recombination Rate

After electrons and holes are generated by photon absorption they can be lost through a variety of recombination mechanisms in solar cells. Electrons and holes can be thermally generated through a similar process. Detailed numerical modeling of solar cells is a useful tool because it not only incorporates the amount of each type of recombination happening inside the solar cell, but also the spatial location of that recombination.

Some types of recombination can occur throughout the device, such as radiative, R_{λ}, Shockley-Read-Hall (SHR), R_{SHR} and Auger, R_{Auger}. Other types of recombination occur to specific regions, such as surface recombination, R_S, at surface traps or interface recombination, R_I, at interface traps. In addition to these common recombination mechanisms, there are also other types of recombination, R_{other}, that occur in certain types of solar cells, these recombination mechanism include amphoteric dopants, and band tails.

The total recombination at each point in the device is

$$R_T = R_{\lambda} + \left[\sum_{traps} R_{SLT} \right] + R_{Auger} + R_{other} \quad (6.33)$$

The single layer traps will be defined to include the SHR recombination, surface recombination, interface recombination, dopant recombination and recombination in the band tails.

Each of the recombination mechanisms has n and p terms, so they are inherently doping density and minority free carrier concentration dependent. The coefficient of each equation can have additional dependencies, which will be discussed in the following sections.

The semiconductor equations (Equations (6.2) and (6.3)) need R_p and R_n. Often it is assumed that $R_p = R_n = R_T$, however the recombination coefficients for hole and electrons are not always the same.

6.4.1 Radiative Recombination

Radiative recombination occurs when a free electron in the conduction band recombines with a free hole in the valence band and emits a photon. As discussed in Section 4.2.2, this occurs often in direct bandgap materials and less frequently in indirect bandgap materials, with the help of a phonon. Each term in the radiative recombination equation, Equation (4.4), is T dependent.

The T dependence of B has been measured by multiple groups. Measurements by Varshni [118, 119] and by Michaelis [185] indicated that B increases with T in Si. While latter measurements by Trupke [121] and by Schlangenotto [120] indicated that the B decreased as the T increased. It has been reported that the change is due to the more precise n_i values available [121]. Cases in which B increases and decrease, can be simulated, however, because Si is an indirect bandgap material, it will have a smaller effect on the overall T dependent performance than SHR and Auger recombination.

6.4.1.1 Carrier concentration

The p can be defined as the difference between the intrinsic Fermi energy, E_i, and the quasi Fermi energy for holes, F_p.

$$p = n_i e^{(E_i - F_p)/kT} \tag{6.34}$$

The n_i was defined in Equation (4.16). The n can be defined in terms of the quasi Fermi energy for electrons, F_n.

$$n = n_i e^{(F_n - E_i)/kT} \tag{6.35}$$

These equations illustrate the T dependent relationship between the carrier densities and the Fermi energies.

The parameters n, p, F_p, F_n and E_i can be calculated using the physics based analytical expressions in the next three sections. A voltage bias will cause the quasi Fermi energy levels, F_n and F_p, to split. In the case of a solar cell the voltage bias is caused by the light induced generation.

The analytical expressions for the F_n and F_p, are

$$F_n = E_i - kT \ln\left(\frac{n}{n_i}\right) \tag{6.36}$$

$$F_p = E_i + kT \ln\left(\frac{p}{n_i}\right). \tag{6.37}$$

The numerical model solves for the F_n and F_p as a function of x, in addition to ϕ. The n and p are found by using Fermi-Dirac statistics.

6.4.1.2 Intrinsic carrier concentration

When the solar cell is in equilibrium $F_n = F_p = E_i$. The n_i is defined in Equation (4.16) and the E_i is defined as

$$E_i = \frac{E_G}{2} + \frac{kT}{2} \ln\left(\frac{N_V}{N_C}\right) \tag{6.38}$$

The N_V was defined in Equation (4.17) and the N_C was defined in Equation (4.19), where $m^*_{d,c}$ is the electron density of state effective mass, and $m^*_{d,v}$ is the hole density of state effective mass respectively.

6.4.1.3 Density of state effective mass

Electrons inside of solid state materials, such as semiconductors will interact with the crystal lattice. Quantum mechanical effects will cause the electrons to move differently in the semiconductor than they would in a vacuum. These effects can be included in a semi-classical model using an effective mass, m^*. The m^* is therefore expected to be affected by the T, doping density, minority free carrier concentration and the electric-field. It will be different for electrons and holes, it can also be different when used to calculate the density of states, the thermal velocity and the mobility. In addition, the m^* can be affected by the direction the electrons are flowing through the crystal.

The thermal velocity effective masses, $m^*_{th,n}$ and $m^*_{th,p}$, will be discussed in Section 6.4.2.2.

The m^*_d is defined as

$$\frac{1}{m^*_d} \equiv \left[\frac{d^2E}{dp^2}\right] = \frac{1}{\hbar^2}\frac{d^2E}{dk^2} \tag{6.39}$$

The density of states effective mass for electrons in the conduction band, $m^*_{d,c}$, depends on the curvature of the conduction E-k bands and the density of state effective mass for hole in the valence band, $m^*_{d,v}$, depends on the curvature of the valence E-k bands.

The $m^*_{d,c}$ is defined as

$$m^*_{d,c} = 6^{2/3}\left(m_t^{*2} m_l^*\right)^{1/3}, \tag{6.40}$$

where 6 is the number of elliptical orbitals in Si, m^*_t is the transverse effective mass and m^*_l is the longitudinal effective mass. The m^*_t has a measured T dependence [92],

$$m^*_t = 0.1905 m_O \frac{E_G(0)}{E_{G,T}}. \tag{6.41}$$

The m^*_l is only weakly T dependence [92],

$$m_l^* = 0.9163 m_O . \tag{6.42}$$

The $m_{d,v}^*$ is defined as

$$m_{d,v}^* = \left(m_{lh}^{*\,3/2} + m_{hh}^{*\,3/2} + \left[m_{so}^* \exp\left(-\frac{\Delta E_S}{kT} \right) \right]^{3/2} \right)^{2/3}, \tag{6.43}$$

where m_{lh}^* is the effective mass of holes in the light hole band, m_{hh}^* is the effective mass of holes in the heavy hole band, m_{so}^* is the effective mass of holes in the split off band and ΔE_S is the split off band energy difference.

The T dependence of $m_{d,v}^*$ has been captured by a semi-empirical curve-fit [92],

$$m_{d,v}^* = m_O \left(\frac{a + bT + cT^2 + dT^3 + eT^4}{1 + fT + gT^2 + hT^3 + iT^4} \right)^{2/3}, \tag{6.44}$$

where, a through i are coefficients of the curve-fit.

While it is likely that the $m_{d,c}^*$ and $m_{d,v}^*$ are dependent on doping density, minority free carrier concentration and the electric-field. Including these effects could lead to double counting, since it is unlikely that they were included when the dependences of other parameters were determined.

6.4.2 Single Level Traps

The total trap recombination at each position in the bulk of the devices can be found by integrating over the trap energies. Single level traps can be defined to include surface, interface, SHR, dopant and band tail recombination,

$$R_{SLT} = \frac{pn - n_i^2}{\tau_{SLT,n}\left(p + p_T\right) + \tau_{SLT,p}\left(n + n_T\right)}, \tag{6.45}$$

where $\tau_{SLT,n}$ is the single level trap lifetime for electrons, $\tau_{SLT,p}$ is the single level trap lifetime for holes, n_T is the filled single level electron trap concentration, p_T is the empty single level hole trap concentration.

$$n_T = n_i e^{(E_T - E_i)/kT} \tag{6.46}$$

$$p_T = n_i e^{(E_i - E_T)/kT} \tag{6.47}$$

In low level injection, the p-type ($p \approx p_o >> n_o$) and the n-type ($n \approx n_o >> p_o$) the single layer traps recombination is [171]

$$R_{SLT} \approx \frac{n - n_o}{\tau_{SLT,n}} \quad \text{for p-type material} \tag{6.48}$$

$$R_{SLT} \approx \frac{p - p_o}{\tau_{SLT,n}} \quad \text{for n-type material} \tag{6.49}$$

The equilibrium electron concentration, n_o, and the equilibrium hole concentration, p_o, are,

$$n_o = N_C e^{(E_F - E_C)/kT} \tag{6.50}$$

$$p_o = N_V e^{(E_V - E_F)/kT}, \tag{6.51}$$

where E_F is the equilibrium quasi Fermi energy for electrons and holes.

In high level injection ($p \approx n >> p_o, n_o$)

$$R_{SLT} \approx \frac{n}{\tau_{SLT,n} + \tau_{SLT,p}} \approx \frac{p}{\tau_{SLT,n} + \tau_{SLT,p}} \tag{6.52}$$

The $\tau_{SLT,n}$ and $\tau_{SLT,p}$ are defined in Equation (4.33). If N_T, v_{th} or σ increases, the lifetime will decrease. The v_{th} will be defined in Equation (6.53). In this work it will be assumed that σ and N_T are temperature independent. It is possible that the σ is temperature dependent [186].

The $\tau_{SLT,n}$ and $\tau_{SLT,p}$ are strongly doping dependent; this is due to the relationship between dopants and defect traps. In this work, the doping density will be used to determine the τ_{SHR} at 25 °C [187]. The value of σN_T will be determined at 25 °C, using a calculated value of v_{th} at 25 °C. The value of σN_T will then be used with v_{th} to determine the τ_{SHR} at other temperatures.

6.4.2.1 Thermal velocity

The mean free path thermal velocity is defined as

$$v_{th,n} = \sqrt{\frac{3kT}{m^*_{th,n}}} \tag{6.53}$$

The $m^*_{th,n}$ has been defined as [188]

$$m^*_{th,n} = \frac{4m^*_l}{\left[1+\sqrt{\left(m^*_l / m^*_t\right)}\,\frac{\sin^{-1}(\delta)}{\delta}\right]^2}, \tag{6.54}$$

where $\delta = \sqrt{\left(m^*_l - m^*_t\right)/m^*_l}$.

The $v_{th,n}$ and $v_{th,p}$ used in this model was based on a published paper by Green which show that the $m^*_{t,n} = 0.28m_O$ and $m^*_{t,p} = 0.41m_O$. These parameters are nearly temperature independent near 300 K [92]. They were characterized based on the average thermal velocity, Equation (6.55), which has the same temperature dependence as Equation (6.53).

$$v_{th,n} = \sqrt{\frac{8kT}{\pi m^*_{t,n}}} \tag{6.55}$$

6.4.2.2 Surface and interface recombination

There can be additional recombination on the outside surfaces of a solar cell and at material interfaces inside the solar cell. These types of recombination will be including using the single level trap methodology, Equation (6.45). Equations (6.48) and (6.49) can be used when the solar cell is operating in low-level injection.

When electrons are the minority carrier the surface recombination

$$R_S \approx S_n\left(n - n_o\right), \tag{6.56}$$

and the surface recombination velocity for electrons is

$$S_n = \sigma_{S,n} v_{th,n} N_{ST,n}. \tag{6.57}$$

This will be the same for holes. Here S_n and S_p are the surface recombination velocity for electrons and holes, $N_{ST,n}$ and $N_{ST,p}$ are the surface density of trap states for electrons and holes, and $\sigma_{S,n}$ and $\sigma_{S,p}$ are the capture cross sections for electrons and holes. The T dependence of $v_{th,n}$ and $v_{th,p}$ can be included in a similar manner as $\tau_{SLT,n}$ and $\tau_{SLT,p}$, in Section 6.4.2.

The measured Si doping dependent surface recombination rate varies between $1x10^2$ [cm/s] and $6x10^4$ [cm/s] [131]. The measured doping dependent surface recombination rate for GaAs also increases with doping concentration [189].

The surface recombination occurs on all of the outside surfaces of the solar cell, this includes the top, bottom and sides. Passivation coating layers are applied to reduce the recombination at the surfaces. A SiO_2 passivation layer on Si can reduce the surface recombination rate to 0.5 [cm/s] [131]. The 1-D model in this work will only include the top and bottom surface recombination.

6.4.3 Auger Recombination

Auger recombination is an intrinsic carrier recombination mechanism in semiconductor devices. It occurs when one carrier transfers its energy to another carrier. The first carrier then recombines with an opposite carrier. The second carrier then losses the extra energy as it thermalizes to the band edge, shown in Equation (4.6).

The T dependence of the Auger recombination coefficient has been measured for Si. The Si Auger recombination rates are [133] and [131]

$$C_n = 1.1x10^{-30}\left(\frac{T}{300}\right)^{0.5} \tag{6.58}$$

$$C_p = 0.3x10^{-30}\left(\frac{T}{300}\right)^{0.5} \tag{6.59}$$

The total Auger recombination coefficient, C, is

$$C = C_n + C_p . \tag{6.60}$$

Measurements have shown that the C_n and C_p coefficients are doping dependent [190]. While there is significant scatter in the data, the C_n and C_p coefficients appear to be constant for n and p values below $1x10^{18}$ [cm^{-3}]. Therefore, this will be more important in concentrator solar cells which operate with higher values of n and p.

6.5 Net Charge

The non-carrier net charge inside of a semiconductor is a combination of many different fixed charges.

$$N = N_D^+ + N_A^- + \left[\sum_{traps} N_{SLT}\right] + N_{it} + N_s + N_{other} \tag{6.61}$$

The components of the net charge are:

$N_D{}^+$, the concentration of electrically active donor atoms

$N_A{}^-$, the concentration of electrically active acceptor atoms

N_{SLT}, the concentration of charge in SLT recombination sites

N_{it}, fixed interface charges

N_S, fixed surface charges

N_{other}, other fixed charges

The SLT charge includes all SLT traps, such as SHR, surface and interface. Other charges may be specific to a material system, such as material defects and additional fixed charges.

6.5.1 Ionized Donor and Acceptor atoms

Donor and acceptor atoms are added to a semiconductor to create an excess number of holes or electrons, these regions are commonly referred to as p-type or n-type. The concentration of donor atoms is N_D and the concentration of acceptor atoms is N_A. The concentration of ionized atoms is T dependent. As the T goes up, the concentration of

ionized atoms will also go up. In this work, only shallow energy levels will be considered.

The concentration of ionized donors is given by

$$N_D^+ = \frac{N_D}{1 + g_D e^{\left(\frac{E_F - E_D}{kT}\right)}} \tag{6.62}$$

Here N_D^+ is the ionized doping concentration for donors, E_D is the energy level of the donor states and g_D is the donor impurity level degeneracy factor, which is 2 for the spin up and spin down states.

The concentration of ionized acceptors is given by

$$N_A^- = \frac{N_A}{1 + g_A e^{\left(\frac{E_A - E_F}{kT}\right)}} \tag{6.63}$$

Here N_A^- is the ionized doping concentrations for acceptors, E_A is the energy level of the acceptor states and g_A is the acceptor impurity level degeneracy factor, which is 4 for the spin up and spin down states of the two degenerate valence bands. When a device is in high-level injection the split-off band can also be included.

6.5.1.1 Donor and acceptor energy levels

The dependencies of E_D and E_A can defined relative to the E_C and E_V respectively. The E_D and E_A are affected by T and $\vec{\mathcal{E}}$. The $\vec{\mathcal{E}}$ dependency can be included using the Stark effect bandgap narrowing.

The T dependency of the donor and acceptor impurity energy levels can be estimated by using the Bohr Theory Hydrogen Atom Model [63].

$$E_H = \frac{m_0 q^4}{32\pi^2 \varepsilon_0^2 \hbar^2} \tag{6.64}$$

This physics based analytical expression can be used with other elements by using the effective mass. The ionization energy for a donor is [63].

$$E_D = \left(\frac{\varepsilon_0}{\varepsilon_s}\right)^2 \left(\frac{m^*_{c,n}}{m_0}\right) E_H \tag{6.65}$$

Where $m^*_{c,n}$ is the conductivity effective mass for electrons. The ionization energy for an acceptor will be similar to a donor.

The calculated E_D and E_A will give answers that are on the same order of magnitude as the measured energy difference. These values could be further corrected by adding a scaling coefficient, which is matched to a measurement at a specific T_O. Then the T dependence could be estimated more accurately at different T_O. In this work it will be assumed that the thermal velocity and conductivity effective masses are equivalent. Due to the likelihood of double counting a measured dependence of other material parameters, these equations will not be included in this work.

6.5.2 Single Level Trap and Fixed Charges

There are a variety of other types of charge in semiconductor devices, these include traps and fixed charges. The various traps can fill and empty depending on the Fermi energy level. The fixed charges are often near or inside of a layer, such as an oxide, interface or defect layer.

The charge contribution of, N_{SLT}, from surface, interface, SHR, dopant and band tail are included, using the probability, P_T, that these traps are occupied.

$$N_{SLT} = P_T N_T \tag{6.66}$$

No additional fixed interface or surface will be included in the Si model.

6.6 Carrier Mobility

As was the case with recombination, there are a variety of scattering mechanisms that affect the carrier mobility, μ, of both electrons, μ_n, and holes, μ_p. The Matthiessen rule is a first-order approximation of the total mobility.

$$\frac{1}{\mu} = \frac{1}{\mu_L} + \frac{1}{\mu_{ii}} + \frac{1}{\mu_{POP}} + \frac{1}{\mu_{other}} \tag{6.67}$$

Common types of scattering mechanisms that reduce the mobility include acoustic phonon scattering, μ_L, also called lattice scattering and ionized impurity scattering, μ_{ii}. Polar-optical-phonon scattering, μ_{POP}, is important in polar semiconductors such as GaAs. Other types of scattering include carrier-carrier scattering, intervalley scattering, neutral impurity and piezoelectric scattering.

The theoretical dependencies of the common scattering mechanisms will be covered in Section 6.6.1. Section 6.6.2 examines the μ that is used in the detailed numerical model and which is compared to measured data.

6.6.1 Theoretical Mobility

Acoustic phonon scattering occurs when carriers are scattered by the phonons traveling through the atomic lattice. As the T increases, the number of phonons and therefore scattering events will increase. This will cause the μ_L to decrease as the T increases.

The μ_L has been defined as [191]

$$\mu_L = \frac{\sqrt{8\pi} q \hbar^4 C_l}{3 E_{ds}^2 m_c^{*5/2} (kT)^{3/2}} \quad \propto \quad \frac{1}{m_c^{*5/2} T^{3/2}}. \tag{6.68}$$

Here, C_l, is the average longitudinal elastic constant of the material, and E_{ds}, is the change of the band edge over the dilation of the lattice. The known T dependence is shown to the right of the equations.

Ionized impurity scattering occurs when carriers are scattered by ionized dopant atoms in the atomic lattice. As the number of dopant atoms increases the μ_{ii} will go down. However as the T increases, the time that each dopant atom interacts with the carrier decreases which will cause the overall μ_{ii} to go up.

The μ_{ii} has been defined as [192]

$$\mu_{ii} = \frac{64\sqrt{\pi}\varepsilon_s^2 (2kT)^{3/2}}{N_I q^3 m^{*1/2}} \left(\ln\left[1 + \left(\frac{12\pi\varepsilon_s kT}{N_I^{1/3} q^2} \right)^2 \right] \right)^{-1} \propto \frac{\varepsilon_s^2 T^{3/2}}{N_I m^{*1/2}}, \tag{6.69}$$

where N_I is the density of the ionized impurities. The μ_L decreases with T to the $-3/2$ power, while the μ_{ii} increases with T to the $3/2$ power. Most semiconductor materials will be limited by the μ_L near 300 K, and will therefore decrease as the T increases.

6.6.2 Mobility Model

The T and doping dependencies of the μ_n and μ_p are accounted for in a semi-empirical equation developed by Arora [193].

$$\mu_A = \mu_{\min} T_n^{\beta_1} + \frac{(\mu_{\max} - \mu_{\min}) T_n^{\beta_2}}{1 + \left(\frac{N_A + N_D}{N_{ref} T_n^{\beta_3}} \right)^{\alpha_\mu T_n^{\beta_4}}} \tag{6.70}$$

Here T_n is the normalized temperature, $T_n = T_O/300$. A similar equation without the T_n power coefficents, was developed by Caughey [194]. The fitted coefficients for $\mu_{A,n}$ and $\mu_{A,p}$ are in Table 6.1.

Table 6.1
Coefficients for the $\mu_{A,n}$ and $\mu_{A,p}$, Equation (6.36)

Coefficients	$\mu_{A,n}$	$\mu_{A,p}$	Units
$\mu_{\max}$	1340	461	$\frac{\text{cm}^2}{\text{Vs}}$
$\mu_{\min}$	88	54.3	$\frac{\text{cm}^2}{\text{Vs}}$
N_{ref}	1.26x1017	2.35 x1017	cm-3
a_{μ}	0.88	0.88	
β_1	-0.57	-0.57	
β_2	-2.33	-2.33	
β_3	2.4	2.4	
β_4	-0.146	-0.146	

The *n* and *p* dependencies of the μ_n and μ_p are included in a semi-empirical equation developed by Dorkel [195].

$$\mu_{pn} = \frac{2x10^{17}T^{1.5}}{\sqrt{pn}}\left[\ln\left(1+8.28x10^{8}T^{2}\left[pn\right]^{-1/3}\right)\right]^{-1} \tag{6.71}$$

The mobility of these two equations is combined using the Matthiessen Rule, Equation (6.67).

The *T*, doping density, and free minority carrier concentration dependent μ model discussed in the following sections is compared to measured Si μ over a range of *T* and N_D in Figure 6.8 [146].

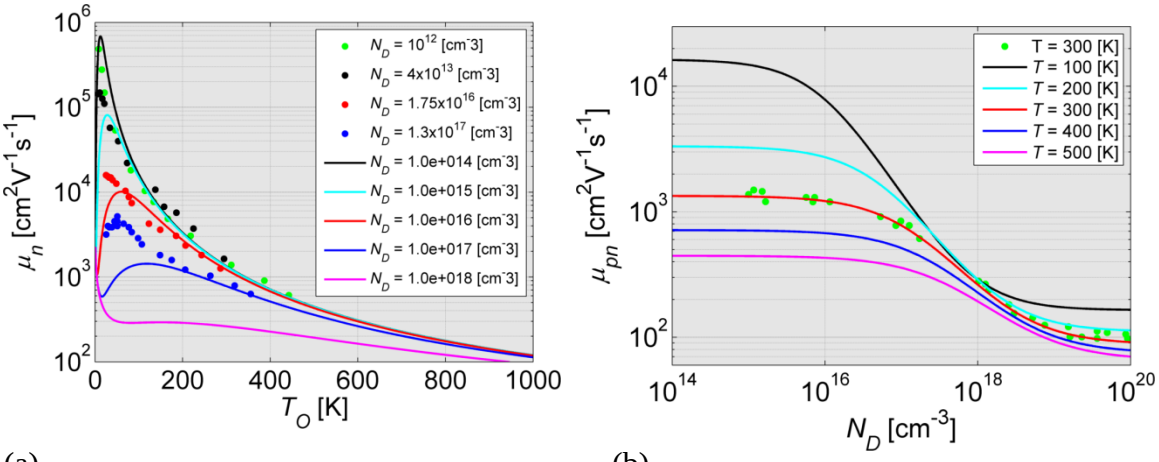

(a) (b)

Figure 6.8. (a) Comparison of measured and modeled μ_n over T for a range of N_D [146]. (b) Comparison of measured and modeled μ_{pn} over N_D at 300 K.

This is model is a particularly good fit (a) to the measured μ_n over the range of measured N_D values between 200 K and 400 K, which covers the T range of interest. The μ_{pn} is also compared to higher N_D values at 300 K in (b).

The high-level injection results are also compared to the measured $\mu_n + \mu_p$ over a range of the *pn* product values.

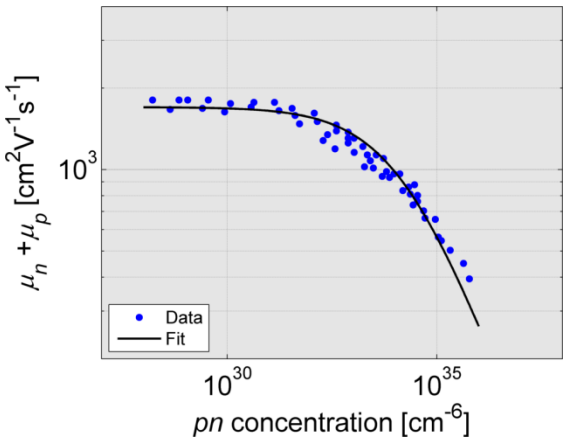

Figure 6.9. Comparison of measured and modeled $\mu_n + \mu_p$ over a range of the *np* product values.

The *pn* product has very little effect on the $\mu_n + \mu_p$ below 1x10^{32} cm^{-6}. The simulated values of $\mu_n + \mu_p$ are on the high side of the measured data from 1x10^{32} cm^{-6} to 1x10^{34} cm^{-6}.

6.7 Band Parameters

Band parameters ϕ_p and ϕ_p are added to the drift terms of the drift-diffusion equations (6.6) and (6.7), to allow for changes in the bandgap, electron affinity, and carrier concentrations. This makes it possible to model heterojunction solar cells. Including the band parameters in numerical models has been studied quite extensively by Lundstrom [151, 152]. Heavy doping effects can also be included [196].

The band parameters for holes and electrons are

$$\phi_n = \chi(x) - \chi_r + kT \log\left[\frac{N_C(x)}{N_{Cr}}\right] + kT \log\left[\frac{F_{1/2}\left(\frac{F_n - E_C}{kT}\right)}{e^{\left(\frac{F_n - E_C}{kT}\right)}}\right] \tag{6.72}$$

$$\phi_p = -(\chi(x) - \chi_r) - (E_G(x) - E_{Gr}) + kT \log\left[\frac{N_V(x)}{N_{Vr}}\right] + kT \log\left[\frac{F_{1/2}\left(\frac{E_V - F_p}{kT}\right)}{e^{\left(\frac{E_V - F_p}{kT}\right)}}\right] \quad (6.73)$$

where N_{Cr} is a reference for the density of states in the conduction band, N_{Vr} is a reference for the density of states in the valence band, E_{Gr} is a reference bandgap energy and X_r is a reference electron affinity.

6.8 Other Parameters

There are three other parameters, $\vec{\mathcal{E}}$, ϕ, and $\vec{P}$, that are needed to solve the semiconductor equations. The ϕ will be found while solving the semiconductor equation as a function of position inside the solar cell. The $\vec{\mathcal{E}}(x)$ can be found using the ϕ as a function of position.

The $\vec{P}$ is significant for semiconductor with Wurtzite crystal structures, such as GaN, AlN and InN [197]. The $\vec{P}$ is small for Si and GaAs. It can be increased through the piezoelectric effect; however the devices model will not be under strain.

6.9 Other Temperature Dependent Effects

There are additional dependencies that can affect the performance of a solar cell. These affects can alter the terminal characteristics and the T dependent terminal characteristics. Some of the dependencies such as the resistivity are related to the 3-D structure of the solar cell (Section 6.9.1). While other dependences are related to the carrier transport physics, such as the breakdown electric field, $\vec{\mathcal{E}}_{br}$, (Section 6.9.2) and carrier saturation velocity (Section 6.9.3) and carrier freeze-out (Section 6.9.4). It is important to check the results for each of these affects.

6.9.1 Metal Resistivity

As discussed in Chapter 5, the resistivity in the solar cell junction, the LCL and the electrodes of the 3-D solar cell can have a profound effect on the terminal characteristics and the *T* dependent terminal characteristics. This is due to the fact that the resistivity of each of these layers often increases as the T_O increases. This increase causes the joule losses and biasing point loss to increase, which can adversely affect the *FF* and the η. It is therefore important to include these losses when attempting to carefully match measured devices.

In addition to the *T* dependence of the R_{Series}, these resistivity effects will also cause the R_{Series} to be dependent on the biasing point. This is important when understanding R_{Series} extracted from measurements. Another factor that influences R_{Series}, is the ideality factor used to extract the R_{Series}.

In this chapter the 3-D resistivity affects have been included through the use of a measured R_{Series}. The measured R_{Series} of this PERC solar cell was reported to be approximately 0.75 Ω/cm^2 [96]. The *T* dependence of the R_{Series} was reported to be similar to 0.5 Ω cm bulk Si, 0.00645 Ω/cm^2/°C [96]. Using the reported values lead to a modeled *FF* that was approximately 5% larger than the measured value. Since the value reported was an estimate and it was not clear how it was determined, the R_{Series} used in the numerical model was adjusted to fit the measured *FF* more closely. It was found that increasing the R_{Series} in the numerical model by 10% was enough to more closely match the measured *FF*.

The measured V_{OC} can also be reduced by circulating current effects [113]. This occurs when electrons and holes generated in the illuminated regions of the solar cell flow to the shadowed and other un-illuminated regions to recombine. This causes a voltage drop to occur across the resistive layers when the solar cell is being illuminated. This affect will increase as the T_O increases, due to the *T* dependent increase of the resistivity.

6.9.2 Breakdown Electric Field

A $\vec{\mathcal{E}}_{br}$ occurs when the $\vec{\mathcal{E}}$ becomes sufficiently large enough that it causes additional carriers to be generated, through tunneling or avalanche multiplication. While this is not expected to happen inside of a solar cell, it is important to check to make sure that the $\vec{\mathcal{E}}_{br}$ has not been exceeded numerically. The $\vec{\mathcal{E}}_{br}$ of direct bandgap, GaAs [198], and of indirect bandgap, Si [63], increases as the doping increases.

In most solar cells there is only a strong $\vec{\mathcal{E}}$ in the narrow depletion regions between layers with different dopings, such as the emitter-base and the base-BSF. The internal $\vec{\mathcal{E}}$ simulated in this chapter does not exceed the $\vec{\mathcal{E}}_{br}$. This can be more important at other T_O and bias-points.

6.9.3 Carrier Saturation Velocity

At very high $\vec{\mathcal{E}}$, typically around 1x10^5 [V/cm], the drift velocity, v_d, of the carriers will be limited by scattering, this is called the carrier saturation velocity, v_{sat}, which is typically 1x10^7 [cm/s] (Si [146] and GaAs [199]). As with the $\vec{\mathcal{E}}_{br}$ it is important to check to make sure that the numerically modeled carriers do not exceed this velocity anywhere inside the solar cell. A T dependent fit has been developed [146] for v_d over $\vec{\mathcal{E}}$, using measured data from -30 °C to 150 °C.

$$v_d = 1.53\times10^9 T^{-0.87} \frac{\left(\dfrac{\vec{\mathcal{E}}}{1.01T^{1.55}}\right)}{\left[1+\left(\dfrac{\vec{\mathcal{E}}}{1.01T^{1.55}}\right)^{2.57\times10^{-2}T^{0.66}}\right]^{\left(1/2.57\times10^{-2}T^{0.66}\right)}} \tag{6.74}$$

Figure 6.10 shows the v_d over $\vec{\mathcal{E}}$ for Si at three different temperatures [146], as the T increases the v_{sat} decreases.

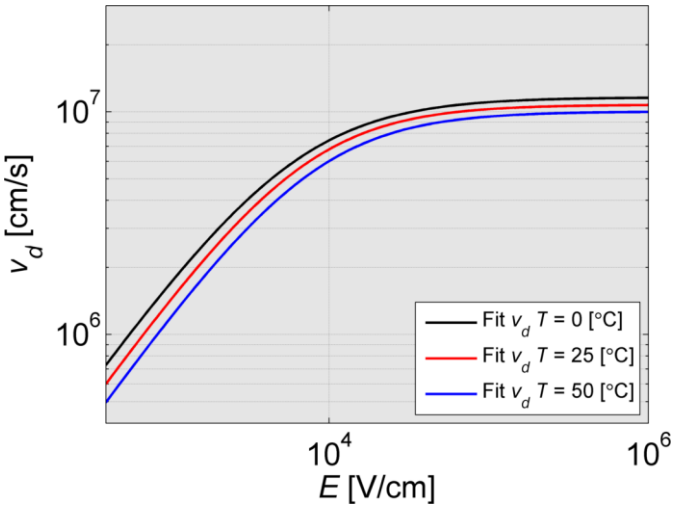

Figure 6.10. The $\vec{\mathcal{E}}$ dependent drift velocity, v_d, for Si at three different temperatures [63]. The carrier saturation velocity, v_{sat}, decrease as the T increases.

As described in the previous section, the strong $\vec{\mathcal{E}}$ in most solar cells occur between the emitter-base and the base-BSF. In the simulated Si solar cell the $\vec{\mathcal{E}}$ is large enough in these regions that it could cause the carrier velocity to saturate, however this strong $\vec{\mathcal{E}}$ occurs over a very narrow region, on the order of 20 nm. Because these regions are so narrow, it is likely that carriers will not scatter while traversing this region, in which case the carrier could overshoot the v_{sat}.

6.9.4 Carrier Freeze-Out

Freeze-out occurs when the carriers no longer have enough thermal energy to be excited. In Si this happens below 150 K (-123.15 °C) [200]. This is well below the expected T_O of terrestrial solar cells, and therefore will not be important in the T_O range of interest explored in this chapter. It is possible that solar cells in space could reach this T_O. This would occur when a satellite passes behind a planet or other celestial body.

6.10 Simulation Results

Analytical models have been used by a wide number of groups to simulate solar cells over a range of temperatures [52, 57, 84, 97], and additional results were reported by the Author in Chapters 3 and 4. These models can be predictive of the terminal characteristics, especially when temperature dependent fitting parameters such as *n* and R_{series} are allowed to vary over temperature. These analytic models require simplifying assuptions to be made, that makes it difficult to gain substantial insight into the sources of the temperature dependencies of the terminal characteristic. The detailed numerical model employed in this chapter can provide additional insights into the sources of the temperature dependencies, by avoiding many of these simplifying assumptions, and modeling the dependencies of the material parameters.

An additional concern regarding the need to use a detailed numerical model is that the $\frac{d\eta}{dT}$ appears to be constant near 25 °C. Green and Emery published results showing that the $\frac{d\eta}{dT}$ is nearly constant from 0 °C to 80 °C for a Si solar cell [48]. The temperature dependencies of the J_{SC}, V_{OC}, FF and η were deemed to be so close to linear, that in later publications a plot of the measured data was not included [48]. This leads to the question of why go to the effort to use a detailed numerical model, if the temperature dependence of η is essentially linear. While it is true that the η is linear near 25 °C, the slope of that line depends on the temperature dependencies of the J_{SC}, V_{OC} and FF. Carefully modeling the solar cell can reveal the material parameter dependencies that are causing the slope of the η. This will be discussed further in the following subsection. In addition, the measurements over T_O can help to verify the simulated model.

By including the material parameter dependencies in the detailed numerical model, the influence of each material parameter dependency can be determined. Some of the device parameters can be modified, such as the layer thicknesses, doping levels, the passivating layer and the optics. By varying these device parameters in the model, it

might be possible to re-engineer the solar cell to have a better performance under a given set of operating conditions.

A PERC Si solar cell developed by Green's group at the UNSW[96], with a measured η close to the world record 25% device [96], and published temperature dependent terminal characteristics was used to validate the simulated solar cell. The material parameter dependencies described in Section 6.3 through Section 6.8 have been used in conjuction with the device parameters in Table 6.2 to simulate the terminal characteristics and temperature dependent terminal characteristics. These results will be compared in Section 6.10.1.

Table 6.2
Device parameters used in the simulations [96, 201, 202]

Device parameter	Value	Units
Emitter τ_n and τ_p	$300x10^{-9}$	s
Emitter thickness, t_E	0.1	um
Emitter N_D	$1x10^{19}$	cm^{-3}
Base τ_n and τ_p	$2x10^{-6}$	s
Base thickness	280	um
Base N_A	$1x10^{17}$	cm^{-3}
Front surface	10	cm/s
Back surface	10	cm/s

Each of these device parameters have been based on the information found in published literature [96, 201, 202]. The front surface of this solar cell is textured with inverted pyramids. The front and back surfaces have been passivated with a $Si0_2$ layer. Holes are then etched through the $Si0_2$ to connect the grid electrodes to the semiconductor. Since the $Si0_2$ passivates the surface, it reduces the overall effective S_n

and S_p. The effective values of the S_n and S_p were adjusted to match the measured terminal characteristics.

The simulated and measured terminal characteristics over temperature will be evaluated in Section 6.10.1 and the temperature dependent terminal characteristics will be evaluated in Section 6.10.2.

6.10.1 Comparison to Measured Devices

The terminal characteristics and the temperature dependent terminal characteristics have been defined and discussed in Section 3.1 and Section 3.1.1. A single detailed numerical model was used to simulate the terminal characteristics from 0 °C to 80 °C, solid line in Figure 6.11. The simulated values are in good agreement with the measured device characteristics, diamonds, over a wide range of T_O. The simulated J_{SC} Figure 6.11(a) is slightly higher than the measured values at each T_O. The simulated V_{OC} and FF are very close to the measured data points. The simulated η is also relatively close to the measured values.

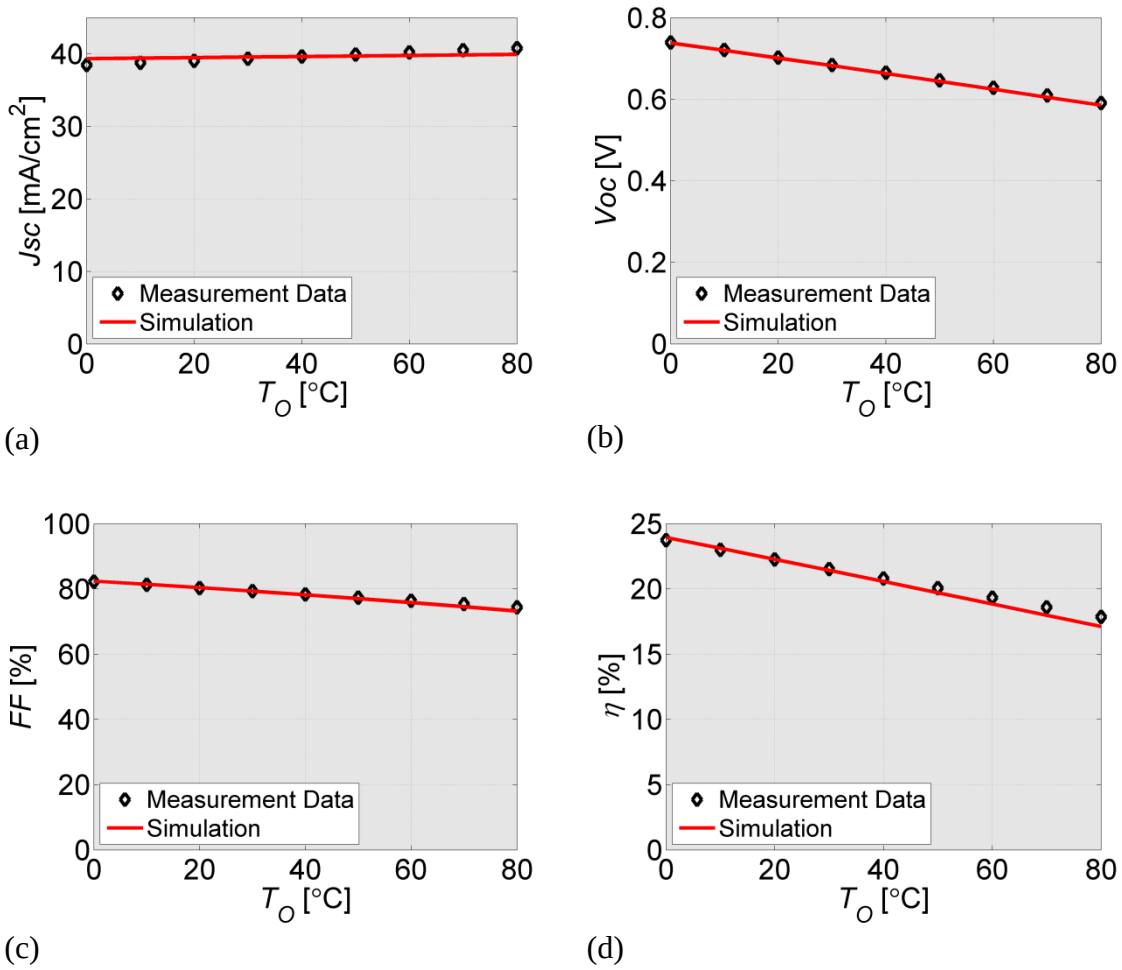

Figure 6.11. The terminal characteristics predicted by a single detailed numerical model over a range of T_O, solid line. Each of the terminal characteristics are relatively close to the measured device characteristics, diamonds. (a) The J_{SC} is slightly higher than the measured characteristics near 25 °C. The (b) V_{OC} and (c) *FF* are essentitally the same as the measured data near 25 °C. The T_O dependent terminal characteristics are shown in Figure 6.12.

These results would likely be considered sufficient if the primary focus was to simulate the terminal characteristics at one T_O. The small 0.9% difference between the simulated and measured J_{SC} is likely caused by a difference in the measured and simulated reflectivity. The measured reflectivity for the measured device does not appear to have been published, so the measured reflectivity from a similar device was used. This

small difference could easily be remedied by adding additional shadowing to the model. This would bring the terminal characteristics at one T_O into even closer agreement, and would likely be more than sufficient for a model developed to use at one temperature. The shadowing however was not adjusted in the model, because it is unlikely that it significantly improve the simulated $\frac{1}{J_{SC}}\frac{dJ_{SC}}{dT}$, which will be discussed in the follow section.

Another interesting detail about the temperature dependence of the η is that it appears to decrease linearly as the temperature increases, even though both the *FF* and V_{OC} decrease linearly, which could cause the η to decrease to the second power [48]. The η temperature dependence is closer to a linear fit because the $\frac{1}{V_{OC}}\frac{dV_{OC}}{dT}$ is 2-3 times larger than the $\frac{1}{FF}\frac{dFF}{dT}$, and because the $\frac{1}{J_{SC}}\frac{dJ_{SC}}{dT}$ nearly cancels the $\frac{1}{FF}\frac{dFF}{dT}$ in Si solar cells. Leaving the η to follow the temperature dependence of the V_{OC}. In addition, as shown in Section 3.1.8, as the solar cell E_G increases the $\frac{1}{J_{SC}}\frac{dJ_{SC}}{dT}$ it is predicted to become larger than the $\frac{1}{FF}\frac{dFF}{dT}$. At even higher E_G the $\frac{1}{J_{SC}}\frac{dJ_{SC}}{dT}$ could eventually become larger than the $\frac{1}{V_{OC}}\frac{dV_{OC}}{dT}$, which will cause the $\frac{1}{\eta}\frac{d\eta}{dT}$ to become positive.

6.10.2 Analysis of Temperature Coefficients

The temperature dependent terminal characteristics are a good way to check the temperature dependencies of the material parameters, used in the model. Figure 6.12 shows the measured, black diamonds, and the simulated results, red dots, temperature dependent terminal characteristics 25 °C plotted with their associated terminal characteristics 25 °C. The range of the terminal characteristics is ± 5% of the measured device characteristics. The simulated J_{SC} Figure 6.12(a) is 0.9% higher than the

measured value and the simulated $\frac{1}{J_{SC}}\frac{dJ_{SC}}{dT}$ is 1/3 of the measured temperature dependent terminal characteristics. The temperature dependent terminal characteristics and terminal characteristics of the V_{OC} Figure 6.12(b) and the *FF* Figure 6.12(c) are essentially the same as the measured data. The V_{OC} in the simulation is off by 1.5 mV which is near the experimental error of the measurements. The $\frac{1}{\eta}\frac{d\eta}{dT}$ is the sum of the $\frac{1}{J_{SC}}\frac{dJ_{SC}}{dT}$, the $\frac{1}{V_{OC}}\frac{dV_{OC}}{dT}$ and the $\frac{1}{FF}\frac{dFF}{dT}$, Equation (3.4). So the difference between the simulated and the measured $\frac{1}{\eta}\frac{d\eta}{dT}$ is primarily caused by the $\frac{1}{J_{SC}}\frac{J_{SC}}{dT}$.

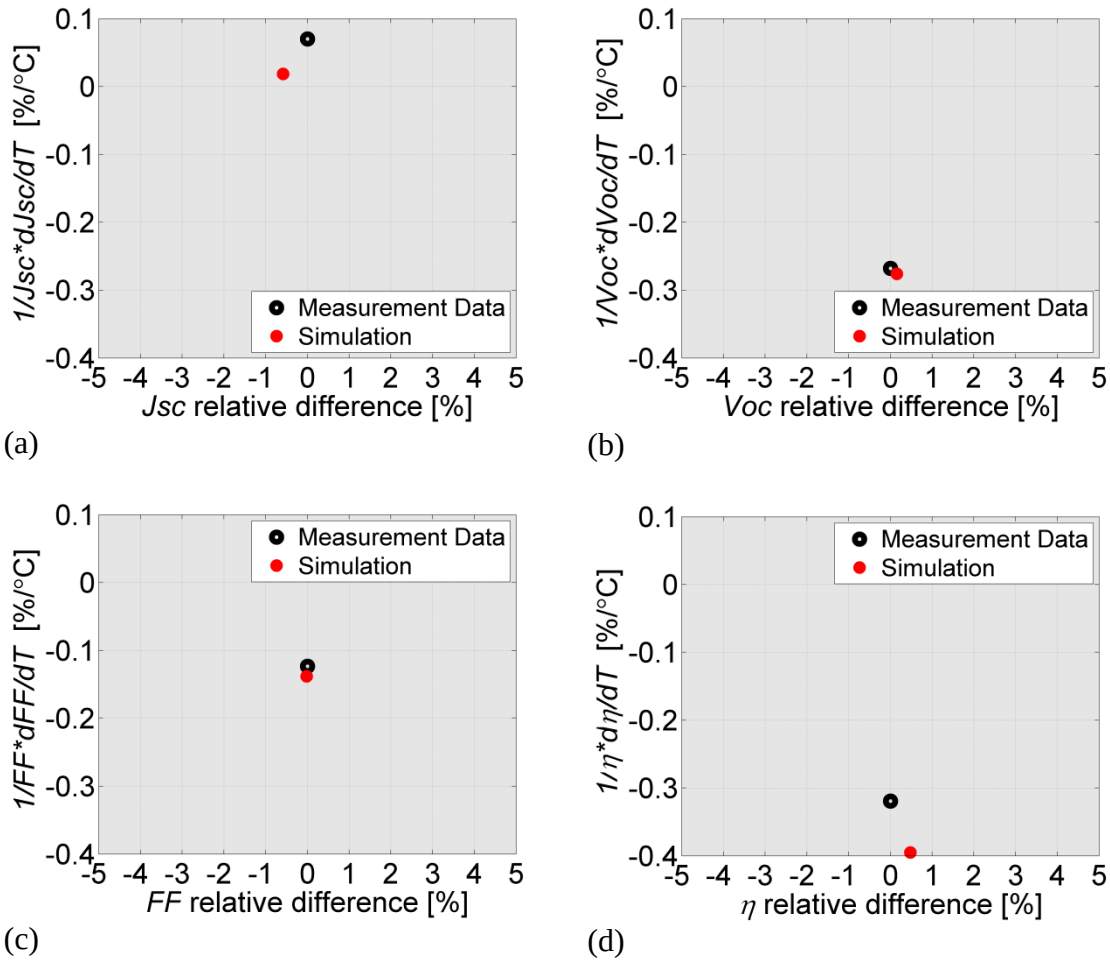

Figure 6.12. The temperature dependent terminal characteristics at 25 °C predicted by the detailed numerical model ploted versus the associated terminal characteristics at 25 °C, red dots, compared to the measured device characteristics, diamonds. The terminal characterics range is ± 1% of the measured characteristics. (a) The simulated J_{SC} is 0.9% higher than the measured characteristics and the $\frac{1}{J_{SC}}\frac{dJ_{SC}}{dT}$ is 1/3 of the measured T_O dependent terminal characteristics. The terminal characteristics and T_O dependent terminal characteristics of V_{OC} (b) and *FF* (c) are essentitally the same as the measured data. The simulated V_{OC} causes the modeled η to be slightly smaller than the measured value. The difference between the simluated and the measured $\frac{1}{\eta}\frac{d\eta}{dT}$ is caused by the $\frac{1}{J_{SC}}\frac{dJ_{SC}}{dT}$.

The V_{OC}, FF, $\frac{1}{V_{OC}}\frac{dV_{OC}}{dT}$ and $\frac{1}{FF}\frac{dFF}{dT}$ are primarily affect by the simulated recombination and resistivity. Because the simulated values for the V_{OC}, FF, $\frac{1}{V_{OC}}\frac{dV_{OC}}{dT}$ and $\frac{1}{FF}\frac{dFF}{dT}$ are close to the measured device, it is likely that the *T* dependence of the simulated material parameters in the numerical model are close to the parameters in the actual device.

While the J_{SC} and $\frac{1}{J_{SC}}\frac{dJ_{SC}}{dT}$ can be affect by the recombination, this is less common in high quality solar cell. Because the $\frac{1}{J_{SC}}\frac{dJ_{SC}}{dT}$ per °C is 1000 times smaller than the J_{SC}, the $\frac{1}{J_{SC}}\frac{dJ_{SC}}{dT}$ is much more sensitive to absorption, reflectivity and the incident solar irradiance near the bandgap edge. Additional measurements and further research are needed to better understand the affect of each of these factors.

The reflectivity and the incident solar irradiance near the bandgap edge can cause the $\frac{1}{J_{SC}}\frac{dJ_{SC}}{dT}$ to increase or cause it to be zero. If there is no incident solar irradiance near the bandgap edge or it is being reduced to zero by the reflectivity, the $\frac{1}{J_{SC}}\frac{dJ_{SC}}{dT}$ of the solar cell can be zero or even negative. If there are spikes in the irradiance produced by a solar simulator near the E_G, the can be much higher than if the solar cell was measured under the AM1.5 standard spectrum. These spikes produced by the solar simulator light source are generally considered acceptable, because they do not significantly affect the J_{SC} measured at one T_O.

In the MPF the temperature dependent narrowing of the electrical E_G was used to shift the absortion model, Section 6.3.3.1.1. Initially when the model was developed it was thought that this would not significantly affect the J_{SC}. However, due to the

sensitivity of the $\frac{1}{J_{SC}}\frac{dJ_{SC}}{dT}$, this may have over simiplified the actual temperature dependence of the optical $\alpha(\lambda)$.

Another factor that is likely affecting the simulated results, is that the simulations were performed in 1-D which simplifies the 3-D light-trapping of the real device. This will affect the absortion in the Urbach tails, since this absorption is strongly dependent on the light-trapping path length.

It is believed that by ultilizing additional measurements and improving the parameters used in this model, the difference between the measured and predicted $\frac{1}{J_{SC}}\frac{dJ_{SC}}{dT}$ can be reduced.

6.11 Summary and Conclusions

Detailed numerical models are useful tools to simulate and analyze the terminal performance and the internal operating conditions of solar cells. The information gained from developing and analyzing these models can be invaluable when endeavoring to improve the peformance of a solar cell. Part of the reason this is ture is that these models require fewer assumptions to be made compared to analytical models. This allows these types of models to more accurately simulate the solar cell performance over a range of operating conditions.

In this chapter an MPF has been developed to simulate the terminal characteristics and temperature dependent terminal characteristics of a high efficiency Si solar cell over a wide T_O range, 0 °C to 80 °C. In order to do this the MPF needed to contain material parameter dependences, such as the temperature, doping density, minority free carrier concentration and electric field dependencies for a wide range of material parameters.

Some of the dependencies used in the MPF are phyiscs based relations while others are semi-emprical fits to meausred data. The MPF used in the this chapter includes over 75 temperature, doping density, minority free carrier concentration and electric field

dependencies, and this is one of the most advanced models used to simulated the perforamnce of a solar cell.

The results of Section 6.10.1 show that the simulated J_{SC}, V_{OC} FF and η match the modeled device near 25 °C. This would be considered a good fit if the model was used to simulate the solar cell at this particular T_O. However, the goal of this work was to simulate the performance of a Si solar cell over a wide range of T_O using a single model.

The simulated V_{OC} and FF match the characteristics of the measured device over most of the T_O range. This indicates that the recombination, mobility and resistivity material parameter dependencies are likely close to those in the actual measured device. There may be some additional effects at higher T_O that are not being fully accounted for in the model. One possible source of the difference could be the 3-D resistivity effects, which are expected to change over the range of T_O. This is due to the fact that the resistivity and bias-point loss both increase as the T_O increases.

The simulated J_{SC} appears to be causing the η to deviate from the measured values as the T_O increases. This could be due to the measurement spectrum, refectivity, temperature dependent $\alpha(\lambda)$ and the 1-D optics model used in these simulations, which may have over simplified the absorption in the Urbach tails. The temperature dependence of the J_{SC} turned out to be significantly more sensitive then was originally anticipated.

6.11.1 Future Work

This work has clearly shown that by including the necessary dependencies it is possible to simulating a solar cell over a wide range of T_O. This model could be further improved by modeling the Urbach tails more carefully and by comparing the simulation results to addition measurements done on the exact same device. Useful measurements include temperature dependent dark $J-V$, IQE or EQE and resistivity. The IQE or EQE

would be particularly useful in validating the $\alpha(\lambda)$ model. Additional measurements and simulation of the 3-D optics and resistivity could also be used to improve the simulation results.

7. CONCLUSIONS

The temperature dependent performance of solar cells is very important for real world applications. In this work measure devices performance and a variety of models have been used to understand the source of many temperature dependences. The results of this research have been influential in the DARPA Very High Efficiency Solar Cell program. It was also presented in the ARPA-E Solar Beyond Grid Parity: Spectrum-Efficient Solar Energy for Dispatchable Electricity or Fuels workshop and was utilized in preparing the Full-Spectrum Optimized Conversion and Utilization of Sunlight funding opportunity announcement. These results have been published in numerous publications and will continue to be used by researchers to understand the temperature dependent operation of solar cells. Five conclusions have been presented in this work.

Conclusion #1: Improving the V_{OC} will not always yield a better $\frac{1}{\eta}\frac{d\eta}{dT}$

While it may seem logical that improving the V_{OC} will always improve the $\frac{1}{\eta}\frac{d\eta}{dT}$, this is not always the case. Section 3.1.8 showed that while increasing the E_G of a solar cell will increase the V_{OC}, it can also cause the $\frac{1}{\eta}\frac{d\eta}{dT}$ to become worse. This is primary caused by the $\frac{1}{J_{SC}}\frac{dJ_{SC}}{dT}$. A similar effect occurred in Section 5.6, while reducing the number of grid lines decreased the shadowing which increased the J_{SC} and therefore the V_{OC}, it also leads to a worse $\frac{1}{\eta}\frac{d\eta}{dT}$.

Conclusion #2: A solar cell with the highest η may not have the best $\frac{1}{\eta}\frac{d\eta}{dT}$

Sections 3.2.2, 4.3.4 and 5.6 each showed that the design with the best η at one T_O is usually not the solar cell design with the best $\frac{1}{\eta}\frac{d\eta}{dT}$. The degraded $\frac{1}{\eta}\frac{d\eta}{dT}$ can lead to an overall lower η at higher T_O, which is important when designing a solar that will operator over a range of temperatures.

Conclusion #3: A solar cell with the highest η or with the best $\frac{1}{\eta}\frac{d\eta}{dT}$ may not yield the best performance over a range of temperature

Due to the fact that a solar cell with one design can have the highest η while a solar cell with another design can have the best $\frac{1}{\eta}\frac{d\eta}{dT}$ (conclusion #2), and because there is a trade-off in performance between the two designs, in most cases the design with the best performance over a range of T_O will not have the highest η or the best $\frac{1}{\eta}\frac{d\eta}{dT}$. Therefore, optimizing for either will lead to a design with a lower performance over a given range of T_O.

Conclusion #4: Need to optimize for the best yearly performance

Since optimizing for the highest η or the best $\frac{1}{\eta}\frac{d\eta}{dT}$ will not produce the best performance over a range of temperatures (conclusion #3), another metric will be needed to optimize the solar cell. One way to do this is to identifying a characteristic T_O. This would be similar to the AM1.5 solar spectrum, which is characteristic spectrum for a standard solar year. A possible better method for optimizing the yearly performance would involve optimizing the solar cell using a set of T_O and solar spectra throughout the year. A number of yearly performance metrics can be used to optimize the solar cell design for real world use.

Possible optimization metrics:

- Highest kWh out per year
- Lowest LCOE
- Higher energy during a particular season

        - Need more energy during the Summer
        - More efficient during the Winter
    - Most beneficial for the power grid
        - Reduce the peak load
        - Broad over the entire day
    - Longest system lifetime

As the number of installed solar cells increase, the most important metric may become the design that is most benefical to the power grid.

Conclusion #5: A detailed numerical model can be used understand the operating condition dependencies

The simulation results presented in Section 6.10.1 and Section 6.10.2 showed that a solar cell can be modeled over a wide range of temperatures with a single detailed numerical model. The simulated results showed good agreement with the measured values for the terminal characteristics J_{SC}, V_{OC}, FF, η, $\frac{1}{V_{OC}}\frac{dV_{OC}}{dT}$ and $\frac{1}{FF}\frac{dFF}{dT}$. The $\frac{1}{J_{SC}}\frac{dJ_{SC}}{dT}$ and $\frac{1}{\eta}\frac{d\eta}{dT}$ were likely limited by the reflectivity and the T dependent absorption model used.

7.1 Future Work

The results in Section 4.3 are being used by various groups submitting project proposal to the funding opportunity announcement Full-Spectrum Optimized Conversion and Utilization of Sunlight. This work is being used to identify materials that would be optimal for various system designs.

The resistivity model Section 5.6 was for a base case with low concentration and zero resistivity in the grid and busbar bar electrodes. This work can be extended by modeling cases with higher concentrations, as well as cases which include finite resistance in the grid electrodes and in the busbar. Including either of these will significantly increase the temperature dependent affect of the resistivity and the biasing point loss.

The detailed numerical model presented in Section 6.10.1 showed that the temperature dependences of solar cells can be simulated over a range of temperatures. The MDF can be inhanced by improving the Urbach tails model, modeling the 3-D light-trapping optics and including a better estimate of the 3-D resistivity losses.

LIST OF REFERENCES

LIST OF REFERENCES

[1] Global Wind Energy Council, "Global wind report 2010," Dec 3, 2011; http://www.gwec.net/index.php?id=180.

[2] Solar Energy Industries Association, "2010 year in review," Dec 2, 2011; http://www.seia.org/galleries/pdf/SMI-YIR-2010-ES.pdf.

[3] PVinsights.com, http://pvinsights.com/Report/ReportDisplay.php.

[4] V. Smil, *Energy at the crossroads : Global perspectives and uncertainties*, p. 241, Cambridge, Mass.: MIT, 2005.

[5] U.S. Energy Information Administration, "International energy statistics," Dec 3, 2011; http://www.eia.gov/cfapps/ipdbproject/IEDIndex3.cfm?tid=44&pid=44&aid=2.

[6] O. Morton, "Solar energy: A new day dawning?: Silicon valley sunrise," *Nature*, vol. **443**, no. 7107, pp. 19-22, 2006.

[7] Solar Energy Industries Association, "Major solar projects," Dec 2, 2011; http://www.seia.org/galleries/pdf/Major%20Solar%20Projects.pdf.

[8] Wikipedia, "List of photovoltaic power stations," Dec 2, 2011; http://en.wikipedia.org/wiki/List_of_photovoltaic_power_stations.

[9] SunPower, "Sunpower e19 / 320 solar pane," Nov 21, 2011; http://us.sunpowercorp.com/cs/BlobServer?blobkey=id&blobwhere=1300258626967&blobheadername2=Content-Disposition&blobheadername1=Content-Type&blobheadervalue2=inline%3B+filename%3Dsp_e19320wh_ds_en_ltr_w_223%252C0.pdf&blobheadervalue1=application%2Fpdf&blobcol=urldata&blobtable=MungoBlobs.

[10] "Global energy: Unshackling carbon from water," *Lux Research*, June 2009.

[11] W. G. J. H. M. van Sark, G. W. Brandsen, M. Fleuster, and M. P. Hekkert, "Analysis of the silicon market: Will thin films profit?," *Energy Policy*, vol. **35**, no. 6, pp. 3121-3125, 2007.

[12] "A painful eclipse," *The Economist*, 2011.

[13] L. L. Kazmerski, “Solar photovoltaics: No longer an outlier," Dec 3, 2011; ftp://ftp2.nrel.gov/pub/ewc-keei/Paper2_and_PPT2_Kazmerski_%28final%29.pdf.

[14] SunShot, “Sunshot initiative," Nov 21, 2011; http://www1.eere.energy.gov/solar/sunshot/index.html.

[15] H. Branz, “Solar beyond grid parity: Spectrum-efficient solar energy for dispatchable electricity or fuels," May 29, 2013; http://arpa-e.energy.gov/?q=arpa-e-events/solar-beyond-grid-parity-spectrum-efficient-solar-energy-dispatchable-electricity-or.

[16] A. Luque, and A. Martí, “Limiting efficiency of coupled thermal and photovoltaic converters,” *Solar Energy Materials and Solar Cells*, vol. **58**, no. 2, pp. 147-165, 6//, 1999.

[17] A. White, G. Parks, and C. N. Markides, “Thermodynamic analysis of pumped thermal electricity storage,” *Applied Thermal Engineering*, vol. **53**, no. 2, pp. 291-298, 5/2/, 2013.

[18] Greentechmedia, “Breakthrough in energy storage: Isentropic energy," July 4, 2013; http://www.greentechmedia.com/articles/read/breakthrough-in-utility-scale-energy-storage-isentropic.

[19] M. W. Wanlass, T. J. Coutts, J. S. Ward, K. A. Emery, T. A. Gessert, and C. R. Osterwald, "Advanced high-efficiency concentrator tandem solar cells," *22nd IEEE Photovoltaic Specialists Conference.* pp. 38-45, 1991.

[20] A. H. S. Luque, *Handbook of photovoltaic science and engineering*, p. 370, Chichester: Wiley, 2011.

[21] P. B. Andreea Boca, Kevin Crist, Greg Flynn, James McCarty, Pravin Patel, , and P. S. Charles Sarver, Rick Stall, Mark Stan, and Cory Tourino, "Array-design considerations for the solar probe plus mission " *Photovoltaic Specialists Conference (PVSC), 2011 37th IEEE*.

[22] T. G. Gerald Siefer, Michael Schachtner, Alexander Wekkeli, Andreas W. Bett, "Improved grating monochromator set-up for eqe measurements of multi-junction solar cells," *Photovoltaic Specialists Conference (PVSC), 2013 39th IEEE*.

[23] G. A. Landis, R. P. Raffaelle, and D. Merritt, *High temperature solar cell development*, Glenn Research Center, 19th European Photovoltaic Solar Energy Power Conference; 7-11 Jun. 2004; Paris; France, 2004.

[24] J. Gray, "High temperature pv at concentration," *ARPA-E Workshop, Solar Beyond Grid Parity: Spectrum-Efficient Solar Energy for Dispatchable Electricity or Fuels*.

[25] National Renewable Energy Laboratory: Solar Radiation Research Laboratory, “Nrel: Midc/srrl baseline," Nov 17, 2011; http://www.nrel.gov/midc/srrl_bms/.

[26] National Renewable Energy Laboratory, “Nsrdb: 1991- 2005 update: Tmy3," Nov 17, 2011.

[27] A. Luque, and S. Hegedus, *Handbook of photovoltaic science and engineering*, p. 148: John Wiley & Sons.

[28] M. Fuentes, “A simplified thermal model for flat-plate photovoltaic arrays,” *Sandia Tech. Report*, May 1987.

[29] A. E. Becquerel, “Recherches sur les effets de la radiation chimique de la lumiere solaire au moyen des courants electriques,” *Comptes Rendus de L’Academie des Sciences*, vol. **9**, pp. 145–148, 1939.

[30] W. Smith, “Effect of light on selenium during the passage of an electric current,” *Nature*, pp. 303, 20 February 1873.

[31] W. G. Adams, and R. E. Day, “The action of light on selenium,” *Proceedings of the Royal Society of London*, vol. **A25**, pp. 113-117, January 1, 1876.

[32] C. E. Fritts, "On a new form of selenium photocell," *Proceedings of the American Association for the Advancement of Science.* p. 97.

[33] H. Hertz, *Wied. Ann.*, vol. **31**, 1887.

[34] M. A. Stoletow, “On a kind of electrical current produced by ultra-violet rays,” *Philosophical Magazine Series 5*, vol. **26**, no. 160, pp. 317-319, 1888/09/01, 1888.

[35] A. Einstein, “Über einen die erzeugung und verwandlung des lichtes betreffenden heuristischen gesichtspunkt,” *Annalen der Physik*, vol. **322**, no. 6, pp. 132-148, 1905.

[36] J. Czochralski, *Zeitschrift für Physikalische Chemie*, vol. **92**, 1916.

[37] J. Zhao, A. Wang, and M. A. Green, “24·5% efficiency silicon pert cells on mcz substrates and 24·7% efficiency perl cells on fz substrates,” *Progress in Photovoltaics: Research and Applications*, vol. **7**, no. 6, pp. 471-474, 1999.

[38] R. Ohl, *Light sensitive device*, USA, USPTO, 1946.

[39] D. Trivich, “Photovoltaic cells and their possible use as power converters for solar energy,” *Ohio Journal of Science*, vol. **53**, no. 5, pp. 300-314, 1953.

[40] F. Treble, “Milestones in the development of crystalline silicon solar cells,” *Renewable Energy,* vol. **15**, no. 1-4, pp. 473-478.

[41] J. M. Woodall, and H. J. Hovel, “An isothermal etchback-regrowth method for high-efficiency Ga[sub 1 - x]Al[sub x]As-GaAs solar cells,” *Applied Physics Letters,* vol. **30**, no. 9, pp. 492-493, 1977G

[42] "The history of solar," Dec 3, 2011; http://www1.eere.energy.gov/solar/pdfs/solar_timeline.pdf.

[43] D. J. Friedman, S. R. Kurtz, K. A. Bertness, A. E. Kibbler, C. Kramer, J. M. Olson, D. L. King, B. R. Hansen, and J. K. Snyder, "GaInP/GaAs monolithic tandem concentrator cells," *Photovoltaic Energy Conversion, 1994., Conference Record of the Twenty Fourth. IEEE Photovoltaic Specialists Conference - 1994, 1994 IEEE First World Conference on.* pp. 1829-1832 vol.1822.

[44] R. R. King, R. A. Sherif, D. C. Law, J. T. Yen, M. Haddad, C. M. Fetzer, K. M. Edmondson, G. S. Kinsey, H. Yoon, M. Joshi, S. Mesropian, H. L. Cotal, D. D. Krut, J. H. Ermer, and N. H. Karam, “New horizons in iii-v multijunction terrestrial concentrator cell research,” in 21st European Photovoltaic Solar Energy Conference and Exhibition, Dresden, Germany, 2006.

[45] M. A. Green, K. Emery, Y. Hishikawa, W. Warta, and E. D. Dunlop, “Solar cell efficiency tables (version 38),” *Progress in Photovoltaics: Research and Applications,* vol. **19**, no. 5, pp. 565-572, 2011.

[46] M. A. Green, “Crystalline silicon solar cells," Dec 3, 2011; http://www.icpress.co.uk/etextbook/p139/p139_chap4.pdf.

[47] M. A. Green, K. Emery, Y. Hishikawa, W. Warta, and E. D. Dunlop, “Solar cell efficiency tables (version 41),” *Progress in Photovoltaics: Research and Applications,* vol. **21**, no. 1, pp. 1-11, 2013.

[48] M. A. Green, K. Emery, and A. W. Blakers, “Silicon solar cells with reduced temperature sensitivity,” *Electronics Letters*, vol. **18**, no. 2, pp. 97-98, 1982.

[49] S. Yoon, and V. Garboushian, "Reduced temperature dependence of high-concentration photovoltaic solar cell open-circuit voltage (voc) at high concentration levels," *Photovoltaic Energy Conversion, 1994., Conference Record of the Twenty Fourth. IEEE Photovoltaic Specialists Conference - 1994, 1994 IEEE First World Conference on.* pp. 1500-1504 vol.1502.

[50] K. Emery, J. Burdick, Y. Caiyem, D. Dunlavy, H. Field, B. Kroposki, T. Moriarty, L. Ottoson, S. Rummel, T. Strand, and M. W. Wanlass, "Temperature dependence of photovoltaic cells, modules and systems," *Photovoltaic Specialists Conference, 1996., Conference Record of the Twenty Fifth IEEE.* pp. 1275-1278.

[51] J. J. Wysocki, and P. Rappaport, “Effect of temperature on photovoltaic solar energy conversion,” *Journal of Applied Physics,* vol. **31**, no. 3, pp. 571-578, 1960.

[52] J. C. C. Fan, “Theoretical temperature dependence of solar cell parameters,” *Solar Cells,* vol. **17**, no. 2-3, pp. 309-315, 1986.

[53] S. R. Kurtz, P. Faine, and J. M. Olson, “Modeling of two-junction, series-connected tandem solar cells using top-cell thickness as an adjustable parameter,” *Journal of Applied Physics,* vol. **68**, no. 4, pp. 1890-1895, 1990.

[54] A. Hovinen, “Fitting of the solar cell iv -curve to the two diode model,” *Physica Scripta,* vol. **T54**, pp. 175, 1994.

[55] M. Meusel, R. Adelhelm, F. Dimroth, A. W. Bett, and W. Warta, “Spectral mismatch correction and spectrometric characterization of monolithic iii–v multi-junction solar cells,” *Progress in Photovoltaics: Research and Applications,* vol. **10**, no. 4, pp. 243-255, 2002.

[56] A. W. Haas, J. R. Wilcox, J. L. Gray, and R. J. Schwartz, "Extracting a series resistance from ln[jsc]-voc and ff-voc characteristics," *Photovoltaic Specialists Conference (PVSC), 2011 37th IEEE*.

[57] D. J. Friedman, "Modelling of tandem cell temperature coefficients," *Photovoltaic Specialists Conference, 1996., Conference Record of the Twenty Fifth IEEE.* pp. 89-92.

[58] S. R. Kurtz, D. Myers, and J. M. Olson, "Projected performance of three- and four-junction devices using gaas and gainp," *Photovoltaic Specialists Conference, 1997., Conference Record of the Twenty-Sixth IEEE.* pp. 875-878.

[59] W. V. Roosbroeck, *Bell System Tech. J,* vol. **29**, pp. 560-607, 1950.

[60] P. A. Markowich, *The stationary semiconductor device equations*, New York: Springer_Verlag, 1986.

[61] C. M. Snowden, *Introduction to semiconductor device modeling*: World Scientific, 1986.

[62] M. R. Pinto, “Comprehensive semiconductor device simulation for silicon ulsi,” Department of Electrical Engineering, Stanford University, 1990.

[63] S. Sze, *Physics of semiconductor devices*, 3rd ed., p. 109: John Wiley & Sons, Inc., 2006.

[64] Y. Li, and K.-Y. Huang, "Numerical simulation of self-heating InGaP/GaAs heterojunction bipolar transistors computational science – iccs 2005," Lecture notes in computer science V. Sunderam, G. van Albada, P. Sloot *et al.*, eds., p. 137-156: Springer Berlin / Heidelberg, 2005.

[65] G. Tan, K. Lee, and J. M. Xu, "Finite element light emitter simutator (feles): A new 2d software design tool for laser devices," *Japanese Journal of Applied Physics*, vol. **32**, no. Copyright (C) 1993 Publication Board, Japanese Journal of Applied Physics, pp. 583, 1993.

[66] S. P. Philipps, R. Hoheisel, T. Gandy, D. Stetter, M. Hermle, F. Dimroth, and A. W. Bett, "An experimental and theoretical study on the temperature dependence of GaAs solar cells," *Photovoltaic Specialists Conference (PVSC), 2011 37th IEEE*.

[67] SILVACO, "Atlas website," Nov 17, 2011; http://www.silvaco.com/products/device_simulation/atlas.html.

[68] CROSSLIGHT, "Crosslight website," Nov 17, 2011; http://www.crosslight.com/.

[69] B. P. Rand, P. Peumans, and S. R. Forrest, "Long-range absorption enhancement in organic tandem thin-film solar cells containing silver nanoclusters," *Journal of Applied Physics*, vol. **96**, no. 12, pp. 7519-7526, 2004.

[70] M. C. Vecchi, M. Rudan, and G. Soncini, "Numerical simulation of optical devices," *Computer-Aided Design of Integrated Circuits and Systems, IEEE Transactions on*, vol. **12**, no. 10, pp. 1557-1569, 1993.

[71] J. R. Wilcox, "A comparison of detailed numerical modeling programs for pv," https://docs.google.com/spreadsheet/ccc?authkey=COrlsdwI&key=0ArAZqTjsWfLpdE1pYXAycVUyeWdBX1lhWmJxcjJ2X0E&authkey=COrlsdwI#gid=0.

[72] J. Gray, "Adept website," Nov 17, 2011; https://nanohub.org/resources/adept.

[73] M. Burgelman, "Scaps website," Nov 17, 2011; http://trappist.elis.ugent.be/ELISgroups/solar/projects/scaps.html.

[74] P. A. Basore, D. A. Clugston, "Pc1d website," Nov 17, 2011; http://www.pv.unsw.edu.au/info-about/our-school/products-services/pc1d.

[75] R. Stangl, "Afors-het website," Nov 17, 2011; http://www.helmholtz-berlin.de/forschung/enma/si-pv/projekte/asicsi/afors-het/index_en.html.

[76] S. J. Fonash, "Amps-1d website," Nov 17, 2011; http://ampsmodeling.org/default.htm.

[77] B. E. Pieters, "Asa website," Nov 17, 2011; http://www.ewi.tudelft.nl/en/the-faculty/departments/electrical-sustainable-energy/photovoltaic-materials-and-devices/asa-software/.

[78] M. Vukadinovic, “Aspin2 website," Nov 17, 2011; http://lpvo.fe.uni-lj.si/raziskave/fotovoltaika/modeliranje-in-simulacije/elektricno/.

[79] D. W. Winston, “Simwindows website," Nov 17, 2011; http://www-ocs.colorado.edu/SimWindows/simwin.html.

[80] D. W. Winston, “Update log," 2011; http://ecee.colorado.edu/~bart/ecen6355/simwindows/update.pdf.

[81] D. W. Winston, “Simwindows16 and simwindows32 version 1.4.2 user's manual," 2011; http://ecee.colorado.edu/~bart/ecen6355/simwindows/manual.pdf.

[82] G. A. Landis, P. Jenkins, D. Scheiman, and R. Rafaelle, "Extended temperature solar cell technology development," *AIAA 2nd International Energy Conversion Engineering Conference*.

[83] G. A. Landis, D. Merritt, R. P. Raffaelle, and D. Scheiman, "High temperature solar cell development," 2005-213431, NASA John Glenn Research Center, p. p. 241, 2005.

[84] A. Braun, E. A. Katz, and J. M. Gordon, “Basic aspects of the temperature coefficients of concentrator solar cell performance parameters,” *Progress in Photovoltaics: Research and Applications*, pp. n/a-n/a, 2012.

[85] P. Singh, and N. M. Ravindra, “Temperature dependence of solar cell performance—an analysis,” *Solar Energy Materials and Solar Cells*, vol. **101**, no. 0, pp. 36-45, 6//, 2012.

[86] M. Y. Levy, and C. Honsberg, “Rapid and precise calculations of energy and particle flux for detailed-balance photovoltaic applications,” *Solid-State Electronics*, vol. **50**, no. 7–8, pp. 1400-1405, 7//, 2006.

[87] J. L. Gray, J. M. Schwarz, J. R. Wilcox, A. W. Haas, and R. J. Schwartz, "Peak efficiency of multijunction photovoltaic systems," *35th IEEE Photovoltaic Specialists Conference.* pp. 002919-002923, 2010.

[88] K. W. Mitchell, "Computer analysis of resistance and non-uniform illumination effects on concentrator solar cells," *Electron Devices Meeting, 1977 International.* pp. 229-232.

[89] M. Sabry, and A. E. Ghitas, “Influence of temperature on methods for determining silicon solar cell series resistance,” *Journal of Solar Energy Engineering*, vol. **129**, no. 3, pp. 331-335, 2007.

[90] A. W. Haas, J. R. Wilcox, J. L. Gray, and R. J. Schwartz, "Numerical modeling of loss mechanisms resulting from the distributed emitter effect in concentrator solar cells," *34th IEEE Photovoltaic Specialists Conference.* pp. 002244-002249, 2006.

[91] A. W. Haas, J. R. Wilcox, J. L. Gray, and R. J. Schwartz, “Numerical modeling of loss mechanisms resulting from non-uniform illumination in multijunction concentrator solar cells,” *International Journal of Numerical Modelling: Electronic Networks, Devices and Fields*, pp. accepted, 2013.

[92] M. A. Green, “Intrinsic concentration, effective densities of states, and effective mass in silicon,” *Journal of Applied Physics*, vol. **67**, no. 6, pp. 2944-2954, 1990.

[93] E. Radziemska, “Thermal performance of Si and GaAs based solar cells and modules: A review,” *Progress in Energy and Combustion Science*, vol. **29**, no. 5, pp. 407-424, 2003.

[94] C. R. Osterwald, T. Glatfelter, and J. Burdick, "Comparison of the temperature coefficients of the basic i-v parameters for various types of solar cells," *IEEE Photovoltaic Specialists Conference, 19th.* pp. 188-193.

[95] P. Faine, S. R. Kurtz, C. Riordan, and J. M. Olson, “The influence of spectral solar irradiance variations on the performance of selected single-junction and multijunction solar cells,” *Solar Cells*, vol. **31**, no. 3, pp. 259-278, 1991.

[96] J. Zhao, A. Wang, S. J. Robinson, and M. A. Green, “Reduced temperature coefficients for recent high-performance silicon solar cells,” *Progress in Photovoltaics: Research and Applications*, vol. **2**, no. 3, pp. 221-225, 1994.

[97] M. A. Green, “General temperature dependence of solar cell performance and implications for device modelling,” *Progress in Photovoltaics: Research and Applications*, vol. **11**, no. 5, pp. 333-340, 2003.

[98] V. Alex, S. Finkbeiner, and J. Weber, “Temperature dependence of the indirect energy gap in crystalline silicon,” *Journal of Applied Physics*, vol. **79**, no. 9, pp. 6943-6946, 1996.

[99] W. Bludau, A. Onton, and W. Heinke, “Temperature dependence of the band gap of silicon,” *Journal of Applied Physics*, vol. **45**, no. 4, pp. 1846-1848, 1974.

[100] M. B. Panish, and J. H. C. Casey, “Temperature dependence of the energy gap in gaas and gap,” *Journal of Applied Physics*, vol. **40**, no. 1, pp. 163-167, 1969.

[101] M. D. Sturge, “Optical absorption of gallium arsenide between 0.6 and 2.75 ev,” *Physical Review*, vol. **127**, no. 3, pp. 768-773, 1962.

[102] M. E. Levinshtein, S. L. Rumyantsev, and M. Shur, *Properties of advanced semiconductor materials : GaN, AlN, InN, BN, SiC, SiGe*, New York: Wiley, 2001.

[103] R. Passler, “Temperature dependence of fundamental band gaps in group iv, iii--v, and ii--vi materials via a two-oscillator model,” *Journal of Applied Physics*, vol. **89**, no. 11, pp. 6235-6240, 2001.

[104] J. R. Wilcox, A. W. Haas, J. L. Gray, and R. J. Schwartz, "Estimating saturation current based on junction temperature and bandgap," *7th International Conference on Concentrating Photovoltaic Systems*, 2011.

[105] J. Gray, "Personal communication," 2011.

[106] J. Piprek, *Semiconductor optoelectronic devices : Introduction to physics and simulation*, Amsterdam; Boston: Academic Press, 2003.

[107] M. S. Dresselhaus, "Solid state physics: Part ii optical properties of solids."

[108] A. International, "Astm g173-03," 2003.

[109] W. Xufeng, M. R. Khan, M. A. Alam, and M. Lundstrom, "Approaching the shockley-queisser limit in GaAs solar cells," *Photovoltaic Specialists Conference (PVSC), 2012 38th IEEE*. pp. 002117-002121.

[110] S. M. Durbin, “Numerical modeling of photon recycling in iii-v optoelectronic devices,” 9523341, Purdue University, United States -- Indiana, 1994.

[111] M. A. Green, “Accuracy of analytical expressions for solar cell fill factors,” *Solar Cells*, vol. **7**, no. 3, pp. 337-340, 1982.

[112] A. R. Goi, A. Cantarero, K. Syassen, and M. Cardona, “Effect of pressure on the low-temperature exciton absorption in GaAs,” *Physical Review B*, vol. **41**, no. 14, pp. 10111-10119, 05/15/, 1990.

[113] J. L. Gray, R. J. Schwartz, and R. D. Nasby, "Two dimensional effects in conventional solar cells operated at high intensities," *Electron Devices Meeting, 1982 International*. pp. 510-513.

[114] P. B. M. Ryyan Khan, and Muhammad A. Alam, "Thermodynamic limits of solar cells with non-ideal optical response," *Photovoltaic Specialists Conference (PVSC), 2013 39th IEEE*.

[115] F. K. Reinhart, “A heuristic approach to precisely represent optical absorption and refractive index data for photon energies below, at, and above the band gap of semiconductors: The case of high-purity GaAs. Part i,” *J. Appl. Phys.*, vol. **97**, no. 12, pp. 123534, 2005.

[116] H. Casey, “Concentration dependence of the absorption coefficient for n? And p?Jour GaAs between 1.3 and 1.6 ev,” *J. Appl. Phys.*, vol. **46**, no. 1, pp. 250, 1975.

[117] J. R. H. Wilcox, Alex W.; Gray, Jeffery L.; Schwartz, Richard J. , "A method for estimating temperature dependent short circuit current," *Photovoltaic Specialists Conference (PVSC), 2011 37th IEEE*.

[118] Y. P. Varshni, "Band-to-band radiative recombination in groups iv, vi, and iii–v semiconductors (ii)," *physica status solidi (b),* vol. **20**, no. 1, pp. 9-36, 1967.

[119] Y. P. Varshni, "Band-to-band radiative recombination in groups iv, vi, and iii-v semiconductors (i)," *physica status solidi (b),* vol. **19**, no. 2, pp. 459-514, 1967.

[120] H. Schlangenotto, H. Maeder, and W. Gerlach, "Temperature dependence of the radiative recombination coefficient in silicon," *physica status solidi (a),* vol. **21**, no. 1, pp. 357-367, 1974.

[121] T. Trupke, M. A. Green, P. Wurfel, P. P. Altermatt, A. Wang, J. Zhao, and R. Corkish, "Temperature dependence of the radiative recombination coefficient of intrinsic crystalline silicon," *Journal of Applied Physics,* vol. **94**, no. 8, pp. 4930-4937, 2003.

[122] T. Matsusue, and H. Sakaki, "Radiative recombination coefficient of free carriers in GaAs-AlGaAs quantum wells and its dependence on temperature," *Applied Physics Letters,* vol. **50**, no. 20, pp. 1429-1431, 1987.

[123] G. W. t Hooft, M. R. Leys, and H. J. Talen-v.d. Mheen, "Temperature dependence of the radiative recombination coefficient in GaAs・(Al, Ga)As quantum wells," *Superlattices and Microstructures,* vol. **1**, no. 4, pp. 307-310, //, 1985.

[124] S. M. Durbin, and J. L. Gray, "Numerical modeling of photon recycling in solar cells," *Electron Devices, IEEE Transactions on,* vol. **41**, no. 2, pp. 239-245, 1994.

[125] B. M. Kayes, H. Nie, R. Twist, S. G. Spruytte, F. Reinhardt, I. C. Kizilyalli, and G. S. Higashi, "27.6% conversion efficiency, a new record for single-junction solar cells under 1 sun illumination," *Photovoltaic Specialists Conference (PVSC), 2011 37th IEEE,* 2011.

[126] W. Xufeng, M. R. Khan, J. L. Gray, M. A. Alam, and M. S. Lundstrom, "Design of GaAs solar cells operating close to the shockley–queisser limit," *Photovoltaics, IEEE Journal of,* vol. **3**, no. 2, pp. 737-744, 2013.

[127] W. K. Metzger, M. W. Wanlass, R. J. Ellingson, R. K. Ahrenkiel, and J. J. Carapella, "Auger recombination in low-band-gap n-type InGaAs," *Applied Physics Letters,* vol. **79**, no. 20, pp. 3272-3274, 2001.

[128] Y. C. Shen, G. O. Mueller, S. Watanabe, N. F. Gardner, A. Munkholm, and M. R. Krames, "Auger recombination in InGaN measured by photoluminescence," *Applied Physics Letters,* vol. **91**, no. 14, pp. 141101, 2007.

[129] T. H. Gfroerer, L. P. Priestley, M. F. Fairley, and M. W. Wanlass, "Temperature dependence of nonradiative recombination in low-band gap In[sub x]Ga[sub 1 - x]As/InAs[sub y]P[sub 1 - y] double heterostructures grown on InP substrates," *Journal of Applied Physics,* vol. **94**, no. 3, pp. 1738-1743, 08/01/, 2003.

[130] K. T. Delaney, P. Rinke, and C. G. V. d. Walle, "Auger recombination rates in nitrides from first principles," *Applied Physics Letters,* vol. **94**, no. 19, pp. 191109, 2009.

[131] M. Levinshtein, *Handbook series on semiconductor parameters,* p. 22: World Scientific, 1996.

[132] K. G. Svantesson, and N. G. Nilsson, "The temperature dependence of the auger recombination coefficient of undoped silicon," *Journal of Physics C: Solid State Physics,* vol. **12**, no. 23, pp. 5111, 1979.

[133] J. Dziewior, and W. Schmid, "Auger coefficients for highly doped and highly excited silicon," *Applied Physics Letters,* vol. **31**, no. 5, pp. 346-348, 1977.

[134] U. Strauss, W. W. Ruhle, and K. Kohler, "Auger recombination in intrinsic GaAs," *Applied Physics Letters,* vol. **62**, no. 1, pp. 55-57, 1993.

[135] V. Everett, J. Harvey, S. Surve, E. Thomsen, M. Vivar, M. Fuentes, S. Rahman, Y. O. Mayon, and A. Blakers, "Hybrid cpv-t microconcentrator system," *37th IEEE Photovoltaic Specialists Conference* 2011

[136] M. Vivar, M. Clarke, J. Pye, and V. Everett, "A review of standards for hybrid cpv-thermal systems," *Renewable and Sustainable Energy Reviews,* vol. **16**, no. 1, pp. 443-448, 1//, 2012.

[137] Committee on Materials for High-Temperature Semiconductor Devices Commission on Engineering and Technical Systems National Research Council, *Materials for high-temperature semiconductor devices*: The National Academies Press, 1995.

[138] H. C. Casey, Jr., and G. L. Pearson, "Diffusion in semiconductors," *Point defects in solids,* J. Crawford, Jr. and L. Slifkin, eds., p. 163-255: Springer US, 1975.

[139] C. H. Henry, "Limiting efficiencies of ideal single and multiple energy gap terrestrial solar cells," *Journal of Applied Physics,* vol. **51**, no. 8, pp. 4494-4500, 1980.

[140] M. Wolf, and H. Rauschenbach, "Series resistance effects on solar cell measurements," *Advanced Energy Conversion,* vol. **3**, no. 2, pp. 455-479, 1963.

[141] N. C. Wyeth, “Sheet resistance component of series resistance in a solar cell as a function of grid geometry,” *Solid-State Electronics,* vol. **20**, no. 7, pp. 629-634, 1977.

[142] A. Antonini, M. Stefancich, D. Vincenzi, C. Malagù, F. Bizzi, A. Ronzoni, and G. Martinelli, “Contact grid optimization methodology for front contact concentration solar cells,” *Solar Energy Materials and Solar Cells,* vol. **80**, no. 2, pp. 155-166, 2003.

[143] A. W. Haas, J. R. Wilcox, J. L. Gray, and R. J. Schwartz, "A distributed emitter model for solar cells: Extracting an equivalent lumped series resistance," *35th IEEE Photovoltaic Specialists Conference* pp. 002044-002049, 2010.

[144] J. R. Wilcox, and J. L. Gray, "A distributed emitter model for solar cells: Extracting a temperature dependent lumped series resistance," *Photovoltaic Specialists Conference (PVSC), 2012 38th IEEE.* pp. 002122-002127.

[145] D. Weldon, “Solar junction breaks world record with 43.5% efficient cpv production cell," May 28, 2012; http://www.sj-solar.com./downloads/Solar_Junction_World_Record_%20Efficiency_14April11.pdf.

[146] C. Jacoboni, C. Canali, G. Ottaviani, and A. Alberigi Quaranta, “A review of some charge transport properties of silicon,” *Solid-State Electronics,* vol. **20**, no. 2, pp. 77-89, 1977.

[147] S. Sze, *Physics of semiconductor devices*, 3rd ed., p. 30, Hoboken, New Jersey: John Wiley & Sons, Inc., 2006.

[148] C. Jacoboni, F. Nava, C. Canali, and G. Ottaviani, “Electron drift velocity and diffusivity in germanium,” *Physical Review B,* vol. **24**, no. 2, pp. 1014-1026, 1981.

[149] G. Ottaviani, C. Canali, F. Nava, and J. W. Mayer, “Hole drift velocity in high-purity Ge between 8 and 220 [degree]k,” *Journal of Applied Physics,* vol. **44**, no. 6, pp. 2917-2918, 1973.

[150] Y. C. Kao, and O. Eknoyan, “Electron and hole carrier mobilities for liquid phase epitaxially grown gap in the temperature range 200--550 k,” *Journal of Applied Physics,* vol. **54**, no. 5, pp. 2468-2471, 1983.

[151] M. S. Lundstrom, and R. J. Schuelke, “Modeling semiconductor heterojunctions in equilibrium,” *Solid-State Electronics,* vol. **25**, no. 8, pp. 683-691, 1982.

[152] M. S. Lundstrom, and R. J. Schuelke, “Numerical analysis of heterostructure semiconductor devices,” *Electron Devices, IEEE Transactions on,* vol. **30**, no. 9, pp. 1151-1159, 1983.

[153] J. L. Gray, "Adept: A general purpose numerical device simulator for modeling solar cells in one-, two-, and three-dimensions," *Photovoltaic Specialists Conference, 1991., Conference Record of the Twenty Second IEEE.* pp. 436-438 vol.431.

[154] J. Zhao, A. Wang, M. A. Green, and F. Ferrazza, "19.8% efficient ``honeycomb'' textured multicrystalline and 24.4% monocrystalline silicon solar cells," *Applied Physics Letters,* vol. **73**, no. 14, pp. 1991-1993, 1998.

[155] I. Repins, M. A. Contreras, B. Egaas, C. DeHart, J. Scharf, C. L. Perkins, B. To, and R. Noufi, "19·9%-efficient ZnO/CdS/CuInGaSe2 solar cell with 81·2% fill factor," *Progress in Photovoltaics: Research and Applications,* vol. **16**, no. 3, pp. 235-239, 2008.

[156] Y. Hagiwara, T. Nakada, and A. Kunioka, "Improved jsc in cigs thin film solar cells using a transparent conducting ZnO:B window layer," *Solar Energy Materials and Solar Cells,* vol. **67**, no. 1-4, pp. 267-271, 2001.

[157] G. Martin A, "Crystalline and thin-film silicon solar cells: State of the art and future potential," *Solar Energy,* vol. **74**, no. 3, pp. 181-192, 2003.

[158] M. D. Lammert, and R. J. Schwartz, "The interdigitated back contact solar cell: A silicon solar cell for use in concentrated sunlight," *Electron Devices, IEEE Transactions on,* vol. **24**, no. 4, pp. 337-342, 1977.

[159] J. D. McCambridge, M. A. Steiner, B. L. Unger, K. A. Emery, E. L. Christensen, M. W. Wanlass, A. L. Gray, L. Takacs, R. Buelow, T. A. McCollum, J. W. Ashmead, G. R. Schmidt, A. W. Haas, J. R. Wilcox, J. Van Meter, J. L. Gray, D. T. Moore, A. M. Barnett, and R. J. Schwartz, "Compact spectrum splitting photovoltaic module with high efficiency," *Progress in Photovoltaics: Research and Applications*, 2010.

[160] F. C. Nix, and D. MacNair, "The thermal expansion of pure metals: Copper, gold, aluminum, nickel, and iron," *Physical Review,* vol. **60**, no. 8, pp. 597, 1941.

[161] L. A. A. Pettersson, L. S. Roman, and O. Inganas, "Modeling photocurrent action spectra of photovoltaic devices based on organic thin films," *Journal of Applied Physics,* vol. **86**, no. 1, pp. 487-496, 1999.

[162] G. A. Samara, "Temperature and pressure dependences of the dielectric constants of semiconductors," *Physical Review B,* vol. **27**, no. 6, pp. 3494-3505, 1983.

[163] G. D. Cody, T. Tiedje, B. Abeles, B. Brooks, and Y. Goldstein, "Disorder and the optical-absorption edge of hydrogenated amorphous silicon," *Physical Review Letters,* vol. **47**, no. 20, pp. 1480-1483, 1981.

[164] G. S. Kinsey, and K. M. Edmondson, "Spectral response and energy output of concentrator multijunction solar cells," *Progress in Photovoltaics: Research and Applications,* vol. **17**, no. 5, pp. 279-288, 2009.

[165] R. J. Van Overstraeten, and R. P. Mertens, "Heavy doping effects in silicon," *Solid-State Electronics,* vol. **30**, no. 11, pp. 1077-1087, 1987.

[166] G. P. Smestad, *Optoelectronics of solar cells*, Bellingham, WA: SPIE Press, 2002.

[167] H. Weakliem, "Temperature dependence of the optical properties of silicon," *J. Appl. Phys.,* vol. **50**, no. 3, pp. 1491, 1979.

[168] G. E. Jellison, Jr., and F. A. Modine, "Optical functions of silicon between 1.7 and 4.7 ev at elevated temperatures," *Physical Review B,* vol. **27**, no. 12, pp. 7466-7472, 1983.

[169] G. E. Jellison, Jr., S. P. Withrow, J. W. McCamy, J. D. Budai, D. Lubben, and M. J. Godbole, "Optical functions of ion-implanted, laser-annealed heavily doped silicon," *Physical Review B,* vol. **52**, no. 20, pp. 14607-14614, 1995.

[170] J. I. Pankove, *Optical processes in semiconductors*, p. 28-29: Dover, 1971.

[171] A. Luque, and S. Hegedus, "Handbook of photovoltaic science and engineering," John Wiley & Sons.

[172] K. P. Odonnell, and X. Chen, "Temperature dependence of semiconductor band gaps," *Applied Physics Letters,* vol. **58**, no. 25, pp. 2924-2926, 1991.

[173] R. Pässler, "Parameter sets due to fittings of the temperature dependencies of fundamental bandgaps in semiconductors," *physica status solidi (b),* vol. **216**, no. 2, pp. 975-1007, 1999.

[174] G. G. Macfarlane, T. P. McLean, J. E. Quarrington, and V. Roberts, "Exciton and phonon effects in the absorption spectra of germanium and silicon," *Journal of Physics and Chemistry of Solids,* vol. **8**, no. 0, pp. 388-392, 1959.

[175] J. R. Haynes, M. Lax, and W. F. Flood, "Analysis of intrinsic recombination radiation from silicon and germanium," *Journal of Physics and Chemistry of Solids,* vol. **8**, no. 0, pp. 392-396, 1959.

[176] K. L. Shaklee, and R. E. Nahory, "Valley-orbit splitting of free excitons? The absorption edge of Si," *Physical Review Letters,* vol. **24**, no. 17, pp. 942-945, 1970.

[177] J. del Alamo, S. Swirhun, and R. M. Swanson, "Simultaneous measurement of hole lifetime, hole mobility and bandgap narrowing in heavily doped n-type silicon," *Electron Devices Meeting, 1985 International.* pp. 290-293.

[178] S. E. Swirhun, Y. H. Kwark, and R. M. Swanson, "Measurement of electron lifetime, electron mobility and band-gap narrowing in heavily doped p-type silicon," *Electron Devices Meeting, 1986 International.* pp. 24-27.

[179] J. W. Slotboom, and H. C. de Graaff, "Measurements of bandgap narrowing in Si bipolar transistors," *Solid-State Electronics,* vol. **19**, no. 10, pp. 857-862, 1976.

[180] G. Salace, "Temperature dependence of the electron affinity difference between Si and SiO2 in polysilicon (n+)?Oxide?Silicon (p) structures: Effect of the oxide thickness," *J. Appl. Phys.,* vol. **85**, no. 11, pp. 7768, 1999.

[181] G. Pananakakis, "Temperature dependence of the fowler?Nordheim current in metal?Oxide?Degenerate semiconductor structures," *J. Appl. Phys.,* vol. **78**, no. 4, pp. 2635, 1995.

[182] M. Lenzlinger, "Fowler?Nordheim tunneling into thermally grown SiO2," *J. Appl. Phys.,* vol. **40**, no. 1, pp. 278, 1969.

[183] F. J. Himpsel, G. Hollinger, and R. A. Pollak, "Determination of the fermi-level pinning position at Si(111) surfaces," *Physical Review B,* vol. **28**, no. 12, pp. 7014-7018, 1983.

[184] E. Yablonovitch, B. J. Skromme, R. Bhat, J. P. Harbison, and T. J. Gmitter, "Band bending, fermi level pinning, and surface fixed charge on chemically prepared GaAs surfaces," *Applied Physics Letters,* vol. **54**, no. 6, pp. 555-557, 1989.

[185] W. Michaelis, and M. H. Pilkuhn, "Radiative recombination in silicon p-n junctions," *physica status solidi (b),* vol. **36**, no. 1, pp. 311-319, 1969.

[186] A. M. Lepadatu, I. Stavarache, S. Lazanu, V. Iancu, M. R. Mitroi, R. R. Nigmatulin, and M. L. Ciurea, "Temperature dependence of capture coefficients in trapping phenomena," *Semiconductor Conference (CAS), 2010 International.* pp. 371-374.

[187] J. A. del Alamo, and R. M. Swanson, "Modelling of minority-carrier transport in heavily doped silicon emitters," *Solid-State Electronics,* vol. **30**, no. 11, pp. 1127-1136, 1987.

[188] R. G. Humphreys, "Valence band averages in silicon: Anisotropy and non-parabolicity," *Journal of Physics C: Solid State Physics,* vol. **14**, no. 21, pp. 2935, 1981.

[189] D. E. Aspnes, "Recombination at semiconductor surfaces and interfaces," *Surface Science,* vol. **132**, no. 1-3, pp. 406-421, 1983.

[190] Y. Vaitkus, and V. Grivitakas, "Dependence of the rate of interband auger recombination on the carrier density in silicon," *Sov. Phys. Semicond.,* vol. **15**, pp. 1102-1108, October 1981.

[191] J. Bardeen, and W. Shockley, "Deformation potentials and mobilities in non-polar crystals," *Physical Review,* vol. **80**, no. 1, pp. 72-80, 1950.

[192] E. Conwell, and V. F. Weisskopf, "Theory of impurity scattering in semiconductors," *Physical Review,* vol. **77**, no. 3, pp. 388-390, 1950.

[193] N. D. Arora, J. R. Hauser, and D. J. Roulston, "Electron and hole mobilities in silicon as a function of concentration and temperature," *Electron Devices, IEEE Transactions on,* vol. **29**, no. 2, pp. 292-295, 1982.

[194] D. M. Caughey, and R. E. Thomas, "Carrier mobilities in silicon empirically related to doping and field," *Proceedings of the IEEE,* vol. **55**, no. 12, pp. 2192-2193, 1967.

[195] J. M. Dorkel, and P. Leturcq, "Carrier mobilities in silicon semi-empirically related to temperature, doping and injection level," *Solid-State Electronics,* vol. **24**, no. 9, pp. 821-825, 1981.

[196] M. S. Lundstrom, R. J. Schwartz, and J. L. Gray, "Transport equations for the analysis of heavily doped semiconductor devices," *Solid-State Electronics,* vol. **24**, no. 3, pp. 195-202, 1981.

[197] J. Singh, "Electronic and optoelectronic properties of semiconductor structures."

[198] A. S. Kyuregyan, and S. N. Yurkov, "Room-temperature avalanche breakdown voltages of p-n junctions made of Si, Ge, SiC, GaAs, GaP, and InP," *Soviet Physics - Semiconductors,* vol. **23**, no. 10, pp. 1126-1131, 1989.

[199] B. Kramer, and A. Mircea, "Determination of saturated electron velocity in gaas," *Applied Physics Letters,* vol. **26**, no. 11, pp. 623-625, 1975.

[200] R. G. Pires, R. M. Dickstein, S. L. Titcomb, and R. L. Anderson, "Carrier freezeout in silicon," *Cryogenics,* vol. **30**, no. 12, pp. 1064-1068, 12//, 1990.

[201] A. W. Blakers, A. Wang, A. M. Milne, J. Zhao, and M. A. Green, "22.8% efficient silicon solar cell," *Applied Physics Letters,* vol. **55**, no. 13, pp. 1363-1365, 1989.

[202] M. A. Green, A. W. Blakers, and C. R. Osterwald, "Characterization of high-efficiency silicon solar cells," *Journal of Applied Physics,* vol. **58**, no. 11, pp. 4402-4408, 1985.

[203] A. Flat, and A. G. Milnes, “Optimization of multi-layer front-contact grid patterns for solar cells,” *Solar Energy,* vol. **23**, no. 4, pp. 289-299, //, 1979.

[204] A. R. Moore, *An optimized grid design for a sun-concentrator solar cell*, vol. **40**, RCA, 1979.

[205] J. R. Wilcox, A. W. Haas, J. L. Gray, and R. J. Schwartz, "Combining solar cell and optical modeling in multijunction systems," *Photovoltaic Specialists Conference (PVSC), 2009 34th IEEE.* pp. 000636-000641.

[206] J. R. Wilcox, A. W. Haas, J. L. Gray, and R. J. Schwartz, "A solar cell model for use in optical modeling of concentrating multijunction photovoltaic systems," *Photovoltaic Specialists Conference (PVSC), 2010 35th IEEE.* pp. 003104-003108.

[207] D. Aiken, M. Stan, C. Murray, P. Sharps, J. Hills, and B. Clevenger, "Temperature dependent spectral response measurements for iii-v multi-junction solar cells," *Photovoltaic Specialists Conference, 2002. Conference Record of the Twenty-Ninth IEEE.* pp. 828-831.

[208] L. Liu, N. Chen, Y. Bai, M. Cui, H. Zhang, F. Gao, Z. Yin, and X. Zhang, “Quantum efficiency and temperature coefficients of GaInP/GaAs dual-junction solar cell,” *Science in China Series E: Technological Sciences,* vol. **52**, no. 5, pp. 1176-1180, 2009.

[209] J. L. Gray, A. W. Haas, J. R. Wilcox, and R. J. Schwartz, "Efficiency of multijunction photovoltaic systems," *Photovoltaic Specialists Conference, 2008. PVSC '08. 33rd IEEE.* pp. 1-6.

[210] Y. P. Varshni, “Temperature dependence of the energy gap in semiconductors,” *Physica,* vol. **34**, no. 1, pp. 149-154, 1967.

[211] C. D. Thurmond, “The standard thermodynamic functions for the formation of electrons and holes in Ge, Si, GaAs, and GaP,” *Journal of The Electrochemical Society,* vol. **122**, no. 8, pp. 1133-1141, 1975.

[212] V. Siklitsky, “New semiconductor materials," May 1, 2011; http://www.ioffe.ru/SVA/NSM/Semicond/Ge/bandstr.html.

[213] S. Paul, J. B. Roy, and P. K. Basu, “Empirical expressions for the alloy composition and temperature dependence of the band gap and intrinsic carrier density in Ga[sub x]In[sub 1 - x]As,” *Journal of Applied Physics,* vol. **69**, no. 2, pp. 827-829, 1991.

[214] S. Raj, A. K. Sinha, and A. K. Panchal, “Solar cell parameters estimation from illuminated i-v characteristic using linear slope equations and newton-raphson technique,” *Journal of Renewable and Sustainable Energy,* vol. **5**, no. 3, pp. 033105, 2013.

[215] J. R. W. Jeffery L. Gray, "The design of multijunction photovoltaic systems for realistic operating conditions," *56th International Midwest Symposium on Circuits and Systems*.

[216] P. Lautenschlager, M. Garriga, S. Logothetidis, and M. Cardona, “Interband critical points of GaAs and their temperature dependence,” *Physical Review B,* vol. **35**, no. 17, pp. 9174-9189, 1987.

[217] E. Grilli, M. Guzzi, R. Zamboni, and L. Pavesi, “High-precision determination of the temperature dependence of the fundamental energy gap in gallium arsenide,” *Physical Review B,* vol. **45**, no. 4, pp. 1638-1644, 1992.

[218] M. El Allali, C. B. So/rensen, E. Veje, and P. Tidemand-Petersson, “Experimental determination of the GaAs and Ga_{1-x}Al_{x}As band-gap energy dependence on temperature and aluminum mole fraction in the direct band-gap region,” *Physical Review B,* vol. **48**, no. 7, pp. 4398-4404, 1993.

[219] P. Kraisingdecha, and M. Gal, “Differential reflectance spectroscopy of GaAs/GaAlAs at elevated temperatures,” *Applied Physics Letters,* vol. **69**, no. 10, pp. 1355-1357, 1996.

[220] M. Fernández, P. Prete, N. Lovergine, A. M. Mancini, R. Cingolani, L. Vasanelli, and M. R. Perrone, “Optical properties of movpe-grown ZnS epilayers on (100) GaAs,” *Physical Review B,* vol. **55**, no. 12, pp. 7660-7666, 1997.

[221] K. Osamura, S. Naka, and Y. Murakami, “Preparation and optical properties of Ga[sub 1 - x]In[sub x]N thin films,” *Journal of Applied Physics,* vol. **46**, no. 8, pp. 3432-3437, 1975.

[222] A. Manoogian, and A. Leclerc, “Determination of the dilation and vibrational contributions to the energy band gaps in germanium and silicon,” *physica status solidi (b),* vol. **92**, no. 1, pp. K23-K27, 1979.

[223] T. Donofrio, G. Lamarche, and J. C. Woolley, “Temperature effects on the optical energy gap values of Cd[sub x]Zn[sub y]Mn[sub z]Te alloys,” *Journal of Applied Physics,* vol. **57**, no. 6, pp. 1932-1936, 1985.

[224] G. S. Kinsey, P. Hebert, K. E. Barbour, D. D. Krut, H. L. Cotal, and R. A. Sherif, “Concentrator multijunction solar cell characteristics under variable intensity and temperature,” *Progress in Photovoltaics: Research and Applications,* vol. **16**, no. 6, pp. 503-508, 2008.

[225] W. Xiaoting, N. Waite, P. Murcia, K. Emery, M. Steiner, F. Kiamilev, K. Goossen, C. Honsberg, and A. Barnett, "Improved outdoor measurements for very high efficiency solar cell sub-modules," *Photovoltaic Specialists Conference (PVSC), 2009 34th IEEE.* pp. 000409-000414.

[226] A. Berk, G. P. Anderson, P. K. Acharya, L. S. Bernstein, L. Muratov, J. Lee, M. Fox, S. M. Adler-Golden, J. J. H. Chetwynd, M. L. Hoke, R. B. Lockwood, J. A. Gardner, T. W. Cooley, C. C. Borel, P. E. Lewis, and E. P. Shettle, "Modtran5: 2006 update," *SPIE.* pp. 62331F-62338, 2006.

[227] C. A. Gueymard, "Smarts, a simple model of the atmospheric radiative transfer of sunshine: Algorithms and performance assessment ", 1995.

[228] A. W. Haas, “Design of a GaInP/GaAs tandem solar cell for maximum daily, monthly, and yearly energy output,” *J. Photon. Energy*, vol. **1**, no. 1, pp. 018001, 2011.

APPENDICES

A. PHYSICAL CONSTANTS

Table A.1
Table of physical constants

Constant	Value	Units
c	2. 99792458x10^{8}	cm/s
q	1.602 x10^{-19}	C
k	8.6173324 x10^{-5}	eV/K
h	4.135667516 x10^{-15}	eV s
m	9.10938188x10^{-31}	kg

B. SIMPLE TEMPERATURE DENPENDENT MODELS

B.1 Estimating the Short Circuit Current Density

Creating reliably solar cell models that can be embedded into optics simulation tools have proven to be very useful to optics and system designers [159]. By simulating the optics and solar cells together, the system designers are able to evaluate tradeoffs and predict real world performance of the complete solar module. The author has published four papers on creating these simple embeddable solar cell models. Paper 1 explored the capability of these models [205]. Papers 2 and 3 extended these models to work over a large range of geometric concentrations [56, 206]. Paper 4 focused on adding temperature dependent $J_{SC}(T)$ to these models, which can be found in [117]. This allowed the solar cell operating temperature, T, to be including in the calculation, which is important optimizing real world performance.[1]

B.1.1 Temperature Dependent J_{SC}

As discussed in section 2.4.1, curve-fits have been applied to experimentally measured J_{SC} values over a range of temperatures [164, 207, 208], while these types of models do estimate the J_{SC} as a function of temperature, they do not incorporate a way for the spectrum modeled to change.

$$J_{SC} = q\int \frac{\phi_i(\lambda)}{hc/\lambda} IQE(\lambda) d\lambda \qquad \text{(B.1)}$$

Here $\phi_i(\lambda)$ is the wavelength dependent photon flux density that is not reflected off of the front surface of the solar cell and not blocked by the grid lines [209].

[1] Sections B.1.1 through B.1.3 are based on the paper "A method for estimating temperature dependent short circuit current" by J. R. Wilcox A. W. Haas, J. L. Gray and R. J. Schwartz, which was published in the *Photovoltaic Specialists Conference* (PVSC) proceedings, *2011* 37th IEEE ({Wilcox, 2011 #95}).

The EQE can be measured or modeled. Without this method for estimating the J_{SC}, EQE would need to be measured at every temperature of interest. This method can be combined with existing $V_{OC}(T)$ and $FF(T)$ models to calculate the efficiency of the solar cells by Fan and others [52, 104].

B.1.2 Quantum Efficiency

Factors that significantly affect the quantum efficiency include shadowing, Fresnel reflection, absorption, transmission and recombination. Other factors include photon coupling, actual shape of the absorption curve, standing waves and dead layers. Of these factors photon absorption appears to be the most significant temperature effect for many high quality solar cells [164].

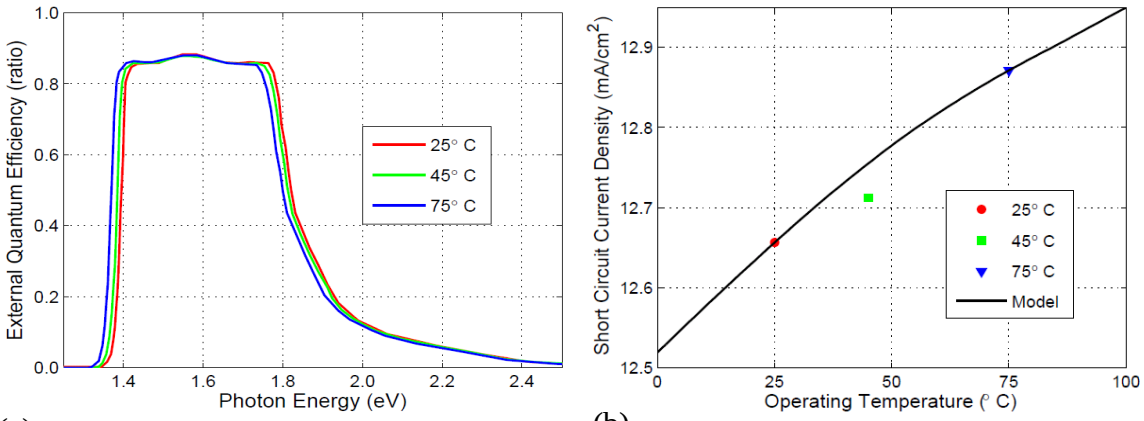

(a) (b)

Figure B.1. (a) GaInAs EQE measured at a range of temperatures. Both the low and high energy portions of the EQE are temperature dependent. (b) Comparison of the GaInAs $J_{SC}(T_O)$ calculated using EQE measured at three temperatures, with the 25º C EQE shifted over a range of operating temperatures (after [117] © 2011 IEEE).

B.1.3 Optical and Electrical Bandgap Comparison

This equation requires the bandgap energy [210]

$$E_G(T) = E_{G\_0K} - \frac{\alpha T^2}{\beta + T}, \tag{B.2}$$

which can be calculated using material dependent parameters α and β, as well as the bandgap energy at 0 K, E_{G_0K}. These parameter varies widely between semiconductor materials. This is one method for calculating the bandgap energy, other methods for calculating the bandgap will be covered in section 6.3.4.1.

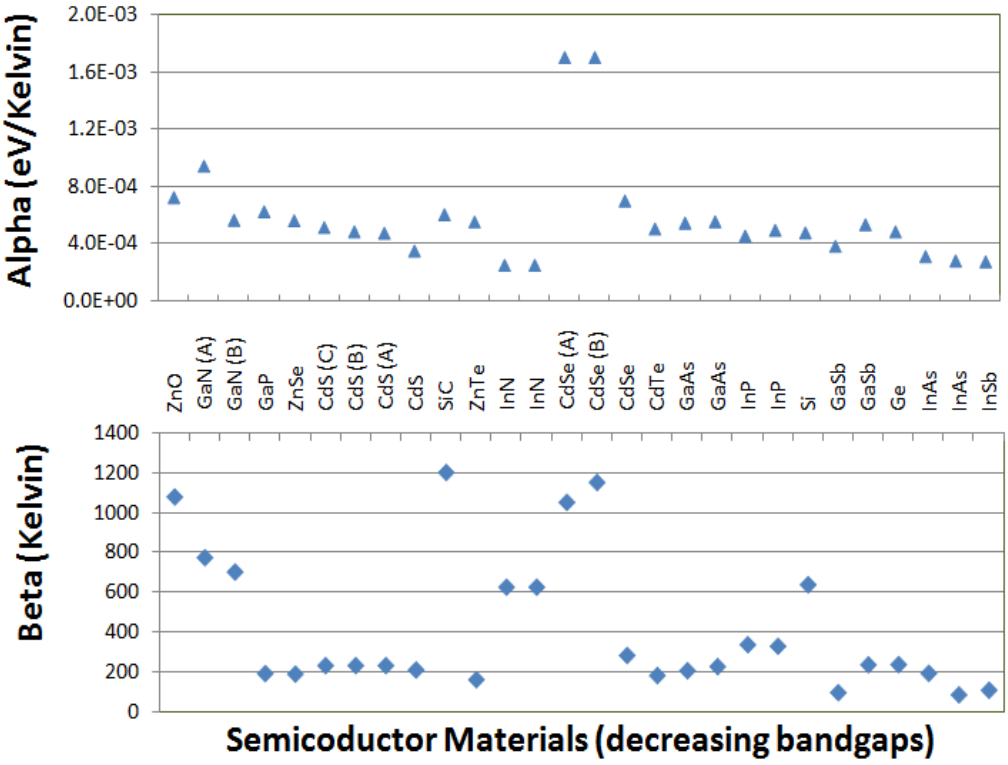

Figure B.2. Varshni bandgap coefficients for a wide variety of semiconductor materials. (after [117] © 2011 IEEE).

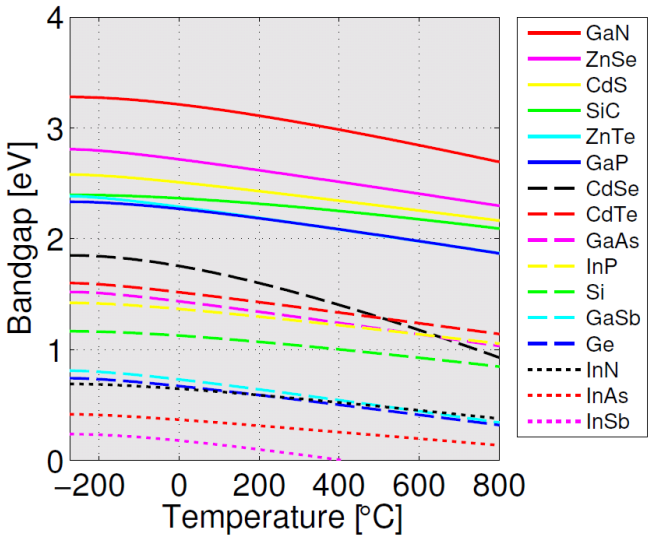

Figure B.3. Bandgap energy temperature dependence for a wide variety of semiconductor materials in Figure B.2.

The calculated electrical $\Delta E_G(T_O)$ for the Ge indirect [211], Ge direct [212], GaIn0.03As0.97 direct [213] and GaInP direct [208] bandgaps, are plotted with the optical $\Delta E_G(T_O)$ extracted from the measured GaInP/GaInAs/Ge tandem stack EQE reported by Kinsey, *et al.* [164] are shown in Figure B.1. The Ge EQE was cutoff near the bandgap so the optical ΔE_G could not be calculated.

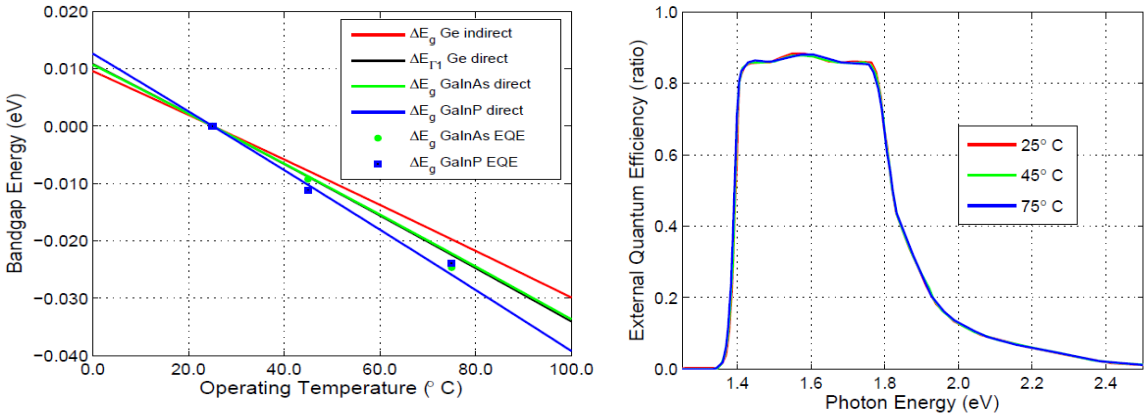

(a) (b)

Figure B.4. (a) Calculated electrical $\Delta E_G(T_O)$ for the GaInP, GaInAs and Ge bandgaps in this tandem solar cell, and measured EQE optical $\Delta E_G(T_O)$ for GaInAs and GaInP. (b) GaInAs EQE shifted by GaInAs electrical $\Delta E_G(T_O)$ to 25° C (after [117] © 2011 IEEE).

This method makes it possible to use an EQE measured at one temperature to estimating the $J_{SC}(T)$ over a range of temperatures.

B.2 Estimating the Reverse Saturation Current Density

A method for estimating the reverse saturation current over a short temperatures range of interest has been developed by the author[2]. This method only requires the saturation current density at 300 K, the bandgap at 300 K and the expected operating temperature of the solar cell. These simple embeddable compact models have proven to be very useful to optics and system designers [159, 205]. This model can be used before specific materials are chosen and material dependent parameters are known. This method is useful for approximating the optimal bandgaps in multijunction concentrator solar cells, for an average spectrum or to maximize yearly energy. Then more accurate models can be used to fine tune the bandgaps.

[2] Sections B.2.1 through B.2.2 are based on the paper "Estimating saturation current based on junction temperature and bandgap" by J. R. Wilcox A. W. Haas, J. L. Gray and R. J. Schwartz, which was published in the *7th International Conference on Concentrating Photovoltaic Systems, 2011* ({Wilcox, 2011 #99}). ©2011 PSE AG.

The development of this curve-fit method is a five step process. First, the state-of-the-art J_O fit is used to calculate the J_O for each of the semiconductors under considerations at 300 K. Second, K_P is found using equation (B.3) for each of these materials at 300 K. Third, the bandgap for a range of temperatures is found using the data plotted in Figure B.2 (a), these bandgaps are then used to calculate J_O using equation (B.3) for each material over the range of temperatures. This assumes that the K_P does not change with temperature. Fourth, slope intercept curve-fits are applied over the range of materials at each temperature. Fifth, polynomial curve-fits are applied to the slope and then to the intercepts over temperature. The terms of the *S'* and *I'* polynomials are given in Table 5.1 and Table 5.2, which are used in Equation (5.5) and then Equation (5.4).

B.2.1 J_O Thermal Effects

Each of the three common recombination mechanism, Radiative, SHR and Auger recombination can be written in this general form of the J_O, which contains a variety of temperature dependencies [52, 63].

$$J_O(T, E_G(T)) = K_P(T) T^{3/n} \exp\left[\frac{-E_G(T)}{n\,kT}\right], \tag{B.3}$$

Here $K_P(T)$ is constants and additional temperature dependencies specific to the recombination mechanism. This equation is derived in Section 3.1.8. This equation requires the bandgap energy. One method for calculating the bandgap energy was described in section B.1.3, other methods for calculating the bandgap are covered in Section 6.3.4.1.

B.2.2 J_O Curve-Fit Model

Pseudo data was generated for the materials in Figure 5.2, using the J_O in Section B.2.1. $K_P(T)$ was assumed to be temperature independent, n was assumed to be 1 and a state-of-the-art curve-fit was used for the J_O at 300 K [87].

$$J_O\left(300\ K, E_{G,300\ K}\right) = exp\left(-40.5\ E_{G,300\ K} + 20.8538\right) \quad \text{(B.4)}$$

Other models such as the Shockley-Queisser limit can be used to calculate the J_O at 300 K.

The data was fit using polynomials for the slope, $S(T)$, and intercept, $I(T)$ inside of the exponential term $K_O(T)$.

$$J_O\left(T, E_{G,300\ K}\right) = K_O(T) J_O\left(300\ K, E_{G,300\ K}\right) \quad \text{(B.5)}$$

$$K_O(T) = exp\left(S'(T) * E_{G,300\ K} + I'(T)\right) \quad \text{(B.6)}$$

The J_{SC} can be estimated by using a linear fit [207] or by shifting the IQE [117]. The difference between the pseudo data and the curve-fit model described was approximately ½kT at 350 K.

C. SIMPLE ANALYTICAL AND NUMERICAL METHODS FOR FINDING THE TERMINAL CHARACTERISTICS

The terminal characteristics are used to analyze the performance of solar cells. The most commonly used terminal characteristic for characterized solar cells are the short circuit current for the open circuit voltage, V_{OC}, the maximum power current J_{MP} maximum power voltage, V_{MP} the fill factor , FF and the conversion efficiency ,η. The FF is defined as

$$FF = \frac{J_{MP}V_{MP}}{J_{SC}V_{OC}}, \tag{C.1}$$

and η is defined as

$$\eta = \frac{J_{MP}V_{MP}}{P_{In}}, \tag{C.2}$$

where P_{In} is the incident power.

These parameters make it easy to compare solar cells, and they are commonly measured empirically and simulated. This appendix will describe a variety of approaches to solve for these characteristics.

Solar cells can be simulated using a variety of models, which can be divided into analytical model and numerical models. When solar cells are modeled numerically, the terminal characteristics will be extracted from the numerical solution. When simulating solar cells with analytical models, it would be preferable to be able to solve for all of the terminal characteristics analytically, however due to the multiple non-linarites in solar cells, this is not always possible.

The vast majority of solar cell models first solve for J_{SC} and then use it to estimate the other terminal characteristics. Methods for finding the J_{SC} were described in Sections 3.1.4 and Appendix B.1. The most common analytical model is the ideal diode equation, which is also called the intrinsic diode model. Often, series resistance, R_{Series}, shunt resistance, R_{Shunt}, and a semiconductor ideality factor are used added allow the analytical

model to more closely match measured *J-V* curves. This is often called the extrinsic diode model.

Since the dominate recombination mechanism can change as the terminal voltage of the solar cell changes, 2 or more diodes in parallel have been used to more closely match the measured devices over the entire *J-V* curve. When a single diode model is used to fit a measured devices with a changing dominate recombination mechanism, R_{Series}, R_{Shunt} and n are used to force the *FF* of the model to match the measured device. This leads to a *J-V* curve that matches the J_{SC}, V_{OC} and *FF*, but does not match well over the rest of the *J-V* curve. It is even more difficult to use a single diode to simulate a solar cell over a range of temperature or solar concentration. Furthermore, it would be valuable to be able to solve for the terminal characteristics for multiple junctions connected in series.

The terminal characteristics are typically found using analytical approximations, fitting analytical models or found numerically. The analytical approximations can be used on single diode models which will be summarized in Section C.1. Often when these analytical models can not be used, various Newton Methods are used to numerically estimate the terminal characteristics. Section C.2 will summarize a set of approaches that can be used to solve for the terminal characteristics in a variety of cases using bisection approaches. Some of these methods can be used to when multiple junctions are connected in series.

C.1 Analytical Approximations

Simple analytical approximations are by far the easiest way to estimate the terminal characteristics. When modeling a single diode, the V_{OC} can be found analytically.

$$V_{OC} = \frac{nkT}{q} \ln\left(\frac{J_{SC} + J_O}{J_O} \right), \tag{C.3}$$

where n is the semiconductor ideality factor, k is Boltzmann's constant, T is the temperature, q is the electric charge and J_O is the saturation current density.

A variety of analytical approximations have been developed by Martin Green and others, these analytical approximations are highly accurate and are summarized in a paper by Green [111]. These approximations can be used when modeling a single diode.

Not only are these approximations highly accurate for a wide variety of conditions, they can also be used over a broad range of temperatures. The V_{OC} used is normalized by nkT/q therefore the terminal characteristic can be calculated so long as the normalize V_{OC} is within the allowed range.

C.2 Numerical Solutions

A variety of numerical models have been developed to approximate the *FF*. Commonly various Newton methods have been used for a variety of cases [214]. While this is a straight forward approach for solving for the terminal characteristics, it can also be computational intensive when simulating a large number of simulations.

A number of bisection methods have been developed at Purdue to find the *FF*, for various cases. These methods converge to the solution in log *O* iterations and can calculate the solution to the desired level of precision. This is a great benefit when simulating a large number of scenarios for parameter studies.

A summary of these approaches are shown in Table C.1 Shows under what conditions each of the bisection approaches can be used numerically finding the *FF*., where *N* is the number is the number of junctions connected in series and *M* is the number of diode connected in parallel. The approach in Section C.2.1 was developed by Gray [215], this approach was used to find the terminal characteristics in [87]. The remaining approaches were developed by the author.

Table C.1
Shows under what conditions each of the bisection approaches can be used numerically finding the *FF*.

Section	Parasitic resistance		Junctions	Parallel connected diodes
	R_{Series}	R_{Shunt}		
C.2.1 [215],	finite	∞	*N*	1
C.2.2	0	finite	1	*M*
C.2.3	finite	finite	1	*M*
C.2.4	finite	∞	*N*	3
C.2.5	finite	finite	*N*	M

Care must be taken when using bisection or Newton's method to find the terminal characteristics. A local maximum can be found if the analytical model causes more than one peak in the power out, *P*.

C.2.1 Bisection Approach: *N* Junctions with 1 Diode in each Junction and Infinite Shunt Resistance

A bisection approach was developed by Gray [215], which can find the J_{MP} and V_{MP} of a series connected tandem solar cell with *N* junctions with 1 diode simulating each junction and finite R_{Series}.

This approach can solve for J_{MP} and V_{MP} to a desired level of precision log *O*., where *O* is the number of simulation points needed to reach the desired precision. The equation for one junction is,

$$J = J_{SC} - J_O\left[\exp\left(\frac{q(V + JR_{Series})}{nkT}\right) - 1\right] - \frac{V + JR_{Series}}{R_{Shunt}}. \qquad \text{(C.4)}$$

Next, solve for *V* and sum the voltage from each junction in series when R_{Shunt} =0.

$$V = \sum_{j=1}^{N}\left\{\frac{n_j kT}{q}\ln\left(\frac{J_{SC} + J_{O,j} - J}{J_{O,j}}\right)\right\} - JR_{Series}, \qquad \text{(C.5)}$$

Where J_{SC} is the short circuit current for all of the series connected tandem solar cell junctions. The V_{OC} can be found when the J through each of the junctions in the stack is zero.

$$V_{OC} = \sum_{j=1}^{N} \left\{ \frac{n_j kT}{q} \ln\left(\frac{J_{SC} + J_{O,j}}{J_{O,j}} \right) \right\}, \tag{C.6}$$

Insert Equation (C.5) into the power out equation.

$$P = JV = J \sum_{j=1}^{N} \left\{ \frac{n_j kT}{q} \ln\left(\frac{J_{SC} + J_{O,j} - J}{J_{O,j}} \right) \right\} - J^2 R_{Series}, \tag{C.7}$$

Take the derivative of P with respect to J.

$$\frac{dP}{dJ} = \sum_{j=1}^{N} \left\{ \frac{n_j kT}{q} \ln\left(\frac{J_{SC} + J_{O,j} - J}{J_{O,j}} \right) \right\} - \sum_{j=1}^{N} \left\{ \frac{n_j kT}{q} \frac{J}{\left(J_{SC} + J_O - J \right)} \right\} - 2JR_{Series} \tag{C.8}$$

Bisection can be used from 0 to J_{SC} to solve for the J that will cause Equation (C.8) to equal to zero. This J is the J_{MP}, V_{MP} can be found by solving Equation (C.5) when V= V_{MP}.

C.2.2 Bisection Approach: *M* Number of Diodes and Zero Series Resistance

A bisection approach has been developed to find J_{MP} and V_{MP} for a single junction with M number of diodes (recombination mechanisms) in parallel and an R_{Shunt}. This method is not limited by the order of the ideality factor of the diodes. The R_{Series} must be equal to zero, an approach for adding R_{Series} will be discussed in Section C.2.3.

$$J = J_{SC} - \sum_{i=1}^{M} \left\{ J_{O,i} \left[\exp\left(\frac{q(V + JR_{Series})}{n_i kT} \right) - 1 \right] \right\} - \frac{V + JR_{Series}}{R_{Shunt}} \tag{C.9}$$

First assume that R_{Series}=0.

$$J = J_{SC} - \sum_{i=1}^{M} \left\{ J_{O,i} \left[\exp\left(\frac{qV}{n_i kT} \right) - 1 \right] \right\} - \frac{V}{R_{Shunt}} \tag{C.10}$$

With more than one diode in parallel, the V_{OC} can be estimated by calculating the V_{OC} of each diode individually and then assuming that the recombination mechanism with the lowest V_{OC} is the dominate recombination mechanism at the V_{OC} point. The R_{Shunt} is assumed to be infinite.

$$V_{OC} = \min\left\{\frac{n_j kT}{q}\ln\left(\frac{J_{SC}+J_{O,j}}{J_{O,j}}\right)\right\} \tag{C.11}$$

The V_{OC} can be found more accurately by using bisection to solve for the V that makes Equation (C.10) equal zero. The bisection V search range is from 0 to the largest V_{OC} for an individual recombination mechanism. This approach will always find the V_{OC}, since the R_{Shunt} will lower the V_{OC} from the ideal cases where R_{Shunt} is infinite, which was solved for in Equation (C.11).

The J_{MP} and V_{MP} can be found by inserting Equation (C.8) into the power out equation.

$$P = VJ = VJ_{SC} - \sum_{i=1}^{M}\left\{VJ_{O,i}\exp\left(\frac{qV}{n_i kT}\right) - VJ_{O,i}\right\} - \frac{V^2}{R_{Shunt}} \tag{C.12}$$

Take the derivative of P with respect to V.

$$\frac{dP}{dV} = J_{SC} - \sum_{i=1}^{M}\left\{J_{O,i}\exp\left(\frac{qV}{n_i kT}\right) + J_{O,i}\frac{qV}{n_i kT}\exp\left(\frac{qV}{n_i kT}\right) - J_{O,i}\right\} - \frac{2V}{R_{Shunt}} \tag{C.13}$$

Bisection can be used from 0 to the V_{OC} to solve for the V that will cause Equation (C.13) to equal zero. This V is the V_{MP}, J_{MP} can be found by solving Equation (C.9) when V=V_{MP}.

C.2.3 Bisection Approach: 1 Junction with *M* Number of Diodes, with Finite Series and Shunt Resistances

The bisection approach in Section C.2.2 can be used to find J_{MP} and V_{MP} for 1 junction with M diodes and R_{Shunt}, however, R_{Series} must be equal to zero. In this section the R_{Series} restriction will be removed. This is possible by using the node voltage between

the series resistor and the diode. This eliminates the need to know the value of J to solve Equation (C.9).

The first step is to substitute the node voltage, V', into the power out equation.

$$P = JV = J\left(V' - JR_{Series}\right) \tag{C.14}$$

Where the terminal voltage, V, is defined as

$$V = V' - JR_{Series}. \tag{C.15}$$

.

Now distribute the J.

$$P = JV' - J^2 R_{Series} \tag{C.16}$$

Solve for the derivative of P with respect to V'.

$$\frac{dP}{dV'} = \frac{d}{dV'}\left(JV' - J^2 R_{Series}\right) \tag{C.17}$$

Which give the terms,

$$\frac{dP}{dV'} = V'\frac{dJ}{dV'} + J - 2JR_{Series}\frac{dJ}{dV'}. \tag{C.18}$$

Need equations for $\frac{dJ}{dV'}$ and J to use bisection to find when the derivative goes to zero.

The equation for J can be found by substituting in the node voltage, $V' = V + JR_{Series}$, into Equation (C.9).

$$J = J_{SC} - \sum_{i=1}^{M}\left\{J_{O,i}\left[\exp\left(\frac{qV'}{n_i kT}\right) - 1\right]\right\} - \frac{V'}{R_{Shunt}} \tag{C.19}$$

This equation no longer contains a J in the right hand side, and therefore can be used with bisection.

Find the derivative of J with respect to V'. This equation also does not contain a J on the right hand side.

$$\frac{dJ}{dV'} = -\sum_{i=1}^{M}\left\{\frac{qJ_{O,i}}{n_i kT}\exp\left(\frac{qV'}{n_i kT}\right)\right\} - \frac{1}{R_{Shunt}} \tag{C.20}$$

Just like in Section C.2.2, with more than one diode in parallel, the V_{OC} can be estimated by calculating the V_{OC} of each diode individually and then assuming that the recombination mechanism with the lowest V_{OC} is dominate at the V_{OC} point. The R_{Shunt} is assumed to be infinite. The R_{Series} will have no effect on the V_{OC}.

$$V_{OC} = \min\left\{\frac{n_j kT}{q}\ln\left(\frac{J_{SC}+J_{O,j}}{J_{O,j}}\right)\right\} \tag{C.21}$$

The V_{OC} can be found more accurately by using bisection to solve for the V that makes Equation (C.9) equal zero, when J=0 mA/cm^2. The bisection V search range is from 0 to the largest V_{OC} for an individual recombination mechanism. This approach will always find the V_{OC}, since the R_{Shunt} will lower the V_{OC} from the ideal situation where R_{Shunt} is infinite, which was solved for in Equation (C.11).

The J_{MP} and V_{MP} can be found by using bisection from 0 to the V_{OC}, to solve for the V', which will cause Equation (C.18) to equal zero. To find J_{MP} simplify solve Equation (C.19) when $V' = V'_{MP}$, then solve for the V_{MP} at the terminal using the node voltage equation, Equation (C.15), when $V' = V'_{MP}$ and $J = J_{MP}$.

C.2.4 Bisection Approach: *N* Junctions with Radiative, Auger and SHR Recombination (Cubic Solution), and Infinite Shunt Resistance

The approach described in this section can be used with analytical models that contain *N* junctions to find J_{MP} and V_{MP}. Each junction can contain radiative, Auger and SHR recombination and each junction is connected to the next junction with an R_{Series}. This approach will not accommodate finite R_{Shunt}.

$$J = J_{SC} - J_{O,Rad}\left[\exp\left(\frac{q(V + JR_{Series})}{kT}\right) - 1\right]... \\ - J_{O,Auger}\left[\exp\left(\frac{q(V + JR_{Series})}{\frac{2}{3}kT}\right) - 1\right]... \\ - J_{O,SHR}\left[\exp\left(\frac{q(V + JR_{Series})}{2kT}\right) - 1\right] - \frac{V + JR_{Series}}{R_{Shunt}} \tag{C.22}$$

First, use a change of variable, $v' = \frac{q(V + JR_{Series})}{2kT}$, and assume that R_{Shunt} is infinite.

$$J = J_{SC} - J_{O,Rad}\left[\exp(2v') - 1\right] - J_{O,Auger}\left[\exp(3v') - 1\right]... \\ - J_{O,SHR}\left[\exp(v') - 1\right] \tag{C.23}$$

Next, distribute the saturation current densities.

$$J = J_{SC} + J_{O,Rad} - J_{O,Rad}\exp(2v') + J_{O,Auger} - J_{O,Auger}\exp(3v')... \\ + J_{O,SHR} - J_{O,SHR}\exp(v') \tag{C.24}$$

Combine all of the non-exponential terms, $j' = J - J_{SC} - J_{O,Rad} - J_{O,Auger} - J_{O,SHR}$.

$$0 = J_{O,Auger}\exp(3v') + J_{O,Rad}\exp(2v') + J_{O,SHR}\exp(v') + j' \tag{C.25}$$

The solutions of *v*' can be solved for using the general cubic polynomial solution, because each of the diode saturation current densities have the same sign, a simpler analytical solution may be available. The V_{OC} can be found using the analytical solution of the Equation (C.25) when *J* is zero. The J_{MP} and V_{MP} can be found in a similar manor to the approach described in Section C.2.1.

This approach can be used with any polynomial that has an analytical solution. There is a general analytic solution for the quartic polynomial function, which was developed by Lodovico Ferrari, through using this general solution might be more difficult than using a numerical solution. There are also solutions for specific higher order polynomials. If an analytical solution to the polynomial does not exist the roots can be found numerically. However, if an analytical solution is not available, rather than numerical solve for the roots, it might be easier to use the approach described in Section C.2.5.

C.2.5 Bisection Approach: *N* Junctions with M Diodes and a Shunt Resistance in Each Junction, with Series Resistance

The global J_{MP} and V_{MP} for the case with *N* junctions connected in series, with *M* diodes and a shunt resistance in each junction, as well as a global series resistance can be solved using an approach similar to Section C.2.3. The V_j of each junction can be found for the first bisection by using bisection to solve for when ΔJ in Equation (C.26) is equal to zero.

$$\Delta J = J_{SC} - \sum_{i=1}^{M} \left\{ J_{O,i} \left[\exp\left(\frac{qV'}{n_i kT} \right) - 1 \right] \right\} - \frac{V'}{R_{Shunt}} - J \qquad \text{(C.26)}$$

C.2.6 Sumary

In some cases it is possible to use an analytical solution to solve for the J_{MP} and V_{MP}. However, in many other cases, particularly cases involving more than one recombination mechanism, this is not always possible. In these cases, the solution can found by using a numerical solver or a brute force technique. Solving for the J_{MP} and V_{MP} using brute force can require a significant amount of CPU time compared to using a numerical solver.

The bisection approaches presented in this appendix can find the J_{MP} and V_{MP} in a variety of cases. The approaches can be used when numerical solver are not available. They also might be easier to implement and could be faster than using built-in numerical solvers.

In addition, the bisection approaches can be easily adapted to be use in other cases.

D. A METHOD FOR FINDING THE OPTIMAL MULTIPLE JUNCTION SOLAR CELLS EFFICIENCY

A method has been developed for finding the optimal peak η of independently connected multiple junction solar cell system. This method can be used to find the optimal peak η to a junction E_G resolution of 0.001 eV, from 2 to an arbitrary number of junctions. This is resolution is below the repeatability of current semiconductor growth technologies. Using a cluster of CPUs the resolution could be enhanced to 0.0001 eV or lower.

This method can also used to find the optimal peak η for series connected solar cell junctions, assuming that the J_{MP} is same in each junction at the optimal η. It may be possible to adapt this method further to eliminate the need to make this simplifying assumption.

Solving for the optimal peak η above a few junctions using brute force, testing every possible solution, is not possible due to the total number of potential solutions to evaluate. Numerical methods can be used to seek the optimal peak η for each number of junctions. However, since the solution space is not smooth, using a solar spectrum, these methods do not guaranty that the global peak η has been found. The method described in this appendix will find the global peak η. It finds the global peak η for each number of junctions, by keeping track of all of the peak η values for the case with one less junctions. This is possible due to the symmetry of the system.

D.1 Example Solution

The method starts by find the η values for the all of the possible combinations of two junctions, Figure D.1. Using these solutions it is easy to find the global peak η for 2 junctions.

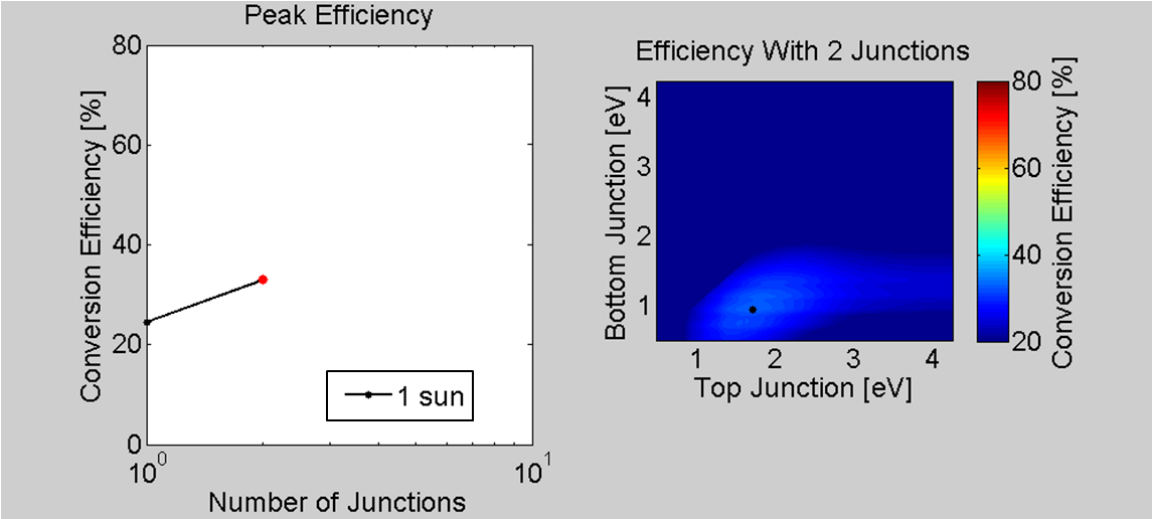

Figure D.1. The 2 junctions peak system conversion efficiency and the corresponding 2-D system conversion efficiencies plotted for all possible top junction and bottom junction combinations.

The method then uses the η solutions for the two junction case, shown in Figure D.1, to find the global peak η for the three junction cases, Figure D.2. This is done by adding a 3rd junction below the other 2 in every cases and then storing the highest η for each combination of 1st (top) junction and 3rd (bottom) junctions. The global peak η for the 3 is shown in Figure D.2.

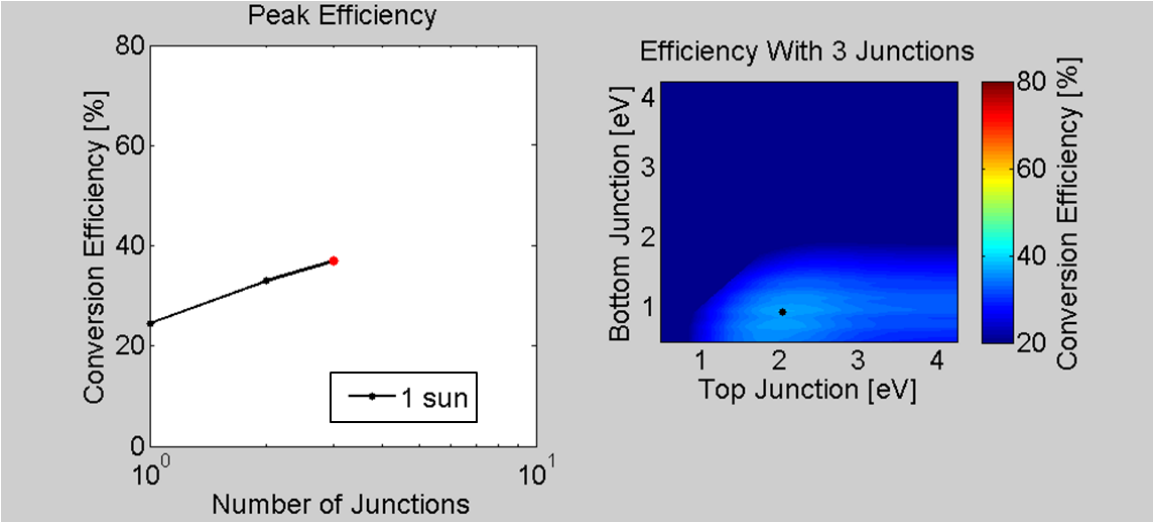

Figure D.2. The 3 junctions peak system conversion efficiency and the corresponding 2-D system conversion efficiencies plotted for all possible top junction and bottom junction combinations.

The process is then repeated by adding a 4th junction under the 3rd junction and so forth. Figure D.3 shows the peak efficiency solution for 10 junctions. The process can be continued until all of the possible bandgap energies in the model have been filled.

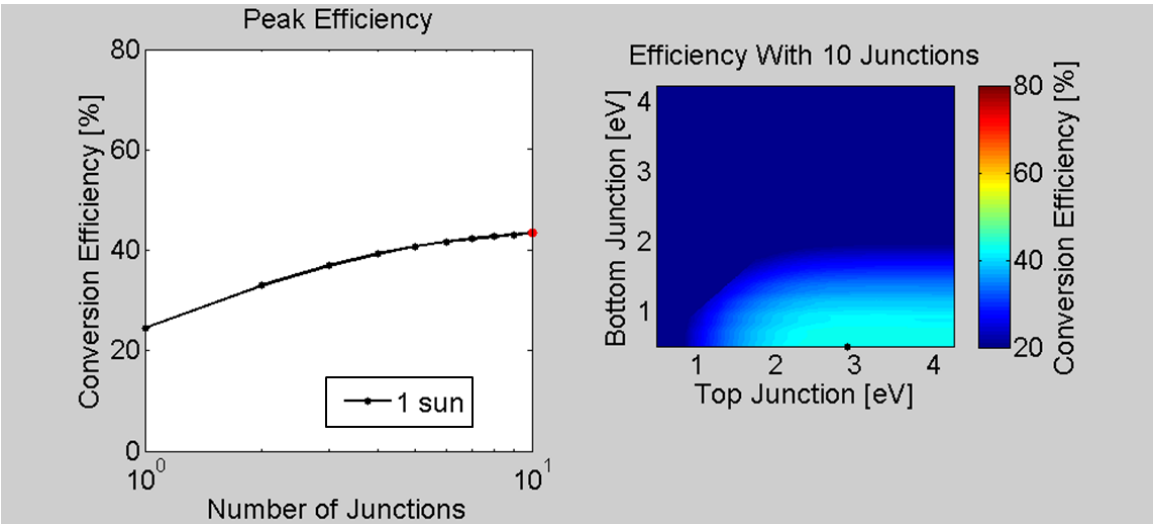

Figure D.3. The 10 junctions peak system conversion efficiency and the corresponding 2-D system conversion efficiencies plotted for all possible top junction and bottom junction combinations.

D.2 Multi-threaded

This method can be multi-threaded by solving for one top junction E_G and all of the possible bottom junction E_G at a time. This is done by finding the highest η for all possible bottom junction E_G for the one top junction E_G. This values will be stored in array for each number of junctions. The E_G of the optimal solution can also be stored in a separate array if desired. After doing the same thing for each of the possible top junction E_G, the highest η in the array for each number of junctions will be evaluated to find the global optimal peak η for that number of junctions.

E. PROPERTIES OF J-V CURVES

This appendix briefly examines the terminal characteristics and *J-V* curves of single junction solar cells. These characteristics are helpful in understanding the similarities and the differences in temperature dependencies.

E.1 Shifting the *J-V* Curves by the Difference of the V_{OC}

This section answers the question, if two *J-V* curves have the same diode ideality factor, *n*, temperature, *T* and short circuit current, J_{SC}, but different J_O values, can the first be shifted over in voltage to match the second *J-V* curve?

Voltage, *V*, of each *J-V* curve for a current, *J* (assuming R_{Shunt} is infinite) is

$$\begin{aligned} V_1 &= \frac{nkT}{q}\ln\left(\frac{J_{SC}+J_{O,1}-J}{J_{O,1}}\right)-JR_{Series} \\ V_2 &= \frac{nkT}{q}\ln\left(\frac{J_{SC}+J_{O,2}-J}{J_{O,2}}\right)-JR_{S\,Series} \end{aligned}. \tag{E.1}$$

The voltage difference, ΔV, between the curves for each value of *J*,

$$\Delta V = V_2 - V_1 . \tag{E.2}$$

Substituting in V_1 and V_2,

$$\begin{aligned} \Delta V = {} & \frac{nkT}{q}\ln\left(J_{SC}+J_{O,2}-J\right)-\frac{nkT}{q}\ln\left(J_{O,2}\right) \\ & -\frac{nkT}{q}\ln\left(J_{SC}+J_{O,1}-J\right)+\frac{nkT}{q}\ln\left(J_{O,1}\right) \end{aligned}. \tag{E.3}$$

Which can be simplifed to,

$$\Delta V = \frac{kT}{q}\ln\left(\frac{J_{O,1}}{J_{O,2}}\right)+\frac{kT}{q}\ln\left(\frac{J_{SC}+J_{O,2}-J}{J_{SC}+J_{O,1}-J}\right). \tag{E.4}$$

E.1.1 Case 1: *J* Away from J_{SC}

If J_{SC}-J >> J_{O1} and J_{SC}-J >> J_{O2}, the second term becomes zero. (Valid along most of the *J-V* curve, except when J~=J_{SC}).

$$\Delta V = \frac{nkT}{q}\ln\left(\frac{J_{O,1}}{J_{O,2}}\right) \tag{E.5}$$

E.1.2 Case 2: *J* Near J_{SC}

If J_{SC}-J ~= J_{O1} and J_{SC}-J ~= J_{O2}, Eqaution (E.4) simplifies to,

$$\Delta V = \frac{kT}{q}\ln\left(\frac{J_{O,1}}{J_{O,2}}\right) + \frac{kT}{q}\ln\left(\frac{J_{O,2}}{J_{O,1}}\right). \tag{E.6}$$

Which rewritten becomes

$$\begin{aligned}\Delta V = {} & \frac{kT}{q}\ln\left(J_{O,1}\right) - \frac{kT}{q}\ln\left(J_{O,2}\right) - \frac{kT}{q}\ln\left(J_{O,1}\right) \\ & + \frac{kT}{q}\ln\left(J_{O,2}\right)\end{aligned}. \tag{E.7}$$

All of the terms cancel.

$$\Delta V = 0 \tag{E.8}$$

Figure E.1 shows the J-V curves with the same values for J_{SC}, T and n, and different values of J_O. The curve *J-V* for $J_{O,1}$ is shifted by the difference of $V_{OC,1}$ and $V_{OC,2}$. Which shows that the shape of the two *J-V* curves are nearly identical. This figure also shows that the max power point changes as the V_{OC} changes.

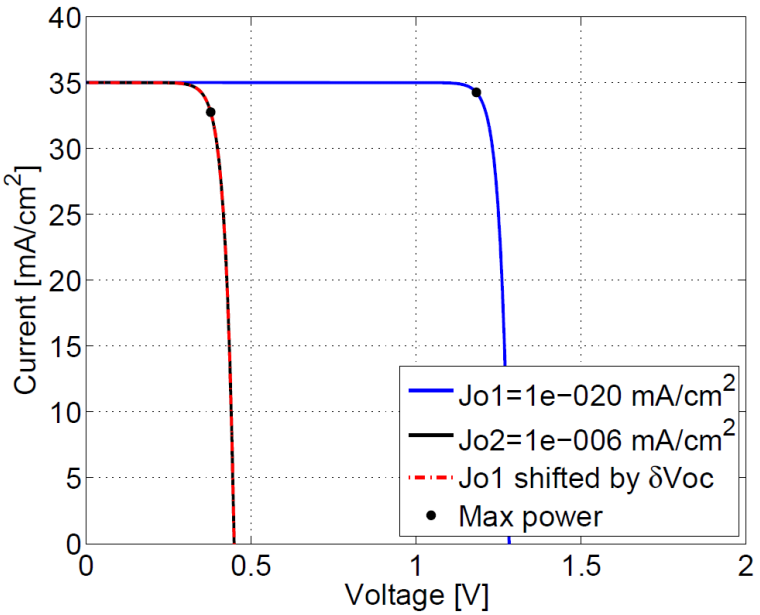

Figure E.1. The blue curve shows the *J-V* curve with the $J_{O,1}$=1x10^{-29} mA/cm^2. The red curve shows the *J-V* curve with the $J_{O,2}$=1x10^{-6} mA/cm^2. The red dot-dash line shows the $J_{O,1}$ curve shifted by the difference of $V_{OC,1}$ and $V_{OC,2}$, which matches the $J_{O,2}$ curve. The max power point changes as the V_{OC} changes.

E.1.3 Summary

How do the max power points compare for *J-V* curves with the same values for J_{SC}, *T* and *n*, and different values of J_O.

1. The max power voltage and the max power current will be unique for each value of J_O.
2. The max power point could be accurately calculated from a shifted *J-V* curve, if J_{SC}- J_{MP} >> $J_{O,2}$.

F. TEMPERATURE DEPENDENT BANDGAP NARROWING

A number of semi-empirical temperature dependent E_G narrowing fits have been developed. Each of these semi-empirical E_G fits have developed by matching measurement data. Some of these fits are a better match to the measured data over various ranges of temperature. Tyically a fit has a range over which it is a good fit of the data. Many of the Si fits in this appendix are compared in Figure 6.7.

Both the direct and indirect bandgaps in a semiconductor material change as a function of temperature. This is particularly important for semiconductor materials in which the direct and indirect bandgaps are close in energy, such a Ge.

F.1 Common Varshi equation

The Varshni equation is the most common semi-empirical temperature dependent bandgap energy equation. This equation gives a good fit to the data over a wide range of temperatures and may be favored for its ease of use [210].

$$E_G = E_{G,V}(0) - \frac{\alpha_V T^2}{\beta_V + T} \tag{F.1}$$

Here $E_{G,V}(0)$ is the bandgap energy at zero K , α_V is a coefficient and β_V is thought to be related to the Debye temperature, however in some cases, such as Diamond and SiC it can be negative [210].

Table F.1
Si and GaAs bandgap coefficients for Varshni's semi-empirical bandgap equation.

Substance	Type of Gap	$E_{G,V}(0)$ [eV]	α_V ($\times 10^{-4}$) [eV/K]	β_V [K]	Debye [K]	Recommend temperature range [K]	Ref.
Si	Indirect	1.1557	7.021	1108	645		[210]
		1.170	4.73	636			[168]
		1.1692	4.9	655			[98]
GaAs	Direct	1.5216	8.871	572	344		[210]
		1.1517	5.5	225		$20<T<500$	[216]
		1.5194	10.6	671		$2<T<280$	[217]
		1.1519	8.95	538		$10<T<300$	[218]
		1.515	5.5	255		$77<T<600$	[219]

A related function with a higher power has also been developed [220]. Coefficients for Si have not been found in the literature.

$$E_G = E_G(0) - \frac{\alpha_G T^4}{(\beta_G + T)^3} \tag{F.2}$$

F.2 Simple polynomial curve-fit

Simple polynomial curve-fit has been used to fit small portions of the Si bandgap energy temperature dependence [99].

$$E_G = E_{G,S}(0) + a_S T + b_S T^2 \tag{F.3}$$

Here $E_{G,S}(0)$ is the bandgap energy at zero Kelvin, a_s and b_s are fitting coefficients.

Table F.2
Si bandgap coefficients for a polynomial bandgap energy curve-fit.

Substance	Type of Gap	$E_{G,S}(0)$ [eV]	a_S ($\times 10^{-5}$) [eV/K]	b_S ($\times 10^{-7}$) [K]	Recommend temperature range [K]	Ref.
Si	Indirect	1.17	1.059	-6.05	$0<T<190$	[99]
		1.1785	-9.025	-3.05	$150<T<300$	[99]
		1.206	-0.273	0	250<T<415	[99]

Above 250 K a first order polynomial has been used, which predicts the bandgap within the experimental accuracy of 1 [meV], $E_{G,S}(0)$=1.206 [eV] and a_S=-2.73x10^{-5} [eV/K] [92].

F.3 Bose-Einstein equation

Bose-Einstein bandgap energy expression as a function of temperature has been used in a variety of forms [54].

$$E_G = E_{G,B}(0) - \alpha_B \left(1 + \frac{2}{e^{\theta_B/T} - 1} \right) \tag{F.4}$$

Here $E_{G,B}(0)$ is the bandgap energy at zero Kelvin, α_B and θ_B are fitting coefficients. This equation can be simplified to [221].

$$E_G = E'_{G,B}(0) - \alpha_B \left(\frac{2}{e^{\theta_B/T} - 1} \right) \tag{F.5}$$

Here $E'_{G,B}(0)$ includes the $-\alpha_B$ term. Equation (F.5) can also be rewritten [216] [217]

$$E_G = E'_{G,B}(0) - \alpha_B \coth(\theta_B / 2T). \tag{F.6}$$

Table F.3
GaAs bandgap coefficients for the Bose-Einstein physics based semi-empirical bandgap equation.

Substance	Type of Gap	$E_{G,B}(0)$ [eV]	α_B (10^{-4}) [eV/K]	θ_B [K]	Recommend temperature range [K]	Ref.
GaAs	Direct	1.571	57	240	$20<T<500$	[216]
		1.5294	10.4	102.4	$2<T<77$	[217]
		1.5620	43.3	202	$2<T<280$	[217]

These bandgap coefficients could be calculated for Si by use the coefficients for Equation (F.7).

By changing and relabeling the coefficients, Equation (F.4) can be rewritten as

$$E_G = E_{G,O}(0) - S < \hbar\Omega > \left[\coth\left(\frac{< \hbar\Omega >}{2kT} \right) - 1 \right] \qquad \text{(F.7)}$$

Table F.4
Si bandgap coefficients for O'Donnell's Bose-Einstein physics based semi-empirical bandgap equation [172].

Substance	Type of Gap	$E_{G,O}(0)$ [eV]	S	$< \hbar\Omega >$ [meV]	Recommend temperature range [K]	Ref.
Si	Indirect	1.170	1.49	25.5	$0<T<300$	[172]

F.4 Two term Bose-Einstein equation

To improve the temperature range, Pässler added a second term to the Bose-Einstein equation [103].

$$E_G = E_{G,P2}(0) - \alpha_{P2} \sum_{i=1,2} \frac{W_i \theta_i}{e^{\theta_i / T} - 1} \qquad \text{(F.8)}$$

All of the terms, except T, are fitting coefficients.

Table F.5
Si and GaAs bandgap coefficients for Pässler's Bose-Einstein physics based semi-empirical bandgap equation.

Substance	Type of Gap	$E_{G,P2}(0)$ [eV]	α_{P2} (10^{-4}) [eV/K]	θ_1 [K]	θ_2 [K]	W_1	W_2	Recommend temperature range [K]	Ref.
Si	Indirect	1.170	3.21	160	596	0.36	0.64	$2<T<415$	[103]
GaAs	Direct	1.519	4.76	90	315	0.28	0.72	$2<T<673$	[103]

F.5 Two term Bose-Einstein equation with lattice expansion

Manoogian took the two term Bose-Einstein equation a step further by adding a power term, to incorporate the lattice expansion [222].

$$E_G = E_{G,M}(0)\left(1+A_M T^{\alpha_M}\right) - B_M\left[\theta_{M1}\coth\left(\frac{\theta_{M1}}{2T}\right) - \theta_{M2}\coth\left(\frac{\theta_{M2}}{2T}\right)\right] \qquad \text{(F.9)}$$

All of the terms, except T, are fitting coefficients. The two term Bose-Einstein equation with a power term is the same as the two term Bose-Einstein equation, when A_M is zero. This equation was also simplified by [223].

F.6 Pässler equation

In addition to the term to the Bose-Einstein equation, Pässler also used a second unique equation for the bandgap energy as a function of temperature [173].

$$E_G = E_{G,P1}(0) - \frac{\alpha_{P1}\theta_{P1}}{2}\left[\sqrt[p]{1+\left(\frac{2T}{\theta_{P1}}\right)^p} - 1\right] \qquad \text{(F.10)}$$

All of the terms, except T, are fitting coefficients.

Table F.6
Si and GaAs bandgap coefficients for Pässler's semi-empirical bandgap equation.

Substance	Type of Gap	$E_{G,P1}(0)$ [eV]	p	α_{P1} (10^{-3}) [eV/K]	θ_{P1} [K]	Recommend temperature range [K]	Ref.
Si	Indirect	1.170	2.33	0.318	406	$2<T<415$	[173]
GaAs	Direct	1.519	2.44	0.472	230	$2<T<673$	[173]

F.7 Summary

While each one of these function can be used to estimate the T dependent E_G narrowing over a range of T. A particular function might match the measured data better over a particular range of T.

G. YEARLY SPECTRAL DATA

The solar spectra indent on a solar cell varies throughout each day of the year. A representative set of solar spectra throughout the year are needed to optimize the bandgaps for yearly performance.

There are many factors that contribute to this change, which includes sun spots, earth-sun distances and the aerosols in the atmosphere. These factors can vary from year to year. The most important factor is the aerosols. When the sun is low in the sky, high airmass, a significant portion of the blue photons are scattered, compared to when the sun is over head, low air mass, reducing the amount of blue light that reaches the solar cells./

The incident solar energy can be broken down into three parts; direct irradiance, the light coming directly from the sun, circumsolar irradiance, the scattered light near the sun, and diffuse irradiance, scatter from aerosols anywhere above the solar cell. In the ASTM G173-03 the direct and circumsolar is combined into one dataset and the all three sources are combined in the global dataset [108].

G.1 Related Research

The annual performance of solar cells has been calculated by a number of groups. Often these annual performance calculations are used to optimize the device performance. The proposed model will include using the extensive MPF with a numerical model to calculate the annual performance. This may be compared to more simplified methods of calculating the annual performance.

The performance of solar cells has been measured over a range of temperatures and spectra intensities by Kinsey [224].

In 2011, Wang optimized and calculated the annual performance for a 3-junction tandem device, for both the 2-terminal and multi-terminal case [225]. This work showed that when optimized, the efficiency was reduced by a smaller amount then had been previously calculated.

G.2 Measured and Simulated Spectra

The yearly spectral data was collected from modeled and measured sources and stored in a Matlab data file. The modeled data was generated using MODerate resolution atmospheric TRANsmission (MODTRAN) [226] model and the Simple Model of the Atmospheric Radiative Transfer of Sunshine SMARTS model [227]. The measured data was collected from the Atmospheric Optical Calibration System (AOCS) operated in the Solar Radiation Research Laboratory (SRRL) at the National Renewable Energy Laboratory (NREL) [25].

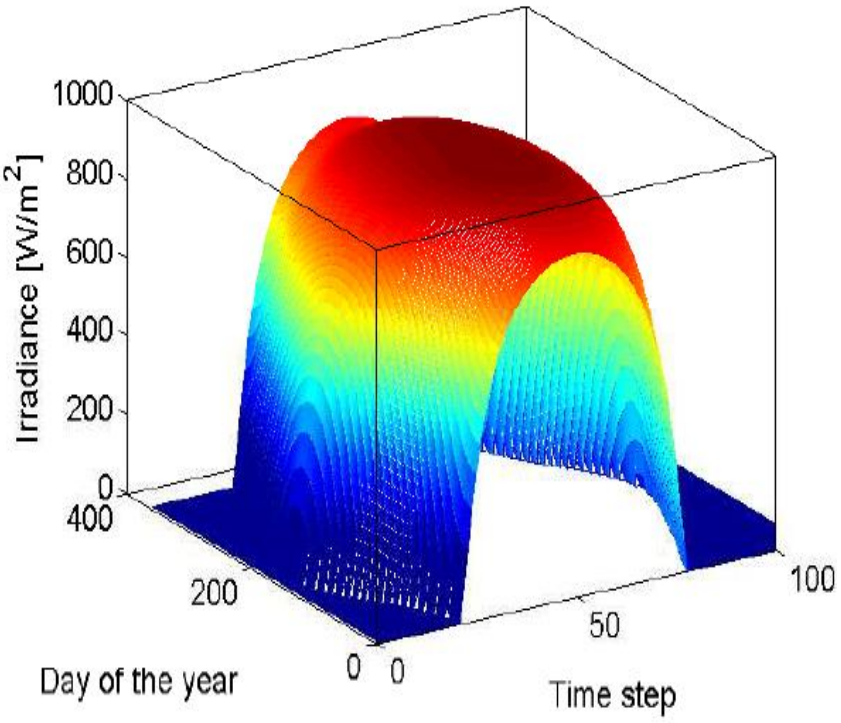

Figure G.1. Direct Normal Incidence (DNI) spectral irradiance data, every ten minutes throughout each day, for every day of the year, data collected by the report author.

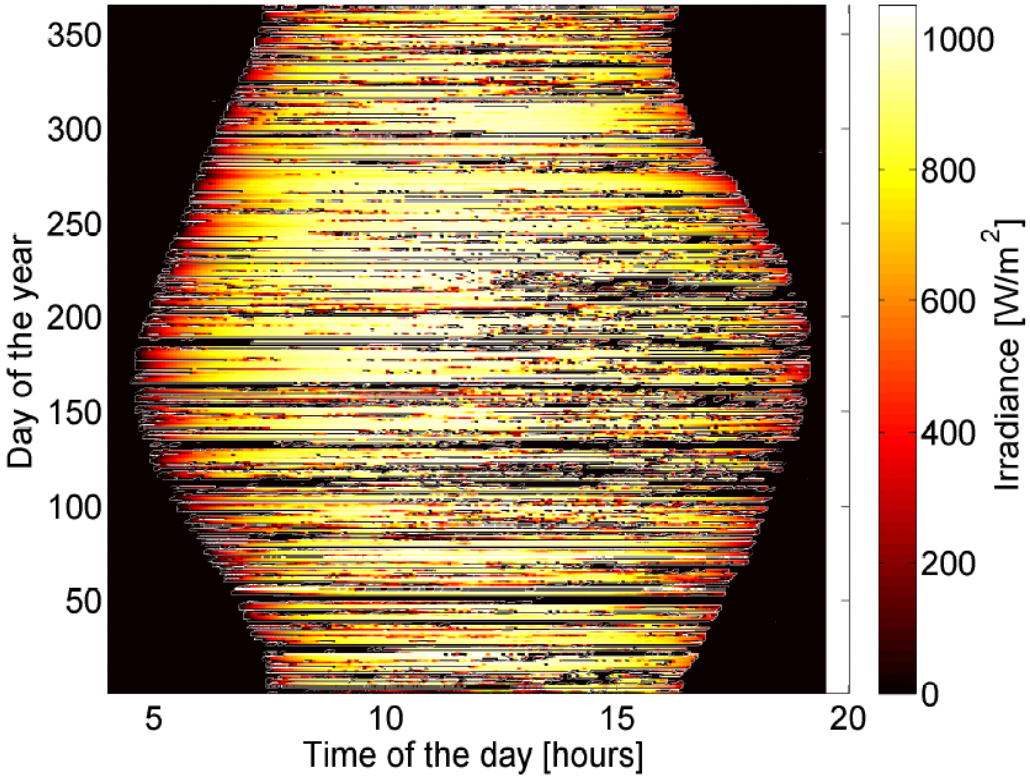

Figure G.2. DNI data measured at NREL in Golden, CO [25], data collected by the author.

The low irradance regions in the measured solar spectra shown in Figure G.2 are caused by cloud cover and other weather related events which filter the solar irradance as it passes through the atmosphere. Due to the high alitutude of Denver, CO, the measured DNI spectrum reaches well over 1000 W/m^2.

G.3 Summary

This data can be use to estimate the year energy that can be generated by a solar cell system. It can also be used to identify the sensitive of system parameters in terms of yearly energy produce. This is particularly important for multiple junction solar cells, which when connected in series will be current limited. The actual solar spectra will vary from site to site and will also vary from year to year.

This data has been used by Alex Haas to optimize a GaInP/GaAs tandem solar cells [228]. It was also used by Professor Jeffery Gray to analyze how temperature affects the optimum bandgaps in a multijunction system [215].

PUBLICATIONS

PUBLICATIONS

Raghu V. K. Chavali, John R. Wilcox, Biswajit Ray, Jeffery L. Gray, and Muhammad A. Alam, “Correlated Non-Ideal Effects of Dark and Light I-V Characteristics in a-Si/c-Si Heterojunction Solar Cells,” Journal of Photovoltaics, submitted Nov. 2013

A. W. Haas, J. R. Wilcox, J. L. Gray and R. J. Schwartz, "Numerical Modeling of Loss Mechanisms Resulting from Non-Uniform Illumination in Multijunction Concentrator Solar Cells," International Journal of Numerical Modelling, accepted Jan 2013

Jeffery L. Gray and John R. Wilcox, “The Design of Multijunction Photovoltaic Systems for Realistic Operating Conditions,” 56th International Midwest Symposium on Circuits and Systems, Columbus, OH, 2013.

Raghu V. K. Chavali, John R. Wilcox, Biswajit Ray, Jeffery L. Gray and Muhammad A. Alam, "A Diagnostic Tool for Analyzing the Current-Voltage Characteristics in a-Si/c-Si Heterojunction Solar Cells," 39th IEEE Photovoltaic Specialists Conference, 2013

J. R. Wilcox and J. L. Gray, "A Distributed Emitter Model for Solar Cells: Extracting a Temperature Dependent Lumped Series Resistance," 38 th IEEE Photovoltaic Specialists Conference, 2012

John R. Wilcox, Raghu V. Chavali and Jeffery L. Gray, "Reducing the Temperature Coefficients of Silicon and Amorphous Silicon Heterojunction Solar Cell," TECHCON 2012, Austin, TX, 2012

Raghu V. Chavali, John R. Wilcox and Jeffery L. Gray, "Analysis of Interface Trap Recombination Process in a-Si/c-Si Heterojunction Solar Cells," TECHCON 2012, Austin, TX, 2012

Raghu V. Chavali, John R. Wilcox and Jeffery L. Gray "The Effect of Interface Trap States on Reduced Base Thickness a-Si/c-Si Heterojunction Solar Cells," 38th IEEE Photovoltaic Specialists Conference, 2012

John R. Wilcox, Alexander W. Haas, Jeffery L. Gray and Richard J. Schwartz, "Estimating Temperature Dependent Terminal Characteristics", Network for Photovoltaic Technology, Annual Review, Purdue University, 2011

John Wilcox, Raghu V. Chavali, and Jeffery L. Gray, "Using Detailed Numerical Models to Analyze Photovoltaic Solar Cells" TECHCON 2011, Austin, TX, 2011

J. R. Wilcox, A. W. Haas, J. L. Gray and R. J. Schwartz, "A Method for Estimating Temperature Dependent Short Circuit Current" 37th IEEE Photovoltaic Specialists Conference 2011

A. W. Haas, J. R. Wilcox, J. L. Gray and R. J. Schwartz, "Extracting a Series Resistance fron In(Jsc)-Voc and FF-Voc Characteristics" 37th IEEE Photovoltaic Specialists Conference 2011

A. W. Haas, J. R. Wilcox, J. L. Gray and R. J. Schwartz, "Design of a GaInP/GaAs Tandem Solar Cell for Maximum Daily, Monthly, and Yearly Energy Output" J. Photon. Energy 1, 018001 (2011)

J. R. Wilcox, A. W. Haas, J. L. Gray and R. J. Schwartz, "Estimating Saturation Current Based on Junction Temperature and Bandgap" 7th International Conference on Concentrating Photovoltaic Systems 2011

Eric L. Christensen, et al., "High Efficiency Spectral Splitting Concentrating Photovoltaic System" 7th International Conference on Concentrating Photovoltaic Systems 2011

James D. McCambridge, et al., "Compact Spectrum Splitting Photovoltaic Module with High Efficiency" Progress in Photovoltaics, Progress in Photovoltaics: Research and Applications, 2010

J. R. Wilcox, A. W. Haas, J. L. Gray and R. J. Schwartz, "Solar Cell Models for Use in Multijunction Concentrating Optical Modeling Systems" 35th IEEE Photovoltaic Specialists Conference 2010

A. W. Haas, J. R. Wilcox, J. L. Gray and R. J. Schwartz, "Design of 2- and 3-Terminal GaInP/GaAs Concentrator Cells for Maximum Yearly Energy Output" 35th IEEE Photovoltaic Specialists Conference 2010

A. W. Haas, J. R. Wilcox, J. L. Gray and R. J. Schwartz, "A Distributed Emitter Model for Solar Cells: Extracting an Equivalent Lumped Series Resistance" 35th IEEE Photovoltaic Specialists Conference 2010

Jeffery L Gray, Jonathan M Schwarz, John R Wilcox, Alexander W Haas, Richard J Schwartz, "Peak Efficiency of Multijunction Photovoltaic Systems" 35th IEEE Photovoltaic Specialists Conference 2010

A. W. Haas, J. R. Wilcox, J. L. Gray and R. J. Schwartz, "Numerical Modeling of Loss Mechanisms Resulting from the Distributed Emitter Effect in Concentrator Solar Cells" 34rd IEEE Photovoltaic Specialists Conference 2009

J. R. Wilcox, A. W. Haas, J. L. Gray and R. J. Schwartz, "A Case Study of System Power Efficiency Loss Mechanisms in a Multijunction Spectral Splitting, Concentrator Solar Cell System" 34rd IEEE Photovoltaic Specialists Conference 2009

J. R. Wilcox, A. W. Haas, J. L. Gray and R. J. Schwartz, "Combining Solar Cell and Optical Modeling in Multijunction Systems" 34rd IEEE Photovoltaic Specialists Conference 2009

J. L. Gray, A. W. Haas, J. R. Wilcox and R. J. Schwartz, "Efficiency of Multi-Junction Photovoltaic Systems" 33rd IEEE Photovoltaic Specialists Conference 2008

Allen Gray, et al. "Multi-terminal dual junction InGaP/GaAs solar cells" 33rd IEEE Photovoltaic Specialists Conference 2008

John Wilcox, Dr. Robert Davis, Lei Pei, Jed Whittaker "A Study of the Selectivity of Si Dioxide and Silane for Rigid Mechanical Attachment of Carbon Nanotubes to Si Substrate" Spring Research Conference Physics and Astronomy BYU 2006

John Wilcox, Michal Lipson, Sameer Pradham, Vaidehee Padgaonkar, "Temperature Dependence of a Si Ring Resonator" Four Corners Meeting of the APS 2004

John Wilcox. Dr. Robert Davis, Dr. Matt Linford, Jed Whittaker, Mike Clemens, "Selectivity of Si Dioxide on Planner Graphite Sheets" BYU's Journal of Undergraduate Research 2003

VITA

VITA

John R. Wilcox is the son of John B. and Diane Wilcox. He graduated from Davis High School in 1999. He then attended Brigham Young University in Provo, UT, graduating with a Bachelor of Science degree in Electric and Computer Engineering in 2006. In August of the same year, he was accepted into the School of Electrical and Computer Engineering at Purdue University, and started as a Graduate Research Assistant with Richard J. Schwartz and Jeffery L. Gray. He graduated with the MSECE degree in 2009 and the Ph.D. degree in Aug, 2013. He has published numerous research papers in journals and conferences.

Wilcox was the President of the Birck Nanotechnology Student Advisory Council and Purdue's Institute for Electrical and Electronics Engineers (IEEE) Electron Device Society (EDS). He is currently a member of IEEE, IEEE EDS, and the IEEE Photonics Society. His research interests include semiconductor device physics, optoelectronics, photovoltaic devices, semiconductor temperature dependencies, numerical modeling and analytical modeling.